Opto-Acoustical Feedback System for Smart Laser Surgery

Inaugural dissertation

to
be awarded the degree of

Dr. sc. med.

presented at the Faculty of Medicine of the University of Basel

by
Hervé Nguendon Kenhagho
From Bélabo, Cameroon

Basel, 2020

Approved by the Faculty of Medicine
On application of

Professor Dr. Azhar Zam, University of Basel, *First examiner*
Professor Dr. Guzman Raphael, University Hospital Basel, *Second examiner*
Professor Dr. Philippe C. Cattin, University Basel, *Further adviser*
Professor Dr. habil. Alexander Douplik, Ph.D, *External expert*

Basel, 26.10.2020

Prof. Dr. Primo Schär
Dean

Contents

Acronyms

A: Ampere

ACT: Air-Coupled Transducer

ANN: Artificial Neural Network

AOD: acoustic-optic beam deflectometry

ASW: acoustic shock wave

BAP: balance amplified photodetector

CCD: Charge-coupled Device

cm: centimeter

CMOS: Complementary Metal–Oxide–Semiconductor

CW-laser: Continuous wave laser

dB: decibel

Er:YAG: Erbium-doped Yttrium Aluminum Garnet

FFT: Fast Fourier Transform

FP: False Positives

FPI: Fabry-Perot interferometer

FBG: fiber Bragg grating

Hz: Hertz

kHz: kilohertz

LDV: laser Doppler vibrometer

µs: microsecond

MDI: metal-dielectric interface

MHz: Megahertz

mm: millimeter

mJ: millijoule

MI: Michelson interferometer

ms: millisecond

mW: milliwatt

MZI: Mach-Zehnder interferometer

NEP: noise-equivalent pressure

NIR: Near-infrared

nm: nanometer

NUV: Near-ultraviolet

Nd:YAG: Neodimium-doped Yttrium Aluminium Garnet

ns: nanosecond

PBS: polarization beam splitter

PCA: Principal Component Analysis

PC: Principal Component

PD: Photodiode

PZT: Piezoelectric Transducer

QPD: quadrant photodiode.

SNR: Signal to Noise Ratio

SVM: Support Vector Machine

TP: True Positives

v: voltage

wt: acoustic signal duration/time

Acknowledgments

Firstly, I would like to express my sincere gratitude to my advisor, Professor Dr. Azhar Zam, for his continuous support during my Ph.D. study and related research, and for his patience, motivation, and immense knowledge. His guidance helped me throughout researching and writing this thesis. I could not have imagined having a better advisor and mentor for my Ph.D. study.

I would like to thank the rest of my thesis committee: Professor Dr. Raphael Guzman, for allowing me to depend on his insightful medical background many times; and Professor Dr. Philippe C. Cattin, for his guidance and support with all signal processing aspects and tissue classification.

I would also like to extend my thanks to all our partners at *the Center for Medical Image Analysis and Navigation (CIAN, Allschwil), Bio-Inspired RObots for MEDicine-Laboratory (BIROMED-Lab, Allschwil), Planning & Navigation team, and Swiss Federal Laboratories for Materials Testing and Research (EMPA, Thun)* for working together in a trusting and fruitful atmosphere; in particular, Dr. Kilian Wasmer and Professor Dr. Georg Rauter for their insightful comments and encouragement, and for asking the hard questions, which motivated me broaden the scope of my research to cover various perspectives.

To my fellow lab mates at the *Biomedical Laser and Optics Group* (*BLOG, Allschwil*), thank you for the stimulating discussions, for the sleepless nights we spent working together to meet deadlines, and for all the fun we have had in the last four years.

Last but not the least, I would like to thank my family: my wife, my parents, and my siblings for supporting me spiritually throughout the thesis process and my life in general.

Summary / Zusammenfassung

Summary

Characterizing acoustic shock waves (ASWs) for tissue differentiation is of vital interest for developing an opto-acoustical feedback system during laser surgery. This is particularly true if the laser system is not controlled by an *in situ* and real-time feedback control system that is not only able to differentiate specific types of human tissues but can automatically stop.

The research presented in this thesis focused on developing an opto-acoustical feedback sensor and on designing an efficient optical method for detecting ASWs for tissue differentiation. The method has advantages to extract physical properties of tissues based on measured ASW features. Some of them are the shock wave rising- and falling-time and the acoustic amplitude-spectrum extracted from the measured emitted shock/acoustic signals.

The work included novel aspects, such as measuring the ASWs generated using advanced custom-made optical technologies, characterizing the measurements by looking at the amplitude frequency band which provides the least average classification error. We used principal component analysis (PCA) combined with advanced signal processing to classify tissue types. Since PCA allows us to keep essential features (variance) of data by reducing their dimensionality, we expected to shorten the time needed to train a classifier and to avoid overfitting (less accuracy when classifying the validation data as compared to the training data) [1]. In this case, the first principal components (PCs) are dominated by the high-variance variables and mostly represent variance— i.e. the acoustic amplitude-spectrum of tissues — of each data.

The approach evolved over three steps. In the first step, four tissue types were initially classified during laser ablation by measuring the ASWs generated with a conventional air-coupled transducer and by processing the information using the Mahalanobis distance method [2]. Later, five tissue types were classified using an artificial neural network (ANN), and quadratic or Gaussian support-vector machine methods (SVM) combined with principal component analysis (PCA) during classification experiments [3]. It was possible to differentiate hard tissue from soft tissue types, but distinguishing between soft tissues remained a challenge.

In the second step, classification errors between soft tissue types were reduced. This was made possible by building a Mach–Zehnder interferometer that acts as a high-frequency microphone to provide accurate measurements of ASWs [4]. PCA and the Mahalanobis distance method were used to differentiate among scores of measured ASWs. The results of this study demonstrated a promising technique for differentiating tissues during laser osteotomy.

The final step was to design and build a fiber-coupled Fabry-Pérot etalon sensor as an alternative compact optical sensor for measuring ASWs. The miniaturized etalon cavity was built to fit into a 5 mm diameter endoscope for minimally invasive smart laser osteotome [5]. The collected data were subsequently investigated by looking at the amplitude frequency band to find the minimum classification error. Tissue classification was performed using PCA combined with the artificial neural network. Based on these results, we argue that this method can be used in endoscopic applications for tissue classification.

This study was part of the Minimally Invasive Robot-Assisted Computer-guided LaserosteotomE (MIRACLE) project. Thus, measuring ASWs using a custom-made fiber-optical-based acoustic sensor for tissue classification was the main goal of this research.

Zusammenfassung

Die Charakterisierung der akustischen Stoßwelle (ASW) zur Gewebedifferenzierung ist für das opto-akustische Rückkopplungssystem während der Laserchirurgie von entscheidendem Interesse. Dies gilt insbesondere dann, wenn das Lasersystem nicht von einem in-situ- und Echtzeit-Rückkopplungsregelungssystem gesteuert wird, das nicht nur bestimmte Arten von menschlichem Gewebe unterscheiden kann, sondern auch automatisch anhalten soll.

Die vorliegende Studie legte den Fokus auf die Entwicklung eines optoakustischen Rückkopplungssensors und die Herausarbeitung der besten optischen Detektionsmethode der ASW zur Gewebedifferenzierung in Echtzeit. Das Verfahren hat Vorteile, um physikalische Eigenschaften von Geweben basierend auf gemessenen ASW-Merkmalen zu extrahieren. Einige davon sind die Anstiegs- und Abfallzeit der Stoßwelle und das akustische Amplitudenspektrum, das aus den gemessenen emittierten Stoß- / akustischen Signalen extrahiert wird.

Die Arbeit umfasste neuartige Aspekte wie die Messung der ASWs, die mit fortschrittlichen maßgeschneiderten optischen Technologien erzeugt wurden, und die Charakterisierung der Messungen durch Betrachtung des Amplitudenfrequenzbandes, das den geringsten durchschnittlichen Klassifizierungsfehler liefert. Wir verwendeten die Hauptkomponentenanalyse (PCA) in Kombination mit einer fortschrittlichen Signalverarbeitung, um Gewebetypen zu klassifizieren. Da PCA es uns ermöglicht, wesentliche Merkmale (Varianz) von Daten durch Reduzierung ihrer Dimensionalität beizubehalten, erwarteten wir, die zum Trainieren eines Klassifikators erforderliche Zeit zu verkürzen und eine Überanpassung zu vermeiden (geringere Genauigkeit bei der Klassifizierung der Validierungsdaten im Vergleich zu den Trainingsdaten) [1]. In diesem Fall werden die ersten Hauptkomponenten (PCs) von den Variablen mit hoher Varianz dominiert und repräsentieren meistens die Varianz - d. H. Das akustische Amplitudenspektrum von Geweben - jeder Daten.

Hierbei werden drei Schritte des gewählten Ansatzes vorgestellt: Im ersten Schritt klassifizierten wir zunächst vier Gewebetypen während der Laserablation, indem wir die mit einem konventionell luftgekoppelten Wandler erzeugten AWSs gemessen und die Informationen mit der Mahalanobis-Distanzmethode [1] verarbeitet haben. In späteren Ansätzen klassifizierten wir im Rahmen von Klassifikationsexperimenten fünf Gewebearten unter Verwendung des künstlichen neuronalen Netzwerks (Artificial Neural Network/ANN), quadratischer oder Gauß-Support-Vector-Machine-Methoden (Support Vector Machine – Methods/SVM) in Kombination mit der Hauptkomponentenanalyse (Principal Component Analysis/PCA) [2]. Während es möglich war, Hartgewebe von Weichgewebetypen zu unterscheiden, blieb die Unterscheidung zwischen Weichgeweben eine Herausforderung.

Im zweiten Schritt konnten wir die Klassifizierungsfehler zwischen Weichteiltypen reduzieren. Dies war möglich, indem ein Mach-Zehnder-Interferometer gebaut wurde, das als Hochfrequenzmikrofon reagiert, um genaue Messungen von ASWs zu ermöglichen [3]. Wir verwendeten PCA und die Mahalanobis-Distanz-Methode, um die Scores der gemessenen ASWs zu differenzieren. Die Ergebnisse dieser Studie zeigten, dass dies eine vielversprechende Technik zur Differenzierung von Geweben während der Laserosteotomie ist.

Basierend auf dem Interferometer Ansatz bestand der dritte Schritt darin, einen fasergekoppelten Fabry-Pérot Etalon Sensor als alternativen, kompakten optischen Sensor zur Messung von ASWs zu entwerfen und zu bauen. Die miniaturisierte Etalon-Kavität wurde so

konstruiert, dass sie in ein Endoskop mit 5 mm Durchmesser für ein minimal invasives Smart-Laser-Osteotom passt [4]. Die gesammelten Daten wurden anschließend untersucht, indem das Amplitudenfrequenzband betrachtet wurde, um den geringsten Klassifizierungsfehler herauszufinden. Gewebeklassifizierungen wurden unter Verwendung der Hauptkomponenten-analyse (PCA) in Kombination mit dem künstlichen neuronalen Netzwerk (ANN) durchgeführt. Basierend auf den Ergebnissen argumentieren wir, dass diese Methode bei endoskopischen Anwendungen zur Gewebedifferenzierung eingesetzt werden kann.
Diese Studie war Teil des Projekts MIRACLE (Minimal Invasive Robot-Assisted Computer-Guided LaserosteotomE). Daher war die Messung von ASWs mit einem maßgeschneiderten faseroptischen akustischen Sensor zur Gewebeklassifizierung das Hauptziel dieser Forschung.

Chapter 1

Introduction

1.1. Motivation

Standard procedures in orthopedic surgery and tumor removals rely on mechanical tools, such as saws, drills, and hammers. These standard surgical tools present significant limitations in terms of accuracy (due to the dimensions of the tools and workspace required), high mechanical load, and severe mechanical vibrations, resulting in heat formation that damages the surrounding tissues [6, 7]. These limitations lead to long operation times and a long wound-healing process [6, 8, 9].

Avoiding heat damage would improve bone cutting procedures, a highly desired aspect in the field of cranio-maxillofacial surgery, orthopedics, traumatology, neurosurgery, otolaryngology, and spinal column surgery. Lasers offer a number of advantages over conventional mechanical tools in bone surgery, such as functional cutting geometry for complex cuts, non-contact interaction, less trauma, and faster wound healing. Depending on the laser's parameters (i.e. pulse duration and wavelength), surface or deep ablation can occur with minimal temperature dissipation in and around the crater. In other words, when using lasers at a wavelength of 2940 nm, deep ablation can occur; this is not the case at 532 nm, where only surface-level ablation is possible. That is why the laser considered most effective for bone surgery is an Er:YAG (Erbium-doped Yttrium Aluminum Garnet) laser source operating at 2940 nm [10, 11]. The Er:YAG laser's operation wavelength corresponds to the highest absorption peak of water and hydroxyapatite, the main component of bone, inducing high ablation efficiency [12, 13]. In contrast to the Er:YAG, the Nd:YAG (Neodimium-doped Yttrium Aluminium Garnet) laser source operating at 532 nm is transparent in water and seems well suited for tissue ablation with a substantial water layer, such as for knee arthroscopy [12, 14]. Combining the Er:YAG or Nd:YAG laser with an endoscope for minimally invasive surgery and with a feedback system for efficient tissue classification would reduce the probability of undesirable tissue damage, thereby enhancing the possible applications of laserosteotomy for the benefit of patients.

Consequently, a study can be directed towards developing a real-time feedback system, capable of identifying the type and properties of the tissues being cut and small enough to be embedded in an endoscope. Ablating tissues with a laser generate acoustic shock waves (ASWs), also known as pressure waves, originating from tissue expansion, plume/plasma expansion, phase transformation, crack formation and ASW propagation.[15-17]. The ASWs emitted mainly depend on the physical properties of the ablated material. Thus, ASWs can be used to further enhance laser osteotomy by providing real-time feedback for tissue classification to avoid damaging vital tissue. Previously, ASWs were measured using conventional

transducers or microphones [18]. Due to the limited bandwidth of commercially available transducers or microphones (not available at near Direct Current (DC) -1 MHz), this method suffers from significant distortions when measuring ASWs and the wave rise time is often overestimated because the spectra of the shock waves extend beyond 1 MHz [19-21]. Therefore, an alternative acoustic sensor system with a usable bandwidth beyond the required spectra range is needed.

In the course of exploring sensors that respond to sharp changes in pressure, a usable bandwidth for optical microphones (interferometer) was developed. The optical method has an estimated bandwidth at near DC-2.5 MHz, which provides more detailed information about the frequency response of the ASWs measured [20, 22]. Interferometry-based techniques are low-cost and offer the most sensitive optical sensor to improve the accuracy of ASW measurements in air [23]. This research took place under the MIRACLE —Minimally Invasive Robot-Assisted Computer-guided LaserosteotomE — project, which aims to develop a robotic endoscope to accomplish contactless bone surgery with smart laser light. Combining laser surgery with endoscopy (minimally invasive surgery) opens the door to an expanded set of medical applications that will ultimately benefit doctors and patients alike. Thus, measuring ASWs using a custom-made fiber-optical-based acoustic sensor for tissue classification was the main goal of this research.

An additional goal was to develop an advanced signal analysis to differentiate bone from surrounding tissues in real time. The method sought to extract the physical properties — i.e. the acoustic amplitude-spectrum — of tissues based on the total variance (i.e. principal component analysis; PCA) of the laser-generated ASWs measured during tissue ablations. This was made possible by extracting and comparing the PCs of ASWs previously stored in our own database to real-time wave measurements. In this way, the method could provide high specificity in laser cutting and prevent the cutting of important and critical tissues. Such a feedback mechanism would therefore help the surgeon to specifically determine the tissue being cut and stop the laser when all of the desired tissues have been removed.

1.2. Contribution

Tissue types — hard and soft bone, muscle, fat and skin from five proximal and distal fresh porcine femurs — were classified using conventional air-coupled transducers (ACTs) and new optical methods like fiber Bragg grating (FBG), for smart laser surgery under both wet and dry conditions [4, 24]. It was found that tissue ablated with a spray irrigation produced very few cracks and minimal thermal damage around the craters, which would ultimately lead to accelerated bone healing. In addition, the classification error, based on the spectral ASW detection from tissues ablated in wet conditions, was less when measured by an FBG compared to an ACT.

This thesis describes a new method of tissue classification using a custom-built Mach-Zehnder interferometer-based sensor during laser osteotomy [25]. Based on the interferometer approaches presented, a first prototype was built to miniaturize the opto-acoustic sensor system using fiber optics [4]. An optimal algorithm for differentiating tissues based on measured ASWs was also investigated for a smart laser surgery system. PCA served to reduce the data from the ASWs measured. This study demonstrates that fiber-coupled Fabry-Pérot interferometer-based optoacoustic analysis, combined with pattern recognition methods, is a promising technique for differentiating hard bone, soft bone, muscle, fat, and skin tissues.

In addition, the sciatic nerve was accurately classified, distinct from other tissue types, based on the new sensor system (fiber-coupled Fabry-Pérot etalon sensor) using laser-generated

ASWs. This work demonstrates the overall opportunity for remotely classifying nerves and other types of tissues with ASW spectroscopy. Using this technology, identifying nerve tissue during femur laser surgery to prevent loss of sensation and motor function in the lower body can be achieved.

In sum, the thesis research produced a new sensor system with improved acoustic sensitivity, more usable bandwidth, a higher sampling rate, and a compact size sufficient for embedding in an endoscope to differentiate tissues during laser surgery. An enhanced algorithm-based method was also developed to automatically differentiate tissue types during real-time measurement of laser-generated ASWs.

1.3. Outline

Chapter 2 elaborates on the medical and technical background of the thesis. Chapters 3, 4, 5 and 6 present the publications arising from the research, as they were submitted to or published in peer-reviewed journals. The first publication introduces machine learning methods to differentiate ablated tissues based on the ASWs measured by a conventional air-coupled transducer sensor. The second publication proposes an improved optoacoustic sensor based on a custom-made Mach-Zehnder interferometer. The third publication describes a miniaturized optoacoustic sensor, using a fiber-coupled Fabry-Pérot etalon sensor, built to fit into a 5 mm×5 mm endoscopic robot for minimally invasive smart laser surgery. The last publication outlines the optimum method for differentiating among six important tissue types, including nerve, from a porcine femur. Chapter 7 highlights some final thoughts on the research, and shares ideas for future work in the field. The thesis concludes with some information about the author and the appendix.

Chapter 2

Background

2.1. Medical Background

In biology, the term “tissue” represents a group of cells identified in a human or an animal body. The cells within a tissue share common embryonic origins and morphological structures, and are organized in a methodical pattern that together carry out a specific function. The four basic types of tissues are epithelial, connective, muscle, and nervous [26-28] (see Fig. 1). (1) **Epithelial tissues** are tissues that protect the body by covering the exterior surface (skin) and by lining the internal cavities (mucous, serous, and synovial tissues); they perform absorption, transportation and secretion functions. (2) **Connective tissues** join the tissues of the body together and serve to support, protect, and integrate all body parts. Connective tissues include fat and other soft padding tissues, tendons, and hard bone. (3) **Muscle tissues** respond to stimulants and contract to offer movement. The three major types or muscles are skeletal, smooth, and cardiac (in the heart). (4) **Nervous tissues** permit the communication of electrochemical signals, known as nerve impulses, that propagate between diverse tissues of the body. Nervous tissues are mostly brain and nerves. The structure and function of cells aids in the study of tissues.

The tissue types used in this Ph.D. work were hard and soft bone, fat, muscle, skin, and sciatic nerve extracted from proximal and distal fresh porcine femurs. The femur was chosen because its anatomy includes complex tissue types, including hard and soft bone, muscle, fat, skin and, most importantly, the sciatic nerve [29, 30]. The sciatic nerve is responsible for motor and sensory function in the lower leg and foot [31, 32]. Fractional damage to the sciatic nerve can cause leg dysfunctions, such as weak foot movements and knee bending [33].

Beyond the sciatic nerve, individual tissues are characterized by specific functions that contribute to the overall health and maintenance of the body. A disruption of the structure is a sign of disease or injury. Such variations can be distinguished through histology, that is, the microscopic study or tomographic study of tissue appearance, organization, and function. When disease or injury is diagnosed, surgeries based on conventional mechanical tools, such as scalpels, saws, and burrs, are often used to make incisions. These standard surgical tools induce severe mechanical vibrations, resulting in heat formation that damages the surrounding tissues, leading to impaired bone regeneration [34, 35] and prolonged healing periods [36]. Avoiding this heat damage would improve tissue cutting outcomes, a highly desired innovation in the field of maxillo-facial-, neuro- and orthopedic surgery.

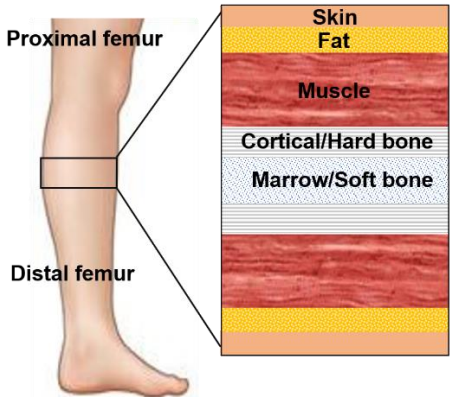

Figure 1. Four basic types of tissues

2.2. Technical Background

2.2.1. Laser-Tissue Interaction

In 1960, Maiman reported the first laser radiation applicable in multiple fields, such as medical laser surgery and biostimulation [37]. The current variety of laser systems and their diverse physical parameters make it possible to carry out numerous procedures worldwide. Among these procedures is the family of minimally invasive surgical procedures, an innovative means of contactless with less blood surgical operations. These two characteristics have propelled the laser towards extensive use as an aid in mechanical surgery and treatment. It is well-known that, in contrast to mechanical tools, laser-ablation has significant advantages, such as non-contact intervention, controlled tissue excision, free-cut geometry, and minimal invasiveness [8, 38, 39]. Several studies have investigated the fundamental processes that take place during laser ablation [40, 41].

During laser-interaction, two main types of laser can be used: the *continuous wave (CW) laser and pulsed laser*. Whereas most gas lasers and a few solid-state lasers belong to the first group, the pulsed laser group largely consists of solid-state lasers, excimer lasers, and certain dye lasers. Regardless of the laser group, it is understood that when laser interacts with matter, it can reflect, scatter, absorb or transmit, depending on the material characteristics (i.e. physical, chemical, composition, and optical properties) and the laser parameters (i.e. exposure time/pulse duration, spatial and temporal coherence, wavelength, and laser energy) [16].

Pulse duration is the most important parameter as it describes the type of interaction with biological tissues. The exposure time/pulse duration scale is grouped into five segments: (1) continuous wave or pulse duration more than 1 s (second), which yields a photo-chemical interaction; (2) 1 s – 1 µs (microsecond) pulse, which induces a thermal interaction; (3) 1 µs –1 ns (nanosecond) pulse, which permits photo-ablation; and (4) (5) pulse duration less than 1 ns, where plasma-mediated ablation and photodisruption occur, due to a photo-physical phenomenon known as optical breakdown [42]. The difference between plasma-mediated ablation and photodisruption relates to the different exposed energy densities at the surface of the tissue. Plasma-mediated ablation is principally based on ionization, while photodisruption is associated with the mechanical effect (Fig. 2). Plasma-mediated ablation is restricted to a short pulse duration, up to 0.5 ns. At longer pulse durations, up to 100 ns, photodisruption ablation occurs, as the energy density essential for accomplishing breakdown already generates important mechanical side effects (Fig. 3).

Figure 2 confirms that the total energy density applicable to medical laser applications varies at around 1 J/cm^2 – 1 kJ/cm^2. The mutual association between pulse duration and power

density reveals that similar energy densities are essential for any type of proposed interaction. Thus, pulse duration appears to be accountable for the different interaction mechanisms. Table 1 summarizes the laser-tissue interactions and applications established during the investigation.

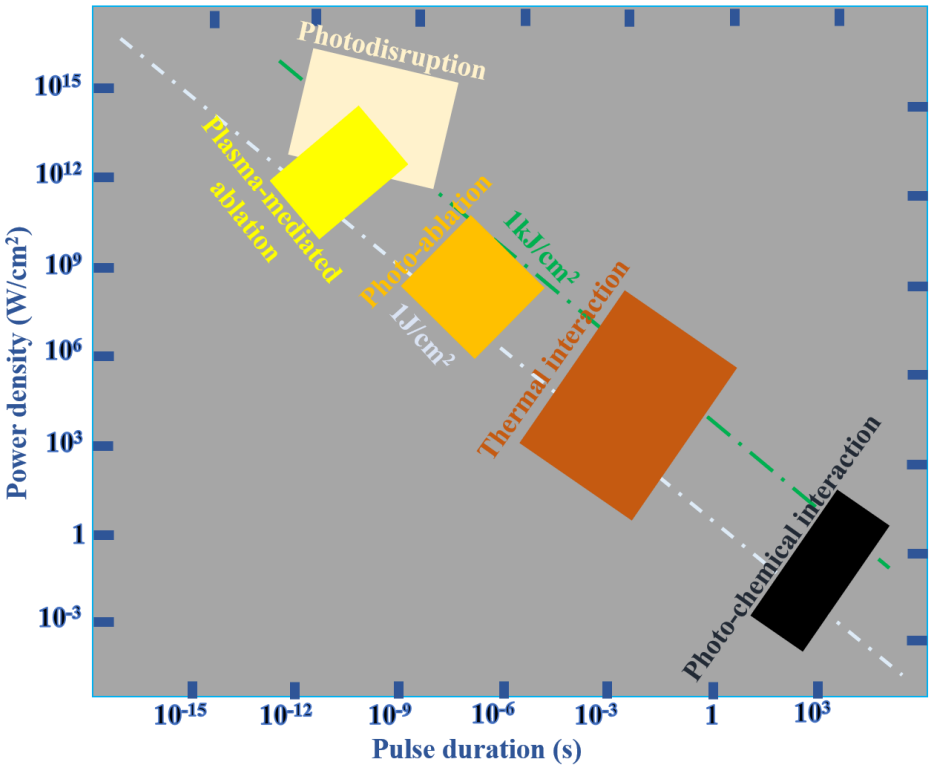

Figure 2. Illustration of laser-tissue interactions. The stretch of the rectangle represents only a rough approximation of associated laser parameters. Modified from [42, 43].

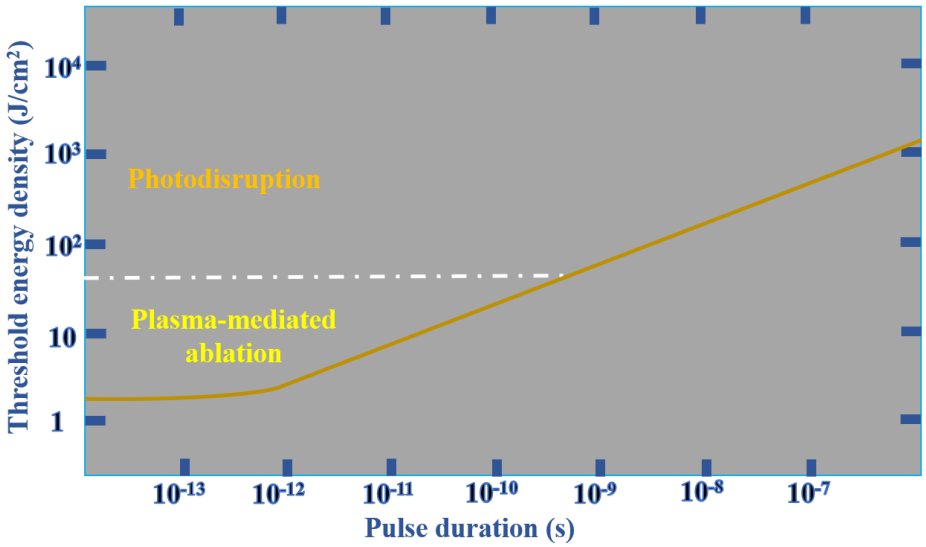

Figure 3. Difference between plasma-induced ablation and photodisruption based on applied energy density. Modified from [42, 43].

Laser wavelength is the second most important parameter as it determines how deep laser radiation can penetrate —that is, in what manner laser energy is scattered and absorbed by— matter, such as tissue (Fig. 4). The total amount of light transmitted through a tissue at a specific

wavelength is determined by the most significant optical tissue properties, such as the reflection, absorption, and scattering coefficients [13, 42].

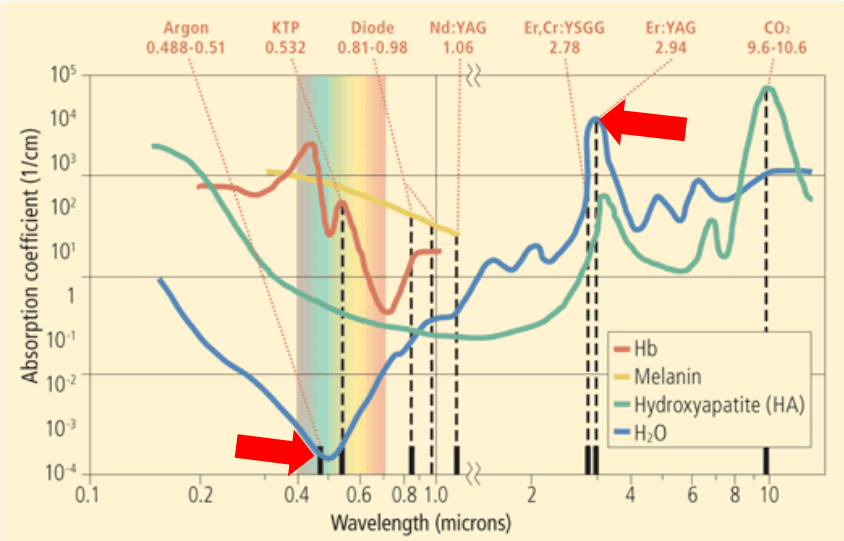

Figure 4. Absorption curves of various tissue components [13].

The third and fourth most important parameters are *energy density (also known as fluence)* and *intensity*, respectively. The *energy density* is the energy of a laser pulse divided by the illumination area and the *intensity* is the ratio of energy density to pulse duration. Beyond the general explanation and influence of laser parameters, advancement in laser surgery can be primarily attributed to the rapid development of pulsed laser systems. Recall that pulse duration in particular governs the *thermal* and *non-thermal effects* on biological tissues. In laser surgery, a rough assumption is that at pulse durations less than 1 µs, thermal effects usually become insignificant if a reasonable repetition rate is applied — i.e. depending on the laser, pulse duration less than 1 µs (non-thermal effect) can add up to a quantifiable increase in temperature if applied at a repetition rate of more than 10 – 20 Hz. However, pulse durations more than 1 µs are frequently associated with quantifiable thermal effects [24]. In other words, when focusing light onto a tissue with a µs-pulsed laser through a lens, ablation (governed by the photo-thermal principle) occurs when the absorbed laser energy is quickly converted into heat in the excited tissue particles. Tissue at the surface is ablated due to the internal stress induced by large temperature gradients inside the exposed tissue.

In this research, a ns-pulsed Nd:YAG laser, operating at 532 nm, and µs-pulsed Er:YAG laser, at a wavelength of 2940 nm, were used to ablate tissues. These two lasers were chosen as ns-pulsed laser ablation is based on the plasma —non-thermal— effect, and the µs-pulsed laser ablation occurs because of the thermal effect [15]. In addition, superficial or deep ablation can be achieved conditional on the wavelength of the laser and on the optical properties of various tissue components [13]. Moreover, depending on the thermal or non-thermal effect, acoustic shock waves can be generated during the ablation [41]. In contrast to photo-thermal ablation, which produces low acoustic amplitude values, laser ablation based on photodisruption generates shock waves with very high amplitude values, which is necessary for optoacoustic applications.

Table 1. Summary of laser-tissue interactions

	Main idea	Observation	Laser	Pulse duration	Power density	Application
Photo-chemical interaction	using a photosensitizer acting as catalyst (only in photodynamic therapy)	no macroscopic observations	red dye lasers, diode lasers	1 s - CW	0.01-50 W/cm^2	photodynamic therapy, biostimulation
Thermal interaction	achieving a certain temperature that leads to the desired thermal effect	either coagulation, vaporization, carbonization or melting	CO_2, Nd:YAG, Er:YAG, Ho:YAG, Argon ion, and diode lasers	$1\,\mu s - 1\,s$	$10–10^6 W/cm^2$	coagulation, vaporization, melting, thermal decomposition, treatment of retinal detachment, laser-induced interstitial thermotherapy
Photo-ablation	direct breaking of molecular bonds by high energy UV photons	very clean ablation, associated with audible report and visible fluorescence	excimer lasers, i.e. ArF, KrF, XeCl, and XeF	$10 - 100\,ns$	$10^7 – 10^{10} W/cm^2$	refractive corneal surgery
Plasma-induced ablation	ablation by ionizing plasma formation	very clean ablation, associated with audible report and blueish plasma sparking	Nd:YAG, Nd:YLF, and Ti:Sapphire	$100\,fs - 0.5\,ns$	$10^{11} – 10^{13} W/cm^2$	refractive corneal surgery, caries therapy
Photo-disruption	fragmentation and cutting of tissue by mechanical forces	plasma sparking, generation of shock waves cavitation, jet formation	solid-state lasers, i.e. Nd:YAG, Nd:YLF, and Ti:Sapphire	$100\,fs – 100\,ns$	$10^{11}–10^{16} W/cm^2$	lens fragmentation, lithotripsy

2.2.2. Laser-Induced Acoustic Shock Waves

Acoustic shock wave (ASW) generation manly depends on the ablated material. However, different laser parameters can also lead to slight variations in ASW generation [44]. In fact, when ablating tissues with the µs-pulsed Er:YAG laser, the temperature increases on the exposed surface and produces acoustic waves, known as thermal mediated acoustic waves. In contrast, the ns-pulsed Nd:YAG laser generates plasma during photodisruption ablation and produces plasma mediated acoustic waves [16].

The plasma ignition (generation) process includes bond-breaking (optical breakdown) and plasma shielding as the laser pulse interacts with the tissue surface. Bond-breaking mechanisms influence the quantity and form of energy (kinetic, ionization and excitation) that atoms and ions can acquire. For low-energy ns-laser pulses (irradiance less than $10^8 W/cm^2$) close to the ablation threshold, Coulomb explosions govern the ablation. The absorbed radiated energy speeds up the movement of electrons in the exposed tissue. Laser energy surpasses the energy necessary to ionize the atoms. As a consequence, a charged cloud of electrons forms above the matter's surface. This cloud of electrons leaves behind a charge density of heated ions (i.e. plasma) on the surface when electrons are ejected from the surface. The expansion of the plasma pulls ions out of the tissue, which, in turn, removes some of the exposed surface layers [45]. In other words, during plasma expansion, one side of the ablation front extends toward the laser while on the other side, the tissue is compressed and moves in the opposite direction. The compressed tissue generates a strong shock wave [41]. Figure 5 illustrates the acoustic shock wave emitted from laser ablation.

For very high-energy ns-laser pulses (irradiance more than $10^{11} W/cm^2$), ablation is characterized by a combination of non-linear absorption, Coulomb explosion, and hypercritical heating. The creation of ASWs is based on plasma mediation, as the plasma-induced ablation exposes the tissue surface to high levels of optical energy concentrated in space and time. Due to high energy intensities, non-linear multiphoton absorption phenomena intensify the degree of laser energy absorbed by the tissue. In turn, photon absorption leads to cascade ionization [38]. Furthermore, the tissue surface is instantly excited, ionized and vaporized into an extremely hot vapor plume, known as a ‘‘plasma plume”, with three main regions: the core, the mid-region and the outer-region. The core, located near the target surface, is the hottest and densest region (ionization state). The mid-region is where ions and neutrals (atoms combined with molecules) coexist due to the ongoing ionization and recombination process. The outer-region is relatively cold and may absorb the radiation from the core and mid-regions of the plasma. The shock wavefront produced by the explosive expansion of plasma travels ahead of the plasma plume. Nearly 30–50 ns later, the front has decelerated to a standard acoustic wave. Plasma creation initiates during the laser pulse and continues for a few nanoseconds, the time required by the free electrons to diffuse into the surrounding medium [42]. Therefore, by placing an ASW sensor at a certain distance from the source, pressure (ultrasound) waves can be measured and converted into an electrical signal.

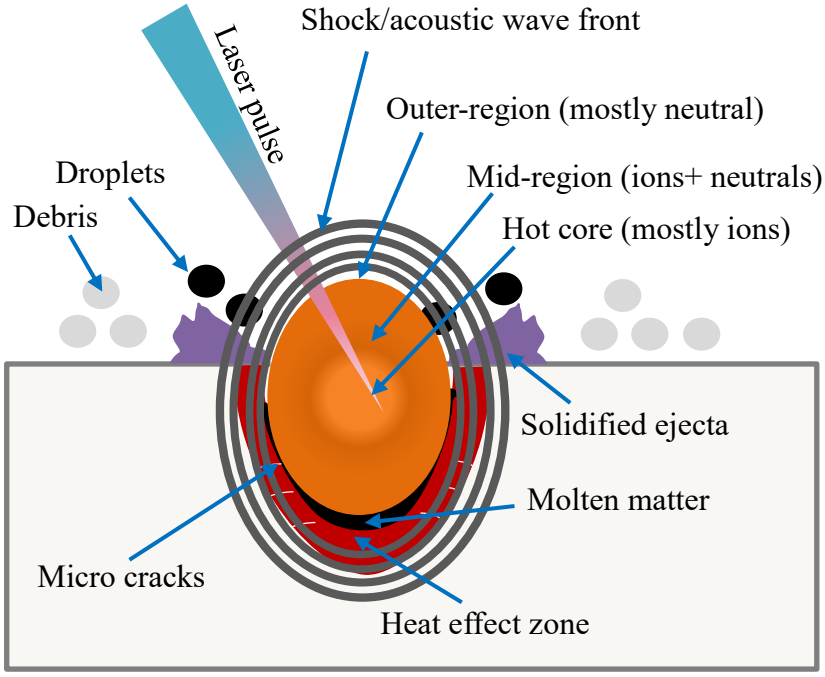

Figure 5. Schematic of laser-induced plasma [46].

2.2.3. Acoustic Sensors

2.2.3.1. Transducer-based Sensors

Sensors for measuring ASWs mainly consist of piezoelectric transducers (PZTs) and air-coupled transducers (microphones) that convert the spherical wave front into electrical signals [46-48]. Piezoelectric transducers combined with gel or water are used for direct contact acoustic detection to avoid the impedance mismatch with air. Air-coupled transducers (ACTs) are used to fulfil the need for contactless measurement. ACTs have a fundamentally low mechanical impedance mismatch with air, which permits broader bandwidth, good sensitivity — expressed as the least detectable signal pressure amplitude. For acoustic sensors, sensitivity is defined in relation to the noise level of the detector expressed in pressure units and is referred to as noise-equivalent pressure (NEP). Acoustic coupling abolishes the need for complex matching layers, which is generally used in piezoelectric transducers [49]. The signal-to-noise ratio (SNR) for air coupled transducers is less than that of the PZTs in direct contact. Furthermore, the -3dB bandwidth of commercial transducers do not typically exceed 900kHz, while ASW spectra extend beyond 1MHz [19]. The restricted bandwidth and resonance of frequency response associated with such transducers result in significant distortions of the measured waveforms and in overestimation of shock rise times [50].

In contrast, miniaturized optical detectors do not suffer from restricted bandwidth. To illustrate, piezoelectric elements with diameters of ~1mm generate a usable bandwidth of 16MHz. Optical fiber-based sensors with an active area of only $0.13 \times 0.27\,mm^2$ can provide a usable bandwidth of 77MHz [51, 52]. Thanks to its large bandwidth, compact optical sound sensors can be considered a universal technology for different optoacoustic spectroscopy and imaging applications that use non-contact measuring procedures [22, 53, 54].

2.2.3.2. Optical-based Sensors

Refractometry and interferometry are the two most common optical methods currently used for detecting acoustic or shock waves [51, 55]. Refractometry-based detection utilizes the photoelectric principle, such that when an ASW interacts with a medium, it induces mechanical stress in that medium, which causes the refractive index (RI) to vary proportionally with the mechanical pressure [56, 57]. The method can detect variation in the RI at the interface between two adjacent media or of a single medium using a probing or interrogating laser beam, in response to traveling ASWs (Fig. 6). Variation in the deflected angle, phase or intensity of the interrogating beam is measured using an optical detector, such as a photodiode (PD), thereby offering information about the ASW signal measured.

Interferometric-based methods detect variations in the optical interference patterns generated by ASWs. Interference pattern variation is due to the ASW pressure that can interact directly with the interrogating beam, vary the resonance frequency, or cause reflector vibration. Depending on how the interferometer is configured, interference pattern variations are triggered by changes in the free path, the optical wavelength, or the optical phase (Fig. 6-10). The resulting variations in intensity or frequency of the interferometer output are measured by a photodiode or a wavelength meter and generate information about the ASW signals. The following section focuses on the operating principles of refractometric and interferometric approaches in optical ASW sensors and discusses the respective benefits and drawbacks for biomedical applications.

❑ Refractometry

Intensity-detection methods

The light intensity of an optical incident beam shining on an interference between two transparent media of different RI — for example, a prism placed between water and glass — varies when ASWs at different intensity values pass through the inference (Figure 6). Hence, ASW measurement is accomplished by using a photodetector to measure illuminance as the light intensity changes. Two basic designs are used to implement intensity-detection methods. The first involves splitting an interrogating beam into two polarized components and measuring ASW-induced variations in intensity in each reflected component individually (Figure 6a). This design diminishes noise in the interrogating beam by computing the reflectance ratio of the two components, thereby enhancing the SNR of the light intensity changes [58, 59]. The second design creates a surface plasmon resonance such that ASWs affect the interrogating beam by changing the plasmons at the water-prism interface (Figure 6b). For this design, a metal-dielectric interface (MDI) coats the bottom of a prism, while a polarized interrogating beam is necessary to generate surface plasmons at the water-prism interface. After fulfilling the resonance conditions for generating plasmons, ASW variations at the water-prism interface alter the light-plasmon coupling, producing variations in the intensity of the reflected interrogating beam [60-62]. The intensity-detection method is more suitable for measuring high frequency ASWs. While ASW measurement is possible over a wide range of 1–180 Mpa [63, 64], this method shows poor sensitivity for typical optoacoustic signal pressures, which are usually less than 0.1 kPa. Additionally, as the optical beam passes through a prism, objectives with relatively low aperture and longer working distance become mandatory for optoacoustic microscopy [58]. Therefore, intensity-detection methods are inefficient for optoacoustic microscopy applications.

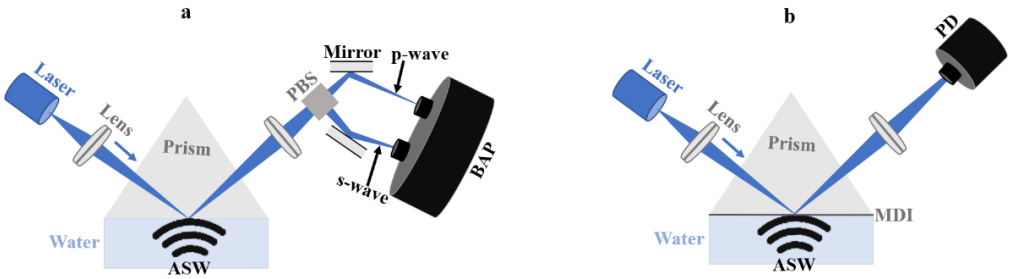

Figure 6. Intensity detection system: (a) ASW detector based on the polarization-dependent reflection of the beam at the water-prism interface and on (b) the reflectivity of the beam at the interface. PD – photodiode; BAP – balance amplified photodetector; PBS – polarization beam splitter; MDI – metal-dielectric interface.

Deflection-detection methods

ASW measurement is based on the deflection of the interrogating beam intersecting the ASW field as illustrated in Figure 7 [65, 66]. ASWs vary the RI of the medium around the interrogating beam, which is deflected according to the pressure gradient of the ASW. A position-sensitive detector, such as a quadrant photodiode, is needed to detect the deflection. In contrast to intensity-detection methods where the frequency bandwidth is estimated based on the photodiode rise time only, deflection-detection requires both the photodiode rise time and a very small interrogating beam diameter, capable of measuring a very large bandwidth. For example, the quotient of the speed of sound in dry air at 20ºC with an interrogating beam diameter of 10µm, yields a theoretical bandwidth of 34MHz [66]. Based on this method, an acoustic-optic beam deflectometry (AOD) experimental approach was designed for non-destructive testing of material. AOD sensitivity is comparable to that of 12Pa piezoelectric transducers and therefore suitable for optoacoustic microscopy applications [65]. Additionally, AOD can be used in applications where image resolution is defined by the optical resolutions of the system, such as in optical-resolution optoacoustic microscopy [65, 66]. One constraint of AOD setups is that the interrogating beam must be narrowed, focused and guided through the medium, near the ASW source. This setup limits the space of optoacoustic microscopy and tomographic setups that require optical guiding components to shine on samples, and further reduces the space available for the interrogating system. In AOD, the existing algorithms for reconstructing tomographic images do not consider how multiple ASW sources interact with the interrogating beam, which suggests that AOD cannot yet be applied in optoacoustic tomography.

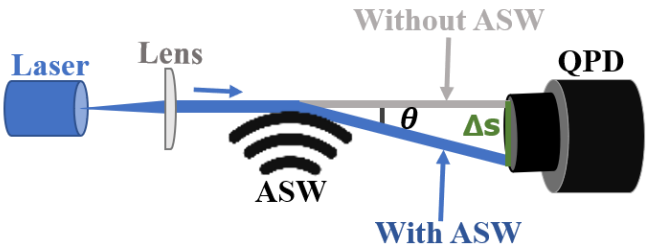

Figure 7. Schematic of a single-beam reflectometry; QPD – quadrant photodiode.

Phase-detection methods

This approach to measuring ASWs consists of detecting the acoustic pressure field (P) by measuring the phase shift (Θ) of a highly collimated interrogating beam [67]. An ASW propagating through a transparent medium changes its RI field. The RI changes produced by the ASW causes the interrogating beam to defect from the original path or scatters some electrons in the beam (Eq. 1).

$$\theta = \frac{2\pi}{\lambda} \times \frac{\mathrm{d}n}{\mathrm{d}P} \int P \times \mathrm{dz} \quad (1)$$

Here, λ is the wavelength of the interrogating beam and dn/dP is the elasto-optic coefficient of the medium in which the ASW field interacts with the beam. To positively or negatively contrast the ASW field, the in-phase photons or out-of-phase photons are selectively removed, respectively. Phase selection is accomplished by tightly focusing the perturbated interrogating beam through a spatial filter in the Fourier plane. Then, through a lens, the beam is recollimated and collected using the complementary metal-oxide-semiconductor (CMOS) or a charge-coupled device (CCD) camera. From the intensity map of the ASW field generated by the camera, a two- or three-dimensional (3-D) image of the ASW signal source can be converted using ordinary tomographic reconstruction techniques.

Phase-sensitive detection methods are already widely used to characterize ASWs and can detect ASWs with a bandwidth of 110 MHz and an NEP of less than 5.1 kPa [68, 69]. Due to its bandwidth and sensitivity, phase-sensitive ASW detection is often implemented in optoacoustic tomography using a variety of experimental setups, such as shadowgraph and Schlieren photography [57]. The shadowgraph and Schlieren techniques use light deflection methods to measure media and interference methods based on the variations of optical path lengths, that is, on the phase [57, 70, 71]. We refer to the 'schlieren object' when analyzing the influence of the object on light, and to the 'phase object' when analyzing its influence on the optical paths. Both techniques are optical systems that project line-of-sight information onto a camera or viewing screen. They are based on light intensity and light ray detection; therefore, a good white light source is essential. Although qualitatively useful for any phenomenon, the techniques are best suited to two-dimensional (2-D) or axisymmetric phenomena, as they integrate information along the light ray path.

In shadowgraph, when there is no object (disturbance) present in the field of view, the collimated light source illuminates the screen uniformly (Figure 8a). However, if there is an object in place, some light rays from the original light source will refract, bend, and deflect, producing a shadow known as a shadowgram. The optical inhomogeneities of the object reallocates the screen illuminance as the light intensity changes. In the shadowgram, the variances in light intensity are proportional to the second spatial derivative or Laplacian of the refractive index field in the transparent medium under investigation. The main drawback of this technique is that when the distance from the transparent disturbance to the generated shadow is too large, the shadow no longer produces meaningful information about the disturbance that caused it. Therefore, shadowgraph techniques are primarily sensitive to sharp variations of acoustic pressure, while gradual ASW pressure differences are lost [50].

Schlieren techniques are more sensitive and can measure an entire waveform [71]. In contrast to shadowgraph, the Schlieren technique requires a sharp cut-off of the refracted light, such as a knife-edge. Figure 8b shows a simple schlieren set-up using a knife-edge positioned at the focal point of the second lens. When introducing an object such as acoustic pressure in the field-of-view, light rays bend away from their initial paths. The refracted rays are no longer on the focal spot of the optical setup. The rising-deflected ray illuminates a spot on the screen, while the falling-deflected ray touches the knife-edge, producing a dark spot against a bright

background. Thus, the vertical gradient of the refractive index is transformed into an amplitude difference. In general, as light intensity changes, the illuminance of the Schlieren image corresponds to the first derivative of the refractive index in a direction perpendicular to the knife-edge.

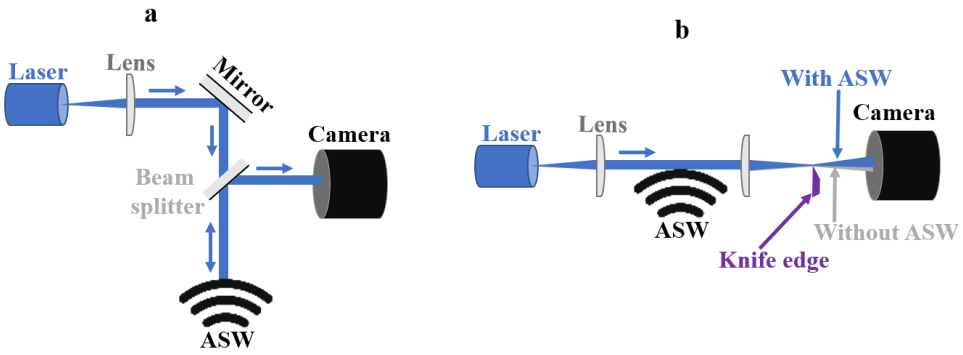

Figure 8. Phase-detection system: (a) schematic of a shadowgraph and (b) a Schlieren setup.

❑ Interferometry

Interferometer-based methods offer the highest sensitivity [72-75]. The physical characteristics of the propagated ASWs (i.e. displacement, pressure) cause spatiotemporal variations of the light's RI. Changes to the RI causes variation in the physical characteristics of the interrogating beam (i.e. optical path length, wavelength, phase) in the optical interferometer system. A photodetector identifies the altered characteristics and converts them into a voltage signal corresponding to the pressure of the ASW. Consequently, the NEP of an interferometric ASW detector is based on the efficiency with which ASW variations are converted into alterations in light characteristics in the interferometer system, and also on the sensitivity of the optical detector system to detect those alterations [51]. Recently, it has been demonstrated that a laser Doppler vibrometer (LDV) provides a bandwidth beyond 10 MHz, which is suitable for measuring the spatial pressure distribution of ASWs [23]. Nevertheless, a cheaper solution of comparable performance is also possible with the Michelson interferometer (MI), Mach-Zehnder interferometer (MZI), fiber Bragg grating (FBG), or Fabry-Pérot interferometer (FPI) [19, 76, 77].

In the MI and MZI, a continuous wave (CW) laser source provides the light source. A beam splitter divides the incident laser beam into an interrogating beam and a reference beam, each with the same path length (Fig. 9). The two beams are combined at the interferometer output and their interference can be detected by a photodiode; ASW-induced variations in the interrogating beam path produce comparative variations in the intensity of the recombined beam [78, 79]. The two beam interferometers are typically applied in free space or fiber-based designs [80-83]. For fiber-based MZIs, ASW signals with a bandwidth of 5 MHz and sensitivities less than 180 Pa were observed [84]. With such limited sensitivity, this method can only be used for low bandwidth ASW signals and is inadequate for optoacoustic spectroscopy. In order to enhance the sensitivity and bandwidth, a free-beam MZI was developed with a sensitivity of 100 Pa and a bandwidth of 17 MHz [80].

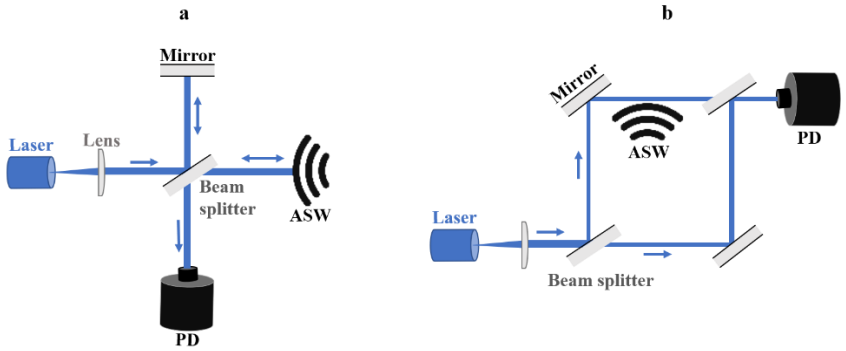

Figure 9. Interferometric ASW detectors: (a) Phase detection in a Michelson interferometer and (b) in a Mach–Zehnder interferometer.

An alternative approach to improving sensitivity and bandwidth is to detect ASWs in an optical resonator or cavity. In this setup, the interrogating beam is confined to a small volume resonator, extending the interaction between the ASW and the beam, thereby enhancing the sensitivity of the beam to acoustic or shock variations. Furthermore, it is well known that ASWs propagating either parallel or perpendicular to the interrogating beam can be detected using an optical resonator, depending on the geometry. Thus, using a micron-scale resonator allows miniaturization of the complete sensor system, since the ASW variation disturbs only the beam within the optical resonator. The most sensitive and compact optical sensor with a large bandwidth is currently the Fabry-Perot interferometer (FPI). FPI sensitivities are less than 50 Pa and bandwidths are as much as 40 MHz [85]. The most recent Fabry-Pérot-based sensors include a diaphragm (membrane) and an in-line fiber etalon [86, 87]. The diaphragm is flexible and subject to deformity caused by the mechanical effects of the ASW. Another sensor design uses a movable part to sense the inbound ASWs. However, the diaphragm has an intrinsic self-resonant frequency, an undesirable trait that induces bumpiness in the frequency response of the sensor [88]. In contrast, the fiber-coupled Fabry-Pérot etalon is a diaphragm-free optical microphone. The undesirable self-resonant frequency is therefore not an issue with this device. The etalon uses two stable mechanical parts, while the incoming ASW is detected in the optical cavity between the mechanical parts (Figure 9a). The sensor measures pressure via refractive index changes of the medium in the optical cavity, which are directly proportional to the density changes produced by the incoming ASW. The sensor is mechanically stable and easy to calibrate [87, 89].

Another compact optical sensor for detecting ASWs with both high sensitivity and bandwidth uses fiber Bragg grating (FBG) (Figure 10b). The FBG-based sensor can deliver a sensitivity of 100 Pa and bandwidths up to 77 MHz [51]. Therefore, both FBG or FPI are suitable for measuring phase objects, such as ASW fields, for tissue classification during laser cutting. ASW properties measured by the FBG or FPI sensors can be used to optimize tissue classification during laser ablation and serve as an optoacoustic feedback system [41]. Due to its compact size, potential applications ideally include minimally invasive measurements, such as for medical endoscopy.

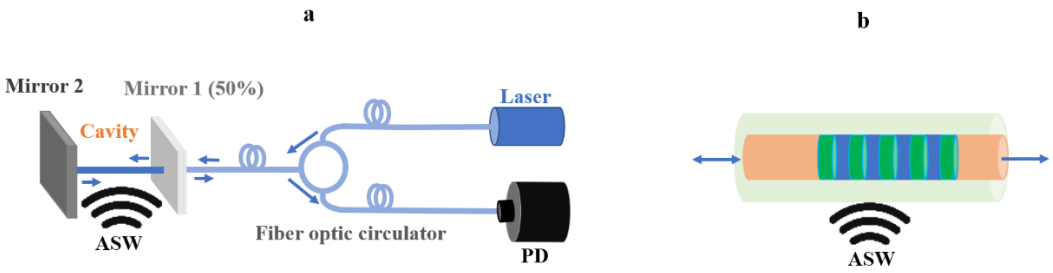

Figure 10. Resonator geometries for ASW detection: (a) Fiber-coupled Fabry-Pérot etalon is a diaphragm-free optical microphone and (b) a phase-shifted fiber Bragg grating based sensor. The optical beam in the resonator is blue.

Chapter 3

Investigating Classification Performance of Acoustic Waves for Feedback System

3.1. Mahalanobis distance-based method

Introduction

We initially classified four tissue types — hard and soft bone, muscle, and fat from a proximal and distal fresh porcine femur — during laser ablation by measuring the acoustic shock waves (ASWs) generated with a conventional air-coupled transducer and by processing the information (average of three spectra) using principal component analysis combined with the Mahalanobis distance-based method. It was possible to classify ablated hard bone from surrounding tissues.

Publication. The findings were published in New Trends in Medical and Service Robotics, MESROB 2020 [2].

[1]Doi.: 10.1007/978-3-030-58104-6_23.

Optoacoustic Tissue Classification for Laser Osteotomes Using Mahalanobis Distance-Based Method

Hervé Nguendon Kenhagho[1(✉)], Yakub Aqib Bayhaqi[1], Ferda Canbaz[1], Raphael Guzman[2], Tomas E. Gomez Alvarez-Arenas[3], Philippe C. Cattin[4], and Azhar Zam[1]

[1] Biomedical Laser and Optics Group, Department of Biomedical Engineering, University of Basel, Gewerbestrasse 14, Allschwil, Switzerland
herve.nguendon@unibas.ch
[2] Department of Neurosurgery, University Hospital Basel, Spitalstrasse 21, Basel, Switzerland
[3] Department of Ultrasonic and Sensors Technologies, Information and Physical Technologies Institute ITEFI, Spanish National Research Council (CSIC), Serrano 144, Madrid, Spain
[4] Center for Medical Image Analysis and Navigation, Department of Biomedical Engineering, University of Basel, Gewerbestrasse 14, Allschwil, Switzerland

Abstract. The use of lasers for bone cutting holds many advantages over mechanical tools, including more functional cuts, contactless interaction and faster wound healing. To avoid undesirable tissue damage, a method to classify the tissue being cut is needed. We classified four tissue types—hard and soft bone, muscle and fat from a proximal and a distal fresh porcine femur—by measuring acoustic shock waves generated using an air-coupled transducer during the ablation process. A nanosecond Nd:YAG laser at 532 nm and a microsecond Er:YAG laser at 2940 nm were used to create ten craters on the surface of each tissue type. We performed the Principal Component Analysis (PCA) combined with the Mahalanobis distance-based method to classify tissue types. A set of 2520 data points (or 840 average of three spectra) measured from the first seven craters in one proximal and distal femurs was used as "training data", while a set of 1080 data points (or 360 average three spectra) measured from last three craters in the remaining proximal and distal femur was considered as "testing data" for both lasers. It was possible to classify each tissue, with an average classification error for all tissues of 7.98% and 36.88%, during laser ablation with the Nd:YAG and Er:YAG, respectively. However using the Er:YAG, it was challenging to classify between soft tissue types. These results show that the Mahalanobis method could be used as feedback for laser osteotomes.

Keywords: Laser ablation · Acoustic signal · Principal Component Analysis · Mahalanobis distance

G. Rauter et al. (Eds.): MESROB 2020, MMS 93, pp. 202–210, 2021.
https://doi.org/10.1007/978-3-030-58104-6_23

1 Introduction

Standard surgeries depend on mechanical tools that often lead to mechanical trauma, bacterial contamination and collateral damage to soft tissues [1]. These side effects lead to extended wound healing periods. Therefore, scientists are studying how to overcome the drawbacks of mechanical tools by using laser technology to cut bone [2]. Lasers have emerged and evolved in recent years to have several advantages over standard surgical tools, including precision cutting, sterility, no mechanical trauma, and shorter recovery times [1]. While laser technologies appear to offer a sophisticated solution to the disadvantages of mechanical tool, a control system is needed to prevent the laser from unwanted tissue damage. Thus, the challenge of distinguishing tissue type during ablation becomes a critical focus of research. When ablating tissues with a laser, energy is generated in various forms such as acoustic shock wave (ASW) emission [3]. The ASW generated varies with the laser parameters and more importantly mainly depends on the type of ablated tissue. Furthermore, when water is applied to the ablated spot, energy absorption at a wavelength of 2940 nm is very high compared to that at 532 nm [4, 5]. Thus, in a wet tissue environment, the frequency-doubled neodymium-doped yttrium aluminium garnet (Q-switched Nd:YAG) laser at 532 nm seems well suited to clinical studies for applications such as meniscus/knee surgery. The erbium-doped yttrium aluminum garnet (Er:YAG) laser at 2940 nm could potentially be used to achieve deeper ablation, with a proper cooling system in place. Based on the emitted ASW measured by a transducer, tissues differentiation method can be performed.

To decrease the computational time during tissue differentiation, the dimensions of each ASW can be reduced using Principal Component Analysis (PCA) [6]. PCA was used to reduce the complexity of high-dimensional data by finding similarity patterns and trends of the measured ASW [7]. Based on the PCA-scores, we used the Mahalanobis distance measure to classify tissue types, because it can be visualized as the distance of a score from the center of a class and translated onto an ellipse whose main direction is that of the data. The ellipse is plotted based on the scores which have the same Mahalanobis distance from the centroid. In the 3-dimensions, axes of the ellipse are scaled with the same length for scores at equal Mahalanobis distance from the center [6].

In this study, we ablated hard bone, soft bone, fat, and muscle tissues using a nanosecond-Nd:YAG pulsed laser at 532 nm and with a microsecond-Er:YAG pulsed laser at 2940 nm. We measured the emitted ASWs using a high efficiency, broadband piezoelectric air-coupled ultrasonic transducer. To simultaneously differentiate tissue types, we performed the PCA combined with the Mahalanobis distance-based method.

2 Method

2.1 Sample Preparation

In the laser tissue ablation experiments, we used one fresh porcine proximal and distal femur purchased from a local butcher (Fig. 1).

Scalpels were used to separate the connective tissues. The specimen was rinsed in distilled water prior to the laser experiments. The dimension of compact bone, soft bone, fat and muscle were all $10 \times 50 \times 5$ mm^3.

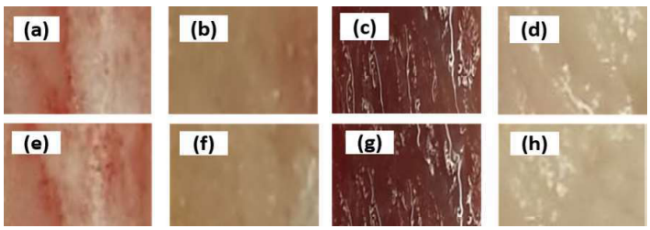

Fig. 1. Tissue samples from one fresh porcine femur. Proximal femur: hard bone (a), soft bone (b), muscle (c), and fat (d); distal femur: hard bone (e), soft bone (f), muscle (g), and fat (h).

3 Laser Ablation System

Excitation sources for the experiments came from a Q-switched frequency-doubled Nd:YAG laser (Q-smart 850, Quantel, Paris, France) at 532 nm (producing 5 ns pulses) and from an Erbium-doped yttrium aluminum garnet laser (Syneron litetouch LI-FG0001A, AOT, Basel, Switzerland) at 2940 nm (producing 400 µs pulses). Several craters were produced ex-vivo on the specimens, using two different lasers (Fig. 2). Each sample was exposed to 180 laser pulses, at a repetition rate of 2 Hz at a single location, for both lasers. This procedure was repeated at ten different ablation locations, spaced 4 mm apart.

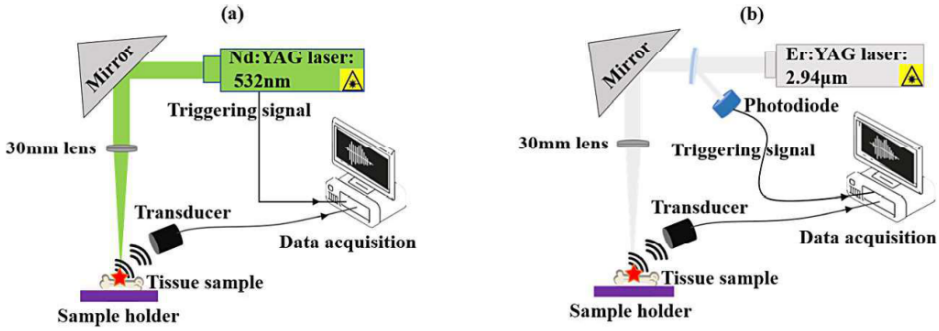

Fig. 2. Schematic of the experimental set-up for laser-induced acoustic shock wave measurement using (a) the nanosecond Q-switched Nd:YAG laser and (b) the microsecond Er:YAG laser during tissue ablation.

The applied pulse energy of the Nd:YAG laser and the Er:YAG laser were 200 mJ and 940 mJ, respectively. Figure 2a shows the ns-frequency-doubled Nd:YAG pulse laser and a data recording element embedded in a single opto-acoustic system for tissue ablation and ASW measurement. An NB1-K13 mirror (Nd:YAG Laser Line Mirrors) placed in the beam path of the Nd:YAG laser (Fig. 2a) was used to reflect the laser pulse at a 90° angle. A CaF_2 bi-convex lens with a focal length of 30 mm served to focus the laser beam onto the surface of the target specimen. Fig. 2b shows the microsecond (µs) Er:YAG laser with a pulse energy of 940 mJ and operating at a wavelength of 2940 nm, which was used for tissue ablation. A CaF_2 window was placed in front of the laser head to split the incident laser beam into two parts—transmitted and reflected light—to allow for a triggering signal. A 30 mm lens was used to focus the transmitted

light onto the surface of the target specimen. The reflected light was collected by a fast PbSe photodiode (PbSe Fixed Gain Detector, PDA20H, 1.5–4.8 μm, Thorlabs, Munich, Germany).

4 Detection and Collection of the Acoustic Shock Wave Signal

Acoustic shock waves (ASWs) emitted from the ablation spot were detected with a self-developed, custom-made air-coupled piezoelectric transducer (manufactured in the ITEFI-Instituto de Technologias Fisicas y de la Information, CSIC, Madrid, Spain), with a resonance frequency of 0.4 MHz, usable frequency band of 0.1–0.8 MHz and 15 mm aperture. The transducer was placed at 45° angle and 5 cm away from the ablated spot while recording the laser-induced acoustic wave during the ablation process. The temporal profile of ASW signals detected by the transducer were amplified by 30 dB and digitized by a PCI Express Data Acquisition Card (16-bit resolution, 4 channels at 10 MS/s each, M4i.44xx-x8, Spectrum Microelectronic GmbH, Grosshansdorf, Germany). The Data were collected using LabVIEW (version 2016a), and the information was extracted from the samples using MATLAB (version R2018b) software. When using the Nd:YAG laser, the laser's CMOS (Complementary metal–oxide–semiconductor) trigger provided the triggering signal for the transducer and data acquisition. For the Er:YAG laser, 4% pulse energy (reflected from the surface of the CaF_2 window, Fig. 2b) was used as the triggering signal. For both lasers, data recording of the temporal profile for ASW signals took place during time windows of 0.82 ms.

5 Signal Processing and Classification Method

A summary of the signal processing and classification methods for tissue classification is given in Fig. 3. Statistical analysis and calculations were performed in MATLAB software. We suppressed the phase shift of the measured ASW signal by converting the time domain signal into the frequency domain, using the Fast Fourier Transform (FFT). The average of three ASW spectra was calculated to improve the signal-to-noise ratio between each measured ASW in the time domain. We split the amplitude spectrum into three equal frequency bands (Low-, Mid- and High-Frequency). Each frequency band was used as an input for PCA. Here, we identified the frequency band which produce the lowest classification error for tissue classification.

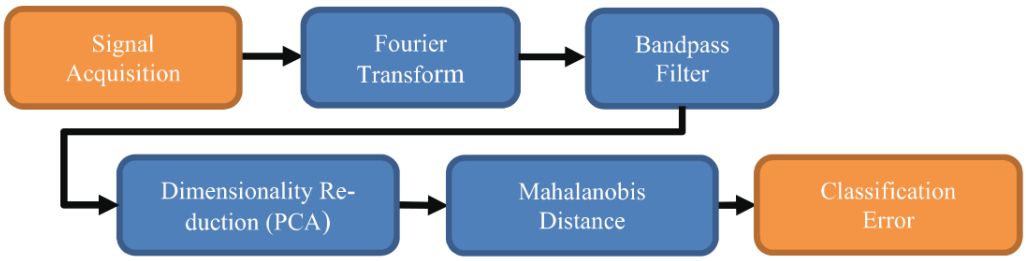

Fig. 3. Summary of the signal processing methods for tissue classification.

For tissue differentiation, we performed the PCA combined with a Mahalanobis distance-based method. We used the first three PCA scores from the set of "training data", combined with the 95% confidence of each ellipsoid and plotted against three orthogonal eigenvectors from the training data scores—we used three-PC scores with the most variance of the "training data" —. Testing scores lying within and close to the plotted ellipsoid were considered true positives and false positives otherwise. We differentiated tissues based on the ellipsoid, where the covariance of the ASW score and the scales of the different variables were considered.

Therefore, ellipsoid is useful for detecting members of the same group and even outliers. A set of 2520 data points (or 840 average of three spectra) measured from the first seven craters in one proximal and one distal femur was used as "training data", while a set of 1080 data points (or 360 average three spectra) measured from last three craters in the remaining proximal and distal femur was considered as "testing data" for both lasers. From the confusion matrix, errors in "testing data"-based scores from each sample were calculated.

6 Results and Discussion

Comparing the ASW of hard bone to surrounding tissues, we found that the peak-to-peak amplitudes of the ASW generated by the hard bone specimen and measured by the air-coupled transducer were higher than those generated by the surrounding/soft tissues (Figs. 4a and 4c). Soft tissues contain around 79% water, while hard bone is made up of 85–95% carbonated hydroxyapatite [8]. Thus, we believe that the carbonated hydroxyapatite resulted in a higher amplitude of sound due to its compact structure [9]. The peak-to-peak value of the ASWs generated for each tissue with the Nd:YAG laser was ~7 times higher than those generated with the Er:YAG laser.

The greater peak-to-peak pressure generated by the Nd:YAG laser was expected, as the ablation is based on plasma mediation, which increases the pressure energy measured by the transducer. The Er:YAG laser depends on thermal ablation, thus, most of the light energy is absorbed by the exposed tissue and transformed into heat [10]. This is also the reason the acoustic signal duration (wt) generated by the Nd:YAG laser ($wt = 1$ ms) was longer compared to the one generated by the Er:YAG laser ($wt = 0.7$ ms). The corresponding frequency domain of the acoustic waves for each tissue is depicted in Figs. 4b and d. The amplitude spectrum of hard bone is higher compared to the surrounding tissues. By splitting the spectrum into three, equal bands, as in Figs. 4b and 4d—the mid-frequency was found to be between 0.27–0.53 MHz—classification between hard bone and surrounding tissues was more accurate than in other bands. Mid-frequency region overlaps with the frequency band in which the transducer has higher sensitivity. The features that were chosen for PCA show 94.74% and 90.36% of the total variance in the acoustic waves generated with the Nd:YAG and the Er:YAG laser, respectively. The first three principal components PC1, PC2, and PC3 demonstrated most of the variation in ASWs. Based on the percentage of total variance, PC1, PC2 and PC3 were used to differentiate tissue types based on the analysis of the measured acoustic shock waves (Fig. 4 and 5).

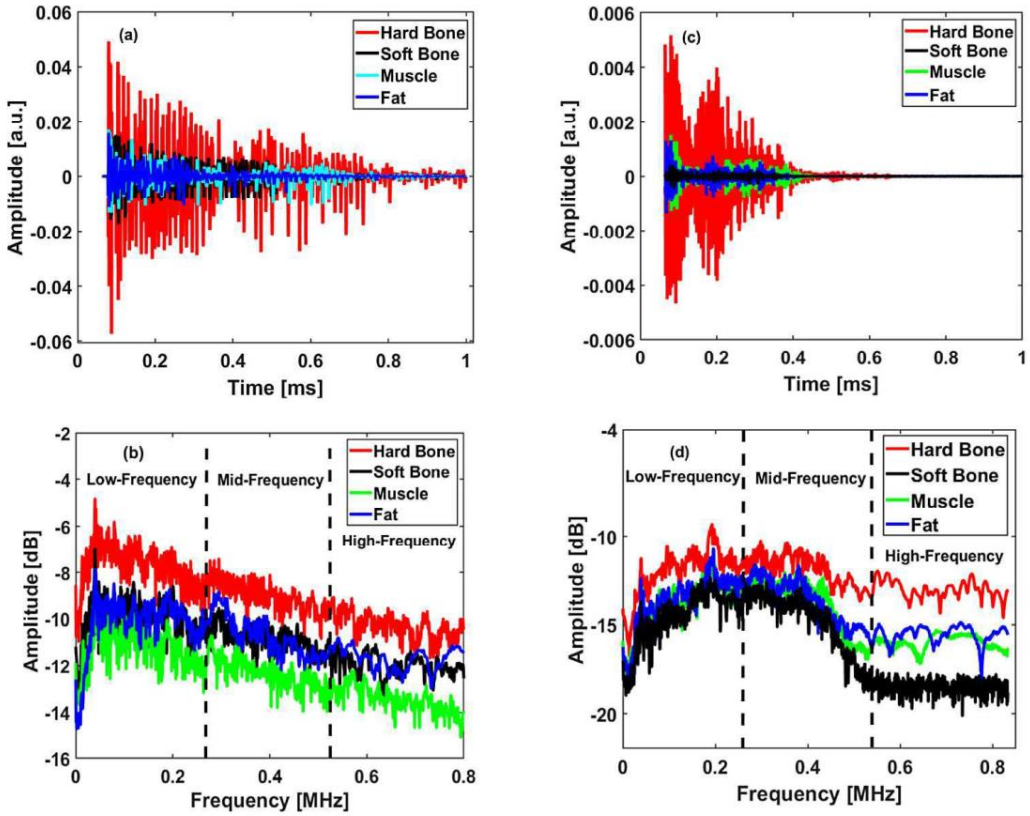

Fig. 4. Measured acoustic shock wave: Time domain of the ASW signal using (a) Nd:YAG laser and (c) Er:YAG laser; frequency domain of the ASW signal using (b) Nd:YAG laser and (d) Er:YAG laser.

During tissue classification, it was possible to differentiate each tissue with an average classification error for all tissues of 7.98% and 36.88%, during laser ablation with the Nd:YAG and Er:YAG, respectively (Table 3). The average classification error for all tissues was higher during Er:YAG cutting than during Nd:YAG cutting. Because, during Er:YAG cutting, it was challenging to differentiate between soft tissues (classification errors in the confusion matrices are in Table 1 and 2); a part of the ellipsoids for soft tissues overlapped (Fig. 5c and d).

Furthermore, when cutting tissues with the Nd:YAG, we did not obtain a single wrong classification with this method, we only found unknown tissue types. This is way better than classifying some tissues as the wrong type, as if the result is unknown, the user must manually check what tissue is being cut. Depending on the ablation process, we believe that important parameters of the ablated material can be found in the emitted ASWs. It is possible that, the classification error during Er:YAG cutting was worse because the ablation process is thermal ablation, where most power of the emitted light of the pulsed laser is absorbed in the exposed material and light is transformed into heat. Thus, only a fraction of light energy contributes to the emitted acoustic waves [3]. This is probably the reason the Mahalanobis method could not properly classify them into the relevant tissue types. It is not the case for the Nd:YAG, where most photons are absorbed by

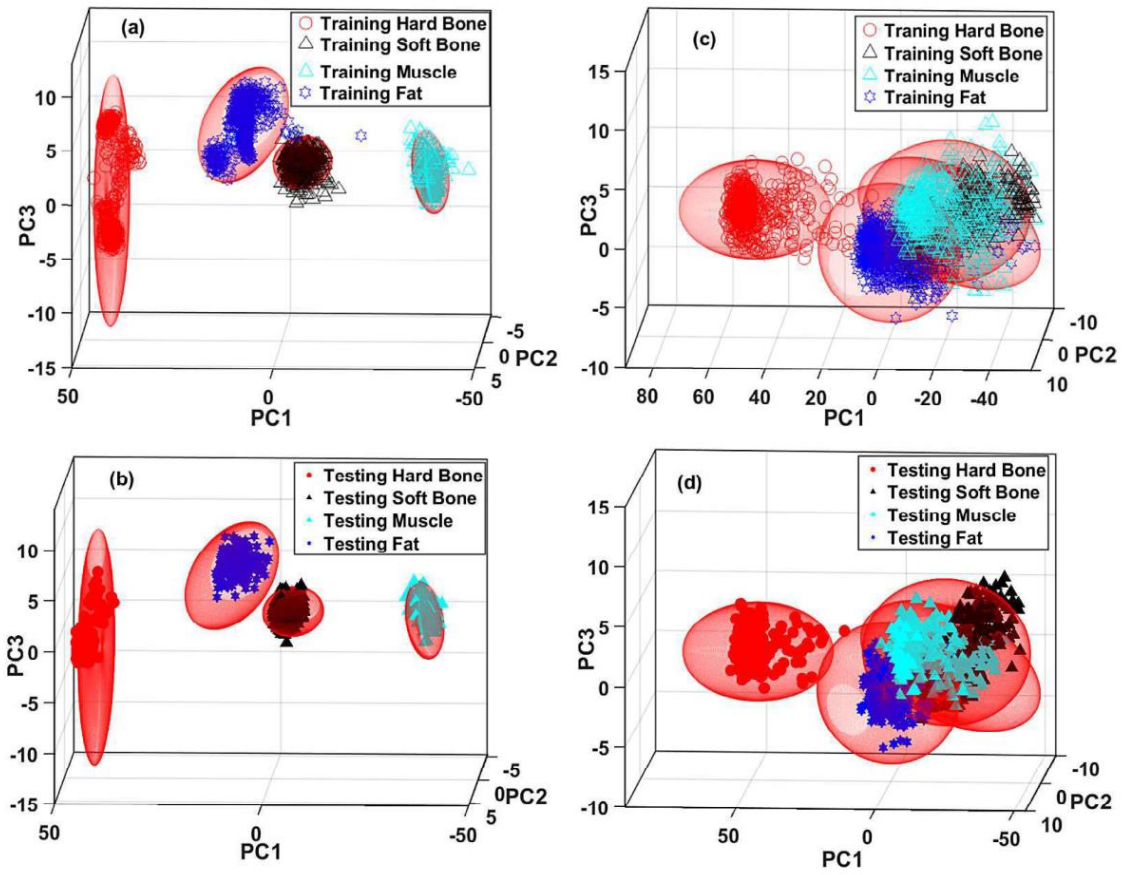

Fig. 5. Ellipsoids based on 840 scores from "training data" (a and c; using ns-Nd:YAG laser and μs-Er:YAG laser, respectively) and classification of 360 scores from the test data (b and d; using ns-Nd:YAG laser and μs-Er:YAG laser, respectively) in each ellipsoid of the "training data" for hard and soft bone, muscle and fat.

the material which created free electrons at the surface of the exposed zone (plasma mediated). When the free electrons returned to equilibrium state, they emitted ASWs [3].

Table 1. Confusion matrix for tissue types during ablation with Nd:YAG laser.

Tissue	Classified as					Classification error
	Hard bone	Soft bone	Muscle	Fat	Unknown	
Hard bone	332	0	0	0	28	7.7%
Soft bone	0	302	0	0	58	16.1%
Muscle	0	0	358	0	2	0. 6%
Fat	0	0	0	333	27	7.5%

Table 2. Confusion matrix for tissue types during ablation with Er:YAG laser.

Tissue	Classified as					Classification error
	Hard bone	Soft bone	Fat	Muscle	Unknown	
Hard bone	327	0	0	0	33	9.17%
Soft bone	0	122	96	62	80	66.11%
Muscle	0	31	26	282	21	21.67%
Fat	0	106	178	70	6	50.56%

Table 3. Average classification error of all tissues for both lasers using Mahalanobis distance-based method.

Nd:YAG laser	7.98%
Er:YAG laser	36.88%

7 Conclusion

Our aim was to simultaneously classify tissue types during laser ablation by measuring the generated ASW with an air-coupled transducer and process the information using the Mahalanobis method. The Mahalanobis method was combined with PCA during classification experiments. In the experiments, we used two different lasers to generate acoustic waves. We found that the ns-Nd:YAG laser generates higher acoustic amplitudes than the µs-Er:YAG laser. It was possible to differentiate each tissue with a classification error for all tissues of 7.98% and 36.88%, during laser ablation with the Nd:YAG and Er:YAG, respectively. Therefore, Mahalanobis distance-based method could be used as optoacoustic feedback for smart laser osteotomes. Future work includes reducing the average classification errors between soft tissues. We will also investigate different methods to classify tissue types such as the Support Vector Machine (SVMs) and Artificial Neural Network (ANN).

Acknowledgement. The authors gratefully acknowledge funding of the Werner Siemens Foundation through the MIRACLE (stands for Minimally Invasive Robot-Assisted Computer-guided LaserosteotomE) project.

References

1. Baek, K.W., et al.: A comparative investigation of bone surface after cutting with mechanical tools and Er:YAG laser. Lasers Surg. Med. **47**(5), 426–432 (2015). https://doi.org/10.1002/lsm.22352
2. Nguendon Kenhagho, H., et al.: Characterization of ablated bone and muscle for long-pulsed laser ablation in dry and wet conditions. Materials **12**(8), 1338 (2019). https://www.mdpi.com/1996-1944/12/8/1338

3. Nguendon, H.K., et al.: Characterization of ablated porcine bone and muscle using laser-induced acoustic wave method for tissue differentiation. In: European Conference on Biomedical Optics, p. 104170N. Optical Society of America (2017)
4. Tulea, C.-A., Caron, J., Gehlich, N., Lenenbach, A., Noll, R., Loosen, P.: Laser cutting of bone tissue under bulk water with a pulsed ps-laser at 532 nm. In: SPIE, vol. 20, p. 9 (2015)
5. Kuscer, L., Diaci, J.: Measurements of erbium laser-ablation efficiency in hard dental tissues under different water cooling conditions. In: SPIE, vol. 18, p. 11 (2013)
6. Brereton, R.G.: The Mahalanobis distance and its relationship to principal component scores. J. Chemom. **29**(3), 143–145 (2015). https://doi.org/10.1002/cem.2692
7. Lever, J., Krzywinski, M., Altman, N.: Principal component analysis. Nat. Methods **14**, 641 (2017). https://doi.org/10.1038/nmeth.4346
8. Curzon, M., Featherstone, J.: Chemical composition of enamel. In: Lazzan, E.P. (ed.) Handbook of Experimental Aspects of Oral Biochemistry, pp. 123–135. CRC Press, Boca Raton (1983)
9. Apel, C., Meister, J., Ioana, R., Franzen, R., Hering, P., Gutknecht, N.: The ablation threshold of Er:YAG and Er:YSGG laser radiation in dental enamel. Lasers Med. Sci. **17**(4), 246–252 (2002)
10. Kenhagho, H.N., Rauter, G., Guzman, R., Cattin, P.C., Zam, A.: Comparison of acoustic shock waves generated by micro and nanosecond lasers for a smart laser surgery system. In: SPIE BiOS, SPIE, vol. 10484, p. 9 (2018)

3.2. Comparing Machine Learning-Based Methods

Introduction

We compared the performance of several machine learning-based methods and extended the number of tissue types to classify, from four to five, during laser ablation. Overall, the error rate when classifying hard tissue from soft tissue types was lowest (best) with the artificial neural network but classification between soft tissues remained a challenge.

Publication. An account of the proposed approach was published in 2020 Lasers in Surgery and Medicine, with peer review [90].

https://doi.org/10.1002/lsm.23290

Lasers in Surgery and Medicine

Machine Learning-Based Optoacoustic Tissue Classification Method for Laser Osteotomes Using an Air-Coupled Transducer

Hervé Nguendon Kenhagho,[1*] Ferda Canbaz,[1] Tomas E. Gomez Alvarez-Arenas,[2] Raphael Guzman,[3,4] Philippe Cattin,[5] and Azhar Zam[1]

[1]*Biomedical Laser and Optics Group, Department of Biomedical Engineering, University of Basel, Gewerbestrasse 14, Allschwil, 4123, Switzerland*

[2]*Department of Ultrasonic and Sensors Technologies, Information and Physical Technologies Institute ITEFI, Spanish National Research Council (CSIC), Serrano 144, Madrid, 28006, Spain*

[3]*Brain Ischemia and Regeneration, Department of Biomedicine, University of Basel, University Hospital of Basel, Basel, 4031, Switzerland*

[4]*Neurosurgery Group, Department of Biomedical Engineering, University of Basel, Allschwil, 4123, Switzerland*

[5]*Department of Biomedical Engineering, Center for Medical Image Analysis and Navigation, University of Basel, Gewerbestrasse 14, Allschwil, 4123, Switzerland*

Background and Objectives: Using lasers instead of mechanical tools for bone cutting holds many advantages, including functional cuts, contactless interaction, and faster wound healing. To fully exploit the benefits of lasers over conventional mechanical tools, a real-time feedback to classify tissue is proposed.

Study Design/Materials and Methods: In this paper, we simultaneously classified five tissue types—hard and soft bone, muscle, fat, and skin from five proximal and distal fresh porcine femurs—based on the laser-induced acoustic shock waves (ASWs) generated. For laser ablation, a nanosecond frequency-doubled Nd:YAG laser source at 532 nm and a microsecond Er:YAG laser source at 2940 nm were used to create 10 craters on the surface of each proximal and distal femur. Depending on the application, the Nd:YAG or Er:YAG can be used for bone cutting. For ASW recording, an air-coupled transducer was placed 5 cm away from the ablated spot. For tissue classification, we analyzed the measured acoustics by looking at the amplitude-frequency band of 0.11–0.27 and 0.27–0.53 MHz, which provided the least average classification error for Er:YAG and Nd:YAG, respectively. For data reduction, we used the amplitude-frequency band as an input of the principal component analysis (PCA). On the basis of PCA scores, we compared the performance of the artificial neural network (ANN), the quadratic- and Gaussian-support vector machine (SVM) to classify tissue types. A set of 14,400 data points, measured from 10 craters in four proximal and distal femurs, was used as training data, while a set of 3,600 data points from 10 craters in the remaining proximal and distal femur was considered as testing data, for each laser.

Results: The ANN performed best for both lasers, with an average classification error for all tissues of $5.01 \pm 5.06\%$ and $9.12 \pm 3.39\%$, using the Nd:YAG and Er:YAG lasers, respectively. Then, the Gaussian-SVM performed better than the quadratic SVM during the cutting with both lasers. The Gaussian-SVM yielded average classification errors of $15.17 \pm 13.12\%$ and $16.85 \pm 7.59\%$, using the Nd:YAG and Er:YAG lasers, respectively. The worst performance was achieved with the quadratic-SVM with a classification error of $50.34 \pm 35.04\%$ and $69.96 \pm 25.49\%$, using the Nd:YAG and Er:YAG lasers.

Conclusion: We foresee using the ANN to differentiate tissues in real-time during laser osteotomy. Lasers Surg. Med. © 2020 Wiley Periodicals LLC

Key words: laser ablation; tissue classification; acoustic shock signal; principal component analysis; support vector machine; artificial network machine

INTRODUCTION

Conventional osteotomy relies on mechanical tools, such as scalpels, saws, and burrs [1,2], which often result in mechanical trauma, metal debris, bacterial contamination, and collateral damage to soft tissues [1]. Major drawbacks of mechanical tools are excessive force, fractures, vibrations, and heat that can damage the surrounding tissue [3]. These side effects lead to prolonged healing periods. In contrast to conventional osteotomy, laser osteotomy (where a laser is

Conflict of Interest Disclosures: All authors have completed and submitted the ICMJE Form for Disclosure of Potential Conflicts of Interest and none were reported.

*Correspondence to: Hervé Nguendon Kenhagho, MSc or Dr. Azhar Zam, Biomedical Laser and Optics Group, Department of Biomedical Engineering, University of Basel, Gewerbestrasse 14, Allschwil, Switzerland.

E-mail: herve.nguendon@unibas.ch (H.N.K.); E-mail: azhar.zam@unibas.ch (A.Z.)

Accepted 14 June 2020

Published online in Wiley Online Library (wileyonlinelibrary.com).

DOI 10.1002/lsm.23290

used to cut the bone) has emerged and evolved in recent years to achieve precision cutting, sterility, and reduced trauma during surgery, followed by fast healing times [4]. Therefore, laser technologies appear to offer a sophisticated solution to overcome the disadvantages of mechanical tools [5,6]. The laser surgery process, which has been considered most effective for bone tissue uses an erbium-doped yttrium aluminum garnet (Er:YAG) laser source operating at 2940 nm [7,8]. The reason being that the operation wavelength of the Er:YAG laser corresponds to one of the highest absorption peak of water and hydroxyapatite, the main component of bone [9]. However, this operation wavelength with microsecond pulse duration leads to ablation by photothermal vaporization [10,11]. To decrease the effects of photo-thermal vaporization, which may result in carbonization and surface roughness during laser cutting, water cooling, or spraying systems (wet environment) are widely used [9,10]. With an appropriate water-cooling system, the Er:YAG laser can be used to achieve greater ablation depth and better surface morphology [10,12,13]. This is because water prevents pulpal heating and dehydration, which are the primary causes of thermal damage and reduced tissue ablation [10,14,15]. Such laser assisted and water-cooled systems showing efficient ablation rates while producing early carbonization have been presented in the literature [7,16,17].

In contrast to the microsecond Er:YAG laser, the nanosecond neodimium-doped yttrium aluminum garnet (Nd:YAG) laser source results in a plasma-based ablation [5,18,19]. Ablation with a nanosecond pulse duration is characterized by a combination of nonlinear absorption and Coulomb explosion without any significant temperature increase to the surroundings in wet environment [19–21]. This is because a very high rate of pulse energy is transformed into heat in the liquid-containing tissue [22]. Therefore, the thermal confinement condition is fulfilled. In other words, in a wet environment, a nanosecond pulse heats tissue more rapidly than the time it requires for the thermoelastic expansion of heated volume to occur [23]. These radiation conditions are known as confined-thermal conditions in which thermal heat does not spread out of the irradiation volume during the time of heat production by the laser pulse [24]. Furthermore, in contrast to the 2940 nm, the wavelength of 532 nm is transparent in water and seems to be well suited for tissue ablation with a substantial water layer such as in knee arthroscopy [9,18]. However, at a wavelength of 1064 nm, water has a higher absorption coefficient providing less penetration depth compared with the wavelength of 532 nm. In other words, in a wet environment, energy absorption at a wavelength of 532 nm is very low compared to that of 1064 nm or 2940 nm [9,18].

Acoustic shock waves (ASWs) are pressure waves produced due to the rapid release of energy when a material is exposed to mechanical or thermal influences. Interaction with laser light also produces ASWs during the ablation process [20,25]. The ASW propagates as a spherical wavefront, which is measured using acoustic emission sensors, such as piezoelectric transducers (PZTs) and air-coupled transducers (ACTs) (microphones), which convert the spherical wavefront into electrical signals [26–28]. PZTs combined with a matching gel or water were used in direct contact acoustic detection to avoid the impedance mismatch with air. Furthermore, the high attenuation of shock waves in the air of 1.6 dB/cm for 1 MHz frequency components also contributes to challenges in detecting ASW signals without direct contact [29]. To improve the mismatch of non-contact ASW detection, ACTs were used. This is because the ACTs have a fundamentally low mechanical impedance mismatch with the air inducing broader bandwidth and good signal-to-noise ratio. This better acoustic coupling abolished the need for complex matching layers, which was generally used in PZTs [30]. However, the signal-to-noise ratio that is provided by ACTs is still less than the PZTs in direct contact.

The features of the ASWs generated are governed by the laser pulse's parameters such as the laser energy and the focusing conditions. However, the ASW mainly depends on the type of material (i.e., hard tissue or soft tissue) being cut [31]. Hence, by analyzing the generated ASWs, tissue types can be classified. Previously, ASWs measured were already used for photothermal therapy such as temperature monitoring during radiofrequency ablation; and forming lesion control in real-time [32–34]. Additionally, ASWs were also investigated for incision depth controlled during laser ablation [22,35]. But, only knowing the temperature and the depth of the incision is not enough. We also want to know which tissue type we are cutting. The method used to classify tissue types based on the ASW emitted can be performed using intensive computational methods such as machine learning. The main reason was, machine leaning combined with acoustic emission sensors were already well established in industry and pre-clinical applications [12,22,35–38]. Other studies demonstrated that acoustic waves can be separated into multiple frequency bands for optoacoustic segmentation and visualization using a truncated k-space [39]. On the basis of this method, the efficiency of image artefacts was better than with zero-padding. We also considered the potential usage of such approaches in classification workflow. Therefore, characterization of frequency band of acoustic waves measured by ACTs were combined with machine learning methods for optoacoustic feedback in laser osteotomy.

Support vector machines (SVMs) represent a major development in pattern recognition for classification [40,41]. SVMs can find a hyperplane that divides samples into two classes with the widest margin between them. Additionally, SVMs extend this concept to a higher dimensional setting using a kernel function to illustrate a similarity measure in the experimental setup [40]. Both innovations can be formulated in a quadratic or Gaussian function framework, whose optimum solution is obtained in the computation time of a polynomial or a radial basis function kernel, respectively [42]. Therefore, SVMs are effective and practical solutions for biomedical signal recognition [40,41].

Another approach to classify tissue types is to use the artificial neural network (ANN) [43]. The ANN is a machine learning that is composed of an input layer, hidden layers that represent features, and an output layer [44]. ANN is a nonlinear model that is easy to use and

understand compared with statistical methods. The reason being that ANN is a nonparametric model, while most of the statistical methods are parametric models that need a higher background of statistics. ANN with the back propagation learning algorithm is widely used in solving various classification and forecasting problems [45,46].

In this study, we ablated hard bone, soft bone, muscle, fat, and skin tissues, using a nanosecond Nd:YAG laser at 532 nm and a microsecond Er:YAG laser at 2940 nm. We measured the emitted ASWs using a high-efficiency broad-band air-coupled piezoelectric ultrasonic transducer. To simultaneously classify tissue types, we used and compared the performances of principal component analysis (PCA) combined with either a quadratic/Gaussian-SVM or the ANN. Here, PCA was used for data reduction to decrease the computational time during tissue classification [47]. To the best of our knowledge, our group was the first one to use these machine learning methods to investigate optoacoustic tissue classification.

MATERIAL AND METHOD

Sample Preparation

In the laser-tissue ablation experiments, we used five fresh porcine proximal and distal femurs. Each fresh porcine proximal and distal femur was purchased at a local butcher each day. With scalpels, the connective tissues (Fig. 1) were carefully separated to extract hard and soft bone, muscle, fat, and skin tissues from each proximal and distal femur. The sample was then rinsed in distilled water before the laser experiments. The dimensions of all compact bone fragments, soft bone, muscle, fat, and skin tissues were $10 \times 50 \times 5\ \text{mm}^3$.

Experimental Set-Up

The laser ablation experiments were conducted with different samples in wet conditions. A spray of distilled water with a flow rate of 0.1 ml/s was directed to the spot of ablation, wetting the sample each time, before the laser pulse hit the tissue. Ablation was performed using a Q-switched frequency-doubled Nd:YAG laser (Q-smart 850; Quantel, Paris, France) at 532 nm (producing 5 nanoseconds pulses) and an Er:YAG laser (litetouch LI-FG0001A; Syneron Candela, Syneron, Israel) at 2940 nm (producing 400 microseconds pulses) (Fig. 2a and b). The output pulse energy of the Nd:YAG laser and the Er:YAG laser were 200 and 940 mJ, respectively.

The triggering signal was collected directly from the Nd:YAG laser. In the case of Er:YAG, a CaF_2 window was placed in front of the laser head to split the incident laser beam into two parts—96% transmitted and 4% reflected light—to allow for a triggering signal. The reflected light was collected by a fast PbSe photodiode (PbSe Fixed Gain Detector, PDA20H, 1500–4800 nm; Thorlabs, Munich, Germany). For both systems, a data recording element was embedded in a single opto-acoustic system (Fig. 2a and b). The trigger signal activates the capturing of the signal received by the transducer. In the experiments, data recording took place during a time window—also known as the data acquisition window for each acoustic wave—of 0.82 milliseconds. This time window was determined based on the measured acoustic signal where a high signal-to-noise ratio was obtained. A corner mirror placed in the beam path of the laser was used to reflect the laser pulse at a 90° angle. The output beam of the laser was then focused on the surface of the target specimen by using a 30 mm lens in each experiment. Several craters were produced *ex vivo* on the specimens, using the two lasers. For both lasers, each sample was exposed to 180 laser pulses at a repetition rate of 2 Hz at a single location. This procedure was repeated at 10 different ablation locations, spaced 4 mm apart. Hence, the number of craters done in each experiment was 500 craters—20 craters at the surface of the same tissue type extracted from each proximal and distal femur.

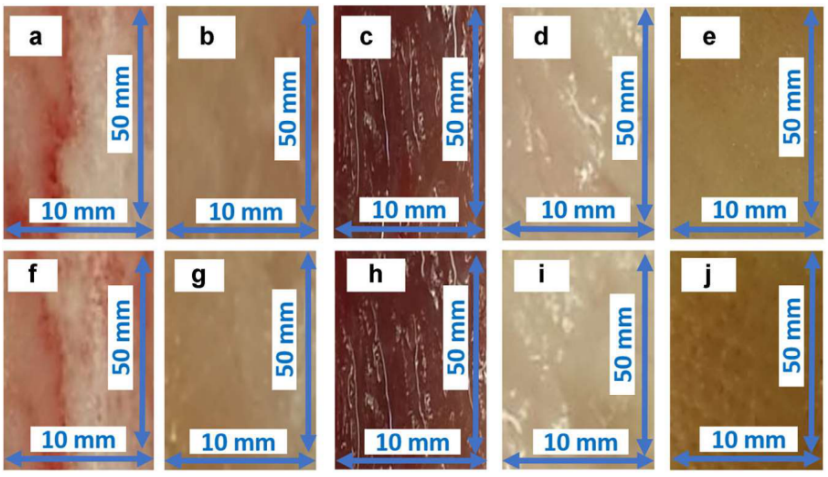

Fig. 1. Tissue samples from one fresh porcine femur. Proximal femur: hard bone (**a**), soft bone (**b**), muscle (**c**), fat (**d**), and skin (**e**); distal femur: hard bone (**f**), soft bone (**g**), muscle (**h**), fat (**i**), and skin (**j**).

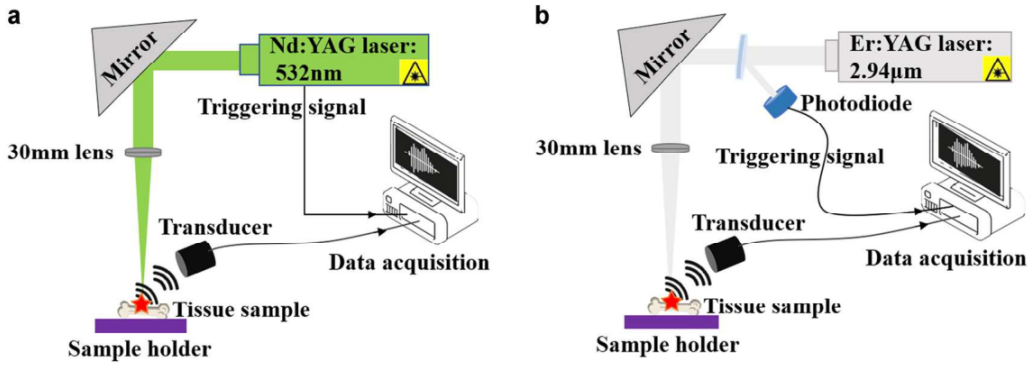

Fig. 2. Schematic of the experimental set-up for the laser-induced acoustic shock wave measurement using (**a**) the nanosecond Q-switched Nd:YAG laser and (**b**) the microsecond Er:YAG laser during tissue ablation. Er:YAG, erbium-doped yttrium aluminum garnet; Nd:YAG, neodimium-doped yttrium aluminum garnet.

The ASW is radiated from the ablation spot into the surrounding media and is picked up by the transducer, where the acoustic wave is converted into an electrical signal [20].

Detection and Analysis of the ASW Signal

This transducer was a self-developed, custom-made air-coupled PZT (manufactured in the ITEFI-Instituto de Technologias Fisicas y de la Information, CSIC, Madrid, Spain), with a resonance frequency of 0.4 MHz, an available frequency band of 0.1–0.8 MHz, and a 15 mm aperture (Fig. 3). The calibration of the frequency band (frequency response) of the transducer in reception mode was obtained by using a calibrated source with flat frequency response in the frequency range 0.1–1 MHz. Being in the low MHz range compared with conventional microphones, the design and fabrication of air-coupled PZTs is complicated due to the enormous impedance mismatch between the piezoelectric element and air. For our application, an optimized stack of detuned quarter wavelength matching layers was used to optimize both transducer bandwidth and sensitivity that are critical in this application [48,49]. The temporal profile of ASW signals detected by the transducer were amplified by 30 dB and digitized by a PCI Express x8 (16-bit resolution, four channels at 10 MS/s each, M4i.44xx-x8; Spectrum Microelectronic GmbH, Grosshansdorf, Germany). The transducer was placed at a 45° angle and 5 cm away from the ablated spot, to avoid saturation of the ultrasonic sensor while recording the laser-induced acoustic wave during plasma formation or the ablation process. Data were collected using LabVIEW (version 2016a) and information was extracted from the samples using MATLAB (version R2018b) software.

Statistical Analysis

Statistical analysis and calculations were performed in MATLAB software. We suppressed the phase shift of the measured ASW signal in the time domain by only using the amplitude spectrum determined using the fast Fourier transform at a sampling rate of 10 MHz. The average of two ASW spectra was calculated to improve the signal-to-noise ratio between each measured ASW amplitude spectrum. We split the amplitude spectrum into three equal frequency bands (low-, mid-, and high-frequency). Each frequency band was used as an input for the PCA. PCA was used to reduce the complexity of high-dimensional data by maintaining the same patterns and trends of the ASW field [50]. To classify tissue, we investigated the processed acoustics by looking at the amplitude-frequency band in which we achieved the best average classification error for each tissue type.

We compared the performance of PCA combined with either a quadratic and Gaussian SVMs or an ANN method. To implement the architecture of the SVM models, we used the *fitcecoc* function available in MATLAB (version R2018b) with the polynomial based kernel (with order of 4) and the gaussian kernel. For the ANN, we used the *pattern network* function combined with the *Tan-Sigmoid activation* function for hidden layers and *Softmax activation* function for the output layer. This is because multilayer networks can use the *Tan-Sigmoid* function and the output neurons are often used for pattern recognition problems. Furthermore, the *Softmax* function which was also known as a normalized

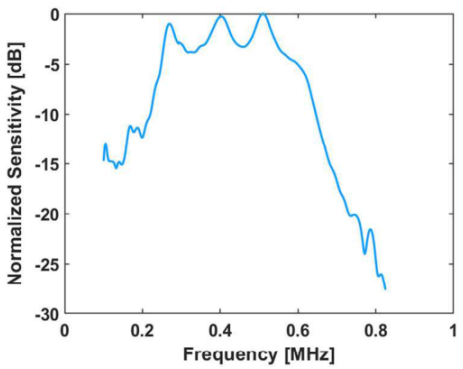

Fig. 3. Measured frequency response of the custom-made air-coupled piezoelectric transducer in reception mode.

exponential function was employed to the layer's output to predict the label [51,52]. We evaluated the performance of our models fairly on a single computer with specification of 2.4 GHz Intel Core i7 processor, 16 GB 1867 MHz DDR3 memory.

During the training phase of the quadratic and Gaussian SVM, we used scores from the set of training data combined with a quadratic and Gaussian function kernel to set the boundary of the trained SVM. Testing scores within the boundary were considered as true positives or correct positive prediction and false positives (FP) also known as incorrect positive prediction otherwise. The criterion used by the two types of SVMs is based on margin maximization between the two data classes of tissues. The margin is the distance between the hyperplanes bounding in each class, wherein the hypothetical perfectly separable case, no observation may lie [53]. For the ANN method, we used one input layer, one hidden layer, and one output layer to build the network. The input layer was made of three neurons. The single hidden layer and the output layer were made of 10 neurons and five neurons, respectively. Then the Backpropagation algorithm was used to train the 10 neurons of the hidden layer using gradient descent. Similar to the SVM methods, the first three PCA scores from the set of data points were used as input sets of the ANN. A summary of the signal processing pipeline for tissue classification is given in Figure 4. For the SVMs, a set of 14,400 data points (or 7,200 averages of two spectra), measured from 10 craters in four proximal and distal femurs, was used as training data, while a set of 3,600 data points (or 1,800 averages of two spectra), measured from ten craters in the remaining proximal and distal femur, was considered as testing data for both lasers.

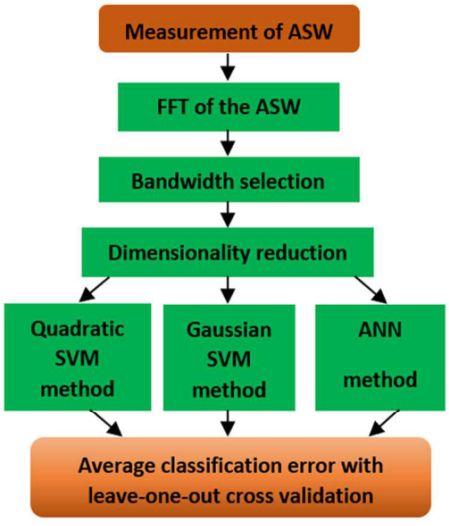

Fig. 4. Flowchart of the signal processing methods for tissue classification. ANN, artificial neural network; ASW, acoustic shock wave; FFT, fast Fourier transform; SVM, support vector machine.

We, then, simultaneously classified classes of tissues, using proximal and distal femur cross-validation. In the case of ANN, a set of 10,800 data points, measured from 10 craters in three proximal and distal femurs from the first three porcine, was used as training data. Then, a set of 3,600 data points, measured from 10 craters in one distal femur from the third porcine, was used as validation data. During the testing phase, a set of 3,600 data points, measured from 10 craters in the remaining proximal and distal femur from the fourth porcine, was considered as testing data for both lasers. The ground truth was obtained by ensuring that the tissue labels were correctly observed, and each tissue was uniformed. During the classification phase, the average error was calculated based on the mean error of five cross validated results from five folds—five proximal and distal femurs extracted from five different porcines. From the confusion matrix, percentage errors rate in the testing-data-based scores from each specimen were calculated as the number of all incorrect predictions divided by the total number of the dataset. The worst error rate is 0 (or 0%), whereas the best is 1 (or 100%) (Equation 1)

$$\%\mathrm{ER} = \frac{\mathrm{FP} + \mathrm{FN}}{\mathrm{Total}_{\mathrm{dataset}}} \times 100 \quad (1)$$

where FN is the false negative or incorrect negative prediction and FP, false positive or incorrect positive prediction.

RESULTS

The acoustic signals in the time domain were acquired during laser ablation for hard bone, soft bone, muscle, fat, and skin using (Fig. 2a) ns-Nd:YAG and (Fig. 2b) μs-Er:YAG lasers. By comparing the ASWs generated by the different tissues, we found that the peak-to-peak amplitude of the ASWs generated by the hard bone specimen and measured by the ACT were higher than those generated by the surrounding tissues (soft bone, muscle, fat, and skin). The peak-to-peak value of the ASWs generated for each tissue with the Nd:YAG laser was ~7 times higher than those generated with the Er:YAG laser. In addition, the acoustic signal duration (wt) generated by the Nd:YAG laser (wt = 0.82 milliseconds) was longer compared with the one generated by the Er:YAG laser (wt = 0.70 milliseconds). The corresponding frequency domain of the ASWs for each tissue is depicted in Figure 5a and b. The amplitude spectrum of hard bone is higher compared with that of the surrounding tissues (Fig. 5a and b). We split the spectrum into three equal frequency bands, as shown in Figure 5a and b. The data suggest at low and mid-frequency between 0.115–0.27 and 0.27–0.53 MHz, the classification of hard bone from the surrounding tissues was more accurate than in other bands when ablating with Er:YAG and Nd:YAG, respectively (Table 2). The classification of tissue types based on the analysis of the measured ASWs is depicted in Figures 6. The features that were chosen for PCA show 96.10% and 97.50% of the total variance in the acoustic waves generated with the

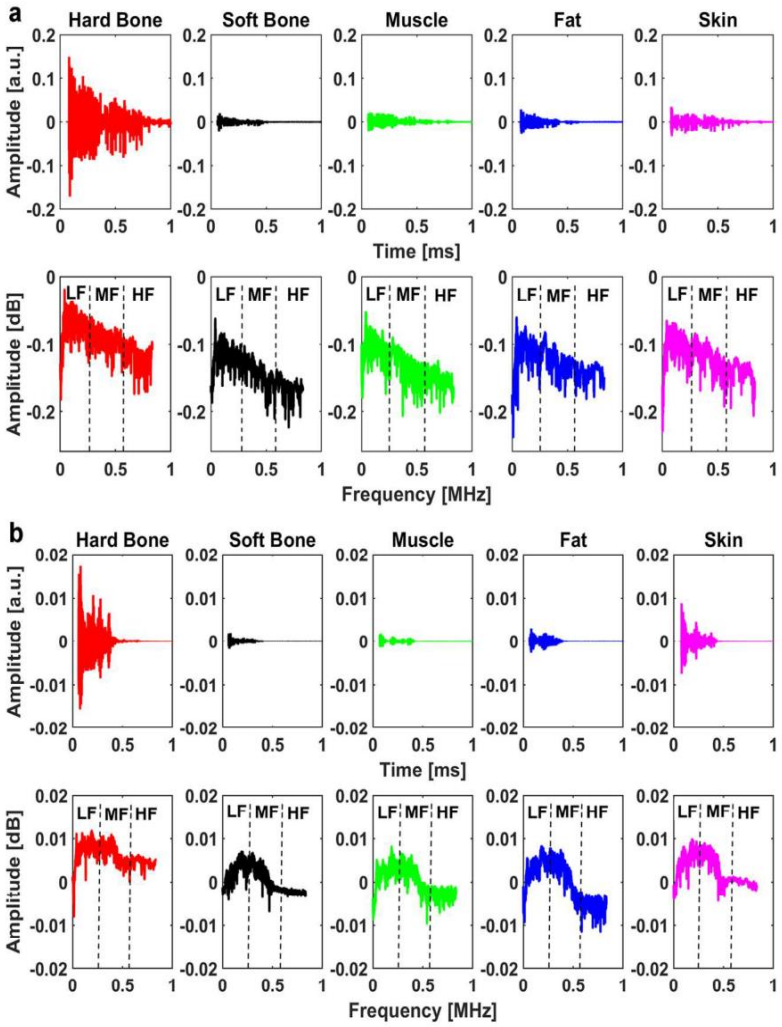

Fig. 5. (**a**) Measured shock wave using ns-Nd:YAG laser with time (Top row) and frequency domain (Bottom row): low-frequency (LF), mid-frequency (MF), high -frequency (HF). (**b**) Measured acoustic wave using μs-Er:YAG laser with time (Top row) and frequency domain (Bottom row): LF, MF, HF. Er:YAG, erbium-doped yttrium aluminum garnet; Nd:YAG, neodimium-doped yttrium aluminum garnet.

Nd:YAG laser and the Er:YAG laser, respectively. We observed a better classification performance with the ANN than with the quadratic and Gaussian SVM methods, for both lasers—at low and mid-frequency for Er:YAG and Nd:YAG, respectively. Table 2 further shows that the ANN performed the best, with an average classification error for all tissues of $5.01 \pm 5.06\%$ and $9.12 \pm 3.39\%$, using the Nd:YAG and Er:YAG lasers, respectively. Then, the Gaussian-SVM performed better than the quadratic SVM during the ablation with both lasers. The Gaussian-SVM yielded average classification errors of $15.17 \pm 13.12\%$ and $16.85 \pm 7.59\%$, using the Nd:YAG and Er:YAG lasers, respectively (Table 2). The worst performance was achieved with the quadratic-SVM with a classification error of $50.34 \pm 35.04\%$ and $69.96 \pm 25.49\%$, using the Nd:YAG and Er:YAG lasers. Average classification errors with leave-one-out cross validation for ANN and SVMs are detailed in Tables 3–5. The computational time for testing the ANN and SVM based model is in the order of 11–20 milliseconds. Summary of each computational time is in Table 6.

DISCUSSION

We observed greater amplitudes for the ASWs generated with the Nd:YAG laser than the ones generated by the Er:YAG laser (Fig. 5a and b). This amplitude value suggests that the generation of acoustic waves is more efficient with the nanosecond Nd:YAG laser. This is because the amplitude of the generated ASWs depends not only energy but also pulse duration, focusing conditions, and mainly tissue type being ablated. In fact, at the same laser pulse duration and focusing conditions, the acoustic amplitude increases with energy [54,55]. Therefore, if both lasers have the same pulse duration, the acoustic amplitude from the Er:YAG laser at 940 mJ, should be

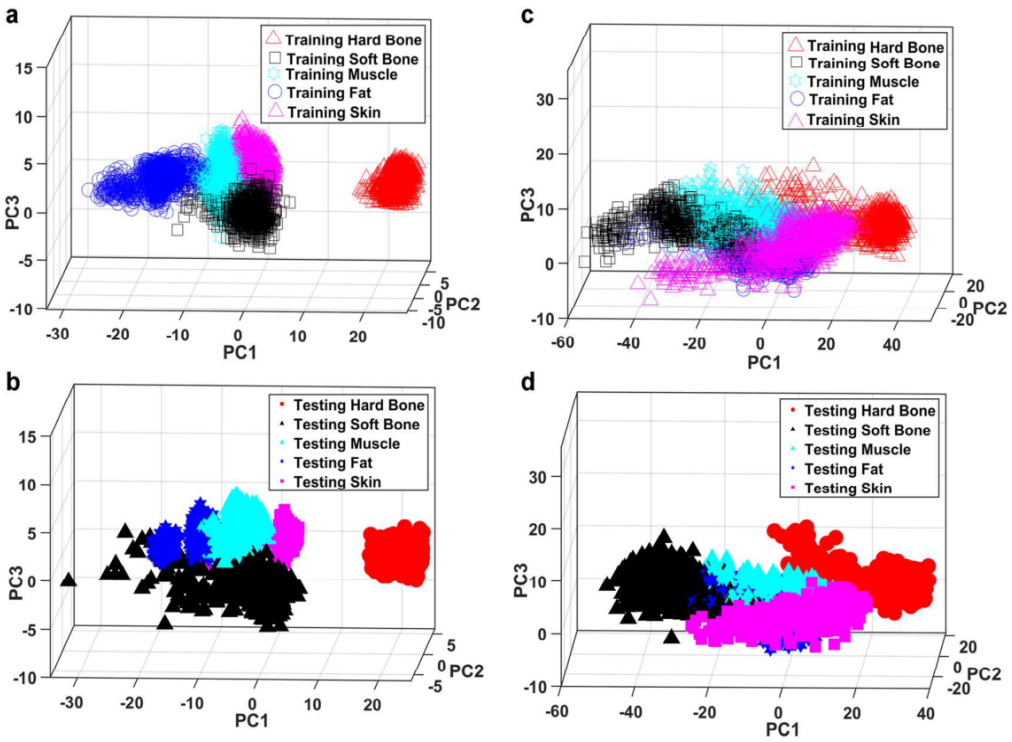

Fig. 6. Seven thousand and two hundred scores from training data (**a** and **c**; using Nd:YAG laser and Er:YAG laser, respectively) and classification of 1,800 scores from testing data (**b** and **d**; using Nd:YAG laser and Er:YAG laser, respectively) based on margin maximization between the five data classes of the training data for hard and soft bone, muscle, fat, and skin. Er:YAG, erbium-doped yttrium aluminum garnet; Nd:YAG, neodimium-doped yttrium aluminum garnet.

higher than that of with the Nd:YAG laser at 200 mJ. However, in this experimental study, both lasers operate at different pulse durations. Therefore, even though the Nd:YAG has less pulse energy than the Er:YAG, we observe greater amplitudes for the ASWs generated with the Nd:YAG laser than the ones generated by the Er:YAG laser (Fig. 5a and b). The Nd:YAG generated acoustic wave is much more effective, generating high frequencies, while Er:YAG is not only less efficient (smaller amplitude) but also more frequency selective, being more efficient in the band 0.1–0.4 MHz. This information could be used to adapt and optimize receiver transducers for this purpose. The higher values were theoretically expected, as the ablation with the Nd:YAG is based on plasma mediation, which increases the pressure energy measured by the transducer. The Er:YAG laser source results in thermal ablation, thus, most of the light energy is absorbed by the exposed tissue and transformed into heat [12,20,56].

This is likely also the reason the acoustic signal duration generated by the Nd:YAG laser was longer as compared to the one generated by the Er:YAG laser (Fig. 5a and c). This behavior (acoustic signal duration) suggests a more resonant ASW generation while using the Nd:YAG laser. The bandwidth of the ASW's response is broad because the measured acoustic waves result from transient signals. For Er:YAG, we used the low-frequency band of 0.115–0.27 MHz (Fig. 5d) to classify tissue types because thermal ablation generates acoustic waves (not shock wave and acoustic wave is always in the low-frequency range); and important parameters of acoustic waves lie in this region. Moreover, the transducer is fully characterized at 0.1–0.8 MHz (Fig. 4), by focusing the analysis

TABLE 1. A Summarizing Table of Both Laser's Parameters for all Five Tissues

Laser types	Pulse energy (mJ)	Pulse duration (μs)	Repetition rate (Hz)	Laser wavelength (nm)	Distance between lens and tissue (mm)	Water flow rate (ml/s)
Nd:YAG	200	5×10^{-3}	2	532	30	0.1
Er:YAG	940	400	2	2940	30	0.1

Er:YAG, erbium-doped yttrium aluminum garnet; Nd:YAG, neodimium-doped yttrium aluminum garnet.

TABLE 2. Average Error of All Tissues for Both Lasers Using SVM and ANN at Low, Mid, and High-Frequency for Both Nd:YAG and the Er:YAG Ablation

Comparison of three methods			
Laser types	Quadratic-SVM	Gaussian-SVM	ANN
Low-frequency: 0.115–0.27 MHz			
Nd:YAG	55.89%	18.37%	8.81%
Er:YAG	69.96%	16.85%	9.12%
Mid-frequency: 0.27–0.53 MHz			
Nd:YAG	50.34%	15.17%	5.01%
Er:YAG	72.4%	30.82%	14.62%
High-frequency: 0.53–0.80 MHz			
Nd:YAG	53.39%	20.04%	10.48%
Er:YAG	76.52%	26.66%	21.15%

ANN, artificial neural network; Er:YAG, erbium-doped yttrium aluminum garnet; Nd:YAG, neodimium-doped yttrium aluminum garnet; SVM, support vector machine.

above 0.1 MHz, we were always able to reduce this unwanted signal component, thereby improving the tissue classification. Confusion matrices indicate that tissue classification has the highest accuracy within this band as highlighted in Table 1. In contrast to the Er:YAG, cutting tissue with Nd:YAG is based on the plasma mediated ablation and emits the shock waves in which spectra extend beyond 1 MHz [57]. However, the −3 dB bandwidth of our commercial microphones do not typically exceed 0.9 MHz and the resonant frequency is at 0.4 MHz. Therefore, using the mid-frequency band 0.27–0.53 MHz (Fig. 5b), the confusion matrices indicate that the tissue classification has the highest accuracy within this band. Another advantage of using this region is it overlaps with the frequency band where the transducer has highest sensitivity.

Hard bone specimens generated higher peak-to-peak ASW values than the soft tissues did because soft tissues contain 79% water, while hard bone is made up of 85–95% carbonated hydroxyapatite [58]. Thus, we believe that the carbonated hydroxyapatite resulted in a higher amplitude due to its compact structure [10,58,59]. On the basis of this compact structure (physical propriety) of hard bone, it was possible to classify hard bone against soft tissues, during both lasers (details are in Table 3 and 4). In general soft tissues—except the classification error for muscle tissue using the Nd:YAG—had the highest average classification errors compared with hard bone. This is probably due to the structure of the soft tissues, which consist of fatty connecting tissue and contain more water than bone, resulting in lower amplitude ASWs as compared with bone.

The ANN method showed a superior classification performance as compared to the quadratic- and Gaussian-SVM methods; the Gaussian-SVM performed better than the quadratic-SVM method (Tables 2–5). One explanation for this result is that we trained our classifier using a large amount of data; with more data, the ANN and Gaussian kernel perform generally better than the polynomial kernels. Therefore, using the ANN and Gaussian kernel, we can model more functions within its function space than using the polynomial kernels. However, if we

TABLE 3. Confusion Matrix for Hard Bone, Soft Bone, Fat, Skin, and Muscle Tissue at Low- and Mid-Frequency During Nd:YAG and the Er:YAG Ablation, Respectively

Quadratic SVM method						
	Classified as					
Tissue	Hard bone	Soft bone	Fat	Muscle	Skin	Average classification error
Hard bone						
Nd:YAG	1645	0	0	139	16	8.60%
Er:YAG	1464	16	63	175	82	18.70%
Soft bone						
Nd:YAG	140	449	1209	1	1	75.10%
Er:YAG	637	265	137	278	483	85.30%
Fat						
Nd:YAG	263	310	609	0	618	66.20%
Er:YAG	643	36	194	319	638	89.22%
Muscle						
Nd:YAG	109	0	0	1667	24	7.40%
Er:YAG	717	132	63	429	459	76.17%
Skin						
Nd:YAG	2	1342	356	0	100	94.40%
Er:YAG	1045	9	41	353	352	80.40%

Numbers in the table are testing-data-based scores from each specimen.
Er:YAG, erbium-doped yttrium aluminum garnet; Nd:YAG, neodimium-doped yttrium aluminum garnet; SVM, support vector machine.

TABLE 4. Confusion Matrix for Hard Bone, Soft Bone, Fat, Skin, and Muscle Tissue at Low- and Mid-Frequency During Nd:YAG and the Er:YAG Ablation, Respectively

Gaussian SVM method						
	Classified as					
Tissue	Hard bone	Soft bone	Fat	Muscle	Skin	Average classification error
Hard bone						
Nd:YAG	1682	0	0	118	0	6.55%
Er:YAG	1718	4	0	0	78	4.56%
Soft bone						
Nd:YAG	0	1669	46	9	76	7.28%
Er:YAG	3	1579	3	30	185	12.30%
Fat						
Nd:YAG	0	273	1322	29	176	26.60%
Er:YAG	0	25	1390	227	159	22.83%
Muscle						
Nd:YAG	0	3	0	1797	0	0.17%
Er:YAG	0	63	194	1473	70	18.17%
Skin						
Nd:YAG	0	171	249	215	1165	35.27%
Er:YAG	105	159	107	105	1324	26.4%

Numbers in the table are testing-data-based scores from each specimen.
Er:YAG, erbium-doped yttrium aluminum garnet; Nd:YAG, neodimium-doped yttrium aluminum garnet; SVM, support vector machine.

TABLE 5. Confusion Matrix for Hard Bone, Soft Bone, Fat, Skin, and Muscle Tissue at Low- and Mid-Frequency During Nd:YAG and the Er:YAG Ablation, Respectively

ANN method						
	Classified as					
Tissue	Hard bone	Soft bone	Fat	Muscle	Skin	Average classification error
Hard bone						
Nd:YAG	1800	0	0	0	0	0%
Er:YAG	1750	0	0	0	50	2.78%
Soft bone						
Nd:YAG	0	1691	41	1	67	6.06%
Er:YAG	0	1653	8	59	80	8.17%
Fat						
Nd:YAG	0	44	1722	0	33	4.28%
Er:YAG	0	109	1594	24	73	11.44%
Muscle						
Nd:YAG	0	7	1	1792	0	0.44%
Er:YAG	0	51	64	1603	82	10.94%
Skin						
Nd:YAG	0	49	208	0	1543	14.28%
Er:YAG	24	99	82	16	1579	12.28%

Numbers in the table are testing-data-based scores from each specimen.
Er:YAG, erbium-doped yttrium aluminum garnet; Nd:YAG, neodimium-doped yttrium aluminum garnet; SVM, support vector machine.

TABLE 6. Average Computational Time to the Test of the SVM and ANN Models for Both Lasers

Laser types	Quadratic-SVM (ms)	Gaussian-SVM (ms)	ANN (ms)
Nd:YAG	20.02	13.08	11.09
Er:YAG	23.14	14.12	11.17

ANN, artificial neural network; Er:YAG, erbium-doped yttrium aluminum garnet; Nd:YAG, neodimium-doped yttrium aluminum garnet; SVM, support vector machine.

had used fewer data, then, a polynomial kernel would have been a much better fit to the measured data than the gradient and Gaussian. In fact, the ANN and Gaussian SVM method are nonparametric methods, meaning that the complexity of the model is potentially infinite; its complexity can grow with the data [53,60]. More data will be able to represent more and more complex relationships—however, this simple classification approach also hase limits as it has a single hidden layer. In contrast, the quadratic-SVM methods have a fixed size (parametric model), so after a certain point, the model will be saturated, and increasing the data would not improve the classifier. In this case, we had a large amount of data and very weak assumptions about the challenge, thus a nonparametric method served us better.

Furthermore, we used leave-one-out cross validation because, in general, there is a tradeoff between accuracy and generalization. The more accurate the classifier is with the training data, the less likely it is to generalize (though it depends on the training data). Furthermore, we used PCA to reduce the data dimensionally at each frequency range. This is because principal components (PCs) consecutively maximize variance and can be obtained from the eigenvalues/eigenvectors of a covariance matrix [61]. When all variables are measured in the same units, covariance-based PCA may be suitable. In general, the first PCs are dominated by high-variance variables and mostly represent the variance of each data. Therefore, by confining the number of eigenvalues and eigenvectors to the first three PCs, we aim to keep the most represent variance of each data and improve the speed of online classifier when transferring feedback sensor to other systems for *in vivo* measurements.

In case that the online classifier produces more error, more PCs can be used as a solution even if the computational time increases. In addition, the angle between the transducer and the ablated spot must be adjusted to 45°. Moreover, the transducer should be placed 5 cm away from the ablated spot to maintain the same condition as in this experimental setup. In case that the machine structure does not allow to fix the sensor position at the mentioned angle and distance, an alternative approach is to fix an omnidirectional transducer at any angle and distance in the linear regime to collect the data. Then, the data need to be normalized in the time domain to avoid the negative impact of the distance between the transducer and the ablated spot (because the amplitude value of the acoustic wave exponentially decays with the distance). To improve the machine learning approach, the system must be trained with a lot of data using femurs from different patients and body parts such as the skull. This is because depending on age, nutrition, and body parts of each patient, it is possible that the tissue response varies slightly. By making the laser cut other body parts such as skull or limb, the laser should be able to rotate around them while cutting. This requires an XYZ machine (controlled rotating holder). Laser combined with a robotic arm or endoscope to be able to control the movements is the next plan of MIRACLE project.

Furthermore, the feedback system must be also regularly trained when transferring results to another system or machine (new condition). This is because the sensor system could have different transfer functions or irrigation conditions, which can affect the raw data of acoustic measured time. Additionally, during ablation by the Er:YAG laser, carbonization can possibly appear at the ablated spot if the water cooling system is not appropriately set. To avoid this, automatic detection for early carbonization (dry tissue vs. wet tissue) must also be integrated in the current feedback to classify the ablated tissue and monitor early carbonization simultaneously in real time. As soon as the feedback system detects early carbonization, water flow rate of the cooling system will be increased to prevent carbonization. Currently, we used distilled water in ablation experiments to prevent earlier carbonization, distilled water can be replaced by physiological water which is more suitable for surgery. We have tested physiological water in our previous experiments in which we got a similar behavior to the distilled water. So, we continued using distilled water because it is already in our laboratory. When using the laser system in the clinic, we will perform experiments with the physiological water.

Moreover, in our previous work, we investigated optimum laser parameters for a long-pulsed high-energy laser to produce craters with minimal thermal damage under wet condition using an optical coherence tomography or confocal microscope, and a scanning electron microscope (SEM) [12]. The pulse duration and pulse energies were 0.5–10 milliseconds and 0.75–15 J, respectively. The confocal microscope was used for calculating the ablation efficiency but SEM was needed for analyzing craters of various morphologies to observe random charring, thermal damage, and cracks of hard and soft tissues. We planned to use the same method to investigate the difference in ablation and burning depth of hard tissue compared with soft tissue, using both lasers. Future work will also include a histological study in a cross-section for each tissue after the laser ablation, to fully evaluate the potential of the technique in terms of the reduction of bone damage compared with other techniques. For bone cutting, we applied fixed high energy pulses to produce ablation. That is why in our case, the light dose is always the same as the laser is used for bone ablation application. Hence, it is not needed to perform a classification with unseen data (at different laser energies) to conclude on the actual utility of the proposed

scheme in realistic situations that might arise in the clinic. In addition, the time for cutting a real bone with laser is longer than when using standard mechanical tools such as a saw; however, the laser has more advantages—including functional cuts, contactless interaction, and faster wound healing—which gives an overall better outcome than mechanical surgery. The ablation rate at the surface (~1 mm depth) is around 10 and 0.1 mm/s for Er:YAG and Nd:YAG, respectively. However, at deeper ablation (~10 mm depth) is 0.2 mm/s for Er:YAG; we have not yet done with Nd:YAG for hole ablation. Additionally, in terms of contamination, for all the debris, we use the extraction system, or we just blow off all the debris using pressurized air. In contrast to the standard mechanical tools, laser ablation produces microparticles, and the bone is completely disintegrated.

Currently, the error rate is less than 10%. This promising result led us to investigate advanced precision in signal classification to further reduce the classification error. To reach efficiency in processing, we plan to involve a cutting-edge deep learning technique such as a one-dimensional Convolutional Neural Network to classify these ASWs. We also plan to filter out misclassified data based on the temporal discrimination of tissue types—that is, when doing a line cut on top of hard bone with laser, we detect hard bone during the last ten shots and suddenly, we detect skin in one shot followed by the detection of hard bone again, the software will just filter out this misclassified skin and considers it as outlier or hard bone. Additionally, we are also investigating sensitive sensors such as optical sensors to improve ASW measurement. We believe that with better data measured, classifiers will better detect tissues types compared to when using the ACT.

CONCLUSION

Our aim was to simultaneously classify tissue types during laser ablation by measuring the ASWs generated with an ACT and by processing the information using three different machine learning methods. The ANN, quadratic or Gaussian-SVM-methods were combined with PCA during classification. In the experiments, we used two different lasers to ablate tissue types and to generate ASWs. The peak-to-peak amplitudes of the ASW generated by the hard bone specimen and measured by the ACT were consistently higher than those generated by the surrounding tissues (soft bone, muscle, fat, and skin). On the basis of the average error for all tissues using both lasers, the ANN performed best in terms of classifying all tissues during ablation. Thus, the measured ASWs can be quantified and used to control the laser cutting process in a feedback control loop. By classifying tissue type during ablation, we avoid damaging an important tissue such as bone marrow (or soft bone). As soon the signal of the ASWs is classified as soft bone, the laser will stop ablating (the stopping point).

Future work includes the development of optical sensors to detect the ASW fields. Optical techniques are very sensitive to sharp changes in pressure with wide bandwidths compared with commercially-available transducers [57].

ACKNOWLEDGMENTS

This project is part of the MIRACLE (short for Minimally Invasive Robot-Assisted Computer-guided LaserosteotomE) project funded by the Werner Siemens Foundation. The ACTs part was funded by (DPI2016-78876-R-AEI/FEDER, UE) from the Spanish State Research Agency (AEI) and the European Regional Development Fund (ERDF/FEDER).

REFERENCES

1. Beltrán L, Abbasi H, Rauter G, Friederich N, Cattin P, Zam A. Effect of laser pulse duration on ablation efficiency of hard bone in microseconds regime. In: Third International Conference on Applications of Optics and Photonics. International Society for Optics and Photonics: Vol 10453. 2017. p 104531S.
2. Abbasi H, Beltrán L, Rauter G, Guzman R, Cattin PC, Zam A. Effect of cooling water on ablation in Er:YAG laser-osteotome of hard bone. In: Third International Conference on Applications of Optics and Photonics. International Society for Optics and Photonics: Vol 10453. 2017. p 104531I.
3. Romeo U, Del Vecchio A, Palata G, Tenore G, Visca P, Maggiore C. Bone damage induced by different cutting instruments: an in vitro study. Brazilian Dent J 2009;20:162–168. http://www.scielo.br/scielo.php?script=sci_arttext&pid=S0103-64402009000200013&nrm=iso
4. Baek K-W, Deibel W, Marinov D, et al. A comparative investigation of bone surface after cutting with mechanical tools and Er:YAG laser. Lasers Surg Med 2015;47(5):426–432. https://doi.org/10.1002/lsm.22352
5. Abbasi H, Rauter G, Guzman R, Cattin PC, Zam A. Differentiation of femur bone from surrounding soft tissue using laser-induced breakdown spectroscopy as a feedback system for smart laserosteotomy (SPIE Photonics Europe). SPIE 2018. 60.
6. Peng Q, Juzeniene A, Chen J, et al. Lasers in medicine. Rep Prog Phys 2008;71(5):056701.
7. Peavy GM, Reinisch L, Payne JT, Venugopalan V. Comparison of cortical bone ablations by using infrared laser wavelengths 2.9 to 9.2 μm. Lasers Surg Med 1999;25(5):421–434.
8. Walsh JT, Jr, Deutsch TF. Er:YAG laser ablation of tissue: measurement of ablation rates. Lasers Surg Med 1989;9(4):327–337.
9. Kuscer L, Diaci J. Measurements of erbium laser-ablation efficiency in hard dental tissues under different water cooling conditions. SPIE 2013;18:11.
10. Kang HW, Rizoiu I, Welch AJ. Hard tissue ablation with a spray-assisted mid-IR laser. Phys Med Biol 2007;52(24):7243–7259. http://stacks.iop.org/0031-9155/52/i=24/a=004
11. Li ZZ, Reinisch L, Van de Merwe WP. Bone ablation with Er:YAG and CO2 laser: Study of thermal and acoustic effects. Lasers Surg Med 1992;12(1):79–85.
12. Nguendon Kenhagho K, Shevchik S, Saeidi F, et al. Characterization of ablated bone and muscle for long-pulsed laser ablation in dry and wet conditions. Materials 2019;12(8):1338. http://www.mdpi.com/1996-1944/12/8/1338
13. Jowett N, Wöllmer W, Reimer R, et al. Bone ablation without thermal or acoustic mechanical injury via a novel picosecond infrared laser (PIRL). Otolaryngol Head Neck Surg 2014;150(3):385–393.
14. Ana PA, Bachmann L, Zezell DM. Lasers effects on enamel for caries prevention. Laser Phys 2006;16(5):865–875. https://doi.org/10.1134/s1054660x06050197
15. Abbasi H, Rauter G, Guzman R, Cattin PC, Zam A. Laser-induced breakdown spectroscopy as a potential tool for autocarbonization detection in laserosteotomy. J Biomed Opt 2018;23(7):071206.

16. Lewandrowski K-U, Lorente C, Schomacker KT, Fiotte TJ, Wilkes JW, Deutsch TF. Use of the Er:YAG laser for improved plating in maxillofacial surgery: Comparison of bone healing in laser and drill osteotomies. Lasers Surg Med 1996;19(1):40–45. https://doi.org/10.1002/(sici)1096-9101(1996)19:1<40::aid-lsm6>3.0.co;2-q
17. Fried D, Ashouri N, Breunig T, Shori R. Mechanism of water augmentation during IR laser ablation of dental enamel. Lasers Surg Med 2002;31(3):186–193.
18. Tulea C-A, Caron J, Gehlich N, Lenenbach A, Noll R, Loosen P. Laser cutting of bone tissue under bulk water with a pulsed ps-laser at 532 nm. SPIE 2015;20:9.
19. Abbasi H, Rauter G, Guzman R, Cattin PC, Zam A. Plasma plume expansion dynamics in nanosecond Nd: YAG laser-osteotome. In: High-Speed Biomedical Imaging and Spectroscopy III. International Society for Optics and Photonics: Vol 10505. 2018. p 1050513.
20. Kenhagho HN, Rauter G, Guzman R, Cattin PC, Zam A. Comparison of acoustic shock waves generated by micro and nanosecond lasers for a smart laser surgery system. SPIE BiOS 2018;10484:9.
21. Jacques SL. Role of tissue optics and pulse duration on tissue effects during high-power laser irradiation. Appl Opt 1993;32(13):2447–2454.
22. Bay E, Deán-Ben XL, Pang GA, Douplik A, Razansky D. Real-time monitoring of incision profile during laser surgery using shock wave detection. J Biophotonics 2015;8(1-2):102–111. https://doi.org/10.1002/jbio.201300151
23. Oraevsky AA, Jacques SL, Tittel FK. Mechanism of laser ablation for aqueous media irradiated under confined-stress conditions. J Appl Phys 1995;78(2):1281–1290.
24. Oraevsky AA, Jacques SL, Esenaliev RO, Tittel FK. Pulsed laser ablation of soft tissues, gels, and aqueous solutions at temperatures below 100°C. Lasers Surg Med 1996;18(3):231–240. https://doi.org/10.1002/(sici)1096-9101(1996)18:3<231::aid-lsm3>3.0.co;2-t
25. Nguendon HK, Faivre N, Meylan B, et al. Characterization of ablated porcine bone and muscle using laser-induced acoustic wave method for tissue differentiation. In: European Conferences on Biomedical Optics. SPIE: Vol 10417. 2017. p 10.
26. Nguendon HK, Faivre N, Meylan B, et al. Characterization of ablated porcine bone and muscle using laser-induced acoustic wave method for tissue differentiation. In: European Conference on Biomedical Optics. Optical Society of America. 2017. p 104170N.
27. Brecht H-PF, Su R, Fronheiser MP, Ermilov SA, Conjusteau A, Oraevsky AA. Whole-body three-dimensional optoacoustic tomography system for small animals. J Biomed Opt 2009;14(6):1–8. https://doi.org/10.1117/1.3259361. 8 [Online]. Available.
28. Fehm TF, Deán-Ben XL, Razansky D. Four dimensional hybrid ultrasound and optoacoustic imaging via passive element optical excitation in a hand-held probe. Appl Phys Lett 2014;105(17):173505.
29. Deán-Ben XL, Pang GA, Montero de Espinosa F, Razansky D. Non-contact optoacoustic imaging with focused air-coupled transducers. Appl Phys Lett 2015;107(5):051105.
30. Michau S, Mauchamp P, Dufait R. Piezocomposite 30MHz linear array for medical imaging: Design challenges and performances evaluation of a 128 elements array. In: IEEE Ultrasonics Symposium, 2004. IEEE: Vol 2. 2004. pp 898–901.
31. Franjic K, Cowan ML, Kraemer D, Miller RJD. Laser selective cutting of biological tissues by impulsive heat deposition through ultrafast vibrational excitations. Opt Express 2009;17(25):22937–22959. https://doi.org/10.1364/OE.17.022937. 12/07 2009.
32. Landa FJO, Özsoy C, Deán-Ben XL, Razansky D. Optoacoustic monitoring of RF ablation lesion progression (SPIE BiOS). SPIE 2019;94:117–123.
33. Rebling J, Landa FJO, Deán-Ben XL, Douplik A, Razansky D. Integrated catheter for simultaneous radio frequency ablation and optoacoustic monitoring of lesion progression. Opt Lett 2018;43(8):1886–1889.
34. Landa FJO, Deán-Ben XL, Sroka R, Razansky D. Volumetric optoacoustic temperature mapping in photothermal therapy. Sci Rep 2017;7(1):9695.
35. Landa FJO, Deán-Ben XL, Montero de Espinosa F, Razansky D. Noncontact monitoring of incision depth in laser surgery with air-coupled ultrasound transducers. Opt Lett 2016;41(12):2704–2707. https://doi.org/10.1364/OL.41.002704. 06/15 2016.
36. Gaja H, Liou F. Defects monitoring of laser metal deposition using acoustic emission sensor. Int J Adv Manuf Technol 2017;90(1–4):561–574.
37. Shevchik SA, Kenel C, Leinenbach C, Wasmer K. Acoustic emission for in situ quality monitoring in additive manufacturing using spectral convolutional neural networks. Addit Manuf 2018;21:598–604. https://doi.org/10.1016/j.addma.2017.11.012. 05/01/2018.
38. Gaja H, Liou F. Defect classification of laser metal deposition using logistic regression and artificial neural networks for pattern recognition. Int J Adv Manuf Technol 2018;94(1-4):315–326.
39. Jaeger M, Schüpbach S, Gertsch A, Kitz M, Frenz M. Fourier reconstruction in optoacoustic imaging using truncated regularized inverse k-space interpolation. Inverse Problems 2007;23(6):S51–S63.
40. Mehta SS, Lingayat NS. Biomedical signal processing using SVM. In: 2007 IET-UK International Conference on Information and Communication Technology in Electrical Sciences (ICTES 2007). 2007. pp 527–532.
41. Dehmeshki J, Chen J, Casique MV, Karakoy M. Classification of lung data by sampling and support vector machine. In: The 26th Annual International Conference of the IEEE Engineering in Medicine and Biology Society. Vol 2. 2004. pp 3194–3197.
42. Memarian N, Alirezaie J, Babyn P. Computerized detection of lung nodules with an enhanced false positive reduction scheme. In: 2006 International Conference on Image Processing. 2006. pp 1921–1924. https://doi.org/10.1109/ICIP.2006.313144
43. Guenther FH. Neural networks: Biological models and applications. In: Smelser NJ, Baltes PB, editors. International Encyclopedia of the Social & Behavioral Sciences. Oxford: Pergamon; 2001. pp 10534–10537.
44. Goodfellow I, Bengio Y, Courville A. Deep Learning. London, England: MIT Press; 2016.
45. Andrearczyk V, Whelan PF. Chapter 4—Deep learning in texture analysis and its application to tissue image classification. In: Depeursinge A, Al-Kadi OS, Mitchell JR, editors. Biomedical Texture Analysis. London, England: Academic Press; 2017. pp 95–129.
46. Alperovich Z, Yamin G, Elul E, Bialolenker G, Ishaaya AA. In situ tissue classification during laser ablation using acoustic signals. J Biophotonics 2019;12:e201800405.
47. Brereton RG. The Mahalanobis distance and its relationship to principal component scores. J Chemom 2015;29(3):143–145. https://doi.org/10.1002/cem.2692
48. Alvarez-Arenas TEG. Acoustic impedance matching of piezoelectric transducers to the air. IEEE Trans Ultrason Eng 2004;51(5):624–633. https://doi.org/10.1109/TUFFC.2004.1320834
49. Álvarez-Arenas TG, Camacho J. Air-coupled and resonant pulse-echo ultrasonic technique. Sensors 2019;19(10):2221.
50. Lever J, Krzywinski M, Altman N. Principal component analysis. Nat Methods 2017;14:641–642. https://doi.org/10.1038/nmeth.4346. 06/29/online
51. Bishop CM. Pattern Recognition and Machine Learning. London, England: Springer Science+ Business Media; 2006.
52. Lehman J, Risi S, Clune J. Creative generation of 3D objects with deep learning and innovation engines. In: Proceedings of the 7th International Conference on Computational Creativity. 2016.
53. Auria L, Moro RA. Support vector machines (SVM) as a technique for solvency analysis. 2008.
54. Dupont A, Caminat P, Bournot P, Gauchon J. Enhancement of material ablation using 248, 308, 532, 1064 nm laser pulse with a water film on the treated surface. J Appl Phys 1995;78(3):2022–2028.
55. Hyun Wook K, Ho L, Shaochen C, Welch AJ. Enhancement of bovine bone ablation assisted by a transparent liquid layer on a

target surface. IEEE J Quantum Electron 2006;42(7):633–642. https://doi.org/10.1109/JQE.2006.875867
56. Manikanta E, Vinoth Kumar L, Venkateshwarlu P, Leela C, Kiran PP. Effect of pulse duration on the acoustic frequency emissions during the laser-induced breakdown of atmospheric air. Appl Opt 2016;55(3):548–555. https://doi.org/10.1364/AO.55.000548. 01/20 2016.
57. Yuldashev P, Karzova M, Khokhlova V, Ollivier S, Blanc-Benon P. Mach-Zehnder interferometry method for acoustic shock wave measurements in air and broadband calibration of microphones. J Acoust Soc Am 2015;137(6):3314–3324. https://doi.org/10.1121/1.4921549
58. Curzon M, Featherstone J. Chemical composition of enamel. In: Lazzan EP, editor. Handbook of Experimental Aspects of Oral Biochemistry. Boca Raton, FL: CRC Press; 1983. pp 123–135.
59. Apel C, Meister J, Ioana R, Franzen R, Hering P, Gutknecht N. The ablation threshold of Er:YAG and Er:YSGG laser radiation in dental enamel. Lasers Med Sci 2002;17(4):246–252.
60. Le T, Nguyen V, Nguyen TD, Phung D. Nonparametric budgeted stochastic gradient descent. In: Artificial Intelligence and Statistics. 2016. pp 654–572.
61. Jolliffe IT, Cadima J. Principal component analysis: A review and recent developments. Philos Trans R Soc A 2016; 374(2065):20150202.

Chapter 4

Wideband Optoacoustic Feedback System for Tissue Classification

Introduction

The publication presented in this chapter described a new method of tissue classification during laser osteotomy. We recorded the acoustic shock waves generated by tissue ablation using a custom Mach-Zehnder interferometer. The resulting waveforms were transformed into the frequency domain. The amplitudes of the spectra were split into discrete frequency bands, which were then used as input for principal component analysis (PCA) to characterize the signals. Overall, the method proved to robustly classify hard bone and soft tissue but it is not ideal for classifying soft bone and fat tissue. However, when comparing tissue classification performance, the ASWs measured by the custom Mach-Zehnder interferometer produced fewer classification errors when distinguishing between soft tissue types than the air-coupled transducer.

Publication. The proposed method was published in 2019 IEEE Transactions on Ultrasonics, Ferroelectrics, and Frequency Control, with peer review [4].

https://doi.org/10.1109/TUFFC.2019.2923696

Optoacoustic Tissue Differentiation Using a Mach–Zehnder Interferometer

Hervé Nguendon Kenhagho, Georg Rauter, Raphael Guzman, Philippe C. Cattin, and Azhar Zam

***Abstract*— Laser osteotomy offers a way to make precise and less traumatic cuts smaller than conventional mechanical bone surgery tools. To fully exploit the advantages of laser osteotomy over conventional osteotomy, real-time feedback to differentiate the hard bone from the surrounding soft tissues is desired. In this study, we differentiated various tissue types—hard and soft bone, fat, muscle, and skin tissues from five proximal and distal fresh porcine femurs—based on cutting sounds. For laser ablation, an Nd:YAG laser was used to create ten craters on the surface of each proximal and distal femurs. For sound recording, the probing beam of a Mach–Zehnder interferometer was placed 5 cm away from each ablation site. For offline tissue differentiation, we investigated the measurements by looking at the amplitude frequency band between 0.83 and 1.25 MHz, which provides the least average classification error. Then, we used principal component analysis to reduce the dimensionality and the 95% confidence ellipsoid (Mahalanobis distance) method to differentiate between tissues based on the acoustic shock wave. A set of 14 400 data points, measured from ten craters in four proximal and distal femurs, was used as "training data," while a set of 3600 data points from ten craters in the remaining proximal and distal femurs was considered as "testing data." As is seen in the confusion matrix, the experimental-based scores of hard and soft bones, fat, muscles, and skin yielded average classification errors (with leave-one-out cross validation) of 0.11%, 57.69%, 0.06%, 0.14%, and 2.92%, respectively. The results of this study demonstrate a promising technique for differentiating tissues during laser osteotomy.**

***Index Terms*— Acoustic tissue response, laser ablation, Mach–Zehnder interferometer, tissue differentiation.**

I. Introduction

LASER osteotomes enable controlled, contactless bone ablation, leading to faster healing and less thermal damage as compared to conventional mechanical osteotomes [1]. To further extend the advantages of laser osteotomes over conventional osteotomes, real-time feedback on the type and properties of tissues being cut is desirable. During nanosecond pulsed laser ablation of tissues, the absorbed laser energy produces free electrons (also known as plasma) and the tissue temperature rises [2]. When the free electrons return to the equilibrium state, they emit energy in different forms, such as light with different wavelengths [3], [4] and acoustic shock waves (ASWs) which propagate as spherical wavefronts [2].

The most common approach in the linear regime is to measure the ASW emission using transducers or microphones, which convert the spherical wavefront into electrical signals [5]. The features of an ASW are mainly governed by the ablated material (i.e., bone, fat, muscle, or skin) [2], [6]. Therefore, ASWs can be used for tissue differentiation. However, the −3-dB bandwidth of commercial microphones does not typically exceed 900 kHz, while spectra of the ASWs extend beyond 1 MHz [7]. Furthermore, measurements by a microphone result in significant distortions of the measured waveforms and steep shock fronts [7]. Consequently, an alternative acoustic sensor system with a usable bandwidth beyond 1 MHz is required.

Optical techniques, with the possibility of nondestructive measurements, are very sensitive to sharp changes in pressure, and therefore are important for measuring phase objects, such as ASW fields [8], [9]. The existing optical techniques include schlieren, shadowgraph, and interferometers [9], [10]. The most sensitive and low-cost technique is provided by interferometers [11]. During the last few decades, interferometers have been used to characterize acoustic sources and spark-generated N-waves in the air [7], [12]–[14]. To the best of our knowledge, the first investigation (preliminary study) of optoacoustic tissue differentiation using a Mach–Zehnder interferometer was done by our group [15]. In this paper, we expand on this work.

To minimize energy loss in the optical path toward the ablation spot in a wet environment, such as during knee surgery, a laser wavelength of 532 nm can be used. A laser wavelength of 532 nm has a very low absorption coefficient in water compared to Er:YAG lasers with a wavelength of 2940 nm [16], [17].

In other words, the absorption coefficient of water is very low, from the near-ultraviolet (NUV) to the near-infrared (NIR) wavelength range. The first harmonic generation of Nd:YAG lasers, with a wavelength of 1064 nm, leads to 80% optical transmission through a 14-nm layer of water. The third harmonic generation, with a wavelength of 355 nm,

Manuscript received December 8, 2018; accepted June 12, 2019. Date of publication June 19, 2019; date of current version August 26, 2019. This work was supported by the Werner Siemens Foundation through the Minimally Invasive Robot-Assisted Computer-guided LaserosteotomE (MIRACLE) Project. *(Corresponding authors: Hervé Nguendon Kenhagho and Azhar Zam.)*

H. N. Kenhagho and A. Zam are with the Biomedical Laser and Optics Group (BLOG), Department of Biomedical Engineering, University of Basel, 4123 Allschwil, Switzerland (e-mail: herve.nguendon@unibas.ch; azhar.zam@unibas.ch).

G. Rauter is with the Bio-Inspired RObots for MEDicine-Lab (BIROMED-Lab), Department of Biomedical Engineering, University of Basel, 4123 Allschwil, Switzerland, with the Sensory-Motor Systems Lab, ETH Zurich, 8006 Zürich, Switzerland, and also with the Spinal Cord Injury Center, University Hospital Balgrist, 8008 Zürich, Switzerland (e-mail: georg.rauter@unibas.ch).

R. Guzman is with the Department of Neurosurgery, University Hospital of Basel, 4031 Basel, Switzerland, and also with the Department of Neurosurgery, University Children's Hospital, 4056 Basel, Switzerland (e-mail: raphael.guzman@usb.ch).

P. C. Cattin is with the Center for Medical Image Analysis and Navigation (CIAN), Department of Biomedical Engineering, University of Basel, 4123 Allschwil, Switzerland (e-mail: philippe.cattin@unibas.ch).

Digital Object Identifier 10.1109/TUFFC.2019.2923696

increases the optical transmission to values greater than 99.5% and offers maximum energy to the exposed tissue. However, the third harmonics are close to the ultraviolet spectrum, and the possibility of cytotoxicity and mutagenicity of ultraviolet radiation to tissues is still a concern, particularly at 248 nm [18], [19]. The second harmonic generation, also known as a frequency double, with a wavelength of 532 nm, produces optical transmission rates between the first and third harmonics below 70% [20], without cytotoxicity and mutagenicity in tissues compared to the third harmonic generation. In wet environments, 532 nm is expected to produce the safest maximum tissue ablation efficiency due to high energy throughput in water. Furthermore, for metal laser ablation, the relaxation time can be smaller than a few nanoseconds [21], [22]. However, for ablated tissues in the wet condition, a nanosecond pulse duration is able to create considerable thermal stress without any significant temperature increase to the surroundings [23], [24]. This is because a very high rate of the pulse energy is transformed into heat in liquid containing tissues [25]. Therefore, the thermal confinement condition is fulfilled.

In this work, we theoretically analyze and build an alternative optical method to measure ASWs. Part of the experimental setup was based on a custom-made Mach–Zehnder interferometer that reacts as a high-frequency microphone. A probe laser beam from the custom-made interferometer with an estimated bandwidth of 2.5 MHz sensed the generated ASWs [7], [12]. With such a wideband optical sensor, accurate measurements of ASWs can be provided. We used principal component analysis (PCA) to reduce the dimensionality of the ASWs measured from each ablated tissue and the Mahalanobis distance method to differentiate the scores of measured ASWs.

II. Materials and Methods

A. Sample Preparation

Five fresh porcine proximal and distal femurs, purchased from a local butcher, were used for the laser-tissue ablation experiments (Fig. 1). To retain the anatomically intact bone/periosteum, the bone sample was only cut and not polished. With the unpolished bone, the ASW parameters might better reflect those of in-vivo experimental conditions. The specimens were then rinsed several times in distilled water prior to ablation. The dimensions of hard and soft bone fragments, fat, muscles, and skin from the five fresh porcine proximal and distal femurs were all 50×10 mm^2.

B. Experimental Setup

1) Laser Ablation System: For laser ablation, we used a frequency-doubled Nd:YAG laser (532 nm) with a pulse repetition rate of 2 Hz, a pulsewidth of 5 ns, and pulse energy of 200 mJ. This wavelength has a very low absorption coefficient in distilled water. Therefore, it is transparent to water and could be clinically studied for its suitability for knee surgery in a wet environment. The laser beam was focused using an N-BK7A coated Bi-convex lens with 3-cm focal distance (LB1757-A, Thorlabs). In all experiments, the focal point was located at approximately 2 mm under the tissue surface to have a deeper ablation. The spot size is 21.69 μm (calculated at a specific level of e^{-2}) at 2 mm below the tissue surface, inducing energy density per pulse at 1.05 kJ/cm^2. Based on the estimated energy density, the ablation employed is plasma-mediated ablation.

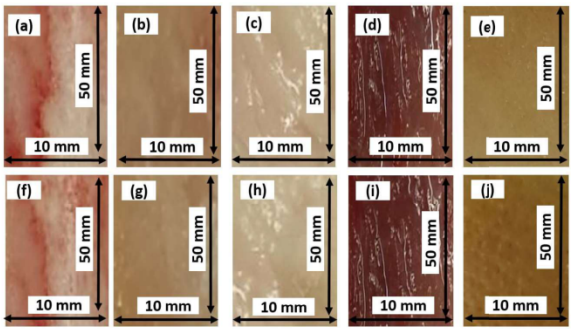

Fig. 1. Proximal femur: (a) Hard bone, (b) soft bone, (c) fat, (d) muscle, and (e) skin; distal femur: (f) hard bone, (g) soft bone, (h) fat, (i) muscle, and (j) skin tissue samples from one of five fresh porcine femurs.

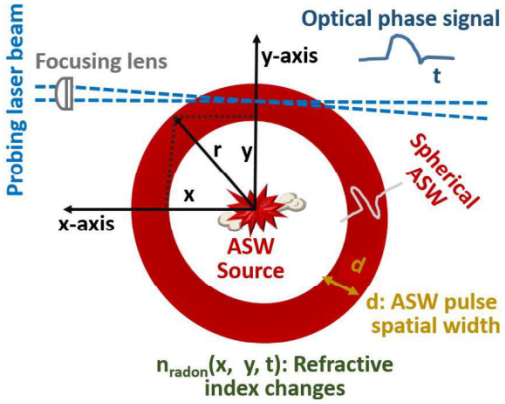

Fig. 2. Operation principle of an optical phase integration along the probing laser beam propagating through a spherical ASW (top view along the z-axis). The emitted ASW changes the refractive index of air and modulates the optical intensity of the interference fringe. The optical intensity changes are measured by a photodiode.

Consecutively, 180 laser pulses were applied to both the proximal and distal femur specimens. To ablate the next spot, the sample holder was moved 4 mm from the preceding spot, along the x-axis, without moving the probing beam (Fig. 2). This procedure was repeated ten times (ten craters) for hard and soft bones, fat, muscles, and skin on the proximal and distal femurs of the same specimen, using the same laser settings. The same ablation procedure was repeated for each of the five fresh porcine proximal and distal femurs.

2) Mach–Zehnder Interferometer:

a) Light fringes modulated by acoustics: During the laser ablation of each crater, we triggered the data acquisition system with an external CMOS trigger of the laser; the time gate window of each measurement was 0.50 ms. A total of 1800 ASWs were measured for each type of tissue. ASW measurements were performed with a Mach–Zehnder

interferometer for contactless, optoacoustic data acquisition from the ablation spot. The recorded signals were digitized with a PCI Express x8 (16-bit resolution, four channels at 10 MS/s each, M4i.44xx-x8, Spectrum Microelectronic GmbH).

To record the data, we used LabVIEW (version 2016); for subsequent data processing, we used MATLAB (version R2016a) software. To record the ASWs, the probing beam of the Mach–Zehnder interferometer was placed 5 cm away from the ablation spot. At any time (t), a propagated ASW caused spatiotemporal variations of the light refractive index distribution, $n_{\text{radon}}(x, y, t)$, and a phase shift, $\theta_{\text{radon}}(x, y, t)$. Thus, the changes in light intensity of the custom-made Mach–Zehnder probing laser beam correspond to the pressure of the ASW. More specifically, the interference fringe at the output of the Mach–Zehnder interferometer shifts when an ASW is introduced at the probing laser beam. The ASW pressure (P) and the refractive index (n) [9] are related as

$$n(x, y, z, t) = n_0 + \text{PK}(x, y, z, t). \tag{1}$$

In (1), n_0 and ê are the refractive index and constant, respectively, under static pressure (without any ASW). In this case, optics and ASW axes are defined as x- and y-directions, and z designates the transversal direction of the ASW axis. The corresponding phase shift term of the refractive index n_0 is

$$\theta_{\text{no}}(x, y, t) = 2\pi/\lambda \int n_0(x, y, z, t)dz. \tag{2}$$

Here, λ is the laser wavelength. Using the Radon transform—i.e., transforming 3-D measurements of ASW fields to 2-D—the projected transversal distribution of the refractive index feature can be integrated along the optical probe axis. Based on (1) and (2), the amplitude [$n_{\text{radon}}(x, y, t)$] and phase [$\theta_{\text{radon}}(x, y, t)$] terms can be estimated, respectively, from

$$n_{\text{radon}}(x, y, t) = \int n(x, y, z, t)dz \tag{3a}$$

$$\theta_{\text{radon}}(x, y, t) = 2\pi K/\lambda \int P(x, y, z, t)dz. \tag{3b}$$

In the experiments, the amplitude and phase are a function of radius, thus the equations can be rewritten as cylindrical coordinates

$$n_{\text{radon}}(r, t) = n_{\text{radon}}(x, y, t) \tag{4a}$$

$$\theta_{\text{radon}}(r, t) = \theta_{\text{radon}}(x, y, t). \tag{4b}$$

The probing laser beam propagating through a radially symmetric ASW is illustrated in Fig. 2.

b) Design and development: A continuous wave (CW) laser source (OBIS Laser 488-nm LX 150 mW, Coherent) with a nominal power of 10 mW was used as a light source in the custom-made Mach–Zehnder interferometer (Fig. 3). A beam splitter (LB5284, Thorlabs) was used to divide the incident laser beam into a probing beam and a reference beam; the path length of each arm was 50 cm. After the beam splitter, focusing lenses (LA1289-A-ML, Thorlabs, focal distance = 15 cm) were mounted to reduce the thickness of the probing beam in the zone where the interaction with the emitted ASW occurs. A thinner probing beam improves the resolution of the measurement scheme [7]. The two resulting beams

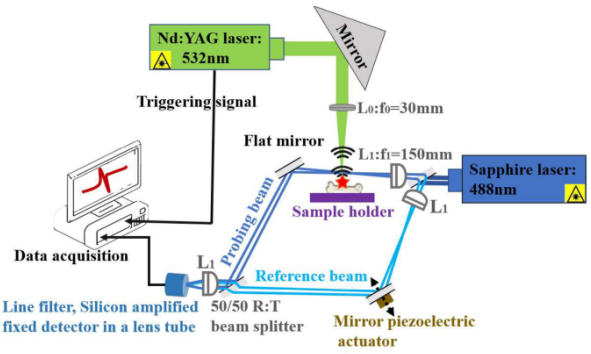

Fig. 3. Schematic of the experimental system (top view). ASW propagated from the ablated spot through the probing laser beam of the Mach–Zehnder interferometer modifying the optical phase difference relative to the reference laser beam.

are reflected by a highly reflective mirror (PF10-03-P01-10, Thorlabs). One of the mirrors was mounted on a translation stage (PT3/M, Thorlabs). The two beams then pass a second beam splitter and are added up to produce an interference intensity pattern on the surface of the detector. The probing beam is first transmitted and then reflected, while the reference beam is first reflected and then transmitted. Therefore, deviations of transmission and reflection coefficients from the 50/50 ratio are compensated and beams have nearly the same light intensities upon exiting the second beam splitter. To collect the total optical power, we focused the beam by using another focusing lens, with 15 cm focal length, on the surface of the photodiode. A laser line filter at 488 ± 0.2 nm (FL488-1, Thorlabs) and a lens tube were used to let through laser radiation at 488 nm and to eliminate background light, respectively. The resulting signal was measured by using an amplified silicon detector (PDA10A-EC, Thorlabs), connected to the data acquisition system.

The low noise amplifier of the photodiode has a maximum beam intensity and a voltage of 10 mW/cm^2 and 1.8 V for ($R_{\text{Op-amp}}$) 50-Ω loads, respectively. The corresponding responsivity (R_{resp}) and the usable bandwidth were 0.2 A/W at 488 nm optical wavelength and 50 MHz, respectively. The light intensity (I_{D}) on the detector is a combination of the intensities of the probing beam (I_{P}) and the reference beam (I_{R}). The optical phase difference between them is (θ). Their relationship can be expressed as

$$I_D = I_P + I_R + 2(I_P I_R)^{1/2} \cos(\theta). \tag{5}$$

Load resistance was used to convert the generated photocurrent into a voltage (V_{out}) for recording with the data acquisition system. To maximize the voltage transfer, a 50-Ω short coaxial cable (characteristic impedance) was used between the output of the amplifier and the input of the data acquisition system, which was also set to 50 Ω. Therefore, the output voltage of the photodiode amplifier is proportional to the beam power (P_{beam}), as in the following equation:

$$V_{\text{out}} = R_{\text{resp}} \times R_{\text{Op-amp}} \times P_{\text{beam}}. \tag{6}$$

When the CW-laser of the Mach–Zehnder interferometer is switched OFF, the photodiode produces a zero output signal. However, when the CW-laser is switched ON, the light intensity (I_D) is directly proportional to the output voltage signal (V_D), as expressed in the following equation:

$$V_D = V_P + V_R + 2(V_P V_R)^{1/2} \cos(\theta) \tag{7}$$

where V_R is the measured voltage of the reference beam when the probing beam is blocked and V_P is the measured voltage of the probing beam when the reference beam is blocked.

During laser tissue ablation, the total phase difference in the output voltage (V_D) is associated with the measured ASW. When a phase ASW is introduced at the probing laser beam, the change in the phase as a function of time [7], [9] is given by

$$\theta(t) = \theta_{\text{no}}(t) + \theta_{\text{radon}}(t). \tag{8}$$

In (8), θ_{no} and θ_{radon} correspond to the refractive indices under static and dynamic pressures, respectively. Under static pressures, the total phase difference is the aggregation of phase differences related to the initial adjustment of the Mach–Zehnder interferometer, which also includes phase differences related to mechanical perturbations, such as ambient air, optic table vibration, and acoustic noise. Under dynamic pressures, the phase difference is produced by the ASW and measured by the photodiode amplifier during laser tissue ablation.

The photodiode amplifier included a reverse-biased PIN photodiode, coupled with a fixed gain transimpedance amplifier and packaged in a rugged housing. The transimpedance amplifier connected to the output of the photodiode provided a linear relationship between the measured light intensity and the output voltage.

3) Statistical Analysis: The goal was to simultaneously differentiate various tissue types, namely hard and soft bone, fat, muscle, and skin tissues from five fresh porcine proximal and distal femurs. During differentiation, we used leave-one-out cross validation.

For offline tissue differentiation, we investigated the data by looking at the amplitude spectrum using the fast Fourier transform (FFT) in MATLAB. In addition, as the spectra of ASWs extended beyond 1 MHz [7], we split the amplitude spectrum into six equal frequency bands (FR1-6). Each frequency band was used as an input for PCA. PCA reduces data dimensionality by extracting principal components from the physical properties of the measured ASW [26]. Then, we identified the frequency band with less average classification error for tissue differentiation. We improved the contrast of the visualization of each ASW using the logarithm of the amplitude spectrum.

To simultaneously differentiate tissue types, we used the first three PCA scores from the set of training data combined with the Mahalanobis distance and plotted the 95% confidence ellipse using the three orthogonal eigenvectors of the scores from the "training data." Scores from the testing data in each ellipsoid that correctly detected tissues were considered true positives; if outside the ellipsoid, scores were considered unknown or false positive. We differentiated tissues based on the ellipsoid because it considers the covariance of the ASW score and the scales of the different variables. Therefore, it is useful for detecting members of the same group and even outliers.

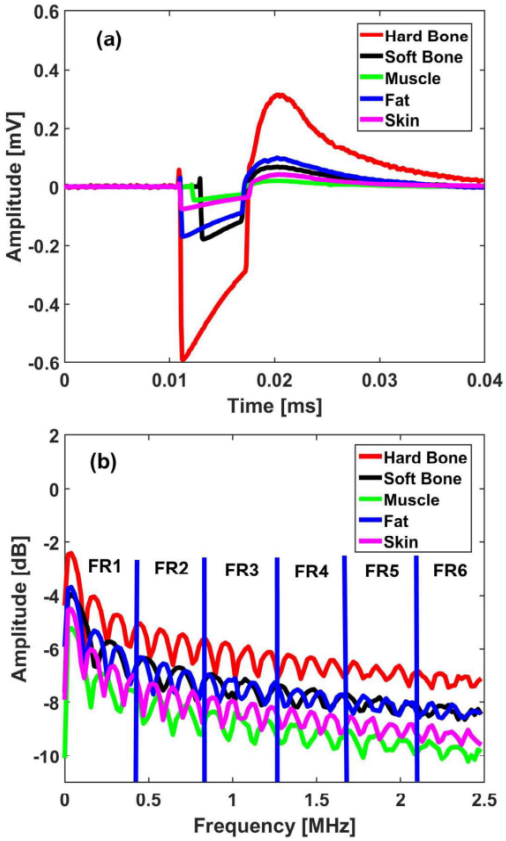

Fig. 4. Comparison of the shock waves measured from hard and soft bone, muscle, fat, and skin tissues in the (a) time and (b) frequency domains.

A set of 14 400 data points from ten craters in four proximal and distal femurs were used as "training data," while a set of 3600 data points from ten craters in the remaining proximal and distal femurs were considered as "testing data." Then, we simultaneously differentiated different classes of tissues, using one proximal and distal cross validation. From the confusion matrix, errors in the "testing data"-based scores from each specimen were calculated.

III. Results

Peak-to-peak amplitudes of the ASWs measured by the photodiode of the Mach–Zehnder interferometer for hard and soft bone, fat, muscle, and skin specimens were 0.90, 0.24, 0.27, 0.07, and 0.11 mV, respectively [Fig. 4(a)]. Analysis of the spectral responses at near direct current (dc) of 2.5 MHz revealed that the hard bone has a higher amplitude than the soft bone and fat, while the soft bone and fat produce a higher amplitude than muscles and skin [Fig. 4(b)]. It was also observed [Fig. 4(b)] that at the lowest frequency band (FR1), the amplitude for all tissues generally overlapped. At the next higher frequency band (FR2), the amplitude for hard tissues (hard bone) was always higher than soft tissues

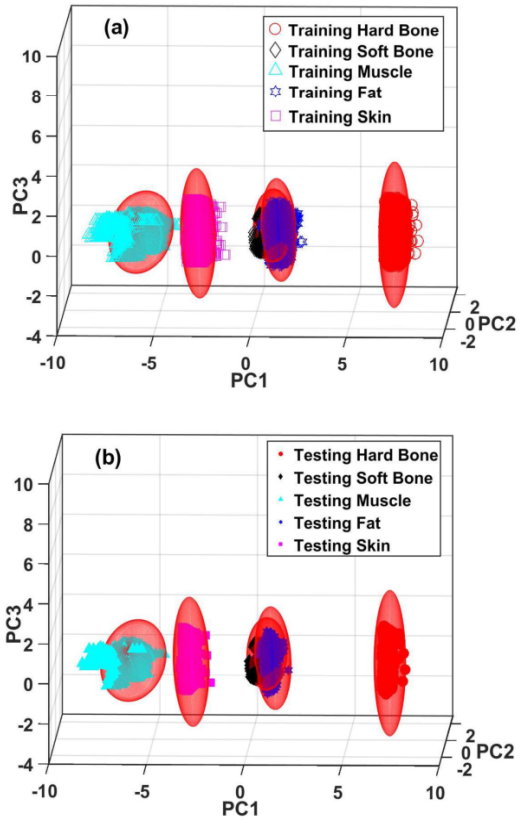

Fig. 5. First three PC scores from the training (a) and testing (b) data for hard and soft bone, muscle, fat, and skin tissues.

(soft bone, fat, muscle, and skin) and the amplitude for soft tissues overlapped with one another. However, at higher frequency bands, from FR3 to FR6, only soft bone and fat tissues had overlapping ASWs.

We used the amplitude of the spectrum from each frequency band as input for PCA (frequency bands are in the appendix except for FR3). The frequency band around 1 MHz (FR3) showed the best results in terms of less average classification error with cross validation between tissues than the other bands. The results of training data and testing data scores from the frequency range FR3 are shown in Fig. 5(a) and (b), respectively. The features that were chosen for PCA explained 93.88% of the variance in the recorded data. The first three principal components PC1, PC2, and PC3 have 89.11%, 2.42%, and 2.35% of the variance, respectively. The results from other frequency bands are given in the appendix. Based on the percentage of the total variance, PC1, PC2, and PC3 were used to differentiate tissue types out of the analysis of measured ASWs. From the confusion matrix, the experimental-based scores of hard and soft bones, fat, muscles, and skin yielded average classification errors (with one-leave-out cross validation) of 0.11%, 57.69%, 0.06%, 0.14%, and 2.92%, respectively (Table I).

TABLE I
CONFUSION MATRIX FOR HARD AND SOFT BONE, FAT, SKIN, AND MUSCLE TISSUES DURING LASER ABLATION AT 0.2-J OF PULSE ENERGY

Tissue	Classified as						Average Classification Error with leave-one-out cross validation
	Hard Bone	Soft Bone	Fat	Muscle	Skin	Unknown	
Hard Bone	3596	0	0	0	0	4	0.11%
Soft Bone	0	1523	1973	0	0	105	57.7%
Fat	0	0	3598	0	0	2	0.06%
Skin	0	0	0	0	3595	5	0.14%
Muscle	0	0	0	3495	0	105	2.92%

IV. DISCUSSION

The ASWs measured from hard tissues (hard bone) had a higher peak-to-peak amplitude than the ASWs from soft tissues (fat, muscle, and skin). Soft tissues are composed of 79% water, while hard bones are made of 85%–95% carbonated hydroxyapatite [27]. Thus, we believe that the carbonated hydroxyapatite resulted in a high amplitude of sound due to its compact structure [27]–[29].

We found that at frequencies between 0.83 and 1.25 MHz (FR3), tissue differentiation was most accurate than in other bands. From the confusion matrix, the experimental-based scores of all tissues yielded an average classification error (with leave-one-out cross validation) of less than 2.92%, except in the case of differentiating between the soft bone and fat, which yielded an error rate of 57.69%, (Table I).

Except for the soft bone and fat, the average error can be reduced to 0% if we consider that testing data scores close to each ellipsoid are just outliers and still belong to the same tissue [30]. Mahalanobis distance can be used to determine whether a sample is a member of a group or an outlier [30]. In this case, scores may be outliers, but they are still members of the corresponding group (close to the true positive ellipsoid). The soft bone and fat showed less performance because the soft bone is mainly made of fat. However, the biological structure of bone tissues reveals that the soft bone, also known as spongious bone or bone marrow, is always inside the hard bone [31], [32]; hence, the authors believe that simple rule-based approaches can easily differentiate between the soft bone and fat.

Differentiation results were best at frequencies between 0.83 and 1.25 MHz (FR3) compared to other frequency bands. The spectrum of an ASW extends beyond 1 MHz, therefore it is possible that at a frequency range around 1 MHz, the most important parameters of the measured ASW signal to differentiate various tissue types are covered [7]. In addition, by focusing at a high-frequency band around 1 MHz, the frequency resolution of the ASW is higher than in the lower frequency band, hence tissue differentiation can be improved (FR1 and 2). Moreover, noise generally goes up to 100 Hz (a fraction of FR1), by focusing the analysis at a very high-frequency band (FR3); we were always able to remove this noise component, thereby improving the distinction between tissue types. Although the system is sensitive enough to measure high-frequency ASWs, we realized that very

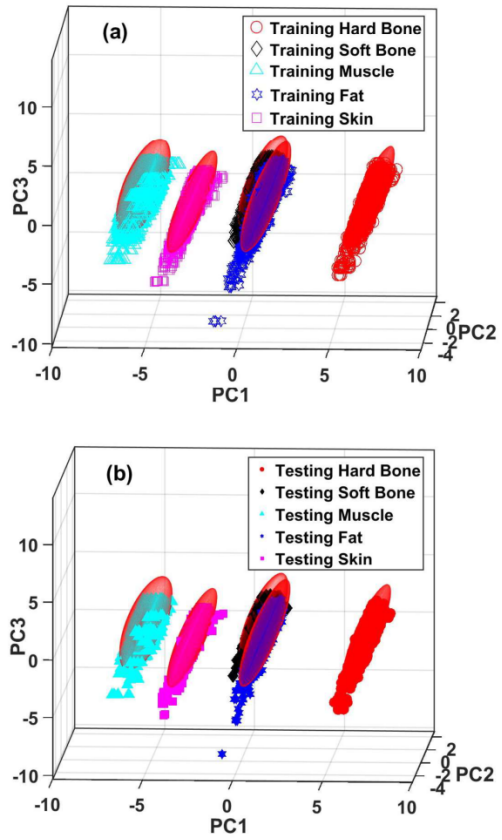

Fig. 6. First three PC scores from the (a) training and (b) testing data for hard and soft bone, muscle, fat, and skin tissues.

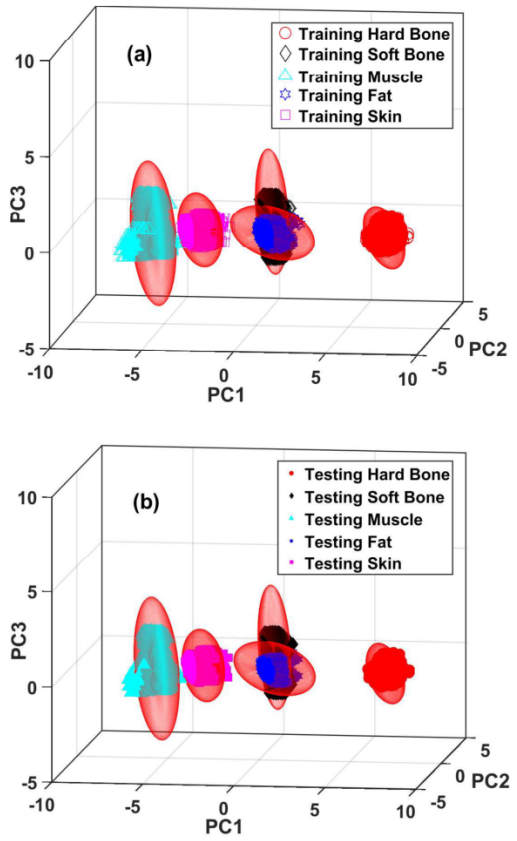

Fig. 7. First three PC scores from the (a) training and (b) testing data for hard and soft bone, muscle, fat, and skin tissues.

TABLE II

CONFUSION MATRIX FOR HARD AND SOFT BONE, FAT, SKIN, AND MUSCLE TISSUES DURING LASER ABLATION AT 0.2-J OF PULSE ENERGY (FR1)

Tissue	Classified as						Average Classification Error with leave-one-out cross validation
	Hard Bone	Soft Bone	Fat	Muscle	Skin	Unknown	
Hard Bone	3556	0	0	0	0	44	1.12%
Soft Bone	0	1578	1981	0	0	41	56.17%
Fat	0	0	3559	71	0	41	1.14%
Skin	0	0	0	0	3553	47	1.31%
Muscle	0	0	0	3529	0	71	1.97%

TABLE III

CONFUSION MATRIX FOR HARD AND SOFT BONE, FAT, SKIN, AND MUSCLE TISSUES DURING LASER ABLATION AT 0.2-J OF PULSE ENERGY (FR2)

Tissue	Classified as						Average Classification Error with leave-one-out cross validation
	Hard Bone	Soft Bone	Fat	Muscle	Skin	Unknown	
Hard Bone	3596	0	0	0	0	4	0.11%
Soft Bone	0	1403	2194	0	0	3	61.03%
Fat	0	0	3600	0	0	41	0%
Skin	0	0	0	0	3588	12	0.33%
Muscle	0	0	0	3466	0	134	3.72%

high-frequency band results in more ASW attenuation in the air compared to the low-frequency ones [5], [7], [33].

The custom-made opto-acoustical sensor was carefully developed to accurately measure ASWs during tissue ablation by laser. By building an optical tool like the Mach–Zehnder interferometer, we were able to accurately measure ASWs. We built our Mach–Zehnder interferometer with a usable bandwidth of around 2.5 MHz. This is 2.77 times better than the usable bandwidth of an air-coupled piezoelectric transducer with a usable bandwidth from dc to 900 kHz. The available bandwidth was broad enough to measure generated ASWs with less distortion.

V. CONCLUSION

We used a custom-made Mach–Zehnder interferometer to differentiate tissues by measuring and classifying ASWs in air. Depending on the change in interference patterns due to traveling ASWs, tissue types can be differentiated. We identified the frequency band between 0.83 and 1.25 MHz (FR3) as having the highest discriminative power for tissue differentiation.

We simultaneously differentiated five classes of tissues, such as hard/soft bones, fat, muscles, and skin, using leave-one-out cross validation. From the confusion matrix, the experimental-based scores of all tissues (hard and soft bones, muscles,

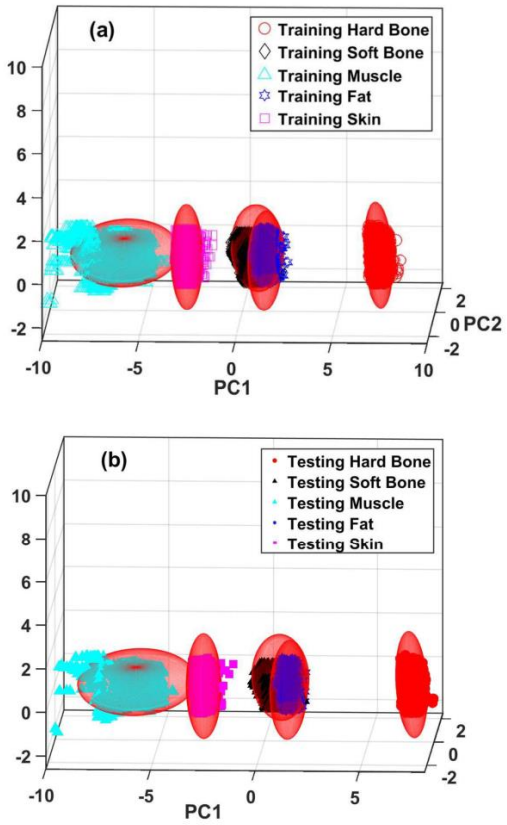

Fig. 8. First three PC scores from the (a) training and (b) testing data for hard and soft bone, muscle, fat, and skin tissues.

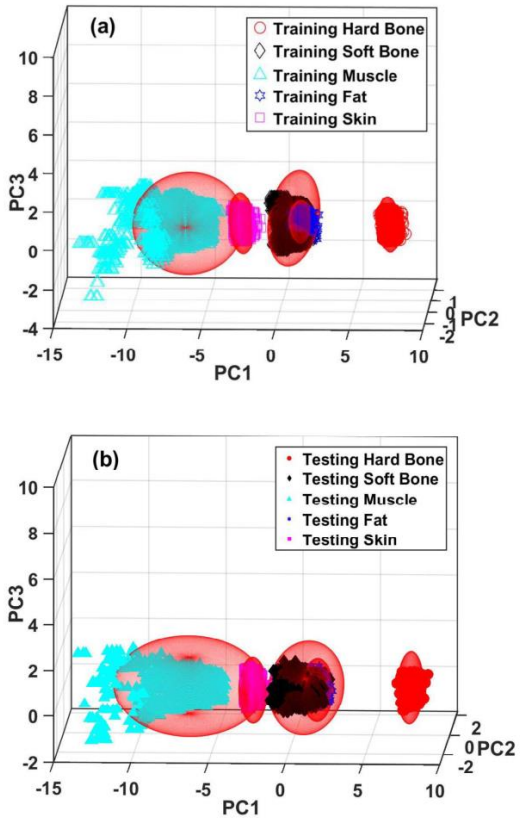

Fig. 9. First three PC scores from the (a) training and (b) testing data for hard and soft bone, muscle, fat, and skin tissues.

TABLE IV

CONFUSION MATRIX FOR HARD AND SOFT BONE, FAT, SKIN, AND MUSCLE TISSUES DURING LASER ABLATION AT 0.2-J OF PULSE ENERGY (FR4)

Tissue	Classified as						Average Classification Error with leave-one-out cross validation
	Hard Bone	Soft Bone	Fat	Muscle	Skin	Unknown	
Hard Bone	2069	0	0	0	0	1531	42.53%
Soft Bone	0	1140	2460	0	0	0	68.33%
Fat	0	0	2274	71	0	1326	36.83%
Skin	0	0	0	0	2565	1035	28.75%
Muscle	0	0	0	3512	0	88	2.44%

TABLE V

CONFUSION MATRIX FOR HARD AND SOFT BONE, FAT, SKIN, AND MUSCLE TISSUES DURING LASER ABLATION AT 0.2-J OF PULSE ENERGY (FR5)

Tissue	Classified as						Average Classification Error with leave-one-out cross validation
	Hard Bone	Soft Bone	Fat	Muscle	Skin	Unknown	
Hard Bone	3595	0	0	0	0	5	0.14%
Soft Bone	0	2013	1572	0	0	15	43.67%
Fat	0	0	3597	0	0	3	0.83%
Skin	0	0	0	0	3588	12	0.33%
Muscle	0	0	0	3467	0	133	3.69%

fat, and skin) yielded an average classification error with leave-one-out cross validation of less than 2.92%, except for the case of differentiating between the soft bone and fat, which had an error rate of 57.69%. The result of this study demonstrates that the Mach–Zehnder interferometer-based optoacoustic measurement, combined with Mahalanobis distances, is a promising technique for simultaneously differentiating several classes of tissues.

Future work will aim to miniaturize the optoacoustic feedback system to fit inside an endoscope. For the first prototype, we will investigate and/or build several fiber-based sensors. The sensor delivering best results will be used as the first prototype. To classify the measured data in real-time, we will use machine learning combined with parallel computing, such as CUDA. The setup has the potential to offer real-time feedback during laser osteotomy. Furthermore, the custom-made Mach–Zehnder interferometer can be used to monitor the incision depth. The incision depth monitoring during laser ablation using an air-coupled transducer has been reported [25], [34]. The incision depth can be useful as complementary information to feedback sensing. This additional information could be integrated into the current feedback system to classify the ablated tissue and monitor the incision depth simultaneously in real time.

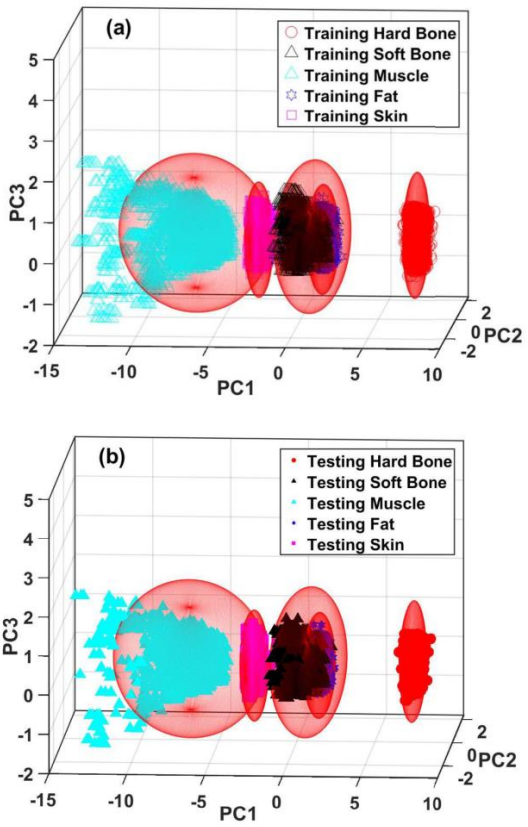

Fig. 10. First three PC scores from the (a) training and (b) testing data for hard and soft bone, muscle, fat, and skin tissues.

TABLE VI

CONFUSION MATRIX FOR HARD AND SOFT BONE, FAT, SKIN, AND MUSCLE TISSUES DURING LASER ABLATION AT 0.2-J OF PULSE ENERGY (FR6)

Tissue	Classified as						Average Classification Error with leave-one-out cross validation
	Hard Bone	Soft Bone	Fat	Muscle	Skin	Unknown	
Hard Bone	3592	0	0	0	0	8	0.22%
Soft Bone	0	2311	1289	0	0	0	35.81%
Fat	0	0	3600	0	0	0	0%
Skin	0	0	7	0	3591	2	0.25%
Muscle	0	0	0	3484	0	136	3.78%

APPENDIX

See Figs. 6–10 and Tables II–VI.

REFERENCES

[1] H. W. Kang, H. Lee, S. Chen, and A. J. Welch, "Enhancement of bovine bone ablation assisted by a transparent liquid Layer on a target surface," *IEEE J. Quantum Electron.*, vol. 42, no. 7, pp. 633–642, Jul. 2006.

[2] H. N. Kenhagho *et al.*, "Characterization of ablated porcine bone and muscle using laser-induced acoustic wave method for tissue differentiation," *Proc. SPIE*, vol. 10417, Aug. 2017, Art. no. 104170N.

[3] H. Abbasi, G. Rauter, R. Guzman, P. C. Cattin, and A. Zam, "Laser-induced breakdown spectroscopy as a potential tool for autocarbonization detection in laserosteotomy," *J. Biomed. Opt.*, vol. 23, no. 7, Mar. 2018, Art. no. 071206.

[4] H. Abbasi, "Plasma plume expansion dynamics in nanosecond Nd:YAG laserosteotome," *Proc. SPIE*, vol. 10505, Feb. 2018, Art. no. 1050513.

[5] Q. Qin and K. Attenborough, "Characteristics and application of laser-generated acoustic shock waves in air," *Appl. Acoust.*, vol. 65, no. 4, pp. 325–340, Apr. 2004.

[6] H. K. N. Kenhagho, G. Rauter, R. Guzman, P. C. Cattin, and A. Zam, "Comparison of acoustic shock waves generated by micro and nanosecond lasers for a smart laser surgery system," *Proc. SPIE*, vol. 10484, Feb. 2018, Art. no. 104840P.

[7] P. Yuldashev, M. Karzova, V. Khokhlova, S. Ollivier, and P. Blanc-Benon, "Mach–Zehnder interferometry method for acoustic shock wave measurements in air and broadband calibration of microphones," *J. Acoust. Soc. Amer.*, vol. 137, no. 6, pp. 3314–3324, May 2015.

[8] G. Hall, "Ultrasonic wave visualization as a teaching aid in non-destructive testing," *Ultrasonics*, vol. 15, no. 2, pp. 57–69, Mar. 1977.

[9] K. Mizutani, T. Ezure, K. Nagai, and M. Yoshioka, "Optical measurement of sound fields information using Mach–Zehnder interferometer," *Jpn. J. Appl. Phys.*, vol. 40, no. 5S, p. 3617, 2001.

[10] W. Merzkirch, *Flow Visualization*. Amsterdam, The Netherlands: Elsevier, 2012.

[11] N. Bilaniuk, "Optical microphone transduction techniques," *Appl. Acoust.*, vol. 50, no. 1, pp. 35–63, Jan. 1997.

[12] M. M. Karzova, P. V. Yuldashev, V. A. Khokhlova, S. Ollivier, and E. Salze, "Characterization of spark-generated N-waves in air using an optical Schlieren method," *J. Acoust. Soc. Amer.*, vol. 137, no. 6, pp. 3244–3252, Jun. 2015.

[13] F. Urgiles, J. Perchoux, and T. Bosch, "Characterization of acoustic sources by optical feedback interferometry," *Proceedings*, vol. 1, no. 4, p. 348, 2017.

[14] M. M. Karzova, P. V. Yuldashev, V. A. Khokhlova, S. Ollivier, and E. Salze, "Characterization of spark-generated N-waves in air using an optical Schlieren method," *J. Acoust. Soc. Amer.*, vol. 137, no. 6, pp. 3244–3252, Jun. 2015.

[15] H. N. Kenhagho, G. Rauter, R. Guzman, P. Cattin, and A. Zam, "Optoacoustic tissue differentiation using a Mach–Zehnder interferometer: Preliminary results," in *Proc. IEEE Int. Ultrason. Symp. (IUS)*, Kobe, Japan, Oct. 2018, pp. 1–9.

[16] R. C. B. Foster and J. M. Stavas, "Bone and soft tissue ablation," *Seminars Interventional Radiol.*, vol. 31, no. 2, pp. 167–179, Jun. 2014.

[17] A. Dupont, P. Caminat, P. Bournot, and J. P. Gauchon, "Enhancement of material ablation using 248, 308, 532, 1064 nm laser pulse with a water film on the treated surface," *J. Appl. Phys.*, vol. 78, no. 3, pp. 2022–2028, Aug. 1995.

[18] I. E. Kochevar, "Cytotoxicity and mutagenicity of excimer laser radiation," *Lasers Surg. Med.*, vol. 9, no. 5, pp. 440–445, 1989.

[19] N. Bhatta, K. Isaacson, K. M. Bhatta, R. R. Anderson, and I. Schiff, "Comparative study of different laser systems," *Fertility Sterility*, vol. 61, no. 4, pp. 581–591, Apr. 1994.

[20] M. V. Rudolf and C. F. P. van Swol, "Laser light delivery systems for medical applications," *Phys. Med. Biol.*, vol. 42, no. 5, p. 869, May 1997.

[21] M. Stafe, C. Negutu, and I. M. Popescu, "Combined experimental and theoretical investigation of multiple-nanosecond laser ablation of metals," *J. Optoelectron. Adv. Mater.*, vol. 8, no. 3, p. 1180, Jun. 2006.

[22] R. N. Oosterbeek, T. Ward, S. Ashforth, O. Bodley, A. E. Rodda, and M. C. Simpson, "Fast femtosecond laser ablation for efficient cutting of sintered alumina substrates," *Opt. Lasers Eng.*, vol. 84, pp. 105–110, Sep. 2016.

[23] S. L. Jacques, "Role of tissue optics and pulse duration on tissue effects during high-power laser irradiation," *Appl. Opt.*, vol. 32, no. 13, pp. 2447–2454, 1993.

[24] V. Venugopalan, N. S. Nishioka, and B. B. Mikić, "The effect of laser parameters on the zone of thermal injury produced by laser ablation of biological tissue," *J. Biomech. Eng.*, vol. 116, no. 1, pp. 62–70, Feb. 1994.

[25] E. Bay, X. L. Deán-Ben, G. A. Pang, A. Douplik, and D. Razansky, "Real-time monitoring of incision profile during laser surgery using shock wave detection," *J. Biophoton.*, vol. 8, nos. 1–2, pp. 102–111, Jan. 2015.

[26] J. Lever, M. Krzywinski, and N. Altman, "Principal component analysis," *Nature Methods*, vol. 14, pp. 641–642, Jun. 2017.

[27] M. Curzon and J. Featherstone, "Chemical composition of enamel," in *Handbook of Experimental Aspects of Oral Biochemistry*, E. P. Lazzan, Ed. Boca Raton, FL, USA: CRC Press, 1983, pp. 123–135.

[28] H. W. Kang, I. Rizoiu, and A. J. Welch, "Hard tissue ablation with a spray-assisted mid-IR laser," *Phys. Med. Biol.*, vol. 52, no. 24, pp. 7243–7259, Dec. 2007.

[29] C. Apel, J. Meister, R. S. Ioana, R. Franzen, P. Hering, and N. Gutknecht, "The ablation threshold of Er:YAG and Er: YSGG laser radiation in dental enamel," *Lasers Med. Sci.*, vol. 17, no. 4, pp. 246–252, 2002.
[30] R. G. Brereton, "The Mahalanobis distance and its relationship to principal component scores," *J. Chemometrics*, vol. 29, no. 3, pp. 143–145, Mar. 2015.
[31] R. Florencio-Silva, G. R. Sasso, E. Sasso-Cerri, M. J. Simões, and P. S. Cerri, "Biology of bone tissue: Structure, function, and factors that influence bone cells," *BioMed. Res. Int.*, vol. 2015, May 2015, Art. no. 421746.
[32] B. Clarke, "Normal bone anatomy and physiology," *Clin. J. Amer. Soc. Nephrology*, vol. 3, pp. S131–S139, Nov. 2008.
[33] P. Yuldashev, S. Ollivier, M. Averiyanov, O. Sapozhnikov, V. Khokhlova, and P. Blanc-Benon, "Nonlinear propagation of spark-generated *N*-waves in air: Modeling and measurements using acoustical and optical methods," *J. Acoust. Soc. Amer.*, vol. 128, no. 6, pp. 3321–3333, Dec. 2010.
[34] F. J. Landa, X. L. Deán-Ben, F. M. de Espinosa, and D. Razansky, "Non-contact monitoring of incision depth in laser surgery with air-coupled ultrasound transducers," *Opt. Lett.*, vol. 41, no. 12, pp. 2704–2707, Jun. 2016.

Hervé Nguendon Kenhagho received the B.Eng. degree (Hons.) in communication and electronic engineering from Northumbria University, Newcastle upon Tyne, U.K., in 2009, and the M.Sc. degree in microelectronic and communication engineering from Northumbria University, in 2010. He is currently pursuing the Ph.D. degree with the Biomedical Laser and Optics Group (BLOG), Department of Biomedical Engineering, University of Basel, Allschwil, Switzerland.

He held a calibration engineer position at the Repair and Cal Ltd., Reading, U.K., and research engineer positions at the University of Lunebürg, Lüneburg, Germany, and the University Carlos Tercero de Madrid, Madrid, Spain. He joined the Department of Biomedical Engineering, University of Basel, as a researcher associated with the Ph.D. candidature, in 2016. He has authored over ten proceedings, peer-reviewed articles, and books. His main research interests focus on the development of smart devices, antenna design and field measurement for electronic communications engineering and medical therapy, diagnostics and monitoring using novel acoustical/optical technologies, including smart laser surgery, optoacoustic, AI-aided acoustical/optical diagnostics, and the Internet of Things (IoT)-based sensors.

Mr. Kenhagho received the Professional Certificate as a Laser Safety Officer from the Universität des Saarlandes, Saarbrücken, Germany, in 2016.

Georg Rauter was born in Oberndorf bei Salzburg, Austria, in 1980. He received the Diplom-Ingenieur for Mechatronics (Dipl.-Ing.) degree in mechanical engineering from the Graz University of Technology, Graz, Austria, in 2000, the degree in mathematical and mechanical modelling from the Engineering School MATMECA, University Bordeaux 1, Talence, France, in 2004, the French Engineering Diploma degree (ing. dipl.) from University Bordeaux 1, in 2006, the Austrian diploma degree in 2008, and the Ph.D. degree from the Sensory-Motor Systems Lab (SMS Lab), ETH Zurich, Zürich, Switzerland, in 2013. His Ph.D. thesis focused on automated robot-assisted human motor learning.

During his first diploma thesis, he was involved in the development of a prototype for diagnosis in spine pathologies with the enterprise AXS Ingenierie, Mérignac, France. In 2007, he joined the SMS Lab, for his second diploma thesis in the field of control and mechanics in tendon-based robots. Since 2013, he has been a Postdoctoral Researcher for research in robot-assisted rehabilitation and motor learning with the University Hospital Balgrist, University of Zurich, Zürich, together with the SMS Lab. In particular, he works on the proximal extremity rehabilitation robot "ARMin." In 2013, he joined the University of Southern California (USC), Los Angeles, CA, USA, with Prof. D. Z. D'Argenio and Prof. F. Valero-Cuevas for half a year, where he developed statistical hierarchical models for the analysis of a clinical multicenter study with the rehabilitation robot ARMin. Since 2015, he has been a Project Manager and a Scientific Advisor for a CTI Project between the Spinal Cord Injury Center, University Hospital Balgrist, University of Zurich, and the enterprise Lutz Medical Engineering, Rüdlingen, Switzerland. This CTI Project aims for the improvement of robot-assisted gait training with body weight support through the rehabilitation robot "the FLOAT."

Raphael Guzman is currently a Professor of neurosurgery and the Vice Chairman of the Department of Neurosurgery, University Hospital of Basel, Basel, Switzerland, and the University Children's Hospital of Basel (UKBB), Basel. His clinical expertise is in pediatric and cerebrovascular neurosurgery. His research group examines the clinical relevance of neural stem/progenitor cells (NPC) in brain ischemia and particularly in neonatal hypoxic-ischemia (HI) with regard to white matter regeneration. Neonatal HI is an important cause of cerebral palsy (CP), leading to devastating sensory-motor, cognitive, and learning deficits in the growing child. White matter injury is a central feature of HI and CP, and defects in myelination are also commonly identified in other neurodevelopmental disorders, including autism spectrum disorders (ASD). White matter myelination generally reflects the progression of functional brain maturation and connectivity in the first years of life and dysfunction in this crucial process might contribute to the etiology of common symptoms found in CP and ASD. His laboratory is currently investigating the molecular and cellular crosstalk between NPCs and resident brain cells, particularly myelinating oligodendrocytes, *in vitro* and in a rodent model of neonatal HI. He is also deeply involved in advancing novel technologies such as virtual and augmented reality and minimally invasive endoscopy to advance neurosurgical teaching and operative techniques in collaboration with the Department of Bioengineering. His research is funded through the Swiss National Science Foundation and several grants from private foundations as well as industry collaborations. He has authored over 200 peer-reviewed articles, book chapters, and scientific meeting proceedings.

Philippe C. Cattin was born in Baden, Switzerland, in 1967. He received the B.Sc. degree from the University of Applied Science in Brugg/Windisch, Windisch, Switzerland, in 1991, and the M.Sc. degree in computer science and the Ph.D. degree in robotics from ETH Zurich, Zürich, Switzerland, in 1995 and 2003, respectively.

From 2003 to 2007, he was a Postdoctoral Fellow with the Computer Vision Laboratory, ETH Zurich. In 2007, he became an Assistant Professor with the University of Basel, Allschwil, Switzerland, and was promoted to Associate Professor in 2015 and to Full Professor in 2019. He is the Founder of the Center for Medical Image Analysis and Navigation (CIAN), Medical Faculty, University of Basel, where he is the Founding Head and still heading the Department of Biomedical Engineering. He joined Brigham and Women's Hospital, Boston, MA, USA, in 2017, as a Research Fellow. He is also the Founder of two spin-off companies and licensed his patents and software to medical device companies. His research interests include medical image analysis, image-guided therapy, robotics-guided laser osteotomy and virtual reality. As a Principal Investigator, he has finished many projects in these areas and published over 250 papers, patents and book chapters.

Azhar Zam received the B.Sc. degree in medical physics from the University of Indonesia, Depok, Indonesia, in 2004, the M.Sc. degree in biomedical engineering from the University of Lübeck, Lübeck, Germany, in 2007, and the Ph.D. degree in advanced optical technologies from the Friedrich–Alexander, University Erlangen–Nuremberg, Erlangen, Germany, with the focus on optical feedback for tissue-specific laser surgery, in 2011, the M.Sc. degree in biomedical engineering from the University of Lübeck, Lübeck, Germany, in 2007, and the Ph.D. degree in advanced optical technologies from the Friedrich-Alexander University Erlangen–Nuremberg, Germany, with the focus on optical feedback for tissue-specific laser surgery, in 2011.

He held research positions at the University of Waterloo, Waterloo, ON, Canada, the National University of Ireland Galway, Galway, Ireland, and the University of California at Davis, Davis, CA, USA. He joined the Department of Biomedical Engineering, University of Basel, Allschwil, Switzerland, in 2016, as an Assistant Professor, where he founded and leads the Biomedical Laser and Optics Group (BLOG). He has authored over 50 peer-reviewed articles, book chapters, books, and patents. His main research interests focus on the development of smart devices for medical therapy, diagnostics and monitoring using novel optical technologies, including smart laser surgery, optical coherence tomography (OCT), photoacoustics, biomedical spectroscopy, AI-aided optical diagnostics, the Internet of Things (IoT)-based wearable sensors, and miniaturized systems.

Chapter 5

Miniaturized Optoacoustic Feedback System for Minimally Invasive Laser Surgery

Introduction

Based on the interferometer approach, we designed and built a fiber-coupled Fabry-Pérot etalon sensor as an alternative and compact optical sensor for measuring acoustic shock waves (ASWs). A miniaturized etalon cavity was built to fit into a 5 mm diameter endoscope for minimally invasive smart laser osteotome. The collected data were subsequently investigated by looking at the amplitude frequency band to find the lowest classification error. Tissue classifications were carried out using the best-performing machine learning method as described in the previous chapter — principal component analysis (PCA) combined with an artificial neural network (ANN) —. The best classification accuracy (100 %) was found for hard bone, while the worst accuracy (88.89 %) was found for fat.

Publication. The proposed design was published in 2020 Sensors and Actuators A: Physical, with peer review [91].

Doi.: 10.1016/j.sna.2020.112394

Miniaturized Optoacoustic Feedback Sensor for Smart Laser Osteotome

Fiber-Coupled Fabry-Pérot Etalon Sensor

Hervé Nguendon Kenhagho *[a], Ferda Canbaz [a], Raphael Guzman[b,c], Philippe Cattin [d], and Azhar Zam *[a]

[a]Biomedical Laser and Optics Group, Department of Biomedical Engineering, University of Basel, Allschwil, Switzerland

[b]Brain Ischemia and Regeneration, Department of Biomedicine, University of Basel, University Hospital of Basel, Switzerland

[c]Neurosurgery Group, Department of Biomedical Engineering, University of Basel, Allschwil, Switzerland

[d]Center for medical Image Analysis and Navigation, Department of Biomedical Engineering, University of Basel, Allschwil, Switzerland

[*]**Corresponding Authors:** E-mail: herve.nguendon@unibas.ch; Tel: +41612075461; www.blog.dbe.unibas.ch

E-mail: azhar.zam@unibas.ch; Tel: +41612075460; www.blog.dbe.unibas.ch

***Abstract*—We report on a custom-made, fiber-coupled Fabry-Pérot etalon sensor to measure the acoustic shock waves (ASW) generated during laser ablation. A frequency-doubled Nd:YAG laser (532nm) with a 5ns pulse duration was used to produce craters on the surfaces of five different tissues —hard and soft bone, muscle, fat and skin— from five fresh porcine proximal and distal femur specimens. After collecting the ASW signals generated during laser ablation, we split the Fourier spectrum of the measured ASW into six equal bands and used each as an input for principal component analysis (PCA). We used PCA to reduce the dimensionality of each band and fed the PCA scores to an Artificial Neural Network (ANN) for classification. The most accurate tissue differentiation occurred at a band of 1.67–2.08 MHz. In total 18,000 data points were collected from the femur samples and split into training (10,800), validation (3,600), and testing (3,600) data. From a confusion matrix and the receiver operating characteristic (ROC), we observed that the experimental-based scores of hard and soft bone, fat, muscle and skin yielded average classification accuracies (with leave-one-out cross-validation) of 100%, 99.55%, 88.89%, 99.33%, and 100%, respectively. The area under the ROC curve (AUC) was more than 98.61%, for all tissue types. The proposed method has the potential to provide real-time feedback during laser osteotomy, to prevent the cutting of vital tissues.**

***Keywords*—Pulse laser tissue ablation, acoustic shock wave, fiber optic, optical fiber sensor, principal component analysis, artificial neural network, tissue differentiation**

I. Introduction

The use of lasers in bone surgery leads to faster healing times, inflicts less thermal damage, and achieves greater precision compared to the use of mechanical tools [1]. During laser ablation, acoustic shock waves (ASW) are emitted from the point of ablation [2, 3]. The characteristics of the ASW emitted mainly depends on the physical properties of the ablated material. Thus, ASW measurements can be used to further enhance laser osteotomy by providing real-time feedback for tissue classification. During laser osteotomy, real-time feedback is crucial to prevent vital tissue damage. Previously, tissue classification was based on the ASW measurements sensed by a microphone transducer [4]. This method, however, suffers from classification errors due to the limited bandwidth of commercially available microphone transducers (typically less than 1MHz) [5]. To enhance the bandwidth of ASW acquisition, we developed a custom-made, free-space Mach-Zehnder Interferometer sensor in a previous study [6]. The optical method has a bandwidth of up to 2.5MHz providing more detailed information about the spectrum of the ASW measured. In other words, optical methods are very sensitive to sharp changes of pressure giving the opportunity to measure phase objects of the ASW fields [7, 8].

To ablate biological tissue with lasers, a wide range of pulse durations has been used. To fulfill thermal confinement conditions, we used a short pulse duration (nanosecond) that is shorter than the tissues' thermal relaxation time [9, 10]. The main reason is that the thermal relaxation time for most biological tissues is longer than the nanosecond pulses [11, 12]. Using picosecond or femtosecond pulses would cause even less thermal damage during tissue ablation. [13, 14]. Furthermore, the use of a second harmonic (532nm) — also referred to as "frequency-doubled"— achieves an optical transmission rate in water between the first (1,064nm) and third harmonic (355nm) wavelengths below 70% [15]. Another advantage of employing a 532nm laser source is that it does not cause cytotoxicity or mutagenicity in tissues, in contrast to the third harmonic (355nm) [16, 17].

This study is part of the Minimally Invasive Robot-Assisted Computer-guided LaserosteotomE (MIRACLE) project. Part of this project is the development of an optoacoustic feedback sensor to prevent vital tissue damage during operations. In particular, we develop a compact optoacoustic sensor able to classify tissues during laser osteotomy. Hence, miniaturization of the ASW feedback sensor was essential such that it could fit into the endoscope developed by our collaborators [18-20]. Previous feedback systems, designed with a microphone and Mach-Zehnder Interferometer, were free space as well but bulky [2, 4, 6]. The compact sensor had to have at least the same usable bandwidth as our previous sensor design [21].

Different design approaches reported in the literature have contributed to reducing the size while improving the sensitivity and bandwidth of these types of sensors. The most recent designs are Fabry-Pérot-based sensors, which include a diaphragm (membrane) and an in-line fiber etalon [22, 23]. The diaphragm material is flexible and subject to deformity caused

This work is part of the MIRACLE (Minimally Invasive Robot-Assisted Computer-guided LaserosteotomE) project, funded by the Werner Siemens Foundation.

by the mechanical effects of the ASW. Another sensor design uses a movable part that senses the inbound ASW. However, the diaphragm material has an intrinsic self-resonant frequency, an undesirable trait that induces bumpiness in the frequency response of the sensor [24]. In contrast, the fiber-coupled Fabry-Pérot etalon is a diaphragm-free optical microphone. The undesirable self-resonant frequency is thus not present in the frequency response of the device. This, as the etalon uses two stable mechanical parts, while the incoming ASW is sensed in the optical cavity between the mechanical parts. The sensor measures pressure via refractive index changes of the medium in the optical cavity, which is directly proportional to the change of density produced by the incoming ASW. The concept of the fiber-coupled Fabry-Pérot etalon sensor has already been proposed for measuring ultrasound waves by optical means. The related studies show that the sensor has an outstanding linear response and a usable bandwidth up to 1 MHz in air and 20 MHz in liquids. The sensor is mechanically stable and easy to calibrate [23, 25]. By integrating a Fizeau interferometer in the fiber-coupled Fabry-Pérot etalon sensor, the resultant intensity can be four times that of either reference or test beam , hence improving the signal to noise ratio of the sensor [26, 27]. Therefore, it is suitable for measuring phase objects, such as ASW fields, for tissue classification during laser cutting.

In our previous study, we classified tissue types with a custom-made Fabry-Perot etalon sensor —with a Fizeau interferometer intergrated— [28]. We used principal component analysis (PCA) combined with the Mahalanobis distance to classify tissue types. Since PCA allows us to keep essential features (variance) of data by reducing their dimensionality, we expected to shorten the time needed to train a classifier and to avoid overfitting (less accuracy when classifying the validation data as compared to the training data) [29]. The drawback to tissue classification using the Mahalanobis distance-based method was the model's fixed size; after a certain point, the model saturated. Therefore, increasing the number of data points did not improve the classification result any further.

In this work, we reduced the size of our first custom-made fiber-coupled Fabry-Pérot etalon sensor to fit into an endoscope. In the ablation experiments, we used a frequency-doubled, Q-switched Nd:YAG laser to produce craters on the surfaces of five different tissues (hard bone, soft bone, muscle, fat, and skin). We used the custom-made sensor to collect the ASW emitted during ablation. The collected data was subsequently analyzed to determine the frequency band with the lowest classification error. Tissue classification was performed using PCA combined with an artificial neural network (ANN).

II. Materials and Methods

A. Experimental setup

1. Sensor system design and development

A schematic of the custom-made fiber-coupled Fabry-Pérot etalon sensor is illustrated in Fig. 1. The optical system uses a single-frequency laser source (SFL1550S, Thorlabs) that emits continuous coherent light, with an output power of 40 mW at 1550 nm. The laser contains an embedded thermoelectric cooler, a thermistor, and an optical isolator (CLD1015, Thorlabs) with a single mode (SM) output fiber tail. As shown in Fig. 2, the output of the fiber tail is coupled into Port 1 (P1) of the single-mode fiber-optic circulator (FOC, 6015-3-APC, Thorlabs). A single-mode 50:50 partial reflector fiber (P5-SMF28ER-50-1, Thorlabs) connects to Port 2 (P2) of the fiber optical coupler (FOC) to split the incident beam into two parts: the transmitted and reflected beams. The reflected light from the coated facet of the fiber is routed to Port 3 (P3). The transmitted light passes through a single-mode pigtailed ferrule with connector (SMPF0115-FC, Thorlabs) and is collimated using a GRIN lens (GRIN2315A, Thorlabs) in the sensor head. A coated double-convex lens (67-593, Edmund Optics) with a focal length of 9 mm and situated in the 4 mm×20 mm optical cavity, focuses the collimated light to the surface of a flat mirror.

However, the 2 mm×6 mm etalon (free space window) was introduced to allow the ASW to travel through the optical cavity, and thereby inducing a change in the refractive index around the detection laser. The propagating beam in the cavity is retroreflected by a flat mirror (31-001, Edmund Optics) and coupled back into the 50:50 partial reflector fiber. The 3 mm×3 mm mirror (minimum possible size available off-the-shelf) fits into a 5 mm×5 mm endoscopic robot for minimally invasive smart laser osteotomy. The retroreflected beam from the flat mirror is also routed by the FOC to P3. The P3 connector of the FOC is mounted to an InGaAs detector with a preamplifier (2/4/6 Preamplifier, physical acoustics, Princeton Junction, NJ, USA) to sense the variation in light intensity.

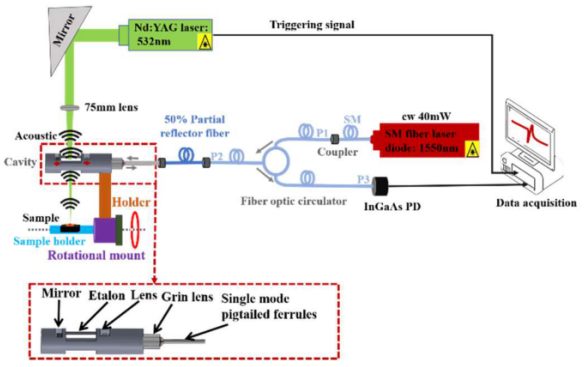

Fig. 1. Illustration of the fiber-coupled Fabry-Pérot etalon system (side view). The acoustic shock wave is detected in the optical cavity as the refractive index in the air cavity changes.

To transmit a high amount of incident light through the optical cavity, the length of the cavity was designed such that constructive interference conditiona are met. During laser tissue ablation, the ASW travels through the cavity and changes the refractive index of the medium. This, in turn, changes the path length of the laser beam, resulting in a change in the interference signal of the reflected light, which can be precisely measured by a photodetector. In other words, any change of the refractive index in the cavity changes the wavelength of the laser, which, consequently, no longer matches the fixed cavity length. This

improves the intensity of the reflected light so that it can be accurately measured by the photodiode [23].

2. Working principle of the optical cavity

Figure 2 shows a schematic of the optical cavity/etalon of the Fabry-Pérot sensor where the ASW signals were collected. The optical cavity was equipped with a protected gold mirror, after a 50% beam splitter, and a collimator. The coated facet of the fiber and the mirror were used to provide positive feedback by returning photons to the optical cavity to simulate more photons. For constructive light interference, the length (L) of the designed cavity must be set in relation to the center wavelength of light (λ) according to (1).

$$L = N \times \frac{\lambda}{2}. \tag{1}$$

Here, N represents an integer. The emerging wave experiences a 180-degree phase shift (the distance of one full round-trip propagation, $z = 2L$) from the total reflected mirror. It propagates back to the coated facet of the fiber. At the coated facet, this wave experiences the same phase shift again and continues to travel. The round-trip phase (ϕ) of the propagated wave is given by

$$\phi = 2\pi \times \frac{z}{\lambda}. \tag{2}$$

Additionally, we used an off-the-shelf collimator to ensure a confined beam inside the cavity [30]. The loss factor $\alpha(z)$ is caused by the decrease of power coupled into the fiber core after each return pass. The corresponding loss factor is a function of propagation distance in the cavity and is given by

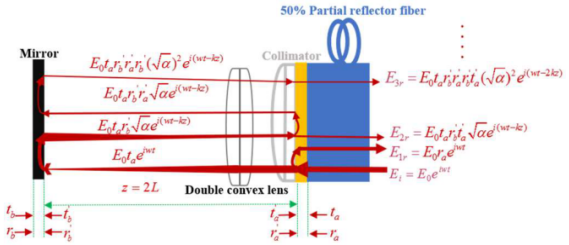

Fig. 2. Illustration of the optical cavity (side view).

$$\alpha(z) = \frac{1 - \exp\{-2[\frac{\omega_0}{\omega(z)}]^2\}}{1 - e^{-2}} \tag{3}$$

where, the beam width [$\omega(z)$] in the cavity can be described based on

$$\omega(z) = \omega_0 \sqrt{1 + (\frac{z\lambda}{\pi\omega_0^2})^2}. \tag{4}$$

In Eq. (4), ω_0 is the beam waist of the light source, which is the output of the fiber in this case. Hence, the beam waist can be equal to the mode field diameter of the fiber. Furthermore, components of the incident electric field (E_i) and the reflected electric field (E_r) in the multiple-beam interference can be expressed [22, 30] as

$$\begin{aligned} &E_i = E_0 e^{iwt}, E_{1r} = E_0 r_a e^{iwt}, \\ &E_{2r} = E_0 t_a r_b' t_a' \sqrt{\alpha} e^{i(wt-kz)}, and \\ &E_{3r} = E_0 t_a r_b' r_a' r_b' t_a' (\sqrt{\alpha})^2 e^{i(wt-2kz)}, \ldots \end{aligned} \tag{5}$$

Where, r_a , r_a' and t_a , t_a' are the respective reflection and transmission coefficients of the fiber's coated facet. As shown in Fig. 2, r_a and t_a are defined for the wave propagating from the reflected surface toward the air, while r_a' and t_a' are defined for waves propagating from the air toward the coated facet of the fiber. r_b is defined as the reflection coefficient of the gold mirror. Considering that reflectivity (R) is defined as $\sqrt{R_a} = r_a = -r_a'$, and $\sqrt{R_b} = r_b$; while transmissivity (T) is described as $T_a = t_a t_a'$, the resultant reflected scalar $E_r(t)$ wave can be expressed as (6)

$$E_r(t) = E_0 e^{iwt} \sqrt{R_a} [1 - \frac{1 - R_a}{R_a} \sum_{m=1}^{\infty} (-1)^m (R_a R_b \alpha(z))^{m/2} e^{-imkz}] \cdot \tag{6}$$

If $E^*(t)$ is the conjugate of $E(t)$ field, the transfer function $H_r(t)$, of the Fabry-Pérot sensor can be given by

$$H_r(t) = \frac{E_r(t) \cdot E_r^*(t)}{E_i(t) \cdot E_i^*(t)}. \tag{7}$$

The Fabry-Pérot sensor (sensing interference) is connected to a read-out interferometer, composed of a 50% partial reflector fiber and a part of the single-mode fiber-optic circulator within P_2 and P_3, as shown in Fig. 2. The associated transfer function, $H_t(t)$ is defined (7).

$$H_t(t) = \frac{E_t(t) \cdot E_t^*(t)}{E_i(t) \cdot E_i^*(t)}. \tag{8}$$

When the light passes the optical cavity, the resultant time-dependent intensity $I_t(t)$ measured by the photodiode can be written as

$$I_t(t) = \frac{1}{4} \int H_r(t) H_t(t) i(k) dk, \tag{9}$$

where $i(k)$ is the input spectrum of the optical laser source.

3. *Characterization of the optical sensor*

3.1 Frequency and directional response

During the calibration procedure, a high-performance black masking tape (T743-2.0, Thorlabs) with homogeneous absorption was used to generate an estimated broadband acoustic source. Reason being that when a pulsed laser is focused on black tape, it emits a broadband acoustic signal needed to measure the spherical-wave response of a sensor under test [31]. The laser parameters used were explained in the laser ablation system [28]. The distance between the exposed spot at the surface of the black tape and the optical sensor was set at 3.5 cm.Two air-coupled transducers (ACTs) were used as reference sensors to measure the acoustic waves generated. The first reference sensor was a calibrated ACT (WSα Sensor, physical acoustics, Princeton Junction, NJ, USA) with -62 dB bandwidth of near direct current (DC), that is, 1 MHz at a resonant frequency of 0.65 MHz. The second reference sensor was a calibrated ACT (Micro200HF sensor, physical acoustics, Princeton Junction, NJ, USA) with -72 dB bandwidth of 0.5–4.5 MHz at a resonant frequency of 2.5 MHz. These two reference ACTs were used to cover the whole frequency range needed for tissue classification. Our previous work demonstrated that the usable bandwidth at DC-2.5 MHz is enough for tissue classification [21, 28]. The optical cavity and transducers were mounted on the same axis of a cage rotation mount, as indicated by the red circle in Fig.3, (CRM1/M, Thorlabs) orthogonal to the detection laser (the orthogonal incident angle is at a 0º angle) axis. This set up was important for measuring the frequency response of the optical sensor. Ten ASW spectra were averaged to improve the signal-to-noise ratio between each measured ASW amplitude spectrum collected by the optical sensor and both ACTs. We then corrected both of the ACT measurements according to their calibration curves (frequency response). Afterward, we compared the ASW spectrum measured by the optical sensor to the corrected curve of both ACTs, resulting from the frequency response of the optical sensor. To measure the directivity response of the optical sensor, the rotational mount accurately rotated the optical cavity via the holder over a 180º angle (range 90º–270º with respect to the sample holder) with a step size of 10º from the preceding spot, along the rotational axis. To fully measure the directional response over a 360º angle, the rotational mount was also rotated from over the angular range 270º–90º with respect to the sample holder (Fig. 3).

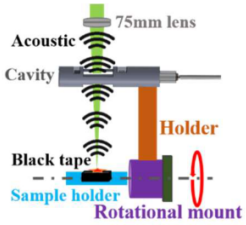

Fig. 3. Illustration of the experimental setup to measure the directional response of the current system (side view).

3.2 Sensitivity

To investigate the sensitivity of the setup, we measured the noise equivalent acoustic pressure of the custom-made optical sensor by measuring the signal to noise ratio (SNR) at 2.5 MHz (the resonant frequency) in the experimental setup as

$$SNR = \frac{A_S}{N_{RMS}}. \tag{10}$$

The experimental setup for measuring the peak amplitude of an ASW signal (A_s) and the root mean square (RMS) noise amplitude in the absence of the ASW signal is illustrated in Fig.4. The optical cavity of the custom-made optical sensor was positioned at an acoustic travel distance of 3.54 cm from the ablated spot using a 1 mm thin glass slide positioned 1 cm above the ablated spot (Fig. 4). The glass slide was oriented at a 45° angle so the focused light beam can travel without changing its direction while the ASWs were reflected at a 90° angle into the optical cavity [3]. By having the ASW reflected into the optical cavity, more acoustic pressure could pass through the optical cavity resulting in a higher acoustic signal. At a total distance of 3.54 cm between the ablated spot and the optical cavity, measurement in the linear regime could be achieved. The SNR was obtained, depending on the distance (d) between the ablated spot on the surface of the black masking tape and the optical cavity. The distance from the ablated spot to the optical cavity was between 3.54–21.32 cm with a stepwise progression of 2.54 cm from each position of the optical cavity.

The measured signals were then analyzed to find the SNR and the time-of-flight (ToF) at various propagation distances. We then compared the measured SNR with the calculated one to illustrate the acoustic pressure decay using (11), [31, 32].

$$SNR(d) = \frac{\exp\left(-\frac{2\pi f d}{v} i\right)}{d} \tag{11}$$

The ToF of the measured ASW signal was measured when the ASW signal reached a defined threshold of 10% of its maximum value. Based on the velocity (v) of the acoustic pressure wave (343 m/s) in dry air at 20ºC, we could obtain the ToF. The measured data was then compared with the calculated one using (12).

$$ToF(d) = \frac{d}{v} \tag{12}$$

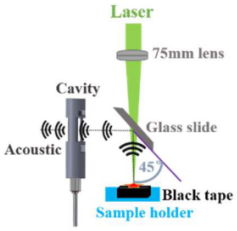

Fig. 4. Illustration of the experimental setup to measure the sensitivity of the current system (side view).

4. *Data acquisition system*

Acoustic shock waves emanating from the ablation spot were measured using the custom-made optical sensor (Fig. 2). Acoustic data acquisition was activated by an external CMOS trigger on the laser. The time gate window of each measurement was 82 µs. The measured analog signals were digitized using a PCI Express x8 (M4i.44xx-x8, Spectrum Microelectronic GmbH, Grosshansdorf, Germany), with a 16-bit transient recorder and a sampling rate of 10 MS/s.

B. *Tissue classification*

1. *Sample preparation*

Hard bone, soft bone, muscle, fat, and skin tissue samples for our experiments were derived from five extracted, fresh porcine proximal and distal femur specimens. The animal specimens were obtained from a slaughterhouse; thus, no ethical authorization was necessary. Connective tissues were thoroughly removed to ensure the homogeneity of the tissue samples from each specimen. All samples were approximately $10\times50\times8\,mm^3$ in size.

2. *Laser ablation system*

A pulsed, frequency-doubled Nd:YAG laser (Q-smart 450, Quantel, Paris, France) with 5 ns pulses was used to ablate the samples (Fig. 1). Ablation was performed with a pulse energy of 200 mJ and a repetition frequency of 10 Hz. We focused the laser beam using an uncoated plano-convex lens, with a 7.5 cm focal distance (LA5042, Thorlabs). The focused beam was transmitted through the optical cavity of the optical sensor to the sample surface. The sample surface was positioned 2 mm above the focal point. The laser spot diameter was estimated by a Gaussian distribution, with a full length at e^{-2} amplitude of 15.6 µm. The incident peak fluence on each sample was estimated to be $209\,kJ/cm^2$. Consequently, ten craters, each 4 mm apart, were created with 180 laser pulses for each crater on the surface of each sample, on both the proximal and distal femur of the same specimen. The same ablation procedure was repeated for each of the five femurs.

III. PROCEDURE FOR TISSUE CLASSIFICATION

To classify hard bone, soft bone, muscle, fat, and skin, we analyzed the measured ASW signals. We removed the phase shift of each signal by observing the amplitude spectrum, using the fast Fourier transform (FFT) in Matlab (version R2018b). We used the logarithm of the amplitude spectrum to enhance the contrast of the visualization of each ASW (Fig. 10b). Then, we split each amplitude spectrum into six equal frequency bands (FR1-6), and we further determined the frequency band with the highest classification accuracy for tissue classification. PCA was used to reduce data at each frequency range. Using the PCA scores, we trained an ANN to classify tissue types. A total of 18,000 ASW were measured from each tissue type. The first three PCA scores from the set of data points (frequency band) were used as input for the ANN.

For the ANN, we used the *pattern network* function combined with the *Tan-Sigmoid activation* function for hidden layers and the *Softmax activation* function for the output layer available in MATLAB (version R2018b) [33, 34]. The ANN model included one input layer (three neurons), one hidden layer (ten neurons), and one output layer (five neurons). Detailed description of the architecture can be found in [35]. The Backpropagation algorithm was used to train the ten neurons of the hidden layer using gradient descent. The first three PCA scores from the set of data points were used as input sets of the ANN. We evaluated the performance of our models on a single computer with a 2.4 GHz Intel Core i7 processor, 16GB, 1867 MHz DDR3 memory.

A set of 10,800 data points, measured from three femurs, was used for *training*. A set of 3,600 data points, measured from the fourth femur, and another set of 3,600 data points, measured from the remaining fifth femur, provided the *validation and testing data*, respectively. Then, we classified tissue types simultaneously, using one femur cross-validation of the testing-data-based scores. the five cross-validations were based on five femurs; for each cross-validation, data sets from three different femurs were used in the training phase. From the remaining two femurs, data set from one femur was used as validation, and the remaining data set from the last femur was used in the testing phase.

From the five confusion matrices and the receiver operating characteristics (ROCs), we calculated the average classification accuracy and the area under the ROC curve (AUC) (with leave-one-out cross-validation), respectively, for each tissue.

IV. RESULTS

4.1 Calibration

The normalized frequency response of the optical sensor is illustrated in Fig. 5. The -30 dB bandwidth (frequency response) of the optical sensor ranges from DC to 4.5 MHz. The corresponding directivity response is shown in Fig. 6. The polar plot presented a relatively flat directional response over a 360º angle, except from 90º–120º and from 240º–300º, with an attenuation factor of 10 dB.

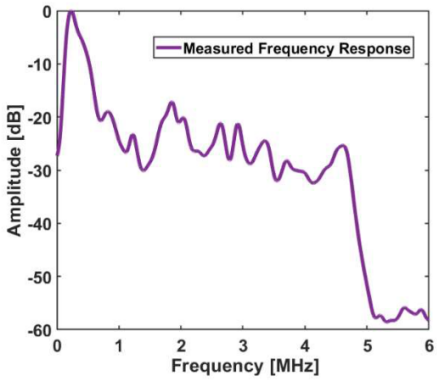

Fig. 5. The measured frequency response of the optical sensor.

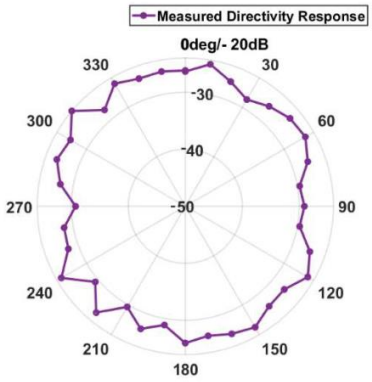

Fig. 6. Measured directivity response of the optical sensor.

Furthermore, Fig. 7 illustrates three time-resolved signals recorded with the custom-made optical sensor at three different distances from the ablated spot: 3.54 cm, 11.16 cm and 21.32 cm. The peak amplitude values were 0.198 mV, 0.076 mV and 0.029 mV. Corresponding ToFs were 0.0408 ms, 0.201 ms and 0.501 ms, respectively.

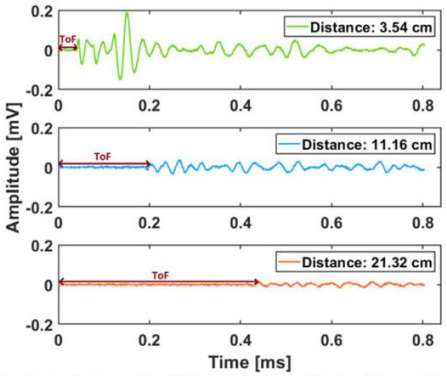

Fig. 7. Evolution of the ToF and peak amplitude at three distances. Each color corresponds to one of three different distances.

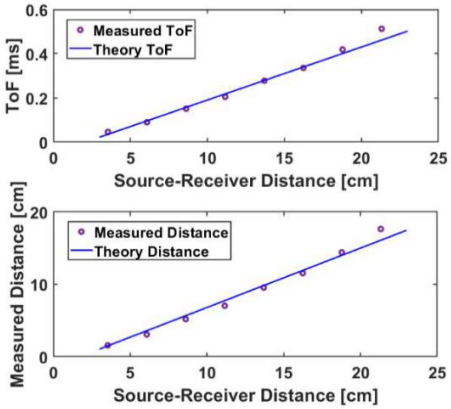

Fig. 8. Sensitivity results based on the ToF measurements of the optical sensor.

By considering the distance from the ablated spot to the optical cavity at 3.54 cm–21.32 cm, with a stepwise progression of 2.54 cm, the ToF increased (Fig. 8) and the peak amplitude of the ASW decreased (Fig. 9).

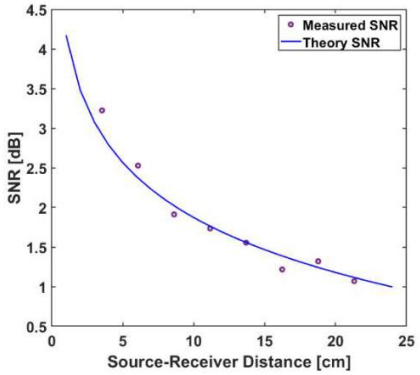

Fig. 9. Sensitivity results based on SNR measurements of the optical sensor.

4.2 *Tissue classification*

During the ablation of hard bone, muscle and fat, the ASW transients were generated and delineated, as shown in Fig. 10. The amplitude value of the ASW signal generated for hard tissue (hard bone) is higher than that for soft tissues. The corresponding frequency domain provides a usable bandwidth in the range of DC - 2.5 MHz. We observed that the spectra overlap for different tissues in the low-frequency region (FR1). However, at higher frequency bands, between 0.41–2.5 MHz (FR2–FR6), the amplitude values of the spectra are mostly separated. We investigated each frequency band for its performance in tissue classification — the results for each frequency band are giben in the appendix (Fig. 13–22, and Table 2–6), except for FR5—. The frequency band around 1.7 MHz (FR5: 1.67–2.08 MHz) resulted in the highest accuracy when classifying tissue types compared to the other bands.

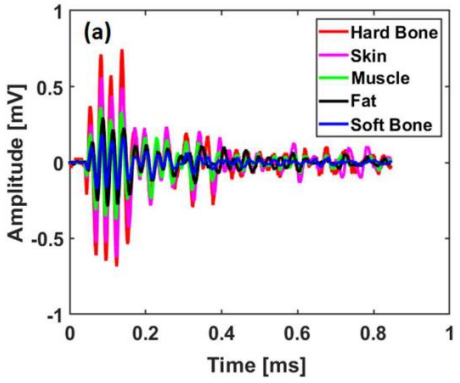

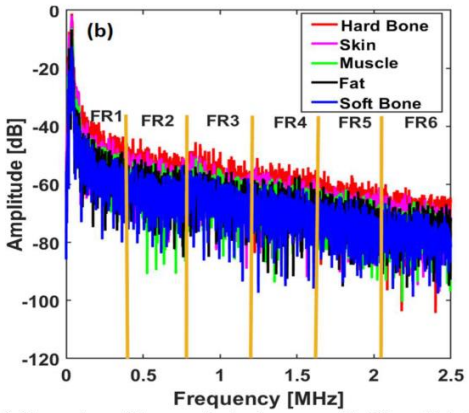

Fig. 10. Comparison of the acoustic shock waves emitted from ablated hard muscle and fat tissues in the time (a) and frequency (b) domain.

Besides, the first three features chosen for PCA explained 94.70% of the variance within the band. Consequently, the first three principal components (PC1, PC2 and PC3) explained 93.20%, 0.93% and 0.57% of frequency band variance, respectively, and were used to differentiate tissue types. Fig. 11a and 11b show 10,800 training data scores and the classification of 3,600 testing data scores, respectively.

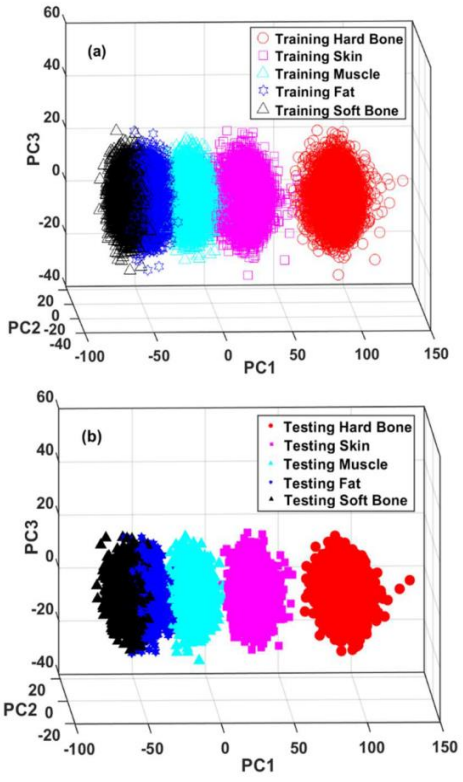

Fig. 11. First three PC scores from the training (a) and testing (b) data for hard and soft bone, muscle, fat and skin (FR5: 1.67-2.08 MHz).

From the confusion matrix and the receiver operating characteristic (ROC), the average classification accuracy (with leave-one-out cross-validation) for each tissue was more than 99.33%, except in the case of differentiating between soft bone and fat, which yielded an accuracy rate of 88.89%. The area under the ROC curve (AUC) was more than 98.61% for all tissue types. The computation time for testing the ANN-based model was in the order of 7-12ms.

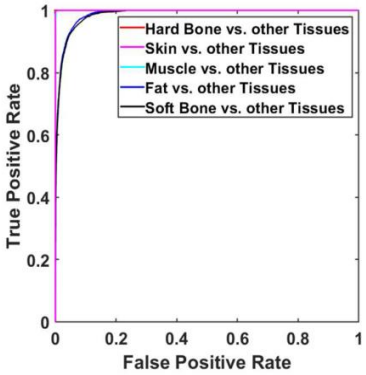

Fig. 12. Receiver operating characteristic (ROC) curve to multi-class, using the ANN models combined with the ns-Nd:YAG laser. Note: The curve of Hard Bone, Skin and Muscle vs. other tissues overlaps (FR5: 1.67-2.08 MHz).

TABLE 1. CONFUSION MATRIX FOR HARD AND SOFT BONE, FAT, SKIN AND MUSCLE TISSUES DURING LASER ABLATION AT 0.2 J PULSE ENERGY.

Tissue	Classified as					Average Classification Accuracy with leave-one-out cross- validation	Area Under ROC Curve
	Hard Bone	Skin	Muscle	Fat	Soft Bone		
Hard Bone	3600	0	0	0	0	100%	100%
Skin	0	3600	0	0	0	100%	100%
Muscle	0	17	3576	7	0	99.33%	99.99%
Fat	0	0	17	3200	383	88.89%	98.61%
Soft Bone	0	0	0	16	3584	99.55%	98.70%

V. DISCUSSION

The SNR was significantly higher when the optical cavity was placed closer to the ablation spot. SNR decreased as optical cavity distance increased (Fig. 7 and 9). This behavior is associated with reduced ASW amplitudes over longer distances between the source and optical cavity as the geometrical wave front spreads [36, 37]. The sensor developed in this study had a maximum working range of 21.32 cm. Additionally, the working distance of the optical sensor can be further increased when the optical cavity distance increases (Fig. 8). These results demonstrated the linearity of the system and thus it is proven that compensation is unnecessary [8].

During tissue ablation, the peak-to-peak amplitude measured from hard bone was higher than that for soft tissues (Fig. 10a). This finding was expected, as the hard bone is mostly made of compact hydroxyapatite. The corresponding amplitude spectrum during hard bone ablation was also higher than during soft tissue ablation. Similar to the peak-to-peak amplitude, the ablation and ASW generation threshold for

tissue types can differ. Hence, we selected the energy levels within a range in which ablation and ASW generation in all tissue types reported in this study was possible. Note that the ablation threshold may also vary slightly for different animals or age. These variations could affect the performance of our classifiers. The average classification accuracy was based on tissue samples extracted from five different fresh porcine proximal and distal femur specimens to account for these variations.

A common method of analyzing classification results is to examine the confusion matrix [38]. The matrix demonstrates precisely which tissue was classified as a combination of different tissues, showing the accuracy/error for each tissue in terms of both percentages and number of signals. Therefore, by splitting the amplitude spectrum of each tissue type into bands, we discovered that classification accuracy was less at low frequencies in the spectral range of DC – 0.42 MHz (FR1). This mainly due to a noise floor of up to 100 Hz. The highest classification accuracy (Table 1) was observed in the frequency band 1.67–2.08 MHz (FR5), which is in accordance to our previous findings [28, 39].

Furthermore, it can be observed from the confusion matrix that the experimental-based scores from all tissues yielded an average classification accuracy (with leave-one-out cross-validation) of more than 99.33%. Except when differentiating between soft bone and fat that only yielded an accuracy of 88.89%. (Table 1). Hence, the corresponding ROC curve for hard bone, skin and muscle vs. other tissues showed the best performance compared to the ROC curve for soft bone and fat (Fig. 12). By considering the natural discrimination of tissue layers (soft bone is always embedded in hard bone and fat is outside of hard bone), the accuracy rate for distingishing between soft bone and fat can be increased to 100%.

Using only the air-coupled transducers the differentiation between soft tissues was challenging due to bandwidth limitations [40]. However, ACT proved to classify hard bone and soft tissue robustly but were not suitable for differentiating between soft bone and fat tissue.

It is well known that ASW attenuation in air increases with frequency; such attenuation can lead to classification errors [6]. The use of a more sensitive optical method, like the one proposed herein, enables detection of ASW signals even if they experienced already a lot of attenuation in the air [5]. The custom-made optical sensor is a wideband (frequency response of at least 4.5 MHz) transducer with an omnidirectional receiving response (directivity response). In contrast, standard air-coupled transducers are mostly narrowband and directional sensors with low sensitivity (Fig. 5 and 6). Given that we expect to apply this technique in minimally invasive settings, where the working distance from the sensor to the ablated spot is less than 5 mm, ASW attenuation will be very low.

VI. CONCLUSION

In this paper, we presented a method for tissue differentiation based on acoustic shock wave detection, using a custom-made fiber-coupled Fabry-Pérot etalon cavity. Tissues were classified using PCA and an ANN. The best classification accuracy (100%) was found for hard bone, while the worst accuracy (88.89%) was found for fat. The area under the ROC curve was more than 98.61% for all tissue types. Based on our analysis, we foresee the possibility of providing real-time feedback during laser osteotomy, to prevent cutting vital tissues. In future work we plan on collecting data from more tissue types, such as nerve, to determine and improve the classification accuracy. Our next step is to analyze whether the transition from bony to soft tissue is detectable. This is crucial to decide on the actual utility of the proposed algorithms for classification in realistic scenarios (where different tissue types co-exist).

APPENDIX

FR1 = 0-0.42 MHz

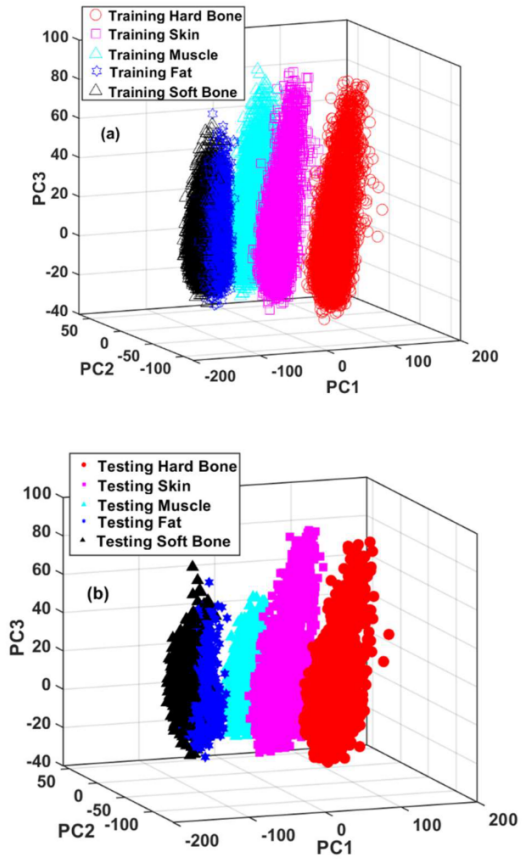

Fig. 13. First three PC scores from the training (a) and testing (b) data for hard and soft bone, muscle, fat and skin.

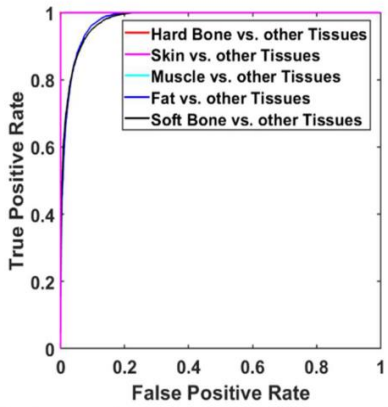

Fig. 14. Receiver operating characteristic (ROC) curve to multi-class using the ANN models combined with the ns-Nd:YAG laser. Note: The curve of Hard Bone, Skin and Muscle vs. other tissues overlaps.

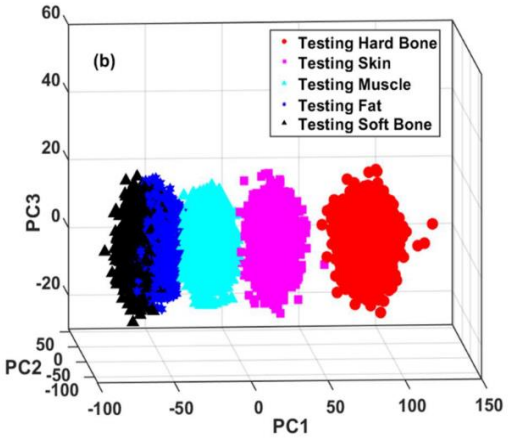

Fig. 15. First three PC scores from the training (a) and testing (b) data for hard and soft bone, muscle, fat and skin.

TABLE 2. CONFUSION MATRIX FOR HARD AND SOFT BONE, FAT, SKIN AND MUSCLE TISSUES DURING LASER ABLATION AT 0.2J PULSE ENERGY.

Tissue	Classified as					Average Classification Error with leave-one-out cross-validation	Area Under Curve in ROC
	Hard Bone	Skin	Muscle	Fat	Soft Bone		
Hard Bone	3600	0	0	0	0	100%	100%
Skin	1	3590	9	0	0	99.72%	99.99%
Muscle	0	13	3584	3	0	99.56%	99.99%
Fat	0	0	0	3066	534	85.17%	98.06%
Soft Bone	0	0	0	630	2970	82.50%	98.09%

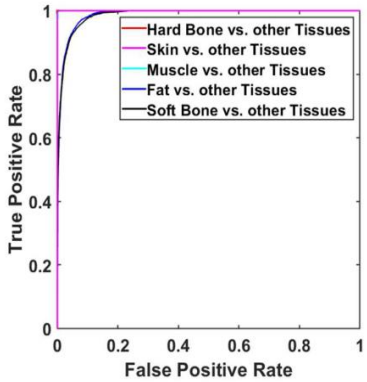

Fig. 16. Receiver operating characteristic (ROC) curve to multi-class using the ANN models combined with the ns-Nd:YAG laser. Note: The curve of Hard Bone, Skin and Muscle vs. other tissues overlaps.

FR2 = 0.42-0.83 MHz

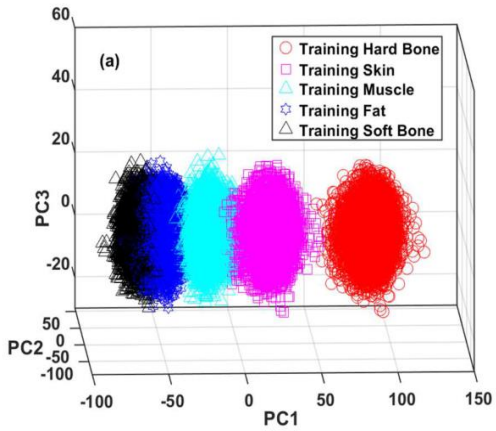

TABLE 3. CONFUSION MATRIX FOR HARD AND SOFT BONE, FAT, SKIN AND MUSCLE TISSUES DURING LASER ABLATION AT 0.2J PULSE ENERGY.

Tissue	Classified as					Average Classification Accuracy with leave-one-out cross-validation	Area Under Curve in ROC
	Hard Bone	Skin	Muscle	Fat	Soft Bone		
Hard Bone	3600	0	0	0	0	100%	100%
Skin	0	3593	7	0	0	99.81%	100%
Muscle	0	17	3572	11	0	99.22%	99.99%
Fat	0	0	7	3183	407	88.50%	98.54%
Soft Bone	0	0	0	468	3132	87%	98.35%

FR3= 0.83–1.25MHz

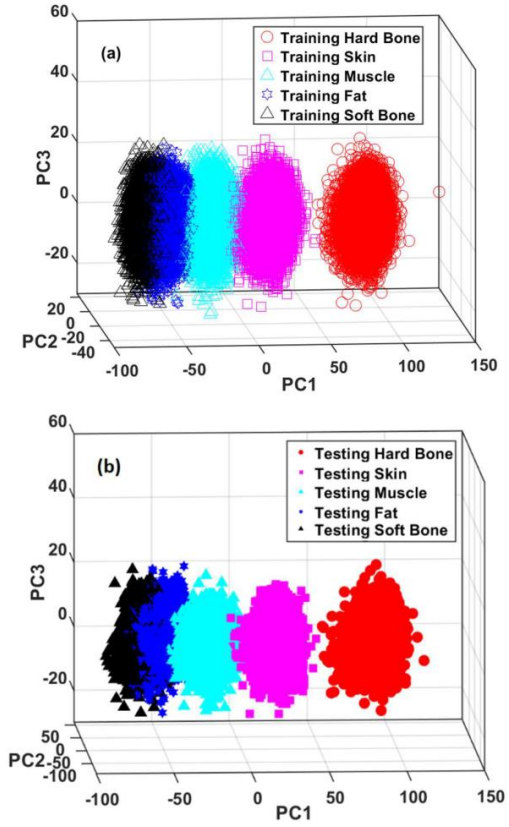

Fig. 17. First three PC scores from the training (a) and testing (b) data for hard and soft bone, muscle, fat and skin.

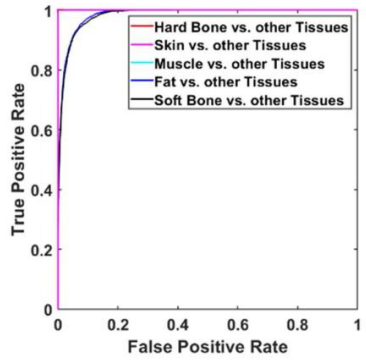

Fig. 18. Receiver operating characteristic (ROC) curve to multi-class, using the ANN models combined with the ns-Nd:YAG laser. Note: The curve of Hard Bone, Skin and Muscle vs. other tissues overlaps.

TABLE 4. CONFUSION MATRIX FOR HARD AND SOFT BONE, FAT, SKIN AND MUSCLE TISSUES DURING LASER ABLATION AT AT 0.2 J PULSE ENERGY.

Tissue	Classified as					Average Classification Accuracy with leave-one-out Cross-validation	Area Under Curve in ROC
	Hard Bone	Skin	Muscle	Fat	Soft Bone		
Hard Bone	3600	0	0	0	0	100%	100%
Skin	0	3600	0	0	0	100%	100%
Muscle	0	12	3577	11	0	99.36%	99.99%
Fat	0	0	16	3185	399	88.47%	98.48%
Soft Bone	0	0	0	496	3104	86.22%	98.59%

FR4 = 1.25-1.67MHz

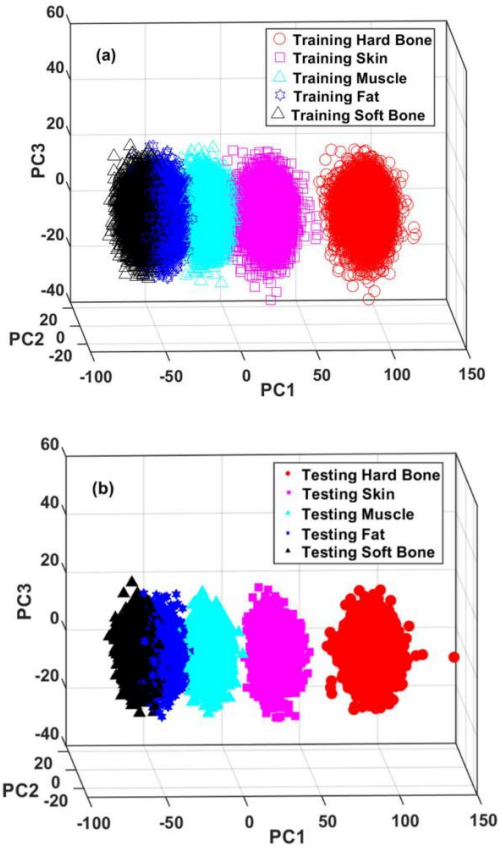

Fig. 19. First three PC scores from the training (a) and testing (b) data for hard and soft bone, muscle, fat and skin.

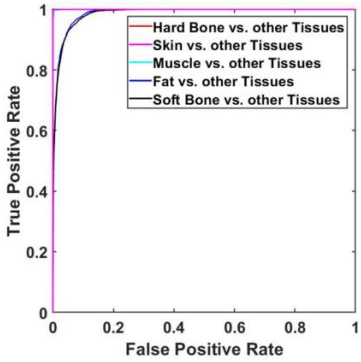

Fig. 20. Receiver operating characteristic (ROC) curve to multi-class, using the ANN models combined with the ns-Nd:YAG laser. Note: The curve of Hard Bone, Skin and Muscle vs. other tissues overlaps.

TABLE 5. CONFUSION MATRIX FOR HARD AND SOFT BONE, FAT, SKIN AND MUSCLE TISSUES DURING LASER ABLATION AT AT 0.2 J PULSE ENERGY.

Tissue	Classified as					Average Classification Accuracy with leave-one-out cross-validation	Area Under Curve in ROC
	Hard Bone	Skin	Muscle	Fat	Soft Bone		
Hard Bone	3598	2	0	0	0	99.94%	100%
Skin	0	3591	9	0	0	99.75%	100%
Muscle	0	18	3560	22	0	98.89%	99.99%
Fat	0	0	12	3089	409	85.81%	98.87%
Soft Bone	0	0	0	604	2996	83.22%	98.61%

FR6 = 2.08-2.50 MHz

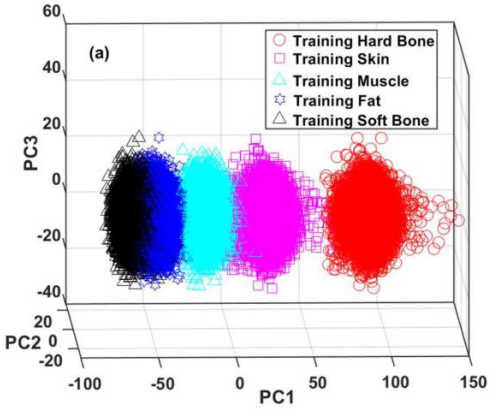

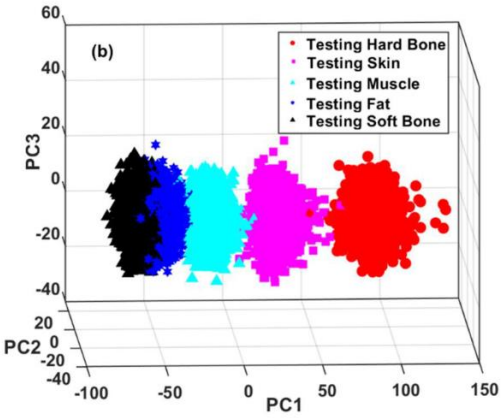

Fig. 21. First three PC scores from the training (a) and testing (b) data for hard and soft bone, muscle, fat and skin.

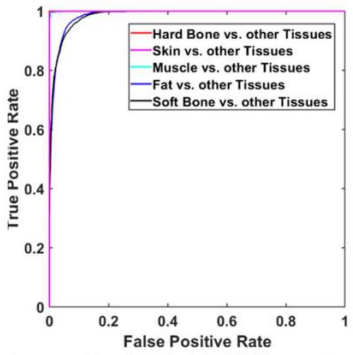

Fig. 22. Receiver operating characteristic (ROC) curve to multi-class, using the ANN models combined with the ns-Nd:YAG laser. Note: The curve of Hard Bone, Skin and Muscle vs. other tissues overlaps.

TABLE 6. CONFUSION MATRIX FOR HARD AND SOFT BONE, FAT, SKIN AND MUSCLE TISSUES DURING LASER ABLATION AT AT 0.2 J PULSE ENERGY.

Tissue	Classified as					Average Classification Accuracy with leave-one-out cross-validation	Area Under Curve in ROC
	Hard Bone	Skin	Muscle	Fat	Soft Bone		
Hard Bone	3600	0	0	0	0	100%	100%
Skin	0	3581	19	0	0	99.47%	99.99%
Muscle	0	15	3569	16	0	99.14%	99.99%
Fat	0	0	14	3242	344	90.06%	98.58%
Soft Bone	0	0	0	611	2989	83.03%	98.67%

ACKNOWLEDGMENT

This work is part of the MIRACLE (short for Minimally Invasive Robot-Assisted Computer-guided LaserosteotomE) project, funded by the Werner Siemens Foundation.

REFERENCES

[1] K.-w. Baek *et al.*, "A comparative investigation of bone surface after cutting with mechanical tools and Er:YAG laser," *Lasers in Surgery and Medicine,* vol. 47, no. 5, pp. 426-432, 2015, doi: 10.1002/lsm.22352.

[2] H. N. Kenhagho, G. Rauter, R. Guzman, P. C. Cattin, and A. Zam, "Comparison of acoustic shock waves generated by micro and nanosecond lasers for a smart laser surgery system," in *SPIE BiOS*, 2018, vol. 10484: SPIE, p. 9.

[3] F. J. O. Landa, X. L. Deán-Ben, F. Montero de Espinosa, and D. Razansky, "Noncontact monitoring of incision depth in laser surgery with air-coupled ultrasound transducers," *Optics Letters,* vol. 41, no. 12, pp. 2704-2707, 2016/06/15 2016, doi: 10.1364/OL.41.002704.

[4] H. Nguendon Kenhagho *et al.*, "Characterization of Ablated Bone and Muscle for Long-Pulsed Laser Ablation in Dry and Wet Conditions," *Materials,* vol. 12, no. 8, p. 1338, 2019. [Online]. Available: http://www.mdpi.com/1996-1944/12/8/1338.

[5] P. Yuldashev, M. Karzova, V. Khokhlova, S. Ollivier, and P. Blanc-Benon, "Mach-Zehnder interferometry method for acoustic shock wave measurements in air and broadband calibration of microphones," *The Journal of the Acoustical Society of America,* vol. 137, no. 6, pp. 3314-3324, 2015, doi: doi:http://dx.doi.org/10.1121/1.4921549.

[6] H. N. Kenhagho, G. Rauter, R. Guzman, P. Cattin, and A. Zam, "Optoacoustic Tissue Differentiation Using a Mach-Zehnder Interferometer: Preliminary Results," in *2018 IEEE International Ultrasonics Symposium (IUS)*, 22-25 Oct. 2018 2018, pp. 1-9, doi: 10.1109/ULTSYM.2018.8579654.

[7] G. Hall, "Ultrasonic wave visualization as a teaching aid in non-destructive testing," *Ultrasonics,* vol. 15, no. 2, pp. 57-69, 1977/03/01/ 1977, doi: https://doi.org/10.1016/0041-624X(77)90066-X.

[8] Koichi Mizutani, Tomohiro Ezure, Keinosuke Nagai, and Masahiro Yoshioka, "Optical Measurement of Sound Fields Information Using Mach-Zehnder Interferometer," *Japanese Journal of Applied Physics,* vol. 40, no. 5S, p. 3617, 2001. [Online]. Available: http://stacks.iop.org/1347-4065/40/i=5S/a=3617.

[9] M. Stafe, C. Negutu, and I. Popescu, "Combined experimental and theoretical investigation of multiple-nanosecond laser ablation of metals," *Journal of optoelectronics and advanced materials,* vol. 8, no. 3, p. 1180, 2006.

[10] J.-I. Youn and J. D. Holcomb, "Ablation efficiency and relative thermal confinement measurements using wavelengths 1,064, 1,320, and 1,444 nm for laser-assisted lipolysis," (in eng), *Lasers in medical science,* vol. 28, no. 2, pp. 519-527, 2013, doi: 10.1007/s10103-012-1100-9.

[11] S. L. Jacques, "Role of tissue optics and pulse duration on tissue effects during high-power laser irradiation," *Appl. Opt.,* vol. 32, no. 13, pp. 2447-2454, 1993.

[12] V. Venugopalan, N. S. Nishioka, and B. B. Mikić, "The Effect of Laser Parameters on the Zone of Thermal Injury Produced by Laser Ablation of Biological Tissue," *Journal of Biomechanical Engineering,* vol. 116, no. 1, pp. 62-70, 1994, doi: 10.1115/1.2895706.

[13] R. N. Oosterbeek, T. Ward, S. Ashforth, O. Bodley, A. E. Rodda, and M. C. Simpson, "Fast femtosecond laser ablation for efficient cutting of sintered alumina substrates," *Optics and Lasers in Engineering,* vol. 84, pp. 105-110, 2016/09/01/ 2016, doi: https://doi.org/10.1016/j.optlaseng.2016.04.007.

[14] S. A. Ashforth, M. C. Simpson, O. Bodley, and R. Oosterbeek, *Ultrashort pulse laser interactions with cortical bone tissue for applications in orthopaedic surgery* (SPIE LASE). SPIE, 2015.

[15] M. V. Rudolf and F. P. v. S. Christiaan, "Laser light delivery systems for medical applications," *Physics in Medicine & Biology,* vol. 42, no. 5, p. 869, 1997. [Online]. Available: http://stacks.iop.org/0031-9155/42/i=5/a=010.

[16] I. E. Kochevar, "Cytotoxicity and mutagenicity of excimer laser radiation," *Lasers in Surgery and Medicine,* vol. 9, no. 5, pp. 440-445, 1989, doi: 10.1002/lsm.1900090503.

[17] N. Bhatta, K. Isaacson, K. M. Bhatta, R. R. Anderson, and I. Schiff, "Comparative study of different laser systems," *Fertility and Sterility,* vol. 61, no. 4, pp. 581-591, 1994/04/01/ 1994, doi: https://doi.org/10.1016/S0015-0282(16)56629-1.

[18] M. Eugster, P. C. Cattin, A. Zam, and G. Rauter, "A Parallel Robotic Mechanism for the Stabilization and Guidance of an Endoscope Tip in Laser Osteotomy," in *2018 IEEE/RSJ International Conference on Intelligent Robots and Systems (IROS)*, 2018: IEEE, pp. 1306-1311.

[19] M. Eugster *et al.*, "Force Estimation for Minimally Invasive Robot-assisted Laser Osteotomy in the Human Knee," in *Joint Workshop on New Technologies for Computer/Robot Assisted Surgery (CRAS)*, 2018.

[20] I. Susic, P. Cattin, A. Zam, and G. Rauter, "Versatile, force range-adjustable, tri-axial force sensor with integrated micro camera for the tip of endoscopic devices," in *The Hamlyn Symposium (2018, accepted)*, 2018.

[21] H. N. Kenhagho, G. Rauter, R. Guzman, P. Cattin, and A. Zam, "Optoacoustic Tissue Differentiation using a Mach-Zehnder Interferometer," *IEEE Transactions on Ultrasonics, Ferroelectrics, and Frequency Control,* pp. 1-1, 2019, doi: 10.1109/TUFFC.2019.2923696.

[22] M. Yu and B. Balachandran, "Acoustic measurements using a fiber optic sensor system," *Journal of Intelligent Material Systems and Structures,* vol. 14, no. 7, pp. 409-414, 2003.

[23] S. Preißer, B. Fischer, and N. Panzer, "Listening to Ultrasound with a Laser: A new way to measure ultrasound waves by optical means," *Optik & Photonik,* vol. 12, no. 5, pp. 22-25, 2017.

[24] B. Fischer, "Miniaturized all-optical Sound Pressure Sensor," in *INTER-NOISE and NOISE-CON Congress and Conference Proceedings*, 2016, vol. 253, no. 2: Institute of Noise Control Engineering, pp. 6376-6382.

[25] O. Volodarsky, Y. Hazan, and A. Rosenthal, "Ultrasound detection via low-noise pulse interferometry using a free-space Fabry-Pérot," *Opt. Express,* vol. 26, no. 17, pp. 22405-22418, 2018.

[26] T. Kajava, H. Lauranto, and A. Friberg, "Interference pattern of the Fizeau interferometer," *JOSA A,* vol. 11, no. 7, pp. 2045-2054, 1994.

[27] J. A. McKay, "Assessment of a multibeam Fizeau wedge interferometer for Doppler wind lidar," *Appl. Opt.,* vol. 41, no. 9, pp. 1760-1767, 2002/03/20 2002, doi: 10.1364/AO.41.001760.

[28] H. N. Kenhagho, F. Canbaz, G. Rauter, R. Guzman, P. Cattin, and A. Zam, "A First Approach to Miniaturized Optoacoustic Feedback Sensor for Smart Laser Osteotome : Fiber-Coupled Fabry-Pérot Etalon Sensor," in *2019 IEEE SENSORS*, 27-30 Oct. 2019 2019, pp. 1-4, doi: 10.1109/SENSORS43011.2019.8956743.

[29] Z. Alperovich, G. Yamin, E. Elul, G. Bialolenker, and A. A. Ishaaya, "In situ tissue classification during laser ablation using acoustic signals," *Journal of biophotonics,* p. e201800405, 2019.

[30] C. Chia-Chen and J. Sirkis, "Multiplexed optical fiber sensors using a single Fabry-Perot resonator for phase modulation," *Journal of Lightwave Technology,* vol. 14, no. 7, pp. 1653-1663, 1996, doi: 10.1109/50.507941.

[31] X. Bai *et al.*, "Sensitivity characteristics of broadband fiber-laser-based ultrasound sensors for photoacoustic microscopy," *Opt. Express,* vol. 25, p. 17616, 07/24 2017, doi: 10.1364/OE.25.017616.

[32] A. Winkler, K. Maslov, and L. Wang, "Noise-equivalent sensitivity of photoacoustics," *Journal of Biomedical Optics,* vol. 18, no. 9, p. 097003, 2013. [Online]. Available: https://doi.org/10.1117/1.JBO.18.9.097003.

[33] C. M. Bishop, *Pattern recognition and machine learning*. Springer Science+ Business Media, 2006.

[34] J. Lehman, S. Risi, and J. Clune, "Creative generation of 3D objects with deep learning and innovation engines," in *Proceedings of the 7th International Conference on Computational Creativity*, 2016.

[35] H. N. Kenhagho *et al.*, "Machine Learning-based Optoacoustic Tissue Classification Method for Laser Osteotomes Using an Air-coupled Transducer," *Submitted to Lasers in Surgery and Medicine,* pp. 1-15, 2020 2020.

[36] Q. Qin and K. Attenborough, "Characteristics and application of laser-generated acoustic shock waves in air," *Applied Acoustics,* vol. 65, no. 4, pp. 325-340, 4// 2004, doi: http://dx.doi.org/10.1016/j.apacoust.2003.11.003.

[37] S. Preisser *et al.*, "All-optical highly sensitive akinetic sensor for ultrasound detection and photoacoustic imaging," *Biomed. Opt. Express,* vol. 7, no. 10, pp. 4171-4186, 2016/10/01 2016, doi: 10.1364/BOE.7.004171.

[38] S. V. Stehman, "Selecting and interpreting measures of thematic classification accuracy," *Remote sensing of Environment,* vol. 62, no. 1, pp. 77-89, 1997.

[39] H. N. Kenhagho, G. Rauter, R. Guzman, P. C. Cattin, and A. Zam, "Optoacoustic Tissue Differentiation using a Mach-Zehnder Interferometer," *Submitted.*

[40] H. N. Kenhagho *et al.*, "Optoacoustic Tissue Classification for Laser Osteotomes Using Mahalanobis Distance-based Method," in *Medical Robotics 2020 (MESROB2020)*, 2020, vol. 1: Springer pp. 1-8.

Hervé Nguendon Kenhagho
BLOG, Department of Biomedical Engineering, University of Basel, Allschwil, Switzerland
herve.nguendon@unibas.ch

Hervé Nguendon Kenhagho received the B.Eng. degree (Hons.) in communication and electronic engineering from Northumbria University, Newcastle upon Tyne, U.K., in 2009, and the M.Sc. degree in microelectronic and communication engineering from Northumbria University, in 2010. He is currently pursuing the Ph.D. degree with the Biomedical Laser and Optics Group (BLOG), Department of Biomedical Engineering, University of Basel, Allschwil, Switzerland. He held a calibration engineer position at the Repair and Cal Ltd., Reading, U.K., and research engineer positions at the University of Lunebürg, Lüneburg, Germany, and the University Carlos Tercero de Madrid, Madrid, Spain. He joined the Department of Biomedical Engineering, University of Basel, as a researcher associated with the Ph.D. candidature, in 2016. He has authored over ten proceedings, peer-reviewed articles, and books. His main research interests focus on the development of smart devices, antenna design and field measurement for electronic communications engineering and medical therapy, diagnostics and monitoring using novel acoustical/optical technologies, including smart laser surgery, optoacoustic, AI-aided acoustical/optical diagnostics, and the Internet of Things (IoT)-based sensors. Mr. Nguendon received the Professional Certificate as a Laser Safety Officer from the Universität des Saarlandes, Saarbrücken, Germany, in 2016.

Ferda Canbaz
BLOG, Department of Biomedical Engineering, University of Basel, Allschwil, Switzerland
ferda.canbaz@unibas.ch

Ferda Canbaz is a postdoctoral researcher in the Department of Biomedical Engineering at University of Basel. She received the B.S. degree in engineering physics from Istanbul Technical University, Istanbul, Turkey, in 2011. She received the M.S. degree in optoelectronics and photonics engineering in 2013 and the PhD degree in physics in 2018 from Koç University, Istanbul, Turkey. Her research interests include mid-infrared solid-state/fiber lasers, ultrafast optics, photoacoustic diagnosis and smart laser surgery.

Raphael Guzman
Department of Neurosurgery
University Hospital
and
University Children's Hospital, Basel, Switzerland
raphael.Guzman@usb.ch

Raphael Guzman is currently a Professor of neurosurgery and the Vice Chairman of the Department of Neurosurgery, University Hospital of Basel, Basel, Switzerland, and the University Children's Hospital of Basel (UKBB), Basel. His clinical expertise is in pediatric and cerebrovascular neurosurgery. His research group examines the clinical relevance of neural stem/progenitor cells (NPC) in brain ischemia and particularly in neonatal hypoxic-ischemia (HI) with regard to white matter regeneration. Neonatal HI is an important cause of cerebral palsy (CP), leading to devastating sensory-motor, cognitive, and learning deficits in the growing child. White matter injury is a central feature of HI and CP, and defects in myelination are also commonly identified in other neurodevelopmental disorders, including autism spectrum disorders (ASD). White matter myelination generally reflects the progression of functional brain maturation and connectivity in the first years of life and molecular and cellular crosstalk between NPCs and resident brain cells, particularly myelinating oligodendrocytes, *in vitro* and in a rodent model of neonatal HI. He is also deeply involved in advancing novel technologies such as virtual and augmented reality and minimally invasive endoscopy to advance neurosurgical teaching and operative techniques in collaboration with the Department of Bioengineering. His research is funded through the Swiss National Science Foundation and several grants from private foundations as well as industry collaborations. He has authored over 200 peer-reviewed articles, book chapters, and scientific meeting proceedings.

Philippe C. Cattin
CIAN, Department of Biomedical Engineering, University of Basel, Allschwil, Switzerland
philippe.cattin@unibas.ch

Philippe C. Cattin was born in Baden, Switzerland, in 1967. He received the B.Sc. degree from the University of Applied Science in Brugg/Windisch, Windisch, Switzerland, in 1991, and the M.Sc. degree in computer science and the Ph.D. degree in robotics from ETH Zurich, Zürich, Switzerland, in 1995 and 2003, respectively. From 2003 to 2007, he was a Postdoctoral Fellow with the Computer Vision Laboratory, ETH Zurich. In 2007, he became an Assistant Professor with the University of Basel, Allschwil, Switzerland, and was promoted to Associate Professor in 2015 and to Full Professor in 2019. He is the Founder of the Center for Medical Image Analysis and Navigation (CIAN), Medical Faculty, University of Basel, where he is the Founding Head and still heading the Department of Biomedical Engineering. He joined Brigham and Women's Hospital, Boston, MA, USA, in 2017, as a Research Fellow. He is also the Founder of two spin-off companies and licensed his patents and software to medical device companies. His research interests include medical image analysis, image-guided therapy, robotics-guided laser osteotomy and virtual reality. As a Principal Investigator, he has finished many projects in these areas and published over 250 papers, patents and book chapters.

Azhar Zam
BLOG, Department of Biomedical Engineering, University of Basel, Allschwil, Switzerland
azhar.zam@unibas.ch

Azhar Zam received the B.Sc. degree in medical physics from the University of Indonesia, Depok, Indonesia, in 2004, the M.Sc. degree in biomedical engineering from the University of Lübeck, Lübeck, Germany, in 2007, and the Ph.D. degree in advanced optical technologies from the Friedrich-Alexander University Erlangen–Nuremberg, Germany, with the focus on optical feedback for tissue-specific laser surgery, in 2011. He held various research positions at the University of Waterloo, Canada, the National University of Ireland Galway, Ireland, the University of California at Davis, USA and Ryerson University, Toronto, Canada. He joined the Department of Biomedical Engineering, University of Basel, Switzerland, in 2016, as an Assistant Professor, where he founded and leads the Biomedical Laser and Optics Group (BLOG). He has authored over 60 peer-reviewed articles, book chapters, books, and patents. His main research interests focus on the development of smart devices for medical therapy, diagnostics and monitoring using novel optical technologies, including smart laser surgery, optical coherence tomography (OCT), photoacoustics, biomedical spectroscopy, AI-aided optical diagnostics and imaging, optical-based smart wearable sensors and miniaturized systems.

Chapter 6

Optoacoustic Sciatic Nerve Detection for Minimally Invasive Smart Laser Surgery

Introduction

With the proposed feedback detection system, it was possible to classify five tissues types — hard bone, soft bone, fat, muscle, and skin — extracted from proximal and distal fresh porcine femurs. In this work, we enhanced the feedback system by adding sciatic nerve tissue and classifying it against the five tissue types using laser-generated acoustic shock waves (ASWs). Tissue classification was carried out using the best-performing machine learning method as described in a previous chapter — principal component analysis (PCA) combined with an artificial neural network (ANN).

Publication. An account of this experiment is ready for submission to 2020 Journal of Biophotonics, with peer review.

https://onlinelibrary.wiley.com/journal/18640648

WILEY-VCH

Original Article

Optoacoustic Sciatic Nerve Detection Using an All-Fiber Optical Sensor for Endoscopic Smart Laser Surgery

Hervé Nguendon Kenhagho[1]*, Ferda Canba[1], Alois Hopf[2], Raphael Guzman[2,3], Philippe Cattin[4], Azhar Zam[1]*

[1]Biomedical Laser and Optics Group, Department of Biomedical Engineering, University of Basel, Allschwil, Switzerland
[2]Brain Ischemia and Regeneration, Department of Biomedicine, University of Basel, University Hospital of Basel, Switzerland
[3]Neurosurgery Group, Department of Biomedical Engineering, University of Basel, Allschwil, Switzerland
[4]Center for medical Image Analysis and Navigation, Department of Biomedical Engineering, University of Basel, Allschwil, Switzerland

*Corresponding Author: *herve.nguendon@unibas.ch* or azhar.zam@unibas.ch

KEYWORDS: Laser ablation, tissue classification, sciatic nerve tissue, acoustic shock signal, principal component analysis, artificial network machine

Abstract

Laser surgery requires efficient tissue classification to reduce the probability of undesirable or unwanted tissue damage. The aim of this study was to investigate acoustic shock wave spectroscopy as a means of classifying sciatic nerve tissue. In this study, we classified sciatic nerve tissue against other tissue types — hard bone, soft bone, fat, muscle, and skin extracted from two proximal and distal fresh porcine femurs — using the acoustic shock waves (ASWs) generated by a laser. A nanosecond frequency-doubled Nd:YAG laser at 532 nm was used to create ten craters on the surface of each tissue type. We used a fiber-coupled Fabry-Pérot sensor to measure the ASWs. The amplitude of the spectrum from each ASW frequency band measured was used as input for principal component analysis (PCA). PCA was combined with an artificial neural network to classify the tissue types. A confusion matrix and receiver operating characteristic (ROC) analysis was used to calculate the accuracy of the testing-data-based scores from sciatic nerve and the area under the ROC curve (AUC) with a 95% confidence-level interval. Based on the confusion matrix and ROC analysis of the model's tissue classification results (leave-one-out cross validation), nerve tissue could be classified with an average accuracy rate and AUC result of 95.78± 1.3% and 99.58± 0.6%, respectively. The results of this work demonstrate the opportunity acoustic shock wave spectroscopy presents for remote classification of nerve and other types of tissue. The technique can serve as the basis of a feedback control system to detect and preserve sciatic nerves in femur laser surgery.

1. INTRODUCTION

Laser surgery offers numerous advantages to both patients and surgeons, such as the ability to ablate organic tissues with high precision and to achieve functional cutting geometry with minimal trauma. Additionally, laser's contact-free ablation allows an advanced level of sterility compared to the use of

mechanical tools in surgery [1, 2]. These advantages are somewhat diminished, however, by a lack of information on the type and depth of ablated tissues. During laser ablation, it is crucial to preserve some tissue types, such as the sciatic nerve. Preservation is particularly challenging when operating on body parts with complex tissue types, such as a femur, which includes hard and soft bone, muscle, fat and skin, and most importantly, the sciatic nerve [3, 4].

The sciatic nerve is the largest nerve in the human body, measuring up to 2cm in diameter. Originating from the lumbar and sacral spine, the sciatic nerve travels through the greater sciatic foramen below the piriformis muscle. Surrounded by a fatty sheath, it follows the back of the upper thigh, from the pelvis to the knee. At the popliteal fossa, which serves as a conduit for blood vessels and nerves in the leg, the sciatic nerve divides into the common peroneal nerve and the tibial nerve. Both are responsible for motor and sensory function in the lower leg and foot [5, 6]. Nerves are embedded in various other tissues, making it challenging for surgeons to discriminate between them, especially smaller diameter nerves. Damaging the anatomical structure of the sciatic nerve or the subsequent common peroneal and tibial nerves can drastically affect sensation over the sole of the foot, the back of the femur, part of the lower femur and the knee [7-9]. Fractional damage to the nerve can cause weakness of foot movements, weakness of knee flexion (bending), trouble bending the foot down (plantar flexion), or bending the foot inward (inversion) [10].

To overcome damaging the facial nerve, methods such as electrical stimulation and diffuse reflectance spectroscopy have been used to detect facial nerve tissue during laser ablation [3, 11]. In this study, we proposed a complementary method to distinguish the sciatic nerve from hard or soft tissue, based on acoustic shock wave (ASW) measurements. When nanosecond pulsed lasers interact with biological tissues, ASWs are generated and can propagate through the air [12]. The propagated ASW can be measured using piezoelectric transducers (PZTs), air-coupled transducers (microphones), and free-space Mach-Zehnder interferometer sensors, which convert the spherical wavefront into electrical signals [13-17]. ASW signal parameters mainly depend on the type of tissue ablated [13]. Therefore, these parameters can be used to differentiate tissue types, indicating the need to stop the laser when important tissues (like nerves) are detected [16, 18]. The bulky sensors that were previously used to measure ASWs had limited bandwidths (typically less than 1MHz) [19]. The need for both a broad bandwidth and compact sensor led to the development of new optical sensors, with extended bandwidths and small designs sufficient for endoscopic applications.

In this work, we used our well-established fiber-coupled Fabry-Pérot etalon system to measure ASWs during laser ablation [20, 21]. Among the advantages of using etalon sensors are their compactness and broad usable bandwidths (exceeding 2.5MHz). We used a frequency-doubled, Q-switched Nd:YAG (Neodimium-doped Yttrium Aluminium Garnet) laser to produce craters on the surface of hard bone, soft bone, muscle, fat, skin, and nerve tissue. We used a nanosecond pulsed laser at 532nm to fulfill the thermal confinement condition. With this laser, we could avoid thermal damage to the tissue [22-24]. We measured the ASWs emitted and then assessed the measurements by looking at the amplitude frequency band that delivered the best accuracy and area under curve. We used principal component analysis (PCA) and an artificial neural network to reduce the dimensionality of data points and to classify sciatic nerve from among other tissue types, respectively.

2. MATERIAL AND METHOD

2.1 Sample Preparation

Six tissue types —hard bone, soft bone, muscle, fat, skin and sciatic nerve— were extracted from two fresh porcine proximal and distal femurs. The connective tissues (Fig. 1) were carefully separated with scalpels. The specimen was then rinsed in distilled water before undergoing the laser experiments.

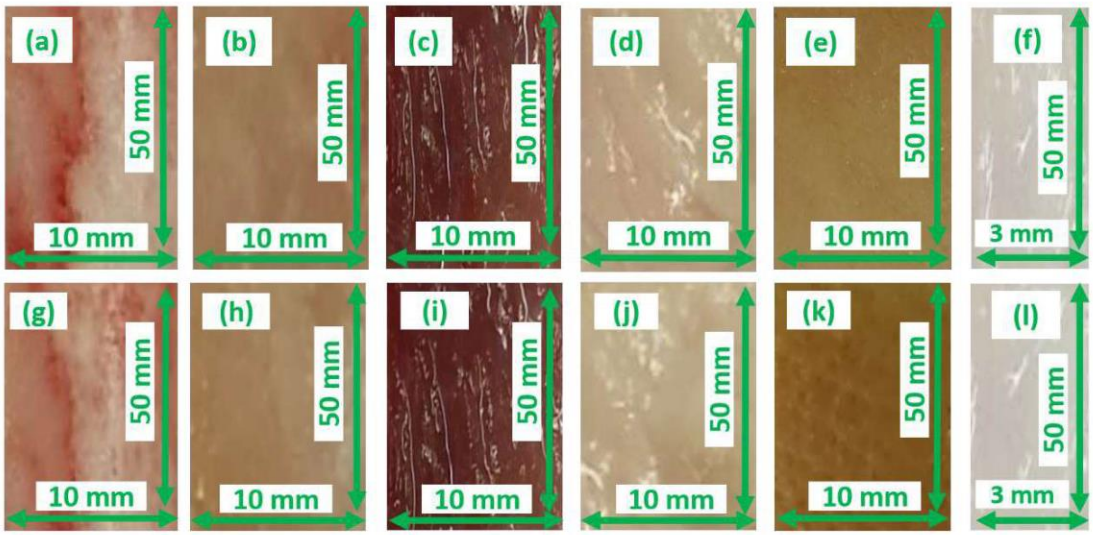

Figure 1. Tissue samples from a fresh porcine femur. Proximal femur: hard bone (a), soft bone (b), muscle (c), fat (d), skin (e) and nerve (f); distal femur: hard bone (g), soft bone (h), muscle (i), fat (j), skin (k) and sciatic nerve (l).

2.2 Experimental Setup

We ablated the samples using a Nd:YAG laser (Q-smart 450, Quantel, Paris, France) with 5 ns-long pulses at 532 nm. The pulse energy was 200 mJ, with a repetition frequency of 10 Hz. The laser beam was focused at a 7.5 cm focal distance (LA5042, Thorlabs), using an anti-reflection coated bi-convex lens. A detailed explanation of the experimental setup, including calibration steps, was reported in a previous work [21]. The focal point was positioned 2 mm under the sample surface to achieve deeper ablation. Using a Gaussian distribution, whereby maximum irradiance is reached at an amplitude of e^{-2}, the laser spot size was estimated to be 15.6 µm. A sequence of 180 laser pulses was applied to the fresh porcine femur. Ten craters, each 4 mm apart, were created on the surface of each sample.

In the optical sensor system, we used a single-frequency laser source (SFL1550S, Thorlabs) that emits continuous coherent light at a center wavelength of 1550 nm, with an output power of 40 mW [21]. The laser contains a single mode (SM) output fiber tail (CLD1015, Thorlabs). The output of the fiber tail is coupled into port 1 (P1 in Fig. 2) of the single-mode fiber-optic circulator (FOC) (6015-3-APC, Thorlabs). A single-mode 50:50 partial reflector fiber (P5- SMF28ER-50-1, Thorlabs) is connected to port2 (P2 in Fig. 2) of the FOC to split the incident beam into two spectral bands: one transmitted and one reflected. The reflected light from the coated facet of the fiber is routed to Port 3 (P3). The transmitted light is collimated at the surface of an anti-reflection coated bi-convex lens (67-593, Edmund Optics). The coated double-convex lens with a focal length of 9 mm is embedded in the 4 mm×20 mm optical cavity to focus the collimated light onto the surface of a flat mirror. The propagating beam in the optical cavity is retroreflected by a protected gold mirror (PF1011-M01, Thorlabs) and coupled back into the 50:50 partial reflector fiber. The retroreflected beam is also routed by the FOC to P3. The P3 connector of the FOC is mounted to an InGaAs detector with a fixed amplified gain (PDA20C2, Thorlabs) to sense the variation in light intensity [21].

During laser tissue ablation, the ASWs generated cause spatiotemporal variations of the air refractive index in the optical cavity. Thus, changes in the light intensity of the probing laser beam in the optical cavity correspond to the pressure of the acoustic shock wave, which can be accurately measured by an InGaAs detector [21]. The custom-made all-fiber Fabry-Pérot sensor is illustrated in Fig. 2.

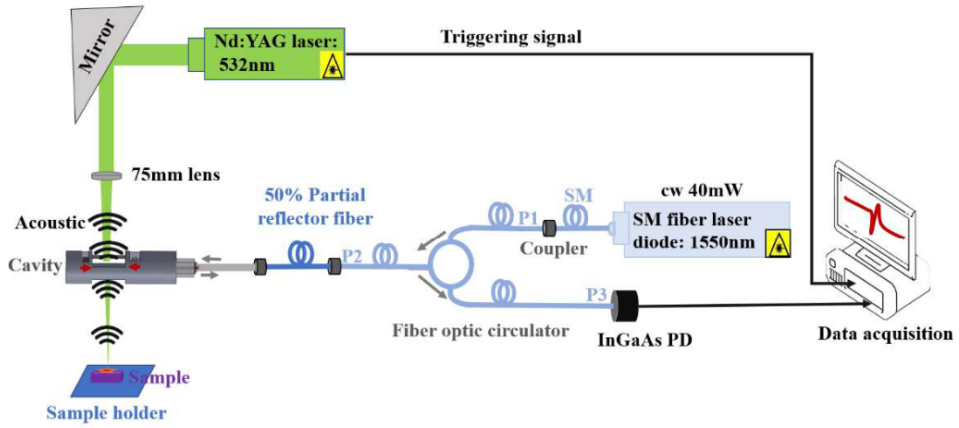

Figure 2. Illustration of the fiber-coupled Fabry-Pérot etalon system (side view). The acoustic shock wave propagated is detected in the optical cavity as the refractive index in the air cavity changes.

2.3 Data Acquisition

During laser tissue ablation, we measured the ASWs emitted, using the custom-made optical sensor (Fig. 2). Acoustic data acquisition was triggered by an external CMOS trigger from the laser. The time gate window of each measurement was 82 µs. The measured analog signals were digitized using a PCI Express x8 (M4i.44xx-x8, Spectrum Microelectronic GmbH, Grosshansdorf, Germany), with a 16-bit transient recorder and a sampling rate of 10 MS/s.

2.4 Classification Matrix

Statistical analysis and calculations were performed with MATLAB software. We suppressed the phase shift of each ASW signal by characterizing the amplitude spectrum, using the fast Fourier transform (FFT). We improved the contrast of the visualization of each ASW using the logarithm of the amplitude spectrum. We split the amplitude spectrum into six equal frequency bands (F1-6). In order to enhance classification performance, we scaled each frequency band value by subtracting the mean of all frequency bands measured. Therefore, a mean of zero was obtained for each frequency range. Each frequency band was used as an input for PCA, which was applied to reduce the complexity of high-dimensional data by maintaining the same patterns and trends of the ASW field [24]. In other words, PCA decomposes the data by generating orthogonal and, thus, independent linear combinations of the variables known as principal components (PC) or PCA scores.

To classify tissue, we investigated the processed acoustics by looking at the amplitude-frequency band in which we achieved the best average classification accuracy and at the area under curve for nerve detection. We combined PCA scores with an artificial neural network (ANN) to carry out classification. To build the network, we used an input, a hidden, and an output layer. The input layer was made of three neurons. The single hidden layer and one output layer were made of ten neurons and six neurons, respectively. Then, the backpropagation algorithm was used to train the ten neurons of the hidden layer, using gradient descent. The first three PCA scores from the set of data points were used as inputs into the ANN. Only a few PCA scores are needed to describe a large quantity of the variation around the data point; the majority of PCA scores accounts for less than 1 % of the data point. Hence, by using only three PCA scores, we were able to reduce the dimensionally of the frequency band while keeping most of the variance of the selected frequency band for classification.

We performed a leave-one-out cross-validation as follows: During the classification phase, a set of 3,600 data points measured from ten craters in one proximal and distal femur, was used as training data. Then, each set of 1,800 data points which was correspondingly measured from ten

craters in one proximal and distal femur from the second porcine specimen, was used as validation and testing data, respectively. A confusion matrix and receiver operating characteristic (ROC) analysis was used to calculate the accuracy of the testing-data-based scores from sciatic nerve and the area under the ROC curve (AUC) with a 95% confidence-level interval. The average classification was calculated based on the mean accurate of two cross validated results from two folds —two proximal and distal femurs extracted from two different porcines—.

3. RESULTS

Acoustic shock waves measured in the time and frequency domains for each ablated tissue are shown in Figs. 3a and 3b. Hard tissue (hard bone) produced higher peak amplitude values in the time and frequency domains than did the soft tissues (soft bone, muscle, fat, skin and nerve). We used the amplitude of the spectrum from each frequency band as inputs for the PCA (see appendix for results at frequency bands, except for FR4).

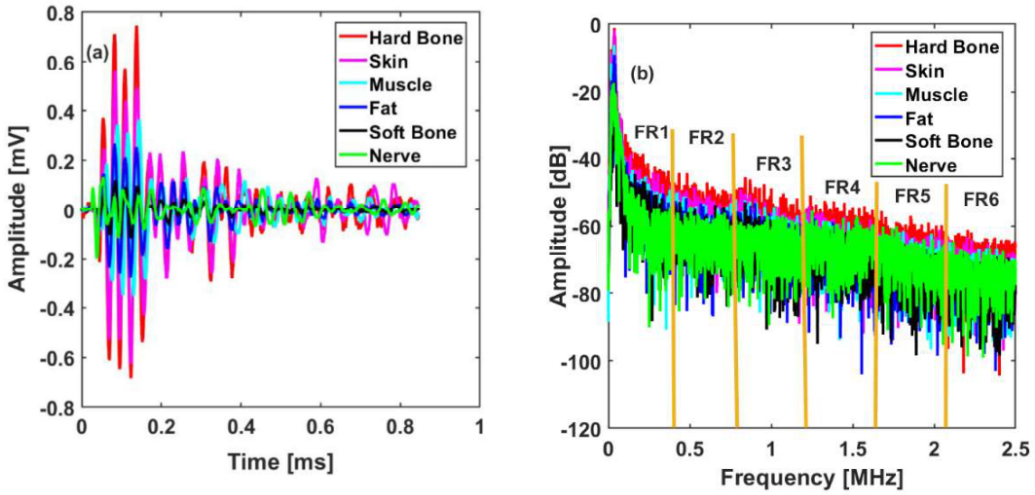

Figure 3. Comparison of the acoustic shock waves emitted from ablated hard muscle and fat tissues in the time (a) and frequency (b) domain.

The analysis of training data and testing data scores from frequency range FR4 are shown in Figs. 4a and 4b, respectively. Results from other frequency bands are in the appendix (Figs. 5-9 and Table 2-6). The three principal components (PCs) selected for differentiation were responsible for 87.5% of the variation around the data point. The first three PCs contributed to 85.28% (PC1), 1.89% (PC2), and 0.33% (PC3) of the frequency band variance for each type of tissue. From the confusion matrix and the receiver operating characteristic (ROC) analysis (Fig. 4c), the average classification accuracy (with leave-one-out cross validation) between nerve tissue and other tissues was more than 95.78± 1.3% (Table 1). The corresponding AUC was more than 99.58± 0.6%, for nerve, against other tissues (Table 1).

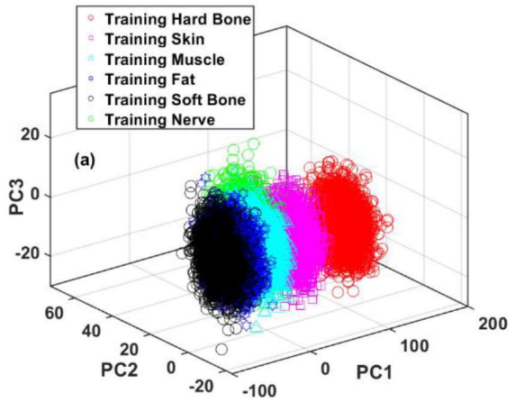

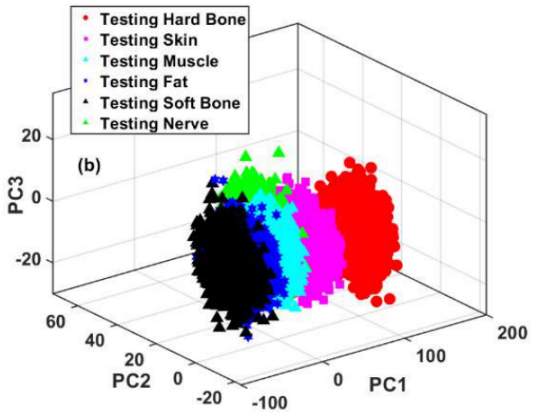

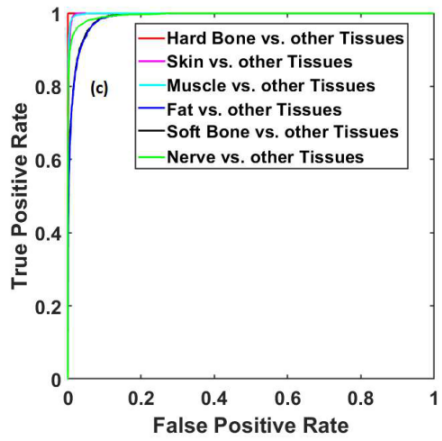

TABLE 1. CONFUSION MATRIX FOR HARD BONE, SKIN,MUSCLE, FAT, SOFT BONE AND NERVE TISSUES DURING LASER ABLATION AT 0.2 J PULSE ENERGY.

Tissue	Classified as						Average Classification Accuracy with leave-one-out cross validation	Area Under ROC Curve
	Hard Bone	Skin	Muscle	Fat	Soft Bone	Nerve		
Hard Bone	1800	0	0	0	0	0	100%	100%
Skin	0	1734	0	0	0	66	99.33%	99.91%
Muscle	0	0	1712	7	0	81	95.11%	99.83%
Fat	0	0	9	1593	198	0	88.50%	98.90%
Soft Bone	0	0	0	198	1602	0	89%	98.98%
Nerve	0	43	33	0	0	1724	95.78%	99.58%

Figure 4. First three PC scores from the training (a) and testing (b) data for hard and soft bone, muscle, fat, skin, and nerve (FR4 = 1.25-1.67MHz). Receiver operating characteristic curve (c) to multi-class using the ANN models combined with the ns-Nd:YAG laser. Note: The curve of Hard Bone-,Skin-, Muscle- and Nerve-tissues vs. other tissues overlaps. The confusion matrix of tissue types (Table 1).

4. DISCUSSION

Based on the confusion matrix and the ROC analysis of the model's tissue classification results, nerve tissue could be classified with an accuracy rate and AUC results of 95.78± 1.3% and 99.58± 0.6%, respectively. The best result, with an accuracy rate and AUC of 100%, was achieved for distinguishing hard bone tissue from all others. The main reason for this high classification rate is that hard tissues, like hard bone, consist of 65% inorganic elements (calcium phosphate compounds, mainly hydroxyapatite) and 35% organic elements (collagen fibrils, water, proteins). In contrast, soft tissue is 79% water, which is its main chromophore, and 20% pigment melanin, lipids and carbohydrates [26]. In other words, the ASWs that emanate from soft tissue are mainly generated by water, while those that emanate from hard bone are mostly based on carbonated hydroxyapatite. Similarly, ASWs propagated during hard bone ablation results in a higher amplitude of sound due to the compact structure of the carbonated hydroxyapatite [27]. The worst classification rate and AUC result was for distinguishing between soft bone and fat (Table 2-6). This tendency for misclassification was already observed in our earlier studies [16, 20]. Since soft bone in the femur is mostly made of fatty tissue, it presents a similar mechanical structure, generating comparable acoustic shock wave signatures [16, 20]. Nevertheless, classification between tissue types was not the main aim of this work, in which we focused on sciatic nerve at a frequency range of 1.25-1.67MHz (FR4). In our previous studies, we showed that the frequency band around 1.7MHz (FR5) yielded the best results in terms of high average classification accuracy and AUCs

with cross validation between tissues [16, 20, 28]. The authors believe by adding nerve tissues the frequency range that provided the best classification accuracy shifted to 1.25-1.67 MHz (FR4). The main reason could be important parameters (variance) of the ASWs from Nerve are in the frequency range of FR4.

To apply this tissue classification method in a closed loop system to control laser ablation in surgery, the computational time needed to analyze the ASW spectra must be less than the pulse repetition time. With an eye towards extending the system for a more general purpose, it would be essential to analyze numerous types of tissue in a very short period of time; an aim that presents both a mathematical and computational challenge. While determining the mandatory time for tissue classification was not the objective of our study, the matter must be examined further before transferring the results of this investigation to a control system. In our study, tissue classification was implemented *ex vivo*. Prior to any clinical use of the model, however, additional tests would be required to examine the impact of blood flow *in vivo*, carbonization and blood loss on the surface of surgical lesions on ASW tissue classification.

The Er:YAG (Erbium-doped Yttrium Aluminum Garnet) laser at 2940 nm is generally used for deep ablation accompanied by a water-cooling system. The reason being that the operation wavelength of the Er:YAG laser corresponds to the highest absorption peak of water and to a strong absorption peak of hydroxyapatite, the main component of bone [29]. In contrast to the Er:YAG, the Nd:YAG laser at 532 nm can be used to ablate surfaces in a wet environment, such as for knee arthroscopy [12, 18, 30]. Depending on the laser pulse parameters, such as laser energy, pulse duration, and focusing conditions [30], the ASW properties can be slightly different [12]. Therefore, investigating tissue classification using the Er:YAG at 2940 nm *In-Vivo* is an essential next step.

5. CONCLUSION

The results of this work show the opportunity that acoustic shock wave spectroscopy presents for remote classification of nerve and other types of tissue (hard and soft bone, muscle, fat, and skin). The average classification accuracy and area under the ROC curve (AUC) result with leave-one-out cross validation was more than 95.78± 1.3% for distinguishing nerve from other tissues. This technology can be used to develop a control system capable of identifying nerve tissue during femur laser surgery, to prevent sensation and motor function loss in the lower body. Future work should focus on tissue classification and carbonization detection with sufficiently short computational time when ablating a wide range of tissue types *in vivo*, using Nd:YAG and Er:YAG at 532 nm and 2940 nm, respectively.

6. APPENDIX

FR1 = 0-0.42 MHz

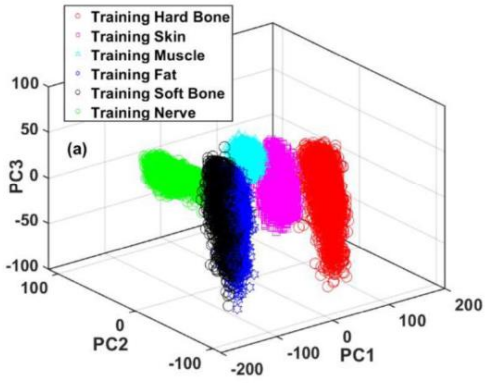

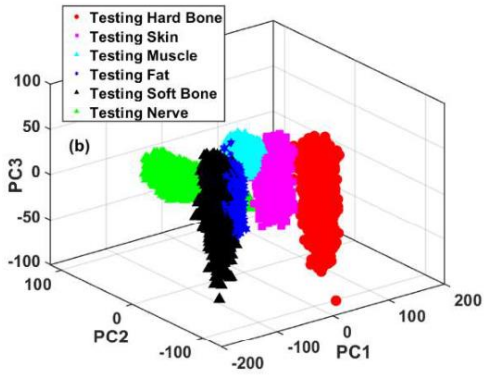

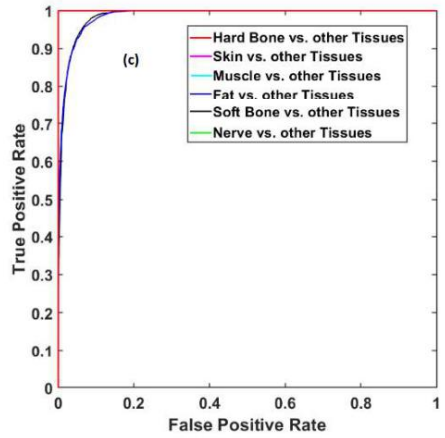

TABLE 2. CONFUSION MATRIX FOR HARD BONE, SKIN,MUSCLE, FAT, SOFT BONE AND NERVE TISSUES DURING LASER ABLATION AT 0.2 J PULSE ENERGY.

Tissue	Classified as						Average Classification Accuracy with leave-one-out cross validation	Area Under ROC Curve
	Hard Bone	Skin	Muscle	Fat	Soft Bone	Nerve		
Hard Bone	1798	2	0	0	0	0	99.88%	100%
Skin	0	1800	0	0	0	0	100%	100%
Muscle	0	0	1797	3	0	0	99.83%	100%
Fat	0	0	321	1479	0	0	82.17%	98.65%
Soft Bone	0	0	0	259	1541	0	85.61%	98.66%
Nerve	0	0	0	0	0	1800	100%	100%

Figure 5. First three PC scores from the training (a) and testing (b) data for hard and soft bone, muscle, fat and skin (FR1 = 0-0.42 MHz). Receiver operating characteristic curve (c) to multi-class using the ANN models combined with the ns-Nd:YAG laser. Note: The curve of Hard Bone-,Skin-, Muscle- and Nerve-tissues vs. other tissues overlaps. The confusion matrix of tissue types (Table 2).

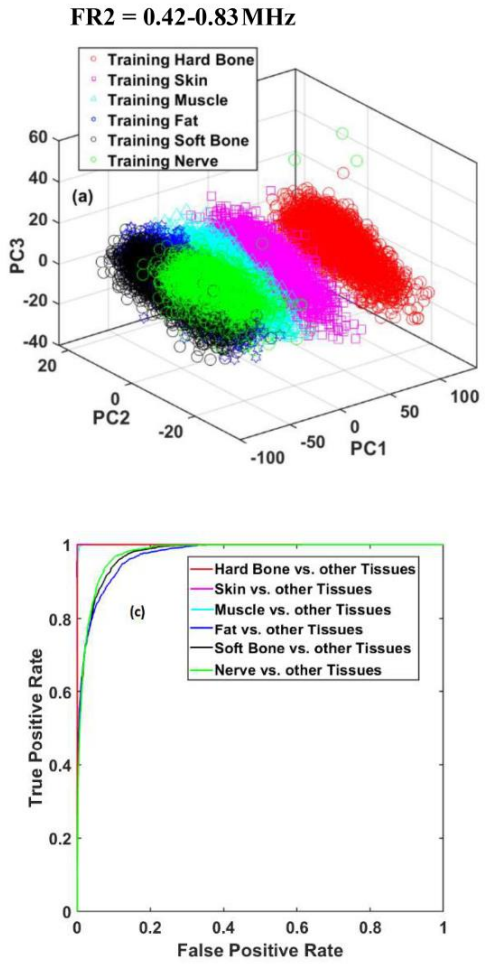

TABLE 3. CONFUSION MATRIX FOR HARD BONE, SKIN,MUSCLE, FAT, SOFT BONE AND NERVE TISSUES DURING LASER ABLATION AT 0.2 J PULSE ENERGY.

Tissue	Classified as						Average Classification Accuracy with leave-one-out cross validation	Area Under ROC Curve
	Hard Bone	Skin	Muscle	Fat	Soft Bone	Nerve		
Hard Bone	1799	1	0	0	0	0	99.94%	100%
Skin	0	1799	0	0	1	0	99.94%	100%
Muscle	0	0	1797	3	0	0	99.61%	99.95%
Fat	0	0	6	1475	185	134	81.94%	97.37%
Soft Bone	0	0	0	214	1448	138	80.44%	97.42%
Nerve	0	0	14	165	192	1429	79.39%	97.72%

Figure 6. First three PC scores from the training (a) and testing (b) data for hard and soft bone, muscle, fat and skin (FR2 = 0.42-0.83 MHz). Receiver operating characteristic curve (c) to multi-class using the ANN models combined with the ns-Nd:YAG laser. Note: The curve of Hard Bone-,Skin-, Muscle- and Nerve-tissues vs. other tissues overlaps. The confusion matrix of tissue types (Table 3).

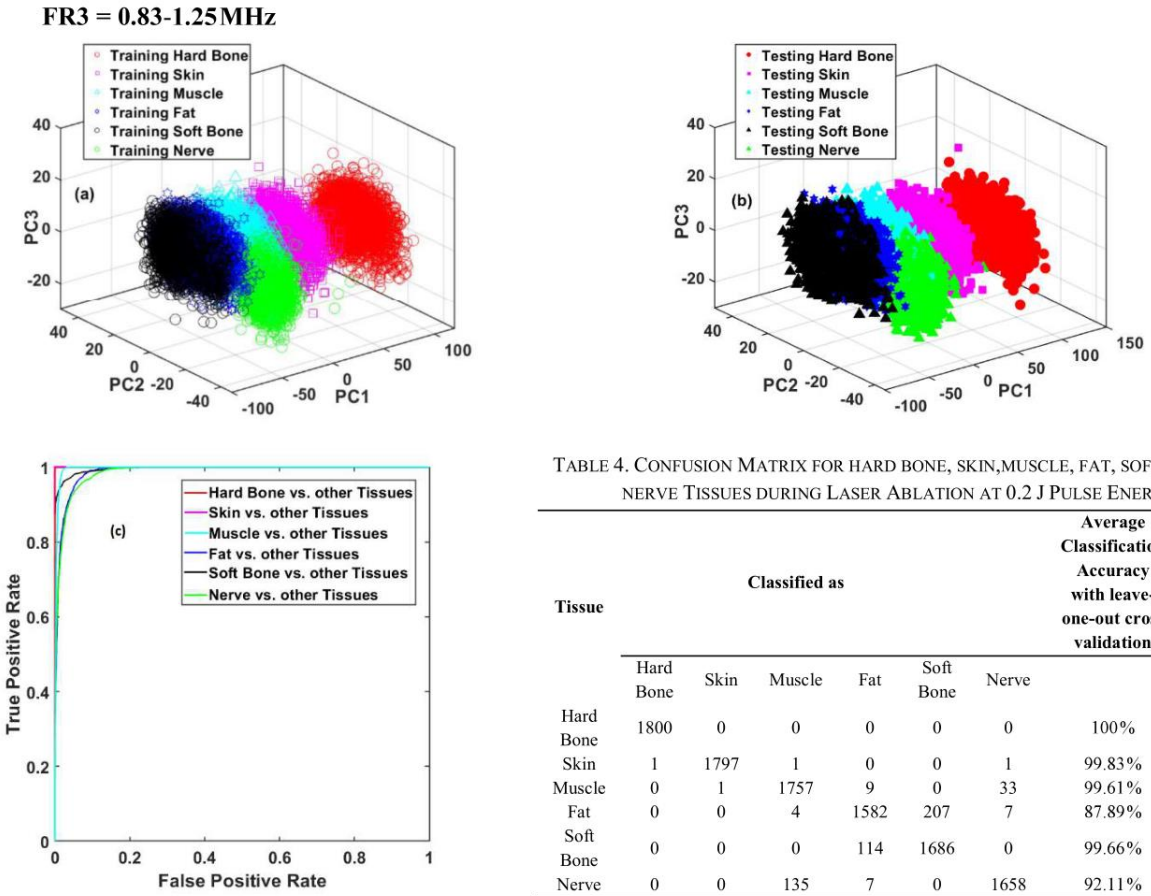

TABLE 4. CONFUSION MATRIX FOR HARD BONE, SKIN,MUSCLE, FAT, SOFT BONE AND NERVE TISSUES DURING LASER ABLATION AT 0.2 J PULSE ENERGY.

Tissue	**Classified as**						**Average Classification Accuracy with leave-one-out cross validation**	**Area Under ROC Curve**
	Hard Bone	Skin	Muscle	Fat	Soft Bone	Nerve		
Hard Bone	1800	0	0	0	0	0	100%	100%
Skin	1	1797	1	0	0	1	99.83%	100%
Muscle	0	1	1757	9	0	33	99.61%	99.95%
Fat	0	0	4	1582	207	7	87.89%	98.68%
Soft Bone	0	0	0	114	1686	0	99.66%	98.85%
Nerve	0	0	135	7	0	1658	92.11%	99.67%

Figure 7. First three PC scores from the training (a) and testing (b) data for hard and soft bone, muscle, fat and skin (FR3 = 0.83-1.25 MHz). Receiver operating characteristic curve (c) to multi-class using the ANN models combined with the ns-Nd:YAG laser. Note: The curve of Hard Bone-,Skin-, Muscle- and Nerve-tissues vs. other tissues overlaps. The confusion matrix of tissue types (Table 4).

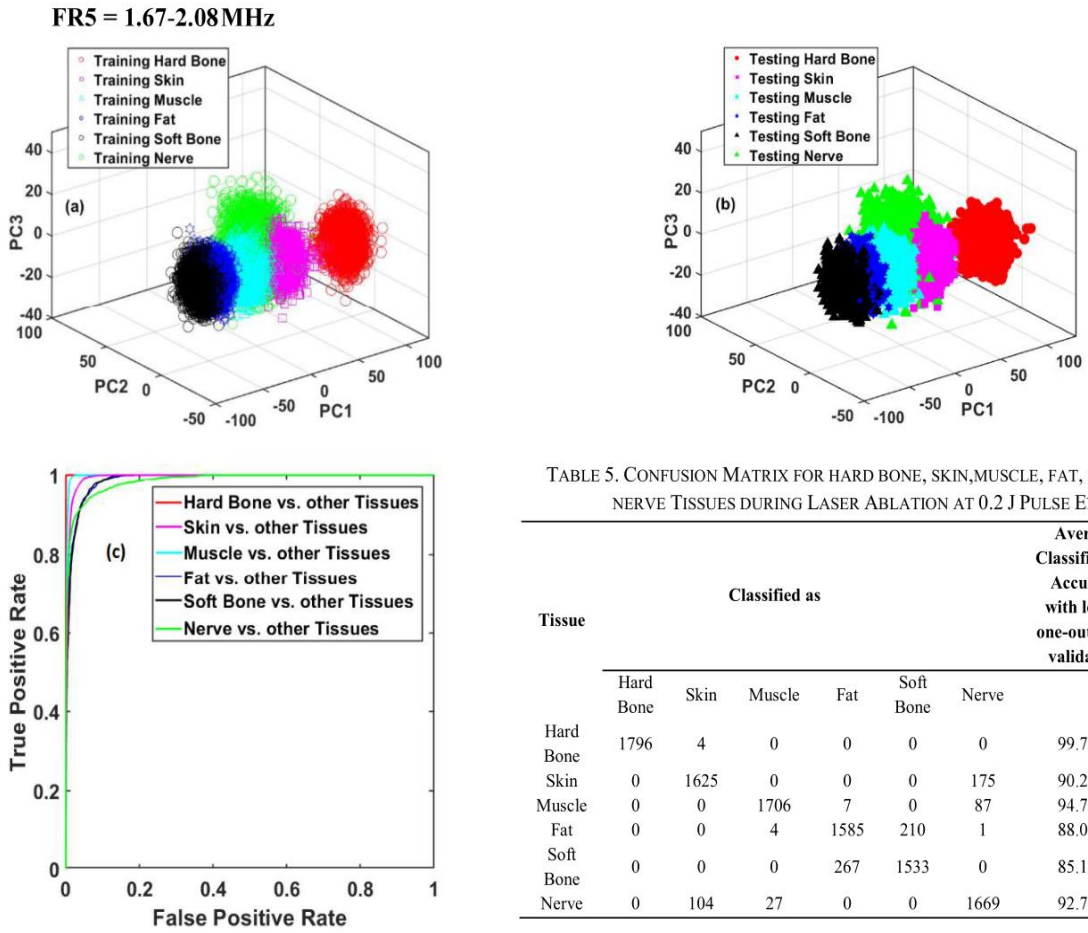

TABLE 5. CONFUSION MATRIX FOR HARD BONE, SKIN,MUSCLE, FAT, SOFT BONE AND NERVE TISSUES DURING LASER ABLATION AT 0.2 J PULSE ENERGY.

Tissue	Classified as						Average Classification Accuracy with leave-one-out cross validation	Area Under ROC Curve
	Hard Bone	Skin	Muscle	Fat	Soft Bone	Nerve		
Hard Bone	1796	4	0	0	0	0	99.78%	100%
Skin	0	1625	0	0	0	175	90.28%	99.44%
Muscle	0	0	1706	7	0	87	94.78%	99.80%
Fat	0	0	4	1585	210	1	88.06%	98.84%
Soft Bone	0	0	0	267	1533	0	85.17%	98.92%
Nerve	0	104	27	0	0	1669	92.72%	98.66%

Figure 8. First three PC scores from the training (a) and testing (b) data for hard bone, soft bone, muscle, fat, skin, and nerve (FR5 = 1.67-2.08 MHz). Receiver operating characteristic curve (c) to multi-class using the ANN models combined with the ns-Nd:YAG laser. Note: The curve of Hard Bone-,Skin-, Muscle- and Nerve-tissues vs. other tissues overlaps. The confusion matrix of tissue types (Table 5).

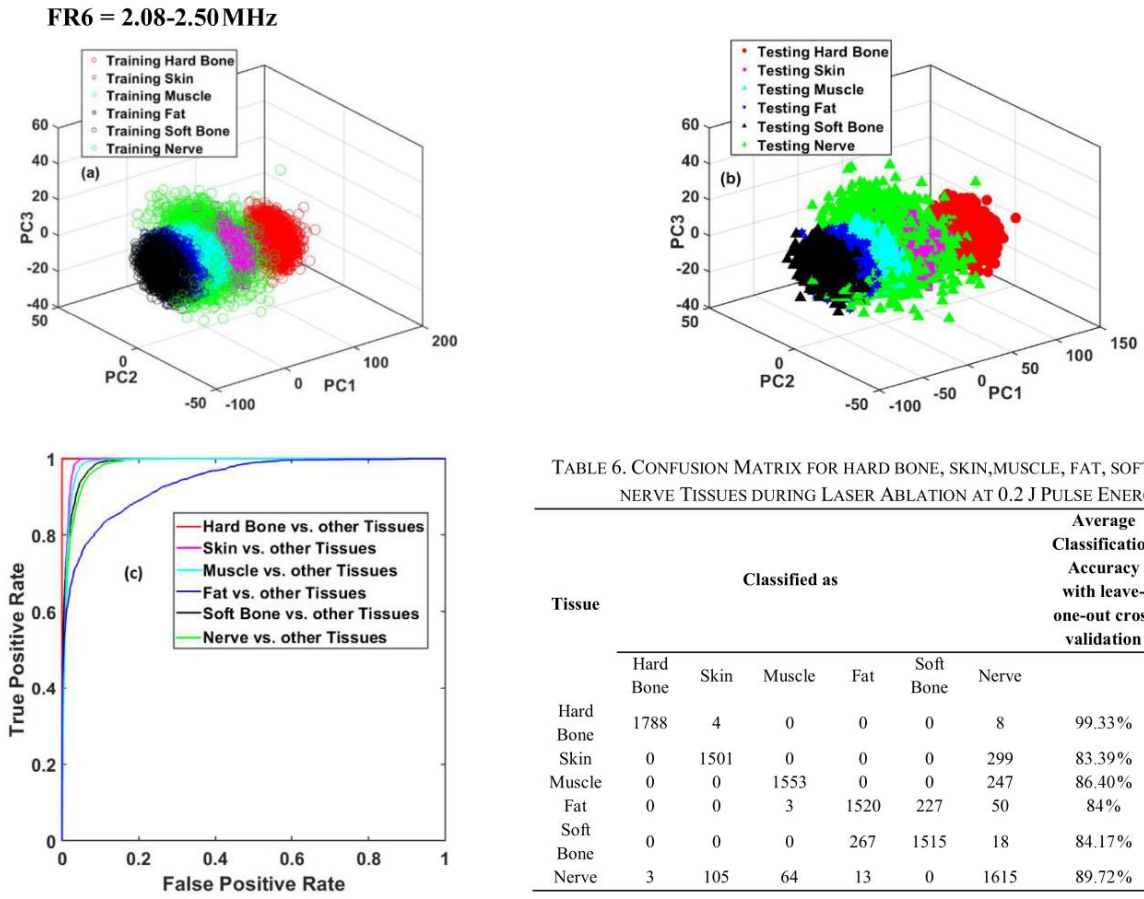

TABLE 6. CONFUSION MATRIX FOR HARD BONE, SKIN,MUSCLE, FAT, SOFT BONE AND NERVE TISSUES DURING LASER ABLATION AT 0.2 J PULSE ENERGY.

Tissue	Classified as						Average Classification Accuracy with leave-one-out cross validation	Area Under ROC Curve
	Hard Bone	Skin	Muscle	Fat	Soft Bone	Nerve		
Hard Bone	1788	4	0	0	0	8	99.33%	100%
Skin	0	1501	0	0	0	299	83.39%	99.41%
Muscle	0	0	1553	0	0	247	86.40%	99.16%
Fat	0	0	3	1520	227	50	84%	98.35%
Soft Bone	0	0	0	267	1515	18	84.17%	98.78%
Nerve	3	105	64	13	0	1615	89.72%	98.53%

Figure 9. First three PC scores from the training (a) and testing (b) data for hard bone, soft bone, muscle, fat, skin, and nerve (FR6 = 2.08 -2.50 MHz). Receiver operating characteristic curve (c) to multi-class using the ANN models combined with the ns-Nd:YAG laser. Note: The curve of Hard Bone-,Skin-, Muscle- and Nerve-tissues vs. other tissues overlaps. The confusion matrix of tissue types (Table 6).

7. ACKNOWLEDGEMENT

This work is part of the MIRACLE (Minimally Invasive Robot-Assisted Computer-guided LaserosteotomE) project, funded by the Werner Siemens Foundation.

8. REFERENCE

[1] J. J. Kuttenberger *et al.*, "Computer-guided CO2-laser osteotomy of the sheep tibia: technical prerequisites and first results," *Photomedicine and laser surgery,* vol. 26, no. 2, pp. 129-136, 2008.

[2] S. Stopp, ast, D. Svejdar, E. v. Kienlin, H. Deppe, and T. C. Lueth, "A New Approach for Creating Defined Geometries by Navigated Laser Ablation Based on Volumetric 3-D Data," *IEEE Transactions on Biomedical Engineering,* vol. 55, no. 7, pp. 1872-1880, 2008, doi: 10.1109/TBME.2008.919737.

[3] F. Stelzle *et al.*, "Optical Nerve Detection by Diffuse Reflectance Spectroscopy for Feedback Controlled Oral and Maxillofacial Laser Surgery," *Journal of Translational Medicine,* vol. 9, no. 1, p. 20, 2011/02/10 2011, doi: 10.1186/1479-5876-9-20.

[4] G. Baxter, D. Walsh, J. Allen, A. Lowe, and A. Bell, "Effects of low intensity infrared laser irradiation upon conduction in the human median nerve in vivo," *Experimental Physiology,* vol. 79, no. 2, pp. 227-234, 1994, doi: 10.1113/expphysiol.1994.sp003755.

[5] J.-P. Valat, S. Genevay, M. Marty, S. Rozenberg, and B. Koes, "Sciatica," *Best Practice & Research Clinical Rheumatology,* vol. 24, no. 2, pp. 241-252, 2010/04/01/ 2010, doi: https://doi.org/10.1016/j.berh.2009.11.005.

[6] H. R. Jones, C. Darryl, and B. T. Darras, *Neuromuscular disorders of infancy, childhood, and adolescence: a clinician's approach*. Butterworth-Heinemann, 2003.

[7] T. Menovsky, M. van den Bergh Weerman, and J. F. Beek, "Effect of CO2 milliwatt laser on peripheral nerves: Part I. A dose-response study," *Microsurgery,* vol. 17, no. 10, pp. 562-567, 1996, doi: 10.1002/(sici)1098-2752(1996)17:10<562::Aid-micr6>3.0.Co;2-s.

[8] M. M. Inserra, D. A. Bloch, and D. J. Terris, "Functional indices for sciatic, peroneal, and posterior tibial nerve lesions in the mouse," *Microsurgery: Official Journal of the International Microsurgical Society and the European Federation of Societies for Microsurgery,* vol. 18, no. 2, pp. 119-124, 1998.

[9] F. L. Burkhart and J. W. Daly, "Sciatic and peroneal nerve injury: a complication of vaginal operations," *Obstetrics & Gynecology,* vol. 28, no. 1, pp. 99-102, 1966.

[10] J. Abitbol, D. Gendron, C. Laurin, and M. Beaulieu, "Gluteal nerve damage following total hip arthroplasty: a prospective analysis," *The Journal of arthroplasty,* vol. 5, no. 4, pp. 319-322, 1990.

[11] N. Garcia-Losarcos, M. Gonzalez-Hidalgo, C. Franco-Carcedo, and J. Poch-Broto, "[Electrical stimulation of the facial nerve with a prognostic function in parotid surgery]," (in spa), *Rev Neurol,* vol. 49, no. 3, pp. 119-22, Aug 1-15 2009. Estimulacion electrica del nervio facial con funcion pronostica en la cirugia de parotida.

[12] H. N. Kenhagho, G. Rauter, R. Guzman, P. C. Cattin, and A. Zam, "Comparison of acoustic shock waves generated by micro and nanosecond lasers for a smart laser surgery system," in *SPIE BiOS*, 2018, vol. 10484: SPIE, p. 9.

[13] H. K. Nguendon *et al.*, "Characterization of ablated porcine bone and muscle using laser-induced acoustic wave method for tissue differentiation," in *European Conference on Biomedical Optics*, 2017: Optical Society of America, p. 104170N.

[14] H.-P. F. Brecht, R. Su, M. P. Fronheiser, S. A. Ermilov, A. Conjusteau, and A. A. Oraevsky, "Whole-body three-dimensional optoacoustic tomography system for small animals," *Journal of Biomedical Optics,* vol. 14, no. 6, pp. 1-8, 8, 2009. [Online]. Available: https://doi.org/10.1117/1.3259361.

[15] T. F. Fehm, X. L. Deán-Ben, and D. Razansky, "Four dimensional hybrid ultrasound and optoacoustic imaging via passive element optical excitation in a hand-held probe," *Applied Physics Letters,* vol. 105, no. 17, p. 173505, 2014.

[16] H. N. Kenhagho, G. Rauter, R. Guzman, P. Cattin, and A. Zam, "Optoacoustic Tissue Differentiation using a Mach-Zehnder Interferometer," *IEEE Transactions on Ultrasonics, Ferroelectrics, and Frequency Control,* pp. 1-1, 2019, doi: 10.1109/TUFFC.2019.2923696.

[17] H. N. Kenhagho *et al.*, "Optoacoustic Tissue Classification for Laser Osteotomes Using Mahalanobis Distance-based Method," in *In: Rauter G., Cattin P.C., Zam A., Riener R., Carbone G., Pisla D. (eds) New Trends in Medical and Service Robotics. MESROB 2020. Mechanisms and Machine Science*, 2021, vol. 93: Springer, Cham, 2020, pp. 2002-2010, doi: https://doi.org/10.1007/978-3-030-58104-6_23.

[18] H. Nguendon Kenhagho *et al.*, "Characterization of Ablated Bone and Muscle for Long-Pulsed Laser Ablation in Dry and Wet Conditions," *Materials,* vol. 12, no. 8, p. 1338, 2019. [Online]. Available: http://www.mdpi.com/1996-1944/12/8/1338.

[19] P. Yuldashev, M. Karzova, V. Khokhlova, S. Ollivier, and P. Blanc-Benon, "Mach-Zehnder interferometry method for acoustic shock wave measurements in air and broadband calibration of microphones," *The Journal of the Acoustical Society of America,* vol. 137, no. 6, pp. 3314-3324, 2015, doi: doi:http://dx.doi.org/10.1121/1.4921549.

[20] H. N. Kenhagho, F. Canbaz, G. Rauter, R. Guzman, P. Cattin, and A. Zam, "A First Approach to Miniaturized Optoacoustic Feedback Sensor for Smart Laser Osteotome : Fiber-Coupled Fabry-Pérot Etalon Sensor," in *2019 IEEE SENSORS*, 27-30 Oct. 2019 2019, pp. 1-4, doi: 10.1109/SENSORS43011.2019.8956743.

[21] H. N. Kenhagho, F. Canbaz, R. Guzman, P. Cattin, and A. Zam, "Miniaturized Optoacoustic Feedback Sensor for Smart Laser Osteotome: Fiber-Coupled Fabry-Pérot Etalon Sensor," *Sensors and Actuators A: Physical,* p. 112394, 2020/11/26/ 2020, doi: https://doi.org/10.1016/j.sna.2020.112394.

[22] R. N. Oosterbeek, T. Ward, S. Ashforth, O. Bodley, A. E. Rodda, and M. C. Simpson, "Fast femtosecond laser ablation for efficient cutting of sintered alumina substrates," *Optics and Lasers in Engineering,* vol. 84, pp. 105-110, 2016/09/01/ 2016, doi: https://doi.org/10.1016/j.optlaseng.2016.04.007.

[23] S. A. Ashforth, M. C. Simpson, O. Bodley, and R. Oosterbeek, *Ultrashort pulse laser interactions with cortical bone tissue for applications in orthopaedic surgery* (SPIE LASE). SPIE, 2015.

[24] C.-A. Tulea, J. Caron, N. Gehlich, A. Lenenbach, R. Noll, and P. Loosen, "Laser cutting of bone tissue under bulk water with a pulsed ps-laser at 532 nm," 2015, vol. 20: SPIE, p. 9.

[25] J. Lever, M. Krzywinski, and N. Altman, "Principal component analysis," *Nature Methods,* vol. 14, p. 641, 06/29/online 2017, doi: 10.1038/nmeth.4346.

[26] M. Curzon and J. Featherstone, "Chemical composition of enamel," in *Handbook of Experimental Aspects of Oral Biochemistry, EP Lazzan, ed*, ed. Boca Raton, Florida: CRC Press, 1983, pp. 123-135.

[27] C. Apel, J. Meister, R. Ioana, R. Franzen, P. Hering, and N. Gutknecht, "The ablation threshold of Er: YAG and Er: YSGG laser radiation in dental enamel," *Lasers in medical science,* vol. 17, no. 4, pp. 246-252, 2002.

[28] H. N. Kenhagho, G. Rauter, R. Guzman, P. Cattin, and A. Zam, "Optoacoustic Tissue Differentiation Using a Mach-Zehnder Interferometer: Preliminary Results," in *2018 IEEE International Ultrasonics Symposium (IUS)*, 22-25 Oct. 2018 2018, pp. 1-9, doi: 10.1109/ULTSYM.2018.8579654.

[29] L. Kuscer and J. Diaci, "Measurements of erbium laser-ablation efficiency in hard dental tissues under different water cooling conditions," 2013, vol. 18: SPIE, p. 11.

[30] E. Manikanta, L. Vinoth Kumar, P. Venkateshwarlu, C. Leela, and P. P. Kiran, "Effect of pulse duration on the acoustic frequency emissions during the laser-induced breakdown of atmospheric air," *Appl. Opt.,* vol. 55, no. 3, pp. 548-555, 2016/01/20 2016, doi: 10.1364/AO.55.000548.

Author Biographies

Hervé Nguendon Kenhagho received the BEng (Hons) in Communication and Electronic Engineering from Northumbria University, England, in 2009, and the MSc. degree in Microelectronic and Communication Engineering from the same university, in 2010. He has also received a professional certificate as a Laser Safety Officer from the Universität des Saarlandes, Germany, in 2016. After a calibration engineer position at the Repair & Cal Ltd, England, and research engineer positions at University of Lunebürg, University Carlos Tercero de Madrid, he joined the Department of Biomedical Engineering at the University of Basel as a researcher associated with the PhD candidature, in 2016. His PhD work is in the Biomedical Laser and Optics Group (BLOG) at the Department of Biomedical Engineering at the University of Basel, Switzerland. His main research interests focus on the development of smart devices and miniaturized systems for various applications.

Ferda Canbaz is a postdoctoral researcher in the Department of Biomedical Engineering at University of Basel. She received the B.S. degree in engineering physics from Istanbul Technical University, Istanbul, Turkey, in 2011. She received the M.S. degree in optoelectronics and photonics engineering in 2013 and the PhD degree in physics in 2018 from Koç University, Istanbul, Turkey. Her research interests include mid-infrared solid-state/fiber lasers, ultrafast optics, photoacoustic diagnosis and smart laser surgery.

Raphael Guzman is currently a Professor of neurosurgery and the Vice Chairman of the Department of Neurosurgery, University Hospital of Basel, Basel, Switzerland, and the University Children's Hospital of Basel (UKBB), Basel. His clinical expertise is in pediatric and cerebrovascular neurosurgery. His research group examines the clinical relevance of neural stem/progenitor cells (NPC) in brain ischemia and particularly in neonatal hypoxic-ischemia (HI) with regard to white matter regeneration. Neonatal HI is an important cause of cerebral palsy (CP), leading to devastating sensory-motor, cognitive, and learning deficits in the growing child. White matter injury is a central feature of HI and CP, and defects in myelination are also commonly identified in other neurodevelopmental disorders, including autism spectrum disorders (ASD). White matter myelination generally reflects the progression of functional brain maturation and connectivity in the first years of life and molecular and cellular crosstalk between NPCs and resident brain cells, particularly myelinating oligodendrocytes, *in vitro* and in a rodent model of neonatal HI. He is also deeply involved in advancing novel technologies such as virtual and augmented reality and minimally invasive endoscopy to advance neurosurgical teaching and operative techniques in collaboration with the Department of Bioengineering. His research is funded through the Swiss National Science Foundation and several grants from private foundations as well as industry collaborations. He has authored over 200 peer-reviewed articles, book chapters, and scientific meeting proceedings.

Philippe Cattin was born in Switzerland in 1967. He received his B.Sc. degree from the University of Applied Science in Brugg/Windisch in 1991. In 1995 he received the M.Sc. degree in computer science and in 2003 the Ph.D. degree in robotics from ETH Zurich, Switzerland. From 2003 to 2007 he was a Postdoctoral Fellow with the Computer Vision Laboratory at ETH Zurich. In 2007 he became an Assistant Professor at the University of Basel and was promoted to Associate Professor in 2015 and to Full Professor in 2019. He is the founder of the Center for medical Image Analysis and Navigation (CIAN) at the Medical Faculty of the University of Basel. He is the founding head and still heading the Department of Biomedical Engineering at the University of Basel. Philippe was in 2017 a Research Fellow at the Brigham and Women's Hospital in Boston/MA. His research interests include medical image analysis, image-guided therapy, robotics-guided laser osteotomy and virtual reality. As a Principal Investigator, he has finished many projects in these areas and published over 250 papers, patents and book chapters. He is also the founder of two spin-off companies and licensed his patents and software to medical device companies.

Azhar Zam received the B.Sc. degree in medical physics from the University of Indonesia, Depok, Indonesia, in 2004, the M.Sc. degree in biomedical engineering from the University of Lübeck, Lübeck, Germany, in 2007, and the Ph.D. degree in advanced optical technologies from the Friedrich-Alexander University Erlangen–Nuremberg, Germany, with the focus on optical feedback for tissue-specific laser surgery, in 2011. He held various research positions at the University of Waterloo, Canada, the National University of Ireland Galway, Ireland, the University of California at Davis, USA and Ryerson University, Toronto, Canada. He joined the Department of Biomedical Engineering, University of Basel, Switzerland, in 2016, as an Assistant Professor, where he founded and leads the Biomedical Laser and Optics Group (BLOG). He has authored over 60 peer-reviewed articles, book chapters, books, and patents. His main research interests focus on the development of smart devices for medical therapy, diagnostics and monitoring using novel optical technologies, including smart laser surgery, optical coherence tomography (OCT), photoacoustics, biomedical spectroscopy, AI-aided optical diagnostics and imaging, optical-based smart wearable sensors and miniaturized systems.

Chapter 7

Discussion and Conclusions

7.1. Discussion

This work aimed to develop an optoacoustical feedback system to fit into an endoscope and to design an efficient optical detection method of ASWs for tissue classification in smart laser surgery. The novelty of this Ph.D. research was measuring the generated ASWs using advanced optical technologies and extracting important features for tissue classification. To achieve this goal, ASWs were characterized for hard and soft bone, muscle, fat, and skin from five, fresh proximal and distal porcine femurs during laser ablation [15].

In a first approach (Chapter 3), an optoacoustic system was developed and ASWs were collected using standard ACT. Following that, an appropriate algorithm for classifying tissues based on the ASWs measured was identified and implemented. It was found that PCA combined with an ANN performed best, compared to the Mahalanobis distance and support vector machine-based method. This method (PCA+ANN), however, suffers from higher classification error due to the limited bandwidth of commercially available microphone transducers (typically less than 1MHz) [19].

In the second approach (Chapter 4), the sensitivity of ASW-based classification was enhanced by developing a custom-made, free-space Mach-Zehnder interferometric sensor. The results of this optical method achieved bandwidths up to 2.5 MHz, making it very sensitive to abrupt changes in pressure [4, 25]. The results also demonstrated that Mach-Zehnder interferometer-based optoacoustic measurement, combined with Mahalanobis distances, produced fewer errors than when ASWs were measured by ACT. In other words, optical methods performed better than standard ACTs for measuring ASWs.

Miniaturization of the ASW feedback sensor is also essential so that it can fit into the endoscope currently being developed by our collaborators [92-94]. Early iterations of the feedback system were designed with a microphone and Mach-Zehnder interferometer in free space and were bulky [15, 24, 25]. Therefore, the final aim was to develop a compact optoacoustic feedback sensor capable of classifying tissues during laser osteotomy. The compact sensor was meant to have at least the same usable bandwidth of the previous sensor design [4]. Therefore, in the third approach (Chapter 5), we built the first prototype of a miniaturized optoacoustic system using fiber optics. Currently, the cavity of the custom-made, fiber-coupled Fabry-Pérot etalon sensor can fit into a 5 mm×5 mm endoscopic robot for minimally invasive smart laser surgery. It should be noted that the bandwidth (frequency response) of the optical sensor was up to 4.5 MHz (higher than the one in free space). The corresponding directivity response measured showed that the polar plot presented a relatively flat directional response over a 360º angle. Furthermore, tissue classifications using the ANN-based method showed comparative performance when collecting ASWs with both optical methods. Therefore, optical methods are a promising technique for simultaneously differentiating tissue types.

The feedback detection method proposed here has been designed and customized to classify tissues extracted from femurs. However, it is possible to train the system to differentiate tissues from other body parts, such as skull, lungs and other nerves. Chapter 6 gives evidence of this possibility, where sciatic nerve tissue was classified against other tissue types, using laser-generated ASWs.

7.2. Further Research

Despite indicating that the method is already well-suited for application in laser surgery, there are still numerous opportunities for enhancing it. For example, it is likely possible to make the optoacoustic sensor system fully automatic. Similarly, the set of data from the ASWs measured by the custom-made miniaturized sensor could be used to train the ANN for automatic tissue classification. To classify the measured data in real-time, machine learning combined with parallel computing, such as CUDA, could be explored.

Furthermore, incision depth was monitored and reported during laser ablation using ACT [18, 21]. Collecting data with the optical sensor for depth control could be one area for research. Incision depth could be useful, complementary information for the feedback mechanism and, therefore, could be integrated into the current feedback system to simultaneously classify the ablated tissue and monitor incision depth in real time. This research has already been started by another member of the same project and can be understood as a prolongation of the current work [95]. Additionally, during laser ablation, carbonization can occur on the surface of the ablated tissue; to avoid it, feedback to classify normal from carbonized bone tissue is desirable. Last but not least, in real scenarios, tissues are connected to each other, therefore, transitioning between two tissues types (i.e. hard and soft bone) should be investigated.

7.3. Conclusion

Based on the results of the hardware and software developed, it is very likely that this method can be used in laser surgery applications. When comparing the accomplishments of this work to the goals of the Ph.D. thesis, indeed, a method was found to successfully ablate and classify tissues in *ex-vivo* experiments. Nevertheless, it is not yet possible to implement the method in real time, even though the computational time has already been considerably enhanced across publications. Instead, the practicability of the method was proved in *ex-vivo* experiments. To make the proposed approaches accessible to the scientific community, unused results will continue to be published in high impact scientific journals.

Bibliography

[1] Z. Alperovich, G. Yamin, E. Elul, G. Bialolenker, and A. A. Ishaaya, "In situ tissue classification during laser ablation using acoustic signals," *Journal of biophotonics*, p. e201800405, 2019.

[2] H. N. Kenhagho *et al.*, "Optoacoustic Tissue Classification for Laser Osteotomes Using Mahalanobis Distance-based Method," in *In: Rauter G., Cattin P.C., Zam A., Riener R., Carbone G., Pisla D. (eds) New Trends in Medical and Service Robotics. MESROB 2020. Mechanisms and Machine Science*, 2021, vol. 93: Springer, Cham, 2020, pp. 2002-2010, doi: https://doi.org/10.1007/978-3-030-58104-6_23.

[3] H. Nguendon Kenhagho, F. Canbaz, T. E. Gomez Alvarez-Arenas, R. Guzman, P. Cattin, and A. Zam, "Machine Learning-Based Optoacoustic Tissue Classification Method for Laser Osteotomes Using an Air-Coupled Transducer," *Lasers in Surgery and Medicine*, vol. n/a, no. n/a, doi: 10.1002/lsm.23290.

[4] H. N. Kenhagho, G. Rauter, R. Guzman, P. Cattin, and A. Zam, "Optoacoustic Tissue Differentiation using a Mach-Zehnder Interferometer," *IEEE Transactions on Ultrasonics, Ferroelectrics, and Frequency Control*, pp. 1-1, 2019, doi: 10.1109/TUFFC.2019.2923696.

[5] H. N. Kenhagho, F. Canbaz, R. Guzman, P. Cattin, and A. Zam, "Miniaturized Optoacoustic Feedback Sensor for Smart Laser Osteotome: Fiber-Coupled Fabry-Pérot Etalon Sensor," *Submitted to IEEE Sensors Journal*, pp. 1-14, 2020.

[6] D. Gabrić, I. Bago, S. Music, K. Molcanov, M. Sušić, and I. Anić, "Morphological and Ultrastructural Comparative Analysis of Bone Tissue After Er: YAG Laser and Surgical Drill Osteotomy," *Photomedicine and laser surgery*, vol. 32, pp. 401-8, 07/01 2014, doi: 10.1089/pho.2014.3711.

[7] D. D. Lo *et al.*, "Femtosecond plasma mediated laser ablation has advantages over mechanical osteotomy of cranial bone," *Lasers in Surgery and Medicine*, vol. 44, no. 10, pp. 805-814, 2012, doi: 10.1002/lsm.22098.

[8] K. w. Baek *et al.*, "A comparative investigation of bone surface after cutting with mechanical tools and Er: YAG laser," *Lasers in surgery and medicine*, vol. 47, no. 5, pp. 426-432, 2015.

[9] N. Jowett *et al.*, "Bone ablation without thermal or acoustic mechanical injury via a novel picosecond infrared laser (PIRL)," *Otolaryngology--Head and Neck Surgery*, vol. 150, no. 3, pp. 385-393, 2014.

[10] G. M. Peavy, L. Reinisch, J. T. Payne, and V. Venugopalan, "Comparison of cortical bone ablations by using infrared laser wavelengths 2.9 to 9.2 μm," *Lasers in surgery and medicine*, vol. 25, no. 5, pp. 421-434, 1999.

[11] J. T. Walsh Jr and T. F. Deutsch, "Er: YAG laser ablation of tissue: measurement of ablation rates," *Lasers in surgery and medicine*, vol. 9, no. 4, pp. 327-337, 1989.

[12] L. Kuscer and J. Diaci, "Measurements of erbium laser-ablation efficiency in hard dental tissues under different water cooling conditions," 2013, vol. 18: SPIE, p. 11.

[13] R. Fekrazad, K. Kalhori, F. Ahrari, and T. Nikoo, "Laser in Orthodontics," 2011.

[14] C.-A. Tulea, J. Caron, N. Gehlich, A. Lenenbach, R. Noll, and P. Loosen, "Laser cutting of bone tissue under bulk water with a pulsed ps-laser at 532 nm," 2015, vol. 20: SPIE, p. 9.

[15] H. N. Kenhagho, G. Rauter, R. Guzman, P. C. Cattin, and A. Zam, "Comparison of acoustic shock waves generated by micro and nanosecond lasers for a smart laser surgery system," in *SPIE BiOS*, 2018, vol. 10484: SPIE, p. 9.

[16] K. Chaudhary, S. Z. H. Rizvi, and J. Ali, *Laser-Induced Plasma and its Applications* (Plasma Science and Technology - Progress in Physical States and Chemical Reactions). 2016.

[17] M. Boustie, T. Berthe, T. De Rességuier, and M. Arrigoni, "Laser Shock Waves: Fundamentals and Applications," presented at the 1st international symposium on Laser Ultrasonics, Montreal, France, 2008-07-16, 2008. [Online]. Available: https://hal.archives-ouvertes.fr/hal-00347927.

[18] F. J. O. Landa, X. L. Deán-Ben, F. Montero de Espinosa, and D. Razansky, "Noncontact monitoring of incision depth in laser surgery with air-coupled ultrasound transducers," *Optics Letters*, vol. 41, no. 12, pp. 2704-2707, 2016/06/15 2016, doi: 10.1364/OL.41.002704.

[19] P. Yuldashev, M. Karzova, V. Khokhlova, S. Ollivier, and P. Blanc-Benon, "Mach-Zehnder interferometry method for acoustic shock wave measurements in air and broadband calibration of microphones," *The Journal of the Acoustical Society of America*, vol. 137, no. 6, pp. 3314-3324, 2015, doi: doi:http://dx.doi.org/10.1121/1.4921549.

[20] S. Horowitz, T. Nishida, L. Cattafesta, and M. Sheplak, "Development of a micromachined piezoelectric microphone for aeroacoustics applications," *The Journal of the Acoustical Society of America*, vol. 122, no. 6, pp. 3428-3436, 2007, doi: doi:http://dx.doi.org/10.1121/1.2785040.

[21] E. Bay, X. L. Deán-Ben, G. A. Pang, A. Douplik, and D. Razansky, "Real-time monitoring of incision profile during laser surgery using shock wave detection," *Journal of Biophotonics*, vol. 8, no. 1-2, pp. 102-111, 2015, doi: 10.1002/jbio.201300151.

[22] Koichi Mizutani, Tomohiro Ezure, Keinosuke Nagai, and Masahiro Yoshioka, "Optical Measurement of Sound Fields Information Using Mach-Zehnder Interferometer," *Japanese Journal of Applied Physics*, vol. 40, no. 5S, p. 3617, 2001. [Online]. Available: http://stacks.iop.org/1347-4065/40/i=5S/a=3617.

[23] N. Bilaniuk, "Optical microphone transduction techniques," *Applied Acoustics*, vol. 50, no. 1, pp. 35-63, 1997/01/01 1997, doi: http://dx.doi.org/10.1016/S0003-682X(96)00034-5.

[24] H. Nguendon Kenhagho *et al.*, "Characterization of Ablated Bone and Muscle for Long-Pulsed Laser Ablation in Dry and Wet Conditions," *Materials*, vol. 12, no. 8, p. 1338, 2019. [Online]. Available: http://www.mdpi.com/1996-1944/12/8/1338.

[25] H. N. Kenhagho, G. Rauter, R. Guzman, P. Cattin, and A. Zam, "Optoacoustic Tissue Differentiation Using a Mach-Zehnder Interferometer: Preliminary Results," in *2018 IEEE International Ultrasonics Symposium (IUS)*, 22-25 Oct. 2018 2018, pp. 1-9, doi: 10.1109/ULTSYM.2018.8579654.

[26] R. Florencio-Silva, G. R. d. S. Sasso, E. Sasso-Cerri, M. J. Simões, and P. S. Cerri, "Biology of bone tissue: structure, function, and factors that influence bone cells," *BioMed research international*, vol. 2015, 2015.

[27] W. D. Comper and T. C. Laurent, "Physiological function of connective tissue polysaccharides," *Physiological reviews*, vol. 58, no. 1, pp. 255-315, 1978.

[28] D. G. Moerman and A. Fire, "16 Muscle: Structure, Function, and Development," *Cold Spring Harbor Monograph Archive*, vol. 33, pp. 417-470, 1997.

[29] F. Stelzle *et al.*, "Optical Nerve Detection by Diffuse Reflectance Spectroscopy for Feedback Controlled Oral and Maxillofacial Laser Surgery," *Journal of Translational Medicine*, vol. 9, no. 1, p. 20, 2011/02/10 2011, doi: 10.1186/1479-5876-9-20.

[30] G. Baxter, D. Walsh, J. Allen, A. Lowe, and A. Bell, "Effects of low intensity infrared laser irradiation upon conduction in the human median nerve in vivo," *Experimental Physiology*, vol. 79, no. 2, pp. 227-234, 1994, doi: 10.1113/expphysiol.1994.sp003755.
[31] J.-P. Valat, S. Genevay, M. Marty, S. Rozenberg, and B. Koes, "Sciatica," *Best Practice & Research Clinical Rheumatology*, vol. 24, no. 2, pp. 241-252, 2010/04/01/ 2010, doi: https://doi.org/10.1016/j.berh.2009.11.005.
[32] H. R. Jones, C. Darryl, and B. T. Darras, *Neuromuscular disorders of infancy, childhood, and adolescence: a clinician's approach*. Butterworth-Heinemann, 2003.
[33] J. Abitbol, D. Gendron, C. Laurin, and M. Beaulieu, "Gluteal nerve damage following total hip arthroplasty: a prospective analysis," *The Journal of arthroplasty*, vol. 5, no. 4, pp. 319-322, 1990.
[34] L. Beltrán, H. Abbasi, G. Rauter, N. Friederich, P. Cattin, and A. Zam, "Effect of laser pulse duration on ablation efficiency of hard bone in microseconds regime," in *Third International Conference on Applications of Optics and Photonics*, 2017, vol. 10453: International Society for Optics and Photonics, p. 104531S.
[35] H. Abbasi, L. Beltrán, G. Rauter, R. Guzman, P. C. Cattin, and A. Zam, "Effect of cooling water on ablation in Er: YAG laserosteotome of hard bone," in *Third International Conference on Applications of Optics and Photonics*, 2017, vol. 10453: International Society for Optics and Photonics, p. 104531I.
[36] U. Romeo, A. Del Vecchio, G. Palata, G. Tenore, P. Visca, and C. Maggiore, "Bone damage induced by different cutting instruments: an in vitro study," *Brazilian Dental Journal*, vol. 20, pp. 162-168, 2009. [Online]. Available: http://www.scielo.br/scielo.php?script=sci_arttext&pid=S0103-64402009000200013&nrm=iso.
[37] A. H. Rawicz, "Theodore Harold Maiman and the invention of laser," in *Photonics, Devices, and Systems IV*, 2008, vol. 7138: International Society for Optics and Photonics, p. 713802.
[38] K. Hyun Wook, L. Ho, C. Shaochen, and A. J. Welch, "Enhancement of bovine bone ablation assisted by a transparent liquid Layer on a target surface," *IEEE Journal of Quantum Electronics*, vol. 42, no. 7, pp. 633-642, 2006, doi: 10.1109/JQE.2006.875867.
[39] Z. Z. Li, L. Reinisch, and W. P. Van de Merwe, "Bone ablation with Er: YAG and CO2 laser: study of thermal and acoustic effects," *Lasers in surgery and medicine*, vol. 12, no. 1, pp. 79-85, 1992.
[40] A. Vogel and V. Venugopalan, "Mechanisms of pulsed laser ablation of biological tissues," *Chemical reviews*, vol. 103, no. 2, pp. 577-644, 2003.
[41] W. Bai, G. J. Diebold, C. M. Wynn, R. W. Haupt, and J. H. Doherty, "A numerical study of shock waves generated through laser ablation of explosives," *Journal of Applied Physics*, vol. 120, no. 19, p. 194903, 2016, doi: doi:http://dx.doi.org/10.1063/1.4967825.
[42] M. H. Niemz, *Laser-tissue interactions: fundamentals and applications*. Springer Science & Business Media, 2013.
[43] J.-L. Boulnois, "Photophysical Processes in Recent Medical Laser Developments: A Review," *Lasers Med Sci*, vol. 1, pp. 47-66, 08/01 1986, doi: 10.1007/BF02030737.
[44] R. O. Esenaliev, A. A. Oraevsky, V. S. Letokhov, A. A. Karabutov, and T. V. Malinsky, "Studies of acoustical and shock waves in the pulsed laser ablation of biotissue," *Lasers in surgery and medicine*, vol. 13, no. 4, pp. 470-484, 1993.
[45] K.-H. Leitz, B. Redlingshöfer, Y. Reg, A. Otto, and M. Schmidt, "Metal ablation with short and ultrashort laser pulses," *Physics Procedia*, vol. 12, pp. 230-238, 2011.

[46] H. K. Nguendon *et al.*, "Characterization of ablated porcine bone and muscle using laser-induced acoustic wave method for tissue differentiation," in *European Conference on Biomedical Optics*, 2017: Optical Society of America, p. 104170N.
[47] H.-P. F. Brecht, R. Su, M. P. Fronheiser, S. A. Ermilov, A. Conjusteau, and A. A. Oraevsky, "Whole-body three-dimensional optoacoustic tomography system for small animals," *Journal of Biomedical Optics*, vol. 14, no. 6, pp. 1-8, 8, 2009. [Online]. Available: https://doi.org/10.1117/1.3259361.
[48] T. F. Fehm, X. L. Deán-Ben, and D. Razansky, "Four dimensional hybrid ultrasound and optoacoustic imaging via passive element optical excitation in a hand-held probe," *Applied Physics Letters*, vol. 105, no. 17, p. 173505, 2014.
[49] S. Michau, P. Mauchamp, and R. Dufait, "Piezocomposite 30MHz linear array for medical imaging: design challenges and performances evaluation of a 128 elements array," in *IEEE Ultrasonics Symposium, 2004*, 2004, vol. 2: IEEE, pp. 898-901.
[50] P. Yuldashev, S. Ollivier, M. Averiyanov, O. Sapozhnikov, V. Khokhlova, and P. Blanc-Benon, "Nonlinear propagation of spark-generated N-waves in air: Modeling and measurements using acoustical and optical methods," *The Journal of the Acoustical Society of America*, vol. 128, no. 6, pp. 3321-3333, 2010, doi: doi:http://dx.doi.org/10.1121/1.3505106.
[51] G. Wissmeyer, D. Soliman, R. Shnaiderman, A. Rosenthal, and V. Ntziachristos, "All-optical optoacoustic microscope based on wideband pulse interferometry," *Optics Letters*, vol. 41, no. 9, pp. 1953-1956, 2016/05/01 2016, doi: 10.1364/OL.41.001953.
[52] A. Rosenthal, D. Razansky, and V. Ntziachristos, "High-sensitivity compact ultrasonic detector based on a pi-phase-shifted fiber Bragg grating," *Optics Letters*, vol. 36, no. 10, pp. 1833-1835, 2011/05/15 2011, doi: 10.1364/OL.36.001833.
[53] G. Hall, "Ultrasonic wave visualization as a teaching aid in non-destructive testing," *Ultrasonics*, vol. 15, no. 2, pp. 57-69, 1977/03/01/ 1977, doi: https://doi.org/10.1016/0041-624X(77)90066-X.
[54] A. Taruttis and V. Ntziachristos, "Advances in real-time multispectral optoacoustic imaging and its applications," *Nature photonics*, vol. 9, no. 4, p. 219, 2015.
[55] S. Preisser *et al.*, "All-optical highly sensitive akinetic sensor for ultrasound detection and photoacoustic imaging," *Biomed. Opt. Express*, vol. 7, no. 10, pp. 4171-4186, 2016/10/01 2016, doi: 10.1364/BOE.7.004171.
[56] M. M. Frocht, "Photoelasticity," 1941.
[57] W. Hauf and U. Grigull, "Optical methods in heat transfer," in *Advances in heat transfer*, vol. 6: Elsevier, 1970, pp. 133-366.
[58] X. Zhu, Z. Huang, G. Wang, W. Li, D. Zou, and C. Li, "Ultrasonic detection based on polarization-dependent optical reflection," *Optics letters*, vol. 42, no. 3, pp. 439-441, 2017.
[59] Z. Xiaoyi, H. Zhiyu, W. Guohe, L. Wenzhao, and L. Changhui, "Polarization-dependent optical reflection ultrasonic detection," in *Proc.SPIE*, 2017, vol. 10064, doi: 10.1117/12.2251079. [Online]. Available: https://doi.org/10.1117/12.2251079
[60] T. Wang *et al.*, "All-optical photoacoustic microscopy based on plasmonic detection of broadband ultrasound," *Applied Physics Letters*, vol. 107, no. 15, p. 153702, 2015.
[61] R. Nuster, G. Paltauf, and P. Burgholzer, "Comparison of surface plasmon resonance devices for acoustic wave detection in liquid," *Opt. Express*, vol. 15, no. 10, pp. 6087-6095, 2007.
[62] G. Hu *et al.*, "High-precision measurement of optical constants of ultra-thin coating using surface plasmon resonance spectroscopic ellipsometry in Otto-Bliokh configuration," *Opt. Express*, vol. 25, no. 12, pp. 13425-13434, 2017/06/12 2017, doi: 10.1364/OE.25.013425.

[63] G. Paltauf, H. Schmidt-Kloiber, K. Köstli, and M. Frenz, "Optical method for two-dimensional ultrasonic detection," *Applied Physics Letters*, vol. 75, no. 8, pp. 1048-1050, 1999.
[64] P. Hajireza, W. Shi, K. Bell, R. J. Paproski, and R. J. Zemp, "Non-interferometric photoacoustic remote sensing microscopy," *Light: Science & Applications*, vol. 6, no. 6, pp. e16278-e16278, 2017.
[65] S. M. Maswadi *et al.*, "All-optical optoacoustic microscopy based on probe beam deflection technique," *Photoacoustics*, vol. 4, no. 3, pp. 91-101, 2016.
[66] R. A. Barnes, S. Maswadi, R. Glickman, and M. Shadaram, "Probe beam deflection technique as acoustic emission directionality sensor with photoacoustic emission source," *Appl. Opt.*, vol. 53, no. 3, pp. 511-519, 2014.
[67] C. Raman and N. N. Nathe, "The diffraction of light by high frequency sound waves: Part I," in *Proceedings of the Indian Academy of Sciences-Section A*, 1935, vol. 2, no. 4: Springer, pp. 406-412.
[68] R. Nuster, P. Slezak, and G. Paltauf, "High resolution three-dimensional photoacoustic tomography with CCD-camera based ultrasound detection," *Biomed. Opt. Express*, vol. 5, no. 8, pp. 2635-2647, 2014.
[69] C. I. Zanelli and S. M. Howard, "Schlieren metrology for high frequency medical ultrasound," *Ultrasonics*, vol. 44, pp. e105-e107, 2006.
[70] M. J. Hargather and G. S. Settles, "Natural-background-oriented schlieren imaging," *Experiments in fluids*, vol. 48, no. 1, pp. 59-68, 2010.
[71] G. S. Settles, *Schlieren and shadowgraph techniques: visualizing phenomena in transparent media*. Springer Science & Business Media, 2012.
[72] T. Mizukaki, "Application of digital phase-shift holographic interferometry to weak shock waves propagating at Mach 1.007," *Shock Waves*, vol. 20, no. 1, pp. 19-27, 2010.
[73] J. Bucaro, H. Dardy, and E. Carome, "Fiber-optic hydrophone," *The Journal of the Acoustical Society of America*, vol. 62, no. 5, pp. 1302-1304, 1977.
[74] P. Shajenko, J. P. Flatley, and M. B. Moffett, "On fiber-optic hydrophone sensitivity," *The Journal of the Acoustical Society of America*, vol. 64, no. 5, pp. 1286-1288, 1978.
[75] M. Layton and J. Bucaro, "Optical fiber acoustic sensor utilizing mode-mode interference," *Appl. Opt.*, vol. 18, no. 5, pp. 666-670, 1979.
[76] R. Kashyap, *Fiber Bragg Gratings*, Second Edition ed. London: Elsevier, Raman Kashyap.
[77] J. K. Holger, O. P. Christian, and R. Ingo, "A fiber-optical microphone based on a Fabry–Perot interferometer applied for thermo-acoustic measurements," *Measurement Science and Technology*, vol. 21, no. 1, p. 015302, 2010. [Online]. Available: http://stacks.iop.org/0957-0233/21/i=1/a=015302.
[78] T. Berer, A. Hochreiner, S. Zamiri, and P. Burgholzer, "Remote photoacoustic imaging on solid material using a two-wave mixing interferometer," *Optics letters*, vol. 35, no. 24, pp. 4151-4153, 2010.
[79] S. J. Park, J. Eom, Y. H. Kim, C. S. Lee, and B. H. Lee, "Noncontact photoacoustic imaging based on all-fiber heterodyne interferometer," *Optics letters*, vol. 39, no. 16, pp. 4903-4906, 2014.
[80] G. Paltauf, R. Nuster, M. Haltmeier, and P. Burgholzer, "Photoacoustic tomography using a Mach-Zehnder interferometer as an acoustic line detector," *Appl. Opt.*, vol. 46, no. 16, pp. 3352-3358, 2007.
[81] J. Bauer-Marschallinger *et al.*, "Low-cost parallelization of optical fiber based detectors for photoacoustic imaging," in *Photons Plus Ultrasound: Imaging and Sensing 2013*, 2013, vol. 8581: International Society for Optics and Photonics, p. 85812M.
[82] T. JK, W. HK, and A. EA, "A Fabry-Perot acoustic surface vibration detector-application to acoustic holography," 1973.

[83] G. Wissmeyer, M. A. Pleitez, A. Rosenthal, and V. Ntziachristos, "Looking at sound: optoacoustics with all-optical ultrasound detection," *Light: Science & Applications*, vol. 7, no. 1, pp. 1-16, 2018.
[84] H. Lamela, D. Gallego, and A. Oraevsky, "Optoacoustic imaging using fiber-optic interferometric sensors," *Optics letters*, vol. 34, no. 23, pp. 3695-3697, 2009.
[85] E. Zhang, J. Laufer, and P. Beard, "Backward-mode multiwavelength photoacoustic scanner using a planar Fabry-Perot polymer film ultrasound sensor for high-resolution three-dimensional imaging of biological tissues," *Appl. Opt.*, vol. 47, no. 4, pp. 561-577, 2008.
[86] M. Yu and B. Balachandran, "Acoustic measurements using a fiber optic sensor system," *Journal of Intelligent Material Systems and Structures*, vol. 14, no. 7, pp. 409-414, 2003.
[87] S. Preißer, B. Fischer, and N. Panzer, "Listening to Ultrasound with a Laser: A new way to measure ultrasound waves by optical means," *Optik & Photonik*, vol. 12, no. 5, pp. 22-25, 2017.
[88] B. Fischer, "Miniaturized all-optical Sound Pressure Sensor," in *INTER-NOISE and NOISE-CON Congress and Conference Proceedings*, 2016, vol. 253, no. 2: Institute of Noise Control Engineering, pp. 6376-6382.
[89] O. Volodarsky, Y. Hazan, and A. Rosenthal, "Ultrasound detection via low-noise pulse interferometry using a free-space Fabry-Pérot," *Opt. Express*, vol. 26, no. 17, pp. 22405-22418, 2018.
[90] H. N. Kenhagho *et al.*, "Machine Learning-based Optoacoustic Tissue Classification Method for Laser Osteotomes Using an Air-coupled Transducer," *Submitted to Lasers in Surgery and Medicine*, pp. 1-15, 2020 2020.
[91] H. N. Kenhagho, F. Canbaz, R. Guzman, P. Cattin, and A. Zam, "Miniaturized Optoacoustic Feedback Sensor for Smart Laser Osteotome: Fiber-Coupled Fabry-Pérot Etalon Sensor," *Sensors and Actuators A: Physical*, p. 112394, 2020/11/26/ 2020, doi: https://doi.org/10.1016/j.sna.2020.112394.
[92] M. Eugster, P. C. Cattin, A. Zam, and G. Rauter, "A Parallel Robotic Mechanism for the Stabilization and Guidance of an Endoscope Tip in Laser Osteotomy," in *2018 IEEE/RSJ International Conference on Intelligent Robots and Systems (IROS)*, 2018: IEEE, pp. 1306-1311.
[93] M. Eugster *et al.*, "Force Estimation for Minimally Invasive Robot-assisted Laser Osteotomy in the Human Knee," in *Joint Workshop on New Technologies for Computer/Robot Assisted Surgery (CRAS)*, 2018.
[94] I. Susic, P. Cattin, A. Zam, and G. Rauter, "Versatile, force range-adjustable, tri-axial force sensor with integrated micro camera for the tip of endoscopic devices," in *The Hamlyn Symposium (2018, accepted)*, 2018.
[95] H. N. Kenhagho, I. Sugiarto, R. Guzman, P. Cattin, and A. Zam, "Contact-free Crater Depth Monitoring Using Measured Acoustic Shock Waves for Smart Laser Surgery Applications: Preliminary Result," in *2019 International Conference on Radar, Antenna, Microwave, Electronics, and Telecommunications (ICRAMET)*, 23-24 Oct. 2019 2019, pp. 118-121, doi: 10.1109/ICRAMET47453.2019.8980427.

Appendix

Optoacoustic Feedback Systems Using Air-Coupled Transducer or Fiber Brag Grating in Long-Pulsed Laser Ablation

Introduction

The publication presented in this appendix is based on results obtained from an optoacoustic system established by a scientific collaborator. In this experimental system, we ablated porcine bones with a 1-micron pulsed fiber laser, delivering long pulses at the millisecond range. We also measured acoustic shock waves generated during the ablation process using an air-coupled transducer and fiber Bragg grating, to identify the type of tissue (muscle or bone) to be ablated. Principal component analysis of the measured acoustic waves and Mahalanobis distances were used to differentiate bone and muscle under wet conditions. Bone and muscle ablated in wet conditions demonstrated a classification error of less than 6.66% and 3.33% when measured by a microphone and a fiber Bragg grating, respectively.

Publication. The findings were published in 2019 MDPI Materials Journal, with peer review [24].

DOI: 10.3390/ma12081338.

materials

MDPI

Article

Characterization of Ablated Bone and Muscle for Long-Pulsed Laser Ablation in Dry and Wet Conditions

Hervé Nguendon Kenhagho [1,*], Sergey Shevchik [2], Fatemeh Saeidi [2], Neige Faivre [2], Bastian Meylan [2], Georg Rauter [3], Raphael Guzman [4], Philippe Cattin [5], Kilian Wasmer [2] and Azhar Zam [1,*]

1 Biomedical Laser and Optics Group, Department of Biomedical Engineering, University of Basel, Gewerbestrasse 14, 4123 Allschwil, Switzerland
2 Laboratory for Advanced Materials Processing, Empa-Swiss Federal Laboratories for Materials Science and Technology, 3602 Thun, Switzerland; Sergey.Shevchik@empa.ch (S.S.); Fatemeh.Saeidi@empa.ch (F.S.); Neige.Faivre@empa.ch (N.F.); Bastian.Meylan@empa.ch (B.M.); Kilian.Wasmer@empa.ch (K.W.)
3 Bio-Inspired RObots for MEDicine-Lab, Department of Biomedical Engineering, University of Basel, Gewerbestrasse 14, 4123 Allschwil, Switzerland; georg.rauter@unibas.ch
4 Department of Neurosurgery, University Hospital Basel, Spitalstrasse 21, 4056 Basel, Switzerland; Raphael.Guzman@usb.ch
5 Center for medical Image Analysis and Navigation, Department of Biomedical Engineering, University of Basel, Gewerbestrasse 14, 4123 Allschwil, Switzerland; philippe.cattin@unibas.ch
* Correspondence: herve.nguendon@unibas.ch (H.N.K.); azhar.zam@unibas.ch (A.Z.); Tel.: +41-612075461 (H.N.K.); +41-612075460 (A.Z.)

Received: 1 April 2019; Accepted: 18 April 2019; Published: 24 April 2019

Abstract: Smart laser technologies are desired that can accurately cut and characterize tissues, such as bone and muscle, with minimal thermal damage and fast healing. Using a long-pulsed laser with a 0.5–10 ms pulse width at a wavelength of 1.07 µm, we investigated the optimum laser parameters for producing craters with minimal thermal damage under both wet and dry conditions. In different tissues (bone and muscle), we analyzed craters of various morphologies, depths, and volumes. We used a two-way Analysis of Variance (ANOVA) test to investigate whether there are significant differences in the ablation efficiency in wet versus dry conditions at each level of the pulse energy. We found that bone and muscle tissue ablated under wet conditions produced fewer cracks and less thermal damage around the craters than under dry conditions. In contrast to muscle, the ablation efficiency of bone under wet conditions was not higher than under dry conditions. Tissue differentiation was carried out based on measured acoustic waves. A Principal Component Analysis of the measured acoustic waves and Mahalanobis distances were used to differentiate bone and muscle under wet conditions. Bone and muscle ablated in wet conditions demonstrated a classification error of less than 6.66% and 3.33%, when measured by a microphone and a fiber Bragg grating, respectively.

Keywords: acoustic tissue response; laser ablation; tissue differentiation; influence of ablation condition

1. Introduction

Cutting tissue with drills and saws results in heat formation that may damage the surrounding tissues, leading to impaired bone regeneration [1–3]. In contrast, laser ablation (a laser used as an osteotomy tool) works without contact force, thereby reducing the severe mechanical vibrations and heat damage generated by conventional cutting tools [2,4]. Avoiding heat damage improves the healing of the cut bone, making laser ablation a highly desired innovation in the field of maxillo-facial-, neuro-

and orthopedic surgery [2]. Moreover, lasers cut with greater precision than conventional tools [5–7]. When irradiating bone and teeth with the Er:YAG laser (2.94 µm), water and hydroxyapatite absorb most of the laser energy. Teeth (with a composition close to bone) consist of 85–95% carbonated hydroxyapatite, 8–12% water, and 2–3% protein and lipids [8–10]. Because the water content and Amide I/II bands in bone absorb so much IR radiation, different lasers for cutting bone in surgical applications have been investigated, including the holmium-doped yttrium aluminum garnet (Ho:YAG), carbon dioxide (CO_2) lasers, the erbium-doped yttrium aluminum garnet (Er:YAG) pulsed laser, and free-electron lasers (FEL) [11–17]. The Er:YAG laser has a wavelength of 2.94 µm, corresponding to one of the absorption peaks of water and hydroxyapatite, the main component of bone [1,7], and corresponding to the wavelength where bone or teeth are ablated by means of photo-thermal vaporization.

The laser ablation process has been optimized for bone tissue and relies on a photothermic mechanism that results in thermal damage to the surrounding tissue unless a cooling system is used [18–21]. Recent investigations have shown that water on the exposed area prevents the carbonization of tissues around craters, thereby improving the ablation efficiency [22–24] and increasing the ablation rate [25,26]. It has been argued that a high laser energy density improves the radiation ablation efficiency in wet conditions by confining the laser-generated plasma in the liquid layer, leading to a greater emission of acoustic and shock waves as compared to ambient air conditions [26,27]. However, high-energy laser systems are not suitable for tissue ablation and regeneration under dry conditions, as they produce a greater temperature dissipation around the exposed zone, which can lead to carbonization and a long wound-recovery time.

Long-pulsed fiber lasers may be more practical in an operating room because of their fiber-coupled output, and their smaller footprint and robustness to environmental vibrations than short-pulsed lasers [28]. Long-pulsed lasers, such as millisecond-pulsed lasers, with several joules of energy, are also much less costly than ultra-short-pulsed lasers, such as femto or nanosecond pulsed ones, with millijoule energy. In addition, fiber lasers with a wavelength of 1.07 µm have a low absorption in water as compared to the Er:YAG lasers [29,30]. To minimize the energy loss in a wet environment, a laser wavelength of 1.07 µm may be appropriate as its absorption is lower than for the wavelength of the Er:YAG lasers [3]. Because the absorption coefficient for a fiber laser at 1.07 µm is low in water (approximately $0.4 cm^{-1}$), the transmission through a 14 mm water layer is around 80% [27,31,32]. Therefore, when a bone is covered with water and irradiated by a fiber laser at 1.07 µm, it does not significantly reduce the energy reaching the bone. In contrast to a wavelength of 2.94 µm, this well-established wavelength for metal welding in the industry (1.07 µm) could be clinically studied for its suitability for knee surgery in a wet environment. Previous investigations were mainly conducted on metals and substrate samples for laser-welding applications [33,34].

However, in addition to being fast and accurate when cutting bone, lasers need to be safe as well. A tissue differentiation method could improve the safety of lasers as an osteotomy tool. This is particularly true if a laser system can be controlled by an *in situ* and real-time automatic feedback system that not only differentiates specific types of human tissues but additionally stops automatically when the laser encounters tissues that are not meant to be ablated [2,4,35]. Acoustic shock waves (ASWs) are generated when ablating material with a laser and can be measured using microphone and Fiber Bragg Grating (FBG) sensors [4,36–38]. Compared to standard microphones, FBG sensors are smaller, more sensitive, lightweight and immune to electromagnetic interference [39,40]. In this work, we investigate the laser tissue ablation of muscle and bone, using a long-pulsed laser with a center wavelength of 1.07 µm and pulse energies in the range of 0.75–15 J, under different ablation conditions (in terms of the ablation efficiency of bone and the impact of water on carbonization). We simultaneously recorded (with a microphone and an FBG) and differentiated the acoustic signals generated by the ablation of porcine bone and muscle. We used a Principle Component Analysis (PCA) to reduce the dimensionality of the ASWs measured from each specimen and the Mahalanobis distances method to differentiate the scores of the measured ASWs. Such a set-up has the potential to act as an optoacoustic feedback sensor for laser osteotomy.

2. Materials and Methods

2.1. Laser Tissue Ablation

For the laser tissue ablation experiments, muscle and bone tissue specimens from a fresh porcine spare rib, purchased from a local slaughterhouse, were used. The bone and muscle were 10.80 and 11.00 mm thick, respectively. We ablated one specimen of the endosteum in the compact bone and muscle tissue. The laser ablation was performed at five different locations 4 mm apart on each specimen. Five craters exposed to ten laser pulses with the same laser parameters is referred to as a "Set". Table 1 shows eight sets of experiments with pulse energies between 0.75 and 15 J. The experiments were conducted on different specimens in wet and dry conditions (see Figure 1 for the bone specimens). To perform the laser ablation under wet conditions, a spray of distilled water with a flow rate of 0.1 mL/s was directed to the ablation spot, to wet the specimen each time before a laser pulse hit the tissue. The dry condition was defined as the ablation without any distilled water sprayed at the ablation location before focusing the laser light. Laser-induced acoustic shock waves were measured during the ablation.

Table 1. Summary of the laser parameters.

Set	1	2	3	4	5	6	7	8
Pulse energy (J)	0.75	1.50	3	5	7	9	13	15
Pulse duration (ms)	0.49	0.98	1.95	3.25	4.55	5.85	8.45	9.75

(**a**) (**b**)

Figure 1. Ablated hard bone in (**a**) wet and (**b**) dry conditions at different pulse energies summarized in Table 1.

2.2. Experimental Set-Up

A laser fiber source (StarFiber 150 P; ROFIN-LASAG AG, Belp, Switzerland) operates at 1.07 µm with a pulse repetition rate of 1 Hz and pulse duration at 0.5–10 ms. A scanner head (HurrySCAN 30; Scanlab GmbH, Puchheim, Germany) was used to precisely ablate the bone and muscle (Figure 2). The laser beam was transmitted through a single-mode optical fiber with a 12 µm core diameter and focused on the surface of the sample with a focusing lens (focal distance of 170 mm). This setup provided a spot size diameter of 30 µm (measured by a beam profilometer at a specific level of e^{-2}) at the focal point, and a maximum pulse energy of 15 J. The acoustic shock wave that was generated during the ablation was measured simultaneously using a non-contact acoustic microphone: (PAC AM41 SNAA05, physical acoustics, Princeton Junction, NJ, USA) with −3 dB bandwidth of 39–42 kHz at a resonant frequency of 40 kHz and an FBG detection system (FFT Corning SMF-28, Corning, New York City, NY, USA) with a first grating position at 1 m, and an FBG length of 10 mm.

2.3. Analysis of Craters

2.3.1. Characterization of Laser-Induced Craters

After the laser ablation process (in both the wet and dry conditions), the resulting holes/craters were characterized using a scanning electron microscope (SEM). The analysis of the bone and muscle surface was performed using a tungsten filament SEM (DSM 962; Carl Zeiss AG, Oberkochen, Germany) and a high-resolution field emission SEM (S-4800; Hitachi High-Technologies Corporation, Tokyo,

Japan). The volume and depth of each crater was calculated based on 3D mapping, using a confocal microscope (VK-8700; Keyence Corporation, Osaka, Japan).

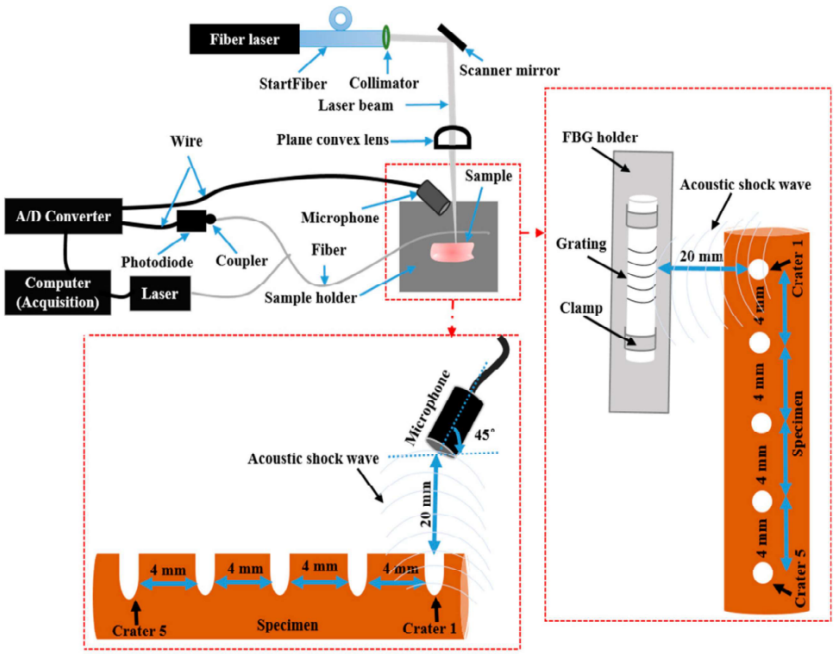

Figure 2. Schematic of the experiment illustrating the laser fiber set-up, an FBG and a microphone for laser-induced acoustic measurements.

2.3.2. Ablation Efficiency

To calculate the ablation efficiency, the depth and volume of the craters in the bone and muscle samples were averaged over the four best craters (the craters were collapsing, especially on the muscle surface, and the worst one was discarded.). The primary purpose of a two-way ANOVA is to understand if there is an interaction between the two independent variables on the dependent variable [41,42]. Hence, based on mean scores for the dependent variable across the two groups and factors (dry bone vs. wet bone and dry muscle vs. wet muscle), we used the two-way ANOVA test in the SPSS Statistics tool to check whether there are significant differences in the ablation efficiency between the wet and dry conditions at each pulse energy level (main effects for dependent variables). The irrigation condition (dry and wet) and energy level were considered as independent variables 1 and 2, respectively. The volume and depth were considered as dependent variables 1 and 2, respectively. When significant differences in the ablation efficiency were observed, we also investigated significant variables that showed a main effect using Bonferroni-corrected post hoc tests [43].

2.4. Characterization of Acoustic Shock Waves

To characterize the acoustic waves, we first determined the background noise level by measuring the environmental/floor noise using a microphone. The environmental noise was measured by switching off the ablation laser and measuring the acoustic signals in the room. Based on the measured floor noise, a signal/system detection was carried out using fixed amplitude thresholding with noise levels below 49 dB (0.28 mV). The fixed amplitude to trigger the measured acoustic signals was then set at 49 dB. To improve the sensitivity of the FBG, we clamped the fiber at both sides of the FBG holder. The FBG was positioned 2 cm away from the first ablated spot on the specimen (Figure 2). The calibrated microphone was fixed at a static position 2 cm away from the ablation spot at a 45° angle (approximately) to record the ASWs (Figure 2). Each sample (bone and muscle) and each condition (wet and dry), at the same location, was exposed to 10 laser pulses at a repetition rate of 1 Hz. The FBG was

fixed with a constant strain, and the FBG read out was carried out at a wavelength of 1547.3 nm with a power of 2 mW. The spectral reflectance characteristics of our FBG sensor are shown in Figure 3a,b (black). According to the principles of the FBG operation [39,40], its structure is distorted by the coming Acoustic Emission (AE), thus shifting the reflectance window as depicted in Figure 3a,b (red). Under these conditions, the wavelength of the read out was chosen to fit the slope of the reflectance window, thus providing the linearly proportional response to the amplitude of the coming AE waves. The full dynamic range of the FBG shift, met in the experiments, provided a 10% and 65% reflectance, as is shown in Figure 3.

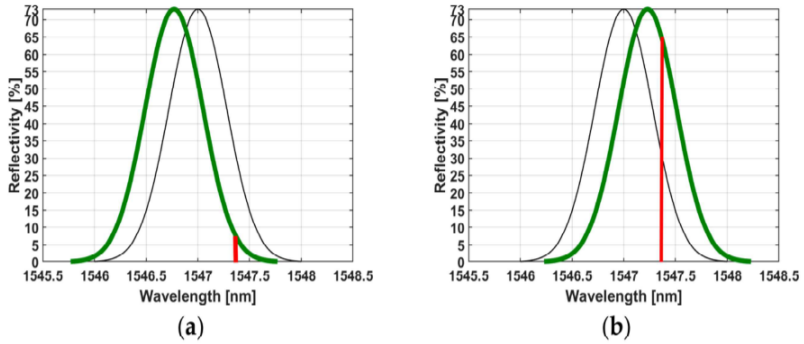

Figure 3. (**a**) Fiber in the compressive state (green) and resting state (black) with a tunable laser at a fixed wavelength of 1547.3 nm and 10% of the light reflected. (**b**) Fiber in the tension state (green) with a tunable laser at a fixed wavelength of 1547.3 nm and 65% of the light reflected.

The detection of the reflected light was done using an InGaAs Switchable Gain Amplified Detector (PDA20CS-EC, Thorlabs, Ann Arbor, MI, USA), with a sensitivity in the spectral range of 800–1700 nm and 2.5 MHz of usable bandwidth. The photodiode detector senses the intensityvariation of the back-reflected light in the time domain, which is correlated to the acoustic signal generated during the laser ablation. The acoustic signal was transferred to the computer for recording and post-processing.

2.5. Tissue Differentiation

To differentiate hard bone and muscle, we looked at the ASW measured from the optimal ablation conditions. In this study, the optimum ablation was defined as the one that produced craters that were relatively clean from random charring and that showed fewer cracks compared to other craters in both conditions. The first twenty ASWs from the first two optimum craters were used as "training data", while the last thirty ASWs from the last optimum three craters were considered "testing data". To eliminate the phase shift effects at each measured ASW, we looked at the amplitude spectrum using the Fast Fourier Transform (FFT) in MATLAB (version R2016a). To reduce the dimensionality of each ASW, we used the amplitude spectrum as the input of the Principle Component Analysis (PCA). Then, we improved the contrast of the visualization of each ASW using the logarithm of the amplitude spectrum. To simultaneously differentiate the tissue types, we used the first three PCA scores from the set of training data combined with the Mahalanobis distance, and we plotted the 95% confidence ellipse using the three orthogonal eigenvectors of the scores from the "training data". The scores from the testing data in each ellipsoid that correctly detected tissues were considered true positives; if they were outside the ellipsoid, the scores were considered unknown or false positive. We differentiated the tissues based on the ellipsoid because it considers the covariance of the ASW scores and the scales of the different variables. Therefore, it is useful for detecting members of the same group and even outliers.

3. Results

3.1. The Ablated Tissues at Different Morphological Craters

Figure 4a,b shows the representative SEM pictures of the ablated bone and muscle surfaces, respectively, in dry and wet conditions for each set of conditions defined in Figure 4. In Figure 4a, the bones ablated in the dry conditions reveal an irregular surface with random propagating cracks at the surface for Sets 1 to 4. Sets 5 to 7 show irregular surfaces with thermal damage. The SEM picture of Set 8 shows a crater with random charring (around the crater as compared to the craters in Sets 1 to 7). For the ablation in wet conditions, Set 1 and Sets 3 to 7 indicate craters with less random charring, fewer cracks around the ablated contours and without any signs of thermal damage. Set 8 indicates some random micro cracks around the crater, setting an upper limit for the optimum laser bone ablation assisted by distilled water. In Figure 4b, the photographs of the muscle in dry and wet conditions in Sets 4 to 8 show no signs of a random star with thermal damage around the craters. It was not possible to reproduce the SEM pictures of the muscles in dry and wet conditions for Sets 1 to 6. During the drying procedure, at least 20% muscle shrinkage from the original state was observed. Sets 7 and 8 show signs of random cracks in the muscle crater under wet conditions only. Based on Figures 4 and 5, we found that, at Set 8, we can ablate faster than for other sets, but we also burned tissues. The optimum ablation for hard bone and muscle was at Set 5 (wet conditions) because the craters were relatively clean of random charring and showed fewer cracks compared to other sets with higher energy in both conditions. Therefore, to see if we could also differentiate the ablated tissues using the measured ASWs, we decided to use the process parameters of Set 5 (7 J and 4.55 ms) in the wet condition.

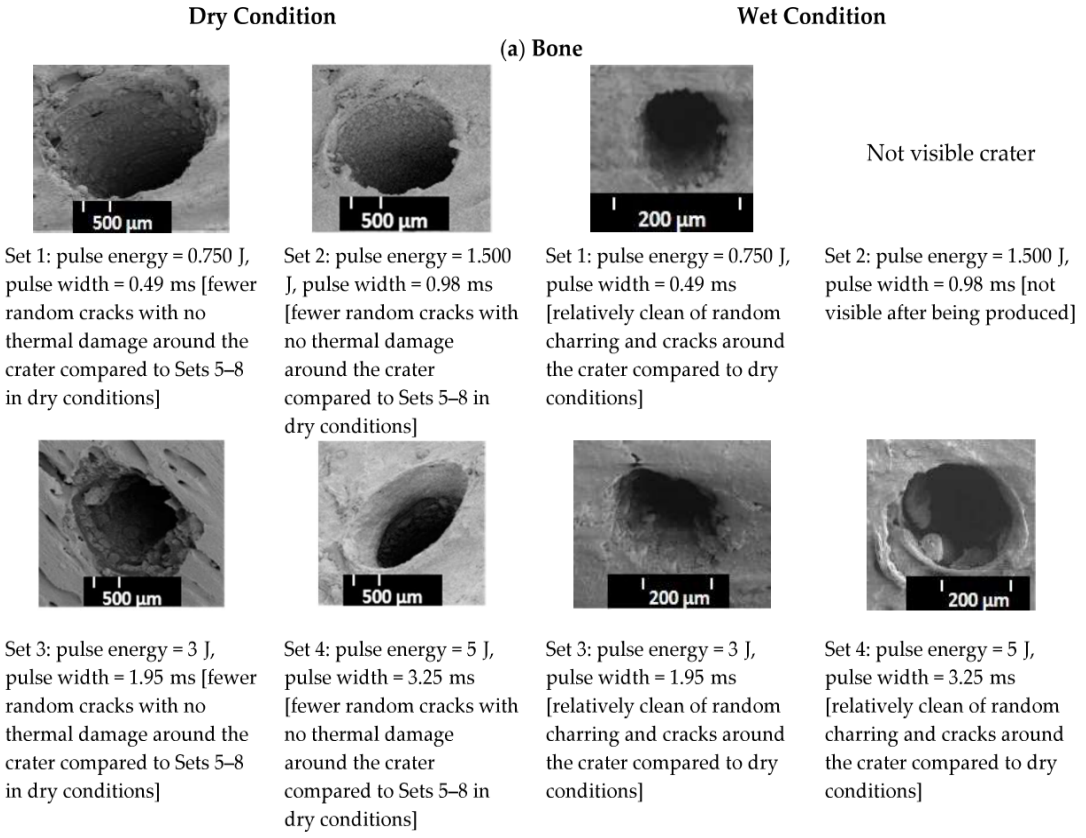

Figure 4. *Cont.*

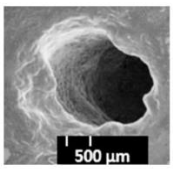

Set 5: pulse energy = 7 J, pulse width = 4.55 ms [random cracks with thermal damage around the crater]

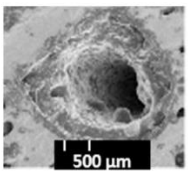

Set 6: pulse energy = 9 J, pulse width = 5.85 ms [random cracks with thermal damage around the crater]

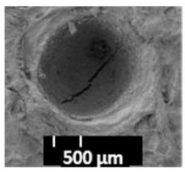

Set 5: pulse energy = 7 J, pulse width = 4.55 ms [relatively clean of random charring and cracks around the crater compared to dry conditions]

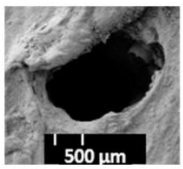

Set 6: pulse energy = 9 J, pulse width = 5.85 ms [relatively clean of random charring and cracks around the crater compared to dry conditions]

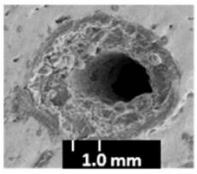

Set 7: pulse energy = 13 J, pulse width = 8.45 ms [random cracks with thermal damage around the crater]

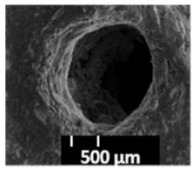

Set 8: pulse energy = 15 J, pulse width = 9.75 ms [random charring and carbonization around the crater]

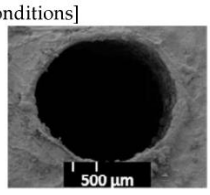

Set 7: pulse energy = 13 J, pulse width = 8.45 ms [relatively clean of random charring and cracks around the crater]

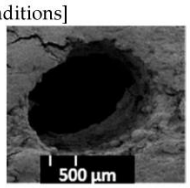

Set 8: pulse energy = 15 J, pulse width = 9.75 ms [random micro-cracks around the crater]

(b) Muscle

Dry Condition **Wet Condition**

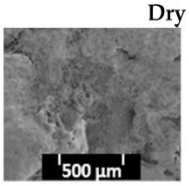

Set 7: pulse energy = 13 J, pulse width = 8.45 ms [No signs of cracks in the crater]

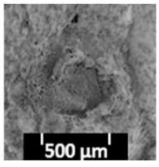

Set 8: pulse energy = 15 J, pulse width = 9.75 ms [No signs of cracks in the crater]

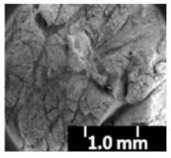

Set 7: pulse energy = 13 J, pulse width = 8.45 ms [Random micro-cracks in the crater]

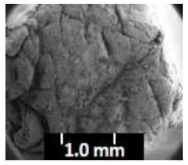

Set 8: pulse energy = 15 J, pulse width = 9.75 ms [Random micro-cracks in the crater]

Figure 4. SEM top-views of (**a**) bone and (**b**) muscle surfaces in the dry and spray ablation after ten laser pulses.

3.2. *Efficiency of Laser Bone and Muscle Ablation*

The mean values and corresponding estimated marginal means with an error bar at a 95% confidence interval for volume and depth in bone and muscle are plotted in Figure 5. Based on the mean, the volume of the craters in bone under the dry conditions was higher than in the wet conditions, except when the pulse energy was set to 0.75 J (Figure 5a). The two-way ANOVA test (Appendix A, Table A1) showed that differences in the mean volume of the craters created in the dry and wet conditions were statistically significant ($p < 0.05$, the p-value is labeled as "Sig." in the SPSS output "Sig." stands for the significance level). However, the difference in depth between the two conditions was not statistically significant ($p > 0.05$), (Appendix A, Table A2). Using the Bonferroni-corrected post hoc tests, the volume showed a simple main effect between the dry and wet conditions at the energy levels of 13 and 15 J ($p < 0.05$), (Appendix A, Table A3). In the muscle, Figure 5c,d shows no ablation until the pulse energy reaches 7 J. From 7 J, the depth and volume of the craters made in the muscle under the wet conditions were greater than those made in the dry conditions. Furthermore, the difference in the volume and depth of the muscle craters made in the dry versus wet conditions are statistically significant ($p < 0.05$), (Appendix A, Tables A4 and A5). From the Bonferroni-corrected post hoc tests, the volume and depth showed a simple main effect (a statistic difference) between the dry and wet conditions at each energy level ($p < 0.05$), (Appendix A, Tables A6 and A7).

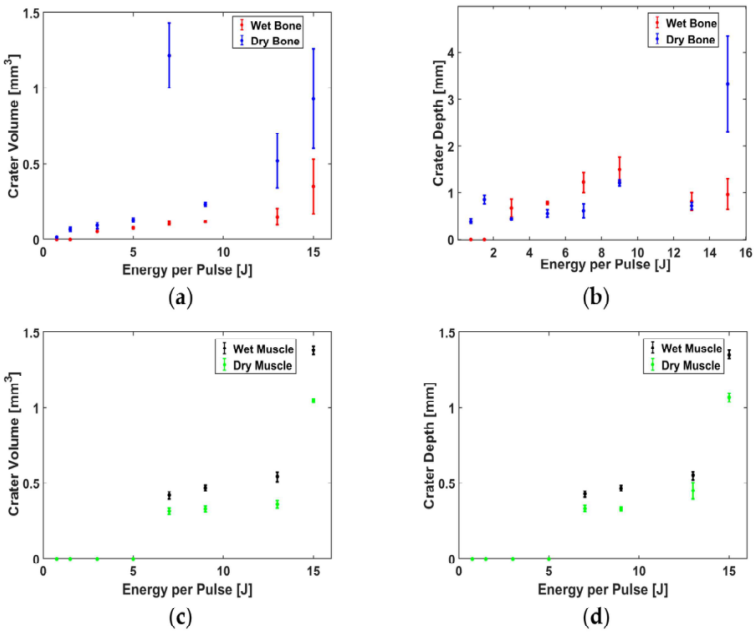

Figure 5. Bone and muscle comparison of the average ablation efficiency for five dry and wet craters as a function of energy with 10 pulses: (**a**) bone crater volume and (**b**) depth ablations; (**c**) muscle crater volume and (**d**) depth ablations.

3.3. Tissue Differentiation Based on Acoustic Measurement Using Microphone and FBG

In Set 5 in the wet condition, the microphone measurements show that ten averaged acoustic signals for the wet-ablated muscle had a lower peak-to-peak amplitude in the time domain (Figure 6a) and a narrower amplitude spectrum than the wet-ablated bone (Figure 6b). In contrast, the peak-to-peak amplitude in the time domain (Figure 7a) and amplitude spectrum of the back-reflected light in the fiber was lower compared to those for the muscle (Figure 7b). The features that were chosen for the first three principle components (PC1, PC2, and PC3) of the PCA explained 99.91% and 22.70% of the variance in the acoustic waves recorded by the microphone and FBG, respectively. We plotted each ellipsoid against the three orthogonal eigenvectors of the training data scores to differentiate the bone and muscle (Figures 6c and 7c). The scores from the testing data in each ellipsoid that correctly detected the tissues were considered as true positives; outside of the ellipsoid, the scores were considered as being unknown (Figures 6d and 7d). From the confusion matrix, we see that the errors from the testing data (distinguishing between bone and muscle) were less than 6.66% for the ASWs measured by microphone (Table 2), and 3.33% for those measured by FBG (Table 3).

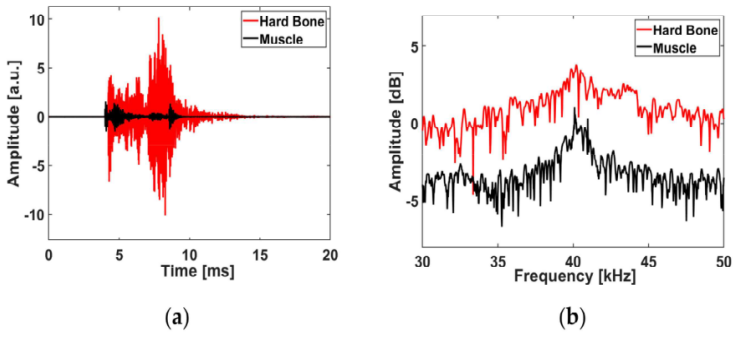

Figure 6. *Cont.*

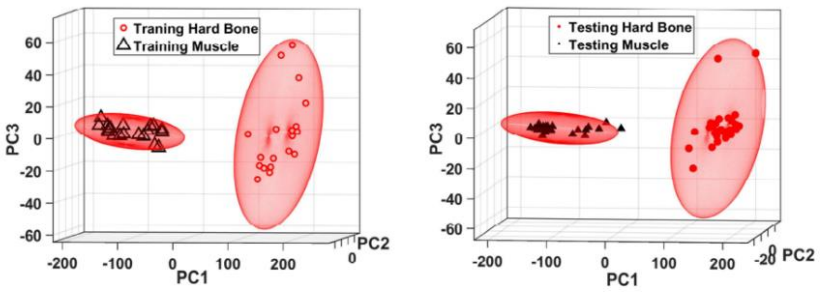

Figure 6. Acoustic shock wave differentiation measured by a microphone during laser pulse energy at 7 J in wet conditions (Set 5): (**a**) ASW in the time domain, (**b**) Spectrum of the ASW, (**c**) Ellipsoids based on 20 scores from training data, (**d**) Classification of 30 scores from the test data in each ellipsoid of the training data.

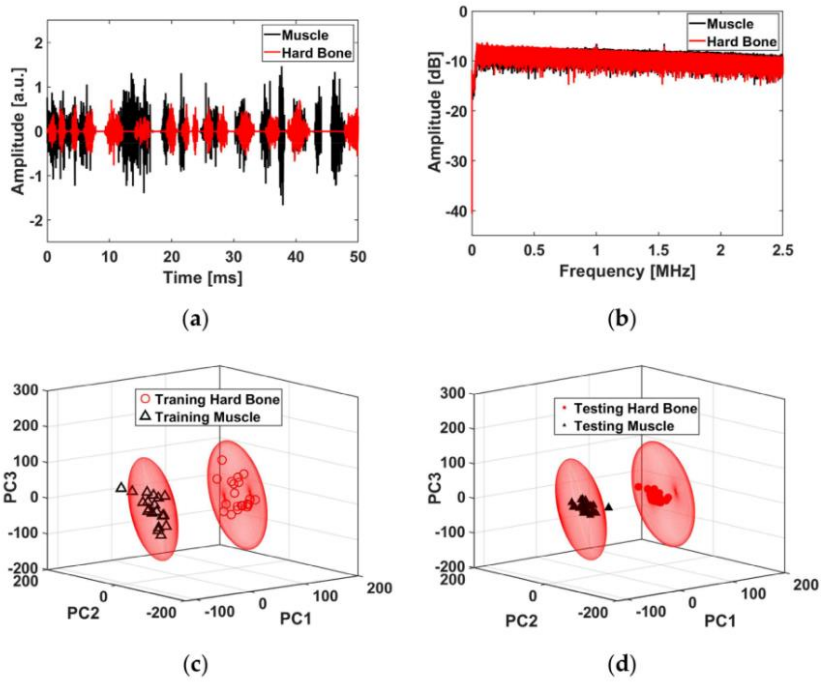

Figure 7. Acoustic shock wave differentiation measured by an FBG during laser ablation at 7 J in wet conditions (Set 5): (**a**) Back reflected light in the time domain, (**b**) Spectrum of the back-reflected light, (**c**) Ellipsoids based on 20 scores from training data, (**d**) Classification of 30 scores from the test data in each ellipsoid of the training data.

Table 2. Confusion matrix for the bone and muscle classification during the laser ablation at 7 J pulse energy.

Tissue	Classified as			Classification Error %
	Bone	Muscle	Unknown	
Bone	29	0	1	3.33%
Muscle	0	28	2	6.66%

Table 3. Confusion matrix for the bone and muscle types during the laser ablation at 7 J pulse energy.

Tissue	Classified as			Classification Error %
	Bone	Muscle	Unknown	
Bone	30	0	0	0%
Muscle	0	29	1	3.33%

4. Discussion

Under the wet conditions, Sets 1 to 7 showed craters with less random charring, fewer cracks around the ablated contours and without any signs of thermal damage, as compared to the dry condition. This is because the water partially hydrates the exposed surface and thus partially prevents the carbonization of healthy tissue, leading to an improvement in the ablation efficiency of the muscle, as compared to the dry conditions (Figure 5c,d).

In contrast to the muscle, the volume of the craters made in the bone under the dry conditions was higher than those made in the wet conditions, except for a pulse energy of 0.75 J (Figure 5a). One possible reason for this outcome is that, in the absence of a water-cooling system, the pulse energy applied in the dry conditions causes more random cracks around the crater compared to those created in the wet conditions, thereby increasing the width and inducing a higher crater volume. In other words, the dry bone at the surface is ablated due to a higher temperature and possible phase transformation taking place in the wet conditions, induced by large temperature gradients inside the exposed material [4]. Apart from the crater volume in the bone created under the dry conditions, Figure 5b and the two-way ANOVA test (Appendix A, Table A2) showed that the difference in the mean depth of the craters made in the dry versus wet conditions was not statistically significant ($p > 0.05$). This is due to the fact that bone rehydration was not sufficiently abundant to prevent an extensive heat diffusion [44]. In this experiment, the laser energy was increased by prolonging the laser pulse; with longer pulse durations, there was more time for the heat to diffuse and create carbonization at the bottom of the craters and saturate the depth of the craters. That is why Sets 4 to 8 presented some random cracks and thermal damage around the craters in the bone, created under the dry conditions. These phenomena are mainly caused by an excessive heat accumulation during and after an exposure to a high laser energy within the range of 7–15 J. Therefore, the range of the laser pulse duration, from approximately 0.5 to 10 ms, is likely to influence the amount of heat spread during the laser pulse [44,45]. The SEM pictures of the craters in the muscle for Sets 7 and 8, created in the dry conditions, presented no signs of random cracks around the craters.

However, when ablated under the wet conditions, these sets presented some signs of random cracks and the depths of the craters made in the muscle were lower than those in the bone (under both conditions). This is probably because the muscle tissue started to shrink directly after the ablation. In Set 5, we observed that the maximum amplitude of the acoustic signal efrom th bone ablated in the wet conditions was higher than that from the muscle. Muscle is composed of 79% water, while hard bone or teeth consist of 85–95% carbonated hydroxyapatite, 8–12% water, and 2–3% protein and lipids. Therefore, we believe that the carbonated hydroxyapatite component in bone produces greater amplitudes of sound, as it is a compact component compared to muscle, which is mostly made of water [8–10].

The resonant frequencies for bone and muscle cannot be used as parameters for tissue differentiation in the current stage of the project. This is mainly due to the limitation of the usable bandwidth (39–42 kHz) of the microphone that we used in this experiment. The spectrums of the acoustic pulses with shocks can extend beyond 1 MHz [46]. Thus, precise frequency measurements of broadband acoustic signals generated during ablation, using broadband pressure sensors, will measure acoustic shock waves with higher frequency components [35,47,48], which could then be used as frequency parameters to distinguish between ablated tissues. That is why the FBG, combined with a photodiode with a bandwidth of 2.5 MHz, resulted in a better classification error than the one measured by a microphone (Tables 2 and 3).

In contrast to the microphone, the FBG measurements show that the bone tissues have a lower maximum amplitude of measured light than the muscle (Figure 7a,b). This was expected, as the higher amplitudes of ASWs from the bone might cause more distortion of the FBG, and more distortion creates more oscillation of the reflected light; thus, the measured reflected light intensity is low. The light intensity measured by the photodiode is reflected from the nonlinear regime of the near-Gaussian function (Figure 3a,b). Thus, the reflected light intensity measured by the photodiode is inferior during the ablation of the bone compared to the ablation of the muscle, which is situated in the linear regime. We measured the stretch and compression of the fiber that is converted into the measured intensity in the time domain (in real-time with an up to sub-nanosecond resolution) of the back-reflected light from the FBG structure. Consequently, the intensity is proportional to the compression strain on the FBG that is caused by acoustic shock waves.

5. Conclusions

The long-pulsed (from 0.5 to 10 ms) laser ablation of bone at a wavelength of 1.07 μm in wet and dry conditions was the focus of this study. The acoustic shock wave characteristics of bone and muscle during a laser ablation were also investigated in an attempt to differentiate between tissues. The tissue ablated with a spray irrigation produced very few cracks and thermal damage around the craters, which would ultimately lead to accelerated bone healing. For the bone and muscle tissue differentiation, we focused on the acoustic signal measured at Set 5 (7 J and 4.55 ms), under wet conditions. At this specific pulse energy, the mean depth of the crater in bone, created under wet conditions, was higher than that created in dry conditions; we also observed a lower ablation volume for craters created under wet conditions, compared to dry conditions. In Set 5, the craters in bone were relatively clean of random charring and showed fewer cracks than he craters made in higher energy sets in either condition. Keeping the ablation volume as small as possible, with less thermal damage and fewer cracks, could potentially improve the ablation efficiency and bone healing time. Using the best laser parameters (Set 5) to generate acoustic waves for tissue differentiation, the peak amplitude of the acoustic signals measured by a microphone for the bone was higher than the ones for muscle, in both dry and wet conditions. The classification error of the experiment, based on the spectral acoustic wave detection of bone and muscle in wet conditions, was less than 6.66% and 3.33%, as measured by a microphone and by FBG, respectively. By quantifying the measured acoustic shock waves, we guarantee an efficient tissue differentiation as feedback to reduce the probability of undesirable cutting of tissues at different depths and pulse energies.

The promising results of this approach motivate us for further improvements. Future work will include a histological study of the bones in a cross-section after the laser ablation, in order to fully evaluate the potentials of the technique in terms of the reduction of bone damage compared to other techniques. Furthermore, the advanced precision in signal differentiation, combined with an extension of the number of involved tissues and ablating regimes, needs to be investigated. This formulation leads to more complex data, and in order to reach efficiency in processing we plan to involve a cutting-edge machine learning technique, simultaneously providing a high temporal resolution and real-time operation of the methods involved. The challenges in this formulation reside in the contradiction between computational complexity, computational speed, and precision. The solution to this problem is planned as the continuation of this work.

Author Contributions: Conceptualization, H.N.K. and A.Z.; methodology, H.N.K. and A.Z.; software, H.N.K. and S.S.; validation, G.R., R.G., P.C., K.W. and A.Z.; formal analysis, H.N.K., S.S., B.M., G.R., P.C. and A.Z.; investigation, H.N.K., F.S., B.M. and N.F.; resources, P.C., K.W. and A.Z.; data curation, H.N.K.; writing— original draft preparation, H.N.K.; writing—review and editing, S.S., B.M., G.R., R.G., P.C., K.W. and A.Z.; supervision, R.G., P.C., K.W. and A.Z.

Funding: This research project was funded by the Werner Siemens Foundation.

Acknowledgments: This project is part of the MIRACLE (short for Minimally Invasive Robot-Assisted Computer-guided LaserosteotomE) project.

Conflicts of Interest: The authors declare no conflict of interest.

Appendix A

Table A1. Tests of Between-Subjects Effects.

Dependent Variable: Volume						
Source	**Type III Sum of Squares**	**df**	**Mean Square**	**F**	**Sig.**	**Partial Eta Squared**
Corrected Model	7.457 [a]	15	0.497	8.528	0.000	0.727
Intercept	4.045	1	4.045	69.384	0.000	0.591
Irrigation Condition	1.370	1	1.370	23.506	0.000	0.329
Energy Level	3.990	7	0.570	9.778	0.000	0.588
Irrigation Condition * Energy Level	2.097	7	0.300	5.138	0.000	0.428
Error	2.798	48	0.058			
Total	14.300	64				
Corrected Total	10.255	63				

Based on estimated marginal means. * The mean difference is significant at the 0.05 level. [a] R Squared = 0.727 (Adjusted R Squared = 0.642).

Table A2. Tests of Between-Subjects Effects.

Dependent Variable: Depth						
Source	**Type III Sum of Squares**	**df**	**Mean Square**	**F**	**Sig.**	**Partial Eta Squared**
Corrected Model	35.387 [a]	15	2.359	6.544	0.000	0.672
Intercept	49.438	1	49.438	137.127	0.000	0.741
Irrigation Condition	1.129	1	1.129	3.133	0.083	0.061
Energy Level	21.608	7	3.087	8.562	0.000	0.555
Irrigation Condition * Energy Level	12.650	7	1.807	5.012	0.000	0.422
Error	17.305	48	0.361			
Total	102.131	64				
Corrected Total	52.693	63				

Based on estimated marginal means. * The mean difference is significant at the 0.05 level. [a] R Squared = 0.672 (Adjusted R Squared = 0.569).

Table A3. Bonferroni-corrected post hoc tests (Irrigation Condition * Energy Level).

Dependent Variable: Volume							
Energy Level	**(I) Irrigation Condition**	**(J) Irrigation Condition**	**Mean Difference (I-J)**	**Std. Error**	**Sig. [b]**	**95% Confidence Interval for Difference [b]**	
						Lower Bound	**Upper Bound**
0.75 J	Dry	Wet	0.015	0.171	0.932	−0.329	0.358
	Wet	Dry	−0.015	0.171	0.932	−0.358	0.329
1.5 J	Dry	Wet	0.065	0.171	0.703	−0.278	0.409
	Wet	Dry	−0.065	0.171	0.703	−0.409	0.278
3 J	Dry	Wet	0.037	0.171	0.829	−0.306	0.380
	Wet	Dry	−0.037	0.171	0.829	−0.380	0.306
5 J	Dry	Wet	0.041	0.171	0.809	−0.302	0.385
	Wet	Dry	−0.041	0.171	0.809	−0.385	0.302
7 J	Dry	Wet	1.111 *	0.171	0.000	0.768	1.455
	Wet	Dry	−1.111 *	0.171	0.000	−1.455	−0.768
9 J	Dry	Wet	0.116	0.171	0.499	−0.227	0.460
	Wet	Dry	−0.116	0.171	0.499	−0.460	0.227
13 J	Dry	Wet	0.373 *	0.171	0.034	0.030	0.717
	Wet	Dry	−0.373 *	0.171	0.034	−0.717	−0.030
15 J	Dry	Wet	0.582 *	0.171	0.001	0.238	0.925
	Wet	Dry	−0.582 *	0.171	0.001	−0.925	−0.238

Based on estimated marginal means. * The mean difference is significant at the 0.05 level. [b] Adjustment for multiple comparisons: Least Significant Difference (equivalent to no adjustments).

Table A4. Tests of Between-Subjects Effects.

Dependent Variable: Volume						
Source	**Type III Sum of Squares**	**df**	**Mean Square**	**F**	**Sig.**	**Partial Eta Squared**
Corrected Model	4.268 [a]	7	0.610	282.055	0.000	0.988
Intercept	11.846	1	11.846	5480.688	0.000	0.996
Irrigation Condition	0.283	1	0.283	130.989	0.000	0.845
Energy Level	3.921	3	1.307	604.659	0.000	0.987
Irrigation Condition * Energy Level	0.064	3	0.021	9.806	0.000	0.551
Error	0.052	24	0.002	-	-	-
Total	16.166	32	-	-	-	-
Corrected Total	4.319	31	-	-	-	-

Based on estimated marginal means. * The mean difference is significant at the 0.05 level. [a] R Squared = 0.988 (Adjusted R Squared = 0.984).

Table A5. Tests of Between-Subjects Effects.

Dependent Variable: Depth						
Source	**Type III Sum of Squares**	**df**	**Mean Square**	**F**	**Sig.**	**Partial Eta Squared**
Corrected Model	4.119 [a]	7	0.588	259.632	0.000	0.987
Intercept	11.834	1	11.834	5220.932	0.000	0.995
Irrigation Condition	0.263	1	0.263	115.947	0.000	0.829
Energy Level	3.810	3	1.270	560.325	0.000	0.986
Irrigation Condition * Energy Level	0.046	3	0.015	6.833	0.002	0.461
Error	0.054	24	0.002	-	-	-
Total	16.008	32	-	-	-	-
Corrected Total	4.174	31	-	-	-	-

Based on estimated marginal means. * The mean difference is significant at the 0.05 level. [a] R Squared = 0.987 (Adjusted R Squared = 0.983).

Table A6. Bonferroni-corrected post hoc tests (Irrigation Condition * Energy Level).

Dependent Variable: Volume							
Energy Level	**(I) Irrigation Condition**	**(J) Irrigation Condition**	**Mean Difference (I-J)**	**Std. Error**	**Sig. [b]**	**95% Confidence Interval for Difference [b]**	
						Lower Bound	**Upper Bound**
7 J	Dry	Wet	−0.103 *	0.033	0.005	−0.170	−0.035
	Wet	Dry	0.103 *	0.033	0.005	0.035	0.170
9 J	Dry	Wet	−0.135 *	0.033	0.000	−0.203	−0.067
	Wet	Dry	0.135 *	0.033	0.000	0.067	0.203
13 J	Dry	Wet	−0.180 *	0.033	0.000	−0.248	−0.112
	Wet	Dry	0.180 *	0.033	0.000	0.112	0.248
15 J	Dry	Wet	−0.335 *	0.033	0.000	−0.403	−0.267
	Wet	Dry	0.335 *	0.033	0.000	0.267	0.403

Based on estimated marginal means. * The mean difference is significant at the 0.05 level. [b] Adjustment for multiple comparisons: Least Significant Difference (equivalent to no adjustments).

Table A7. Bonferroni-corrected post hoc tests (Irrigation Condition * Energy Level).

Dependent Variable: Depth							
Energy Level	(I) Irrigation Condition	(J) Irrigation Condition	Mean Difference (I-J)	Std. Error	Sig. [b]	95% Confidence Interval for Difference [b]	
						Lower Bound	Upper Bound
7 J	Dry	Wet	−0.127 *	0.034	0.001	−0.197	−0.058
	Wet	Dry	0.127 *	0.034	0.001	0.058	0.197
9 J	Dry	Wet	−0.135 *	0.034	0.001	−0.204	−0.066
	Wet	Dry	0.135 *	0.034	0.001	0.066	0.204
13 J	Dry	Wet	−0.150 *	0.034	0.000	−0.219	−0.081
	Wet	Dry	0.150 *	0.034	0.000	0.081	0.219
15 J	Dry	Wet	−0.313 *	0.034	0.000	−0.382	−0.243
	Wet	Dry	0.313 *	0.034	0.000	0.243	0.382

Based on estimated marginal means. * The mean difference is significant at the 0.05 level. [b] Adjustment for multiple comparisons: Least Significant Difference (equivalent to no adjustments).

References

1. Jowett, N.; Wöllmer, W.; Reimer, R.; Zustin, J.; Schumacher, U.; Wiseman, P.W.; Mlynarek, A.M.; Böttcher, A.; Dalchow, V.V.; Lörincz, B.B.; et al. Bone ablation without thermal or acoustic mechanical injury via a novel picosecond infrared laser (PIRL). *Otolaryngol. Head Neck Surg.* **2014**, *150*, 385–393. [CrossRef]
2. Nguendon, H.K.; Faivre, N.; Meylan, B.; Shevchik, S.; Rauter, G.; Guzman, R.; Cattin, P.C.; Wasmer, K.; Zam, A. Characterization of ablated porcine bone and muscle using laser-induced acoustic wave method for tissue differentiation. In Proceedings of the European Conferences on Biomedical Optics, Munich, Germany, 25–29 June 2017; p. 104170N.
3. Romeo, U.; Del Vecchio, A.; Palata, G.; Tenore, G.; Visca, P.; Maggiore, C. Bone damage induced by different cutting instruments: An in vitro study. *Braz. Dent. J.* **2009**, *20*, 162–168. [CrossRef] [PubMed]
4. Kenhagho, H.K.N.; Rauter, G.; Guzman, R.; Cattin, P.C.; Zam, A. Comparison of acoustic shock waves generated by micro and nanosecond lasers for a smart laser surgery system. In Proceedings of the Advanced Biomedical and Clinical Diagnostic and Surgical Guidance Systems XVI, San Francisco, CA, USA, 27 January–1 February 2018; Volume 10484, p. 104840P.
5. Kang, H.W.; Lee, H.; Chen, S.; Welch, A.J. Enhancement of bovine bone ablation assisted by a transparent liquid Layer on a target surface. *IEEE J. Quantum Electron.* **2006**, *42*, 633–642. [CrossRef]
6. Baek, K.W.; Deibel, W.; Marinov, D.; Griessen, M.; Dard, M.; Bruno, A.; Zeilhofer, H.-F.; Cattin, P.; Juergens, P. A comparative investigation of bone surface after cutting with mechanical tools and Er: YAG laser. *Lasers Surg. Med.* **2015**, *47*, 426–432. [CrossRef]
7. Li, Z.Z.; Reinisch, L.; Van de Merwe, W.P. Bone ablation with Er: YAG and CO_2 laser: Study of thermal and acoustic effects. *Lasers Surg. Med.* **1992**, *12*, 79–85. [CrossRef] [PubMed]
8. Kang, H.W.; Rizoiu, I.; Welch, A.J. Hard tissue ablation with a spray-assisted mid-IR laser. *Phys. Med. Biol.* **2007**, *52*, 7243. [CrossRef]
9. Landi, E.; Celotti, G.; Logroscino, G.; Tampieri, A. Carbonated hydroxyapatite as bone substitute. *J. Eur. Ceram. Soc.* **2003**, *23*, 2931–2937. [CrossRef]
10. Apel, C.; Meister, J.; Ioana, R.S.; Franzen, R.; Hering, P.; Gutknecht, N. The ablation threshold of Er: YAG and Er: YSGG laser radiation in dental enamel. *Lasers Med. Sci.* **2002**, *17*, 246–252. [CrossRef]
11. Peavy, G.M.; Reinisch, L.; Payne, J.T.; Venugopalan, V. Comparison of cortical bone ablations by using infrared laser wavelengths 2.9 to 9.2 µm. *Lasers Surg. Med.* **1999**, *25*, 421–434. [CrossRef]
12. Forrer, M.; Frenz, M.; Romano, V.; Altermatt, H.J.; Weber, H.P.; Silenok, A.; Istomyn, M.; Konov, V.I. Bone-ablation mechanism using CO_2 lasers of different pulse duration and wavelength. *Appl. Phys. B* **1993**, *56*, 104–112. [CrossRef]
13. Izatt, J.A.; Sankey, N.D.; Partovi, F.; Fitzmaurice, M.; Rava, R.P.; Itzkan, J.; Feld, M.S. Ablation of calcified biological tissue using pulsed hydrogen fluoride laser radiation. *IEEE J. Quantum Electron.* **1990**, *26*, 2261–2270. [CrossRef]

14. Walsh, J.T., Jr.; Flotte, T.J.; Deutsch, T.F. Er:YAG laser ablation of tissue: Effect of pulse duration and tissue type on thermal damage. *Lasers Surg. Med.* **1989**, *9*, 314–326. [CrossRef]
15. Wong, B.J.F.; Sung, V.; Berns, M.W.; Svaasand, L.O.; Neev, J. Holmium-YAG laser ablation characteristics in calvarial lamellar and cortical bone: The role of water and tissue micro-architecture. *Lasers Med. Sci.* **1995**, *10*, 181–188. [CrossRef]
16. Abbasi, H.; Beltrán, L.; Rauter, G.; Guzman, R.; Cattin, P.C.; Zam, A. Effect of cooling water on ablation in Er: YAG laserosteotome of hard bone. In Proceedings of the Third International Conference on Applications of Optics and Photonics, Faro, Portugal, 8–12 May 2017; Volume 10453, p. 104531I.
17. Beltran, L.; Abbasi, H.; Rauter, G.; Friederich, N.; Cattin, P.; Zam, A. Effect of laser pulse duration on ablation efficiency of hard bone in microseconds regime. In Proceedings of the Third International Conference on Applications of Optics and Photonics, Faro, Portugal, 8–12 May 2017; Volume 10453, p. 104531S.
18. Jacques, S.L. Role of tissue optics and pulse duration on tissue effects during high-power laser irradiation. *Appl. Opt.* **1993**, *32*, 2447–2454. [CrossRef]
19. Rizoiu, I.M.; DeShazer, L.G. New laser-matter interaction concept to enhance hard tissue cutting efficiency. In Proceedings of the Society of Photo-Optical Instrumentation Engineers (SPIE) Conference Series, Los Angeles, CA, USA, 23–29 January 1994; Volume 2134, pp. 309–317.
20. Hibst, R.; Keller, U. Er: YAG laser for dentistry: basics, actual questions, and perspectives. In Proceedings of the International Symposium on Biomedical Optics Europe '94, Lille, France, 6–10 September 1994; Volume 2327, pp. 76–86.
21. Abbasi, H.; Rauter, G.; Guzman, R.; Cattin, P.C.; Zam, A. Laser-induced breakdown spectroscopy as a potential tool for autocarbonization detection in laserosteotomy. *J. Biomed. Opt.* **2018**, *23*, 071206. [CrossRef]
22. Fried, D.; Ashouri, N.; Breunig, T.; Shori, R. Mechanism of water augmentation during IR laser ablation of dental enamel. *Lasers Surg. Med.* **2002**, *31*, 186–193. [CrossRef] [PubMed]
23. Berthe, L.; Fabbro, R.; Peyre, P.; Tollier, L.; Bartnicki, E. Shock waves from a water-confined laser-generated plasma. *J. Appl. Phys.* **1997**, *82*, 2826–2832. [CrossRef]
24. Berthe, L.; Fabbro, R.; Peyre, P.; Bartnicki, E. Wavelength dependent of laser shock-wave generation in the water-confinement regime. *J. Appl. Phys.* **1999**, *85*, 7552–7555. [CrossRef]
25. Dupont, A.; Caminat, P.; Bournot, P.; Gauchon, J.P. Enhancement of material ablation using 248, 308, 532, 1064 nm laser pulse with a water film on the treated surface. *J. Appl. Phys.* **1995**, *78*, 2022–2028. [CrossRef]
26. Zhu, S.; Lu, Y.F.; Hong, M.H.; Chen, X.Y. Laser ablation of solid substrates in water and ambient air. *J. Appl. Phys.* **2001**, *89*, 2400–2403. [CrossRef]
27. Hale, G.M.; Querry, M.R. Optical constants of water in the 200-nm to 200-µm wavelength region. *Appl. Opt.* **1973**, *12*, 555–563. [CrossRef]
28. Leung, B.Y.; Webster, P.J.; Fraser, J.M.; Yang, V.X. Real-time guidance of thermal and ultrashort pulsed laser ablation in hard tissue using inline coherent imaging. *Lasers Surg. Med.* **2012**, *44*, 249–256. [CrossRef] [PubMed]
29. Foster, R.C.B.; Stavas, J.M. Bone and Soft Tissue Ablation. *Semin. Interv. Radiol.* **2014**, *31*, 167–179. [CrossRef] [PubMed]
30. Robertson, C.W.; Williams, D. Lambert absorption coefficients of water in the infrared. *JOSA* **1971**, *61*, 1316–1320. [CrossRef]
31. Nuss, R.C.; Fabian, R.L.; Sarkar, R.; Puliafito, C.A. Infrared laser bone ablation. *Lasers Surg. Med.* **1988**, *8*, 381–391. [CrossRef]
32. Bayly, J.G.; Kartha, V.B.; Stevens, W.H. The absorption spectra of liquid phase H_2O, HDO and D_2O from 0·7 µm to 10 µm. *Infrared Phys.* **1963**, *3*, 211–222. [CrossRef]
33. Saeidi, F.; Shevchik, S.A.; Wasmer, K. Automatic detection of scuffing using acoustic emission. *Tribol. Int.* **2016**, *94*, 112–117. [CrossRef]
34. Vakili-Farahani, F.; Lungershausen, J.; Wasmer, K. Process parameter optimization for wobbling laser spot welding of Ti6Al4V alloy. *Phys. Procedia* **2016**, *83*, 483–493. [CrossRef]
35. Kenhagho, H.N.; Rauter, G.; Guzman, R.; Cattin, P.; Zam, A. Optoacoustic tissue differentiation using a mach-zehnder interferometer: Preliminary results. In Proceedings of the 2018 IEEE International Ultrasonics Symposium (IUS), Kobe, Japan, 22–25 October 2018; p. 18326831.

36. Tsuda, H. Bragg wavelength-insensitive fiber Bragg grating ultrasound detection system based on a fiber ring laser. In Proceedings of the 21st International Conference on Optical Fibre Sensors (OFS21), Ottawa, ON, Canada, 15–19 May 2011; Volume 7753, p. 77538J.
37. Wasmer, K.; Le-Quang, T.; Meylan, B.; Shevchik, S.A. In situ quality monitoring in AM using acoustic emission: A reinforcement learning approach. *J. Mater. Eng. Perform.* **2019**, *28*, 666–672. [CrossRef]
38. Shevchik, S.A.; Kenel, C.; Leinenbach, C.; Wasmer, K. Acoustic emission for in situ quality monitoring in additive manufacturing using spectral convolutional neural networks. *Addit. Manuf.* **2018**, *21*, 598–604. [CrossRef]
39. Othonos, A. Fiber Bragg Gratings. *Rev. Sci. Instrum.* **1997**, *68*, 4309–4341. [CrossRef]
40. Othaonos, A.; Kalli, K. Fiber bragg gratings: Fundamentals and applications in telecommunications and sensing. *Artech House* **1999**, 1–6. [CrossRef]
41. Molugaram, K.; Rao, G.S. Chapter 11-ANOVA (Analysis of Variance). In *Statistical Techniques for Transportation Engineering*; Molugaram, K., Rao, G.S., Shah, A., Davergave, N., Eds.; Butterworth-Heinemann: Oxford, UK, 2017; pp. 451–462.
42. Kéry, M. Chapter 10-Normal two-way ANOVA. In *Introduction to WinBUGS for Ecologists: Bayesian approach to regression, ANOVA, mixed models and related analyses*; Academic Press: Boston, MA, USA, 2010; pp. 129–139.
43. Kucuk, U.; Eyuboglu, M.; Kucuk, H.O.; Degirmencioglu, G. Importance of using proper post hoc test with ANOVA. *Int. J. Cardiol.* **2016**, *209*, 346. [CrossRef] [PubMed]
44. Lukac, N.; Suhovršnik, T.; Lukač, M.; Jezeršek, M. Ablation characteristics of quantum square pulse mode dental erbium laser. *J. Biomed. Opt.* **2016**, *21*, 015012. [CrossRef] [PubMed]
45. Kuscer, L.; Diaci, J. Measurements of erbium laser-ablation efficiency in hard dental tissues under different water cooling conditions. *J. Biomed. Opt.* **2013**, *18*, 108002. [CrossRef] [PubMed]
46. Qin, Q.; Attenborough, K. Characteristics and application of laser-generated acoustic shock waves in air. *Appl. Acoust.* **2004**, *65*, 325–340. [CrossRef]
47. Yuldashev, P.; Ollivier, S.; Averiyanov, M.; Sapozhnikov, O.; Khokhlova, V.; Blanc-Benon, P. Nonlinear propagation of spark-generated N-waves in air: Modeling and measurements using acoustical and optical methods. *J. Acoust. Soc. Am.* **2010**, *128*, 3321–3333. [CrossRef] [PubMed]
48. Bilaniuk, N. Optical microphone transduction techniques. *Appl. Acoust.* **1997**, *50*, 35–63. [CrossRef]

Curriculum Vitae

NGUENDON KENHAGHO, Hervé
Dorfstrasse 36
D-79576 Weil am Rhein
0041612075461
herve.nguendon@unibas.ch
www.linkedin.com/in/nguendon

❑ Education

2016-2020 **Ph.D. in Biomedical Engineering**, *University of Basel, Basel*, Switzerland.
2009-2010 **M.Sc. Microelectronic and Communication Engineering**, *Northumbria University*, Newcastle upon Tyne, England.
2006-2009 **B. (Hons)Eng. Communication and Electronic Engineering**, *Northumbria University, Newcastle upon Tyne, England.*

❑ Professional Certificates

2017-2017 **CTI Start-up Entrepreneurship**, *Innovation center,* Allschwil, Switzerland.
2016-2016 **Laser Safety Officer**, *Saarland University, Saarbrücken, Germany.*

❑ Work Experience

2016-2020 **Research Member (100**%) in the flagship project MIRACLE found by Werner Siemens-Stiftung, *BLOG (University of Basel),* Allschwil, Switzerland.
Research in the field of optoacoustic sensor development as a feedback for smart laser surgery.

2013-2015 **Early Stage Researcher (100%)** in the OILTEBIA and MITHPHO Project found by Marie Curie ITN, ***GOTL*** *(University Carlos III de Madrid)* Leganés, Spain.
Research in the field of laser optoacoustic and Microwave Photonic systems for gold nanorods-nanoparticles, carbon nanotubes and graphene to optimize compact electronic and THz devices.

2012-2013 **Scientific coworker (100%)**, *PPI (Leuphana Universität),* Lüneburg, Germany.
Research in the field of signal processing for UWB Radar and Electromagnetic valve Actuator in medical and automobile applications.

2011-2012 **Calibration Engineer (100%)**, *RCL (*Repair & Calibration Laboratories Ltd), Reading, England.
Measurements, calibrations and maintenance of digital multimeters, oscilloscope capacitances impedance boxes, electromagnetic coils and power sources.

❑ Publications

Journals

Published

Hervé Nguendon, Neige Faivre, Bastian Meylan, Sergey Shevchik, Georg Rauter, Raphael Guzman, Philippe C. Cattin, Kilian Wasmer, Azhar Zam, "Characterization of Ablated Bone and Muscle for Long-Pulsed Laser Ablation in Dry and Wet Conditions," *Materials*, vol. 12, no. 8, p. 1338, 2019. DOI: 10.3390/ma12081338.

Hervé Nguendon, Georg Rauter, Raphael Guzman, Philippe C. Cattin, and Azhar Zam, "Optoacoustic Tissue Differentiation using a Mach-Zehnder Interferometer," IEEE Transactions on Ultrasonics, Ferroelectrics, and Frequency Control, pp. 1435-1443, 2019. DOI: 10.1109/TUFFC.2019.2923696.

Hervé Nguendon, Ferda Canbaz, Raphael Guzman, Philippe C. Cattin, Azhar Zam, " Machine Learning-based Optoacoustic Tissue Classification Method for Laser Osteotomes Using an Air-coupled Transducer," in Lasers in Surgery and Medicine. DOI: 10.1002/lsm.23290.

Hervé Nguendon, Ferda Canbaz, Raphael Guzman, Philippe C. Cattin, Azhar Zam, "Miniaturized Optoacoustic Feedback Sensor for Smart Laser Osteotome: Fiber-Coupled Fabry-Pérot Etalon Sensor," Sensors and Actuators A: Physical. Doi.: 10.1016/j.sna.2020.112394.

Ready to be submitted

Hervé Nguendon, Ferda Canbaz, Alois Hopf, Raphael Guzman, Philippe C. Cattin, Azhar Zam, Optoacoustic Sciatic Nerve Detection Using an All-Fiber Optical Sensor for Endoscopic Smart Laser Surgery," Journal of Biophotonics.

Carlo Seppi, Antal Horváth, Hervé Nguendon, Eva Schnider, Georg Rauter, Azhar Zam, and Philippe C. Cattin, "1D-CNN Tissue Classification with Er:YAG Laser using Acoustic Waves," IEEE Access.

Peer-Reviewed Conference Proceedings

Published

Hervé Nguendon, Neige Faivre, Bastian Meylan, Sergey Shevchik, Georg Rauter, Raphael Guzman, Philippe C. Cattin, Kilian Wasmer, and Azhar Zam, "Characterization of ablated porcine bone and muscle using laser-induced acoustic wave method for tissue differentiation," in European Conferences on Biomedical Optics, 2017, vol. 10417, p. 10: SPIE. Doi: 10.1117/12.2286121.

Hervé Nguendon, Georg Rauter, Raphael Guzman, Philippe C. Cattin, and Azhar Zam, "Comparison of acoustic shock waves generated by micro and nanosecond lasers for a smart laser surgery system," in SPIE BiOS, 2018, vol. 10484, p. 9: SPIE. Doi: 10.1117/12.2290094.

Hervé Nguendon, Georg Rauter, Raphael Guzman, Philippe C. Cattin, and Azhar Zam, "Optoacoustic Tissue Differentiation Using a Mach-Zehnder Interferometer: Preliminary Results," in *2018 IEEE International Ultrasonics Symposium (IUS)*, 2018, pp. 1-9, DoI: 10.1109/ULTSYM.2018.8579654.

Hervé Nguendon, Ferda Canbaz, Raphael Guzman, Philippe C. Cattin, and Azhar Zam, "A First Approach to Miniaturized Optoacoustic Feedback Sensor for Smart Laser Osteotome: Fiber-Coupled Fabry-Pérot Etalon Sensor," in *2019 IEEE SENSORS*, 2019, pp. 1-4, Doi: 10.1109/SENSORS43011.2019.8956743.

Hervé Nguendon, Irena Sugiarto, Raphael Guzman, Philippe C. Cattin, and Azhar Zam, "Contact-free Crater Depth Monitoring Using Measured Acoustic Shock Waves for Smart Laser Surgery Applications: Preliminary Result," In 2019 International Conference on Radar, Antenna, Microwave, Electronics, and Telecommunications (ICRAMET), 2019, pp. 118-121, Doi: 10.1109/ICRAMET47453.2019.8980427.

Hervé Nguendon, Yakub Aqib Bayhaqi, Ferda Canbaz, Raphael Guzman, Philippe C. Cattin, and Azhar Zam, "Optoacoustic Tissue Classification for Laser Osteotomes Using Mahalanobis Distance-Based Method," In: Rauter G., Cattin P.C., Zam A., Riener R., Carbone G., Pisla D. (eds) New Trends in Medical and Service Robotics. MESROB 2020. Mechanisms and Machine Science, 2021, vol. 93: Springer, Cham, 2020, pp. 2002-2010, Doi.: 10.1007/978-3-030-58104-6_23.

Oral Presentations

Hervé Nguendon, Neige Faivre, Bastian Meylan, Sergey Shevchik, Georg Rauter, Raphael Guzman, Philippe C. Cattin, Kilian Wasmer, and Azhar Zam, "Characterization of ablated porcine bone and muscle using laser-induced acoustic wave method for tissue differentiation," Proc. SPIE 10417, Medical Laser Applications and Laser-Tissue Interactions VIII, 104170N, Munich, Germany, 1 August 2017.

Hervé Nguendon, Georg Rauter, Raphael Guzman, Philippe C. Cattin, and Azhar Zam, "Comparison of acoustic shock waves generated by micro and nanosecond lasers for a smart laser surgery system," Proc. SPIE BiOS 10484, Advanced Biomedical and Clinical Diagnostic and Surgical Guidance Systems XVI, 104840P, San Francisco, USA, 12 February 2018.

Hervé Nguendon, Georg Rauter, Raphael Guzman, Philippe C. Cattin, and Azhar Zam,"Optoacoustic Tissue Differentiation using a Mach-Zehnder Interferometer: Preliminary Results," Proc. IEEE Ultrasonics, Ferroelectrics, and Frequency Control Society, Kobe, Japan, 23 October 2018.

Hervé Nguendon, Georg Rauter, Raphael Guzman, Philippe C. Cattin, and Azhar Zam," Optoacoustic Tissue Differentiation for Smart Laser Osteotome," EUCOR Networking Event, ICube Laboratory of the University of Strasbourg, France, 30 April 2019.

Hervé Nguendon, Ferda Canbaz, Tomas E. Gomez Alvarez-Arenas, Raphael Guzman, Philippe C. Cattin, and Azhar Zam, "A First Approach to Miniaturized Optoacoustic Feedback Sensor for Smart Laser Osteotome: Fiber-Coupled Fabry-Pérot Etalon Sensor," Proc. IEEE Sensors, Montreal, Canada, 29 October 2019.

Poster Presentations

Hervé Nguendon, Georg Rauter, Raphael Guzman, Philippe C. Cattin, and Azhar Zam," Measurement of shock wave based on Mach-Zehnder interferometry and microphone for tissue differentiations", Backafallsbyn in Island of Ven, 10 -17 Jun 2017.

Hervé Nguendon, Georg Rauter, Raphael Guzman, Philippe Cattin, and Azhar Zam," Opto-Acoustical System for Laser surgery", 1st DBE Research Day, Zentrum für Lehre und Forschung, Basel, 7 September 2016.

Hervé Nguendon, Georg Rauter, Raphael Guzman, Philippe Cattin, and Azhar Zam," Differentiation of hard and soft tissues using Mach-Zehnder interferometer", International Conference on BioMedical Photonics, Montpellier, France, 16-17 March 2018.

Hervé Nguendon, Georg Rauter, Raphael Guzman, Philippe C. Cattin, and Azhar Zam, "Tissue differentiations based on laser-induced acoustic wave using Fiber Bragg Grating in free space," 2nd DBE Research Day, Zentrum fur Lehre und Forschung, Hebelstrasse 20, 4056 Basel, 23 August 2017.

Azhar Zam, and Hervé Nguendon," Biomedical Laser and Optics Group (BLOG) Project Presentation," Switzerland Innovation Park Basel area, Gewerbestrasse 24, 4123 Allschwil, 28 September 2017.

Hervé Nguendon, Georg Rauter, Raphael Guzman, Philippe Cattin, and Azhar Zam," Opto-Acoustical System for Laser surgery," 3nd DBE Research Day, Zentrum fur Lehre und Forschung, 4056 Basel, 5 September 2018.

Hervé Nguendon, Georg Rauter, Raphael Guzman, Philippe Cattin, and Azhar Zam," Miniaturized Optoacoustic Feedback Sensor for Smart Laser Osteotome," The 4nd DBE Research Day, Zentrum fur Lehre und Forschung, 4056 Basel, 5 August 2019.

Hervé Nguendon, Yakub Aqib Bayhaqi, Ferda Canbaz, Tomas E. Gomez Alvarez-Arenas, Georg Rauter, Raphael Guzman, Philippe Cattin, and Azhar Zam, " Optoacoustic Tissue Classification for Laser Osteotomes Using Mahalanobis Distance-based Method," The European Conferences on Biomedical Optics, SPIE/OSA 11077, Opto-Acoustic Methods and Applications in Biophotonics, Munich, Germany, 23-27 Jun 2019.